INTERNATIONAL ATOMIC ENERGY AGENCY
UNITED NATIONS EDUCATIONAL, SCIENTIFIC AND CULTURAL ORGANIZATION
INTERNATIONAL CENTRE FOR THEORETICAL PHYSICS
I.C.T.P., P.O. BOX 586, 34100 TRIESTE, ITALY, CABLE: CENTRATOM TRIESTE

H4.SMR/841-4

FOURTH ICTP-URSI-ITU(BDT) COLLEGE ON RADIOPROPAGATION:
Propagation, Informatics and Radiocommunication System Planning

30 January - 3 March 1995

Miramare - Trieste, Italy

Climatic Information for Satallite Communication Planning

G.O. Ajayi
Obafemi Awolowo University
Ilfe-Ife, Nigeria

INTERNATIONAL ATOMIC ENERGY AGENCY

AND

UNITED NATIONS EDUCATIONAL SCIENTIFIC AND CULTURAL ORGANIZATION

INTERNATIONAL CENTRE FOR THEORETICAL PHYSICS

CLIMATIC INFORMATION FOR SATELLITE COMMUNICATION PLANNING.

PART 1 - GENERAL BACKGROUND

Prof. G.O. Ajayi
Department of Electronic & Electrical Engineering
Obafemi Awolowo University,
Ile-Ife, Nigeria.

FOURTH ICTP-URSI-ITU (BDT) COLLEGE ON RADIOPROPAGATION:
Propagation, Informatics and Radiocommunication System Planning.

30 January - 3 March, 1995.

1. INTRODUCTION

The satellite communication system can be broadly divided into three segments, viz:

(i) the Earth Station Segment

(ii) the Communication Channel

(iii) the Space Segment.

The basic concept of a satellite communication system is shown in Fig. 1.

The evolution of INTELSAT satellites up to INTELSAT VI is shown in Fig. 2 (Ref. 1).

Table 1(a) shows the frequency bands and ranges of frequencies used in the field of telecommunications while Table 1(b) gives some characteristics of frequencies used for radar and space radiocommunications. The other frequencies used for satellite communication are listed below.

6/4 GHz	5925 - 6425 MHz	Uplink	Commercial
	3700 - 4200 MHz	Downlink	
8/7 GHz	7900 - 8400 MHz	Uplink	Military
	7250 - 7750 MHz	Downlink	
14/11 GHz	14.0 - 14.5 GHz	Uplink	Commercial
	10.7 -13.25 GHz	Downward	
30/20 GHz	27.5 - 30.5 GHz	Uplink	Commercial
	17.7 - 20.2 GHz	Downlink	
30/20 GHz	30.0 - 31.0 GHz	Uplink	Military
	20.2 - 21.2 GHz	Downlink	
44/20 GHz	43.5 - 45.5 GHz	Uplink	Military
	20.2 - 21.2 GHz	Downlink	

2. EARTH STATION SEGMENT

The major component of the earth station is the antenna and the associated transmitting and receiving facilities.

Standard earth stations are those earth stations which conform to the mandatory performance characteristics for operation in the specified frequency band and which have an operating elevation angle to the satellite of not less than the values given below:

(i) 5 degrees for earth stations operating in the C-band (6/4 GHz).

(ii) 10 degrees for earth stations operating in the Ku-band (14/11 GHz).

2.1 Earth Station Technology

Fig. 3 shows the functional block diagram of an earth station. The complexity depends on

(i) whether it is used for TX/RX or TX only or RX only.
(ii) redundancy facilities
(iii) single or dual-polarisation operation
(iv) carrier types
(v) volume of traffic.

Large antennas have very narrow beams, e.g. 0.3 for an 11m antenna at 6 GHz. Automatic satellite tracking is therefore an essential feature of an earth station, except for very small earth stations.

On the downlink, the extremely-weak signal received is amplified by the low-noise amplifier (LNA). For C-band, the signal is in the range 3.7 - 4.2 GHz. and for Ku band, it is 10.95 - 12.75 GHz. Its frequency is changed to the IF (70 or 140 MHz) in the down converter and then the demodulator recovers the traffic signal.

The EIRP and G/T determine RF transmission and reception capabilities of an earth station.

where G = antenna gain at the receive frequency

T = noise temperature of the antenna and receiver referred to its input.

GaAs FET are mostly used LNA and parametric amplifier to a lesser degree. Almost all current cooled LNAs use thermoelectric cooling instead of the old type cryogenically-cooled parametric amplifiers.

The Rf power range for earth stations range from around 1W to 3kW. HPA types are:

(i) TWT amplifiers for the range 20W to 3kW wide operational bandwidth (500MHz) - mostly used.

(ii) Klystron amplifiers are used in high power (> 600W) applications in which the RF power falls within a transponder bandwidth.

(iii) Solid state amplifiers (e.g. single stage GaAs FET) provide about 8W at Ku band and 30W at C-band.

2.1.1 Link Budget

Up-link and down-link parameters are selected to obtain the required carrier-to-noise ratio (C/N) at the satellite and the

earth station respectively.

For the uplink, the earth-station antenna must be large and the RF power high in order to produce sufficient signal strength at the satellite to overcome the noise due to the "hot" earth at which its antenna is pointing.

For the downlink, the power transmitted by the satellite is normally much lower. Fortunately, the earth station's antenna is looking at the coldness of space, so much less noise is received.

For each link, the received carrier-to-noise ratio is given by

$$C/N = E - L + G - N - M \quad dB$$

where

E	=	EIRP
L	=	Path loss
G	=	Gain of the receiving antenna
N	=	Thermal noise power
M	=	Required operating margin.

EIRP	=	f(P,G)	
G	=	f(D,f)	D - diameter, f - frequency
L	=	f(f,d)	d - slant path length.

M - Margin is required to accommodate variations in path length and transmitter power and additional attenuation due to rain.

Thermal noise power N at the receiver is given by

$$N = -228.6 + 10\log_{10} T + 10\log_{10} W + 60 \quad dBW$$

where T = noise temperature, K
W = bandwidth, MHz.

Since the antenna gain increases the signal power, this is equivalent to reducing the noise power. Thus, the equivalent noise power is:

$$N_e = -228.6 - (G/T) + \text{band width factor} \quad dBW$$

where G/T is in dB/K and the bandwidth factor is

$$10\log_{10} W + 60 \quad dBW.$$

There is limitation in satellite EIRP, hence downlink is more critical in terms of noise than the uplink. Link Budget for an 11 GHz downlink to an Earth Station.

Receiver bandwith is 36 MHz.

Satellite HPA output rating (20W)	+13	dBW
Back off	-2	dB
Waveguide losses	-1	dB
Antenna gain	30	dB
Satellite EIRP	40	dBW
Path loss at 11 GHz	205.5	dBW
Received power	-165.5	dBW
Boltzmann's constant	-228.6	dBW/Hz/K
Bandwidth factor (for 36 MHz)	75.6	dB Hz
Earth-station G/T factor	34	dB/K
Equivalent noise power	-187	dBW
C/N = -165.5-(-187)	=21.5	dB

2.2 Standard Earth Stations (Ref. 2)

2.2.1 Standard A

Used widely for international telecommunications. It uses a large parabolic antenna (about 30m in diameter). The G/T (Figure of merit) is nominally 40.7 dB/k. It operates in the 6/4 GHz frequency band. $G/T \geq 35.0 + 20 \log f/4$ dB/K.

where f is the receive frequency in GHz.

2.2.2 Standard B

A standard B earth station which generally has a parabolic antenna of about 11m in diameter and operates in the 6/4 GHz frequency bands is particularly suited for countries with small traffic demands. Figure of merit (G/T) is nominally 31.7 dB/K.

$$G/T \geq 31.7 + 20 \log (f/4) \text{ dB/K}$$

where f is the receive frequency in GHz.

2.2.3 Standard C

The antenna is between 14 and 19 metres in diameter within the frequency bands 14/11 GHz. Figure of merit (G/T) is nominally about 40 dB/K.

$$G/T \geq 37.0 + 20 \log (f/11.2) \text{ dB/K.}$$

f is the receive frequency in GHz.

The above G/T refers to clear weather conditions. For degraded weather conditions (i.e. heavy rain storms), figure of

merit is given by

$$G/T \geq 37.0 + 20 \log \left(\frac{f}{11.2}\right) + X \text{ (dB/K)}$$

where X is the excess (attenuation) of the downlink degradation predicted by local rain statistics over the reference downlink degradation margin given in Table 2. Downlink degradation is the sum of the precipitation attenuation in dB and the increase in receiving system noise temperature in dB for the given time percentage.

2.2.4 Standard D (Vista)

There are two versions of the Standard D earth station: D-1 and D-2. Frequency band is 6/4 GHz.

D-1 is a small (5m) low cost earth station for rural/remote areas providing minimal capacity. Standard D-2 (11m) is equivalent to a Standard B earth station and is used as a central or main station in the "Vista" network.

$G/T \geq 22.7 + 20 \log (f/4)$ dB/K D - 1

$G/T \geq 31.7 + 20 \log (f/4)$ dB/K D - 2

where f is the receive frequency in GHz.

2.2.5 Standard E (IBS)

Frequency bands: 14/12 and 14/11 GHz used for INTELSAT Business services.

There are three versions: E-1 (3.5m), E-2 (5.5m) and E-3 (8m). The G/T values for clear sky conditions are:

$G/T \geq 25.0$ (but < 29.0) $+ 20 \log (f/11)$ dB/K E - 1
$G/T \geq 29.0$ (but < 34.0) $+ 20 \log (f/11)$ dB/K E - 2
$G/T \geq 34.0 + 20 \log (f/11)$ dB/K E - 3

where f is the frequency in GHz.

The G/T values for degraded weather conditions (i.e. heavy rain storms) are:

$G/T \geq 25.0 + 20 \log (f/11) + X$ dB/K E - 1
$G/T \geq 29.0 + 20 \log (f/11) + X$ dB/K E - 2
$G/T \geq 34.0 + 20 \log (f/11) + X$ dB/K E - 3

where X is the excess of the downlink degradation predicted by local rain statistics over the reference downlink degradation

margin shown in Table 2.

2.2.6 Standard F

Frequency band: 6/4 GHz.
Used for business services.

G/T	≥ 22.7 + 20 log (f/4) dB/K	F-1 (5m)
G/T	≥ 27.0 + 20 log (f/4) dB/K	F-2 (7m)
G/T	≥ 29.0 + 20 log (f/4) dB/K	F-3 (9m)

where f is the frequency in GHz.

2.2.7 Standard G

These earth stations can access the INTELSAT space segment through the use of the fractional transponder power and bandwidth.

2.2.8 Standard Z

These are domestic earth stations which use either the 6/4 GHz or 14/11 GHz frequency bands. There is no specific G/T, antenna size requirement, but the characteristics are similar to Standard A, B and C.

2.3 Functional Operation of a "Standard" Earth Station

Fig.3 is a simple block diagram of an earth station showing the communication sub-system only.

The operation in the FDMA/FM mode is similar to that of an LOS radiolink system, except the following variances.

(i) Use of LNA e.g. cryogenically cooled for large earth stations and GaAs FETS for small earth stations.

(ii) An HPA (e.g. 200 to 800 W output).

(iii) Larger high-efficiency antennas and feeds.

(iv) Use of a signal-processing technique that allows nearly constant transmitter loading (e.g. spreading waveform) (FM systems).

(v) Use of threshold extension demodulators in some cases (FM systems only).

(vi) Use of forward error correction (FEC) on many digital systems, and above 10GHz, possibly with interleaving to mitigate rainfall fading.

2.4 The Antenna Subsystem

Earth stations most commonly use parabolic dish reflector antennas or derivatives thereof. Dish diameters range from 1 to 30m. The antenna design and size are largely determined by the required station G/T rather than EIRP. The aperture (e.g. diameter) of the dish determines the antenna gain. The cassegrain feed with a parabolic dish configuration is popular. Antennas of diameter less than about 10m often use a front mounted feed horn for economy.

Antenna side-lobe envelope limits (dB) of $32 - 25 \log \Theta$ relative to the main beam maximum level have been accepted internationally, where Θ is the angular distance in degrees from the main lobe maximum.

Figs. 4 and 5 show a cassegrain antenna and a prime focus antenna functional operation respectively.

3. THE COMMUNICATION CHANNEL

The communication channel for the satellite communication is the propagation medium between the Earth and the Satellite. The propagation characteristics of the medium depend on climatic factors, which also depend on regional factors to some extent. These characteristics are very essential for efficient design of communication systems. Scientific studies have led to reliable modelling of the Earth-satellite communication channel from the propagation data emanating from radio propagation research work.

4. SPACE SEGMENT

The communication satellite configuration is shown in Fig. 6 consisting of the following:

(i) Power supply subsystem
(ii) Attitude and orbit control subsystem
(iii) Telemetry and command subsystem
(iv) Communications subsystems.

Intelsat - IV communication subsystem is shown in Fig.7, while Figures 8 and 9 show respectively single conversion transponder for 6/4 GHz and double conversion for 14/11 GHz. Figures 10(a), (b) and (c) show respectively the uplink model, satellite transponder and downlink model.

4.1 Satellite Orbits

The choice is restricted to three basic types, namely: polar, equatorial and inclined as in Fig.11.

4.1.1 Circular Polar Orbit

This is the only orbit that can provide full global coverage by one satellite but requires a number of orbits to do so. In view of economic, technical and operational disadvantages, it is not popular for telecommunications.

4.1.2 Elliptically Inclined Orbit

Its use is limited mainly to temperate and polar regions. It has been used for the Russian domestic system. In the system, the elliptical orbit has an angle of inclination of 63 degrees and a 12-hour orbit. By using three satellites, suitably phased, continuous coverage of a particular temperate region can be provided. Examples are Orbita and Molniya systems. The elliptical orbit is not suitable for a global network.

4.1.3 Circular Equatorial Orbit

Circular orbits in the equatorial plane permit fewer satellites and ground stations to be used. A satellite in a circular orbit at 35,780 km altitude has a period of 24 hours and therefore appears stationary over a fixed point on the earth's surface. Three such satellites spaced 120° would give global coverage.

4.1.4 Geostationary Orbit Satellites

Some of the salient features of geostationary satellite communications are:

(i) capability of multiple access.
(ii) wide satellite coverage.
(iii) high quality and wideband communications.
(iv) availability for mobile communications.
(v) economic efficiency.

Some of the problems are:

(i) Propagation time

A maximum propagation time of about 270 msecs is required for signals over a single-hop circuit for a geostationary orbit at an altitude of 35,780 km. As a result of mismatch, for example for conversion from two-wire system to the four-wire system, echoes are developed. Echo cancellers are now available to eliminate this defect.

(ii) Eclipse Effect

During the solar eclipse (around the vernal and autumnal equinox seasons), which takes place for 69 minutes maximum a day for about 45 successive days, the solar cells do not generate electricity and therefore the electric power needed has to be supplied from conventional batteries.

(iii) Sun Interference

At the time of the vernal and autumnal equinox the sun approaches toward a geostationary satellite as seen from an earth station and this brings solar noise into the earth station's receiving signals, resulting in a decrease of the S/N for about 10 minutes maximum a day for several days.

Figure 12 shows the relationship between locations of earth station and geostationary satellite, which can be used to obtain elevation angle at a site.

4.2 Low Earth Orbit (LEO) Satellites

In the next century, personal communication system using LEO satellites is expected to provide voice and data communications on a worldwide basis. A constellation of LEO satellites would provide time continuous coverage either regionally or nearly globally.

LEO satellite systems operating below 1 GHz have the following characteristics

- low launch cost
- low mass simple satellites (about 150kg)
- global time continuous coverage requires about 20 satellites in circular inclined orbits with an altitude of 750 - 1,500 km.
- reduced path loss allowing omni-directional terminal antenna.
- low cost hand held terminal with norminal 2 Watt burst transmitter with omni-directional antenna.

LEO mobile satellite systems have been proposed which use FDMA and CDMA techniques.

Considering propagation effects and current technology the most desirable operating frequency is in the 100 - 150 MHz band. Representative parameters for LEO mobile - satellite systems below 1 GHz are shown in Table 3 (Ref. 3).

LEO MSS has also been proposed (IRIDIUM), which consists of a constellation of 77 satellites at a height of 780 km. The constellation of satellites would be in polar orbits and would

occupy 7 planes. The satellite orbits are designed generally to provide continuous line-of sight coverage to and from every point on the earth's surface. The IRIDIUM System Overview and the constellation of satellites for the proposed system are shown in Figures 13(a) and (b) (Ref. 4). The L (1.5/1.6 GHz) and S (2.5/2.6 GHz) bands are being considered for LEOs.

Satellite Orbital Location	Earth Station Location in Satellite Beam	Reference Downlink Degradation Margin (dB)	Percentage of Year Margin can be Exceeded (%)
325.5 - 341.5 and 174 - 180 E	West Spot	13	0.03
	East Spot	11	0.01
307.0 - 310.0 E	West Spot	13	0.02
	East Spot	11	0.02

The margins are for clear-sky conditions

Courtesy of INTELSAT.

Table 2: Reference downlink degradation margin for G/T determination (Ref. 2).

5. REFERENCES

1. INTELSAT - The global telecommunications cooperative

2. Freeman R. L.: Telecommunication Transmission Handbook, John Wiley & Sons Inc., 1991.

3. CCIR Report: Technical and operational bases for the World Administrative Radio Conference 1992 (WARC-92).

4. IRIDIUM: Personal Communications for the World: System Overview and Spectrum Considerations, 1991.

Band number	Symbols	Frequency range (lower limit exclusive, upper limit inclusive)	Corresponding metric subdivision	Metric abbreviations for the bands
3	ULF	300-3 000 Hz	Hectokilometric waves	B.hkm
4	VLF	3-30 kHz	Myriametric waves	B.Mam
5	LF	30-300 kHz	Kilometric waves	B.km
6	MF	300-3 000 kHz	Hectometric waves	B.hm
7	HF	3-30 MHz	Decametric waves	B.dam
8	VHF	30-300 MHz	Metric waves	B.m
9	UHF	300-3 000 MHz	Decimetric waves	B.dm
10	SHF	3-30 GHz	Centimetric waves	B.cm
11	EHF	30-300 GHz	Millimetric waves	B.mm
12		300-3 000 GHz	Decimillimetric waves	B.dmm
13		3-30 THz	Centimiilimetric waves	B.cmm
14		30-300 THz	Micrometric waves	B.µm
15		300-3 000 THz	Decimicrometric waves	B.dµm

Note 1 - "Band number N" extends from 0.3×10^N to 3×10^N Hz.

Note 2 - Symbols:
Hz: hertz
K: kilo (10^3), M: mega (10^6), G: giga (10^9), T: tera (10^{12})
µ: micro (10^{-6}), m: milli (10^{-3}), c: centi (10^{-2}), d: deci (10^{-1})
da: deca (10), h: hecto (10^2), Ma: myria (10^4)

Note 3 - This nomenclature, used for designating frequencies in the field of telecommunications, may be extended to cover the ranges shown below, as is proposed by the International Union of Radio Science (URSI) (see Table 1(b))

Table 1(a)

Letter symbols	Radar (GHz)		Space radiocommunications	
	Spectrum regions	Current limits	Nominal designations	Current limits (GHz)
L	1-2	1.215-1.4	1.5 GHz band	1.525-1.710
S	2-4	2.3-2.5 2.7-3.4	2.5 GHz band	
C	4-8	5.25-5.85	4/6 GHz band	3.7-4.2 5.925-6.425
X	8-12	8.5-10.5	–	
Ku	12-18	13.4-14.0 15.3-17.3	11/14 GHz band 12/14 GHz band	10.7-13.25 14.0-14.5
K	18-27	24.05-24.25	20 GHz band	
Ka	27-40	33.4-36.0	30 GHz band	

Table 1(b)

TABLE 3

Representative parameters for LEO mobile-satellite systems below 1 GHz

	FDMA	CDMA
Antenna type	Whip	Omnidirectional
Minimum G/T	-36.5 dB/K	-30 dB/K
Receive data rate	4800 bit/s	8334 bit/s
Nominal C/N_0	20.7 dBHz	51.4 dBHz
Transmit data rate	2400 bit/s	4116 bit/s
Minimum channel spacing	10 kHz (up link) 15 kHz (down link)	N/A N/A
Omnidirectional Earth-to-space transmission		
– Bandwidth	2.4 kHz (2)	1 MHz
– Antenna gain	1.5 dBi	0 dBi
– e.i.r.p. (1)	9 dBW	3 dBW
– Simultaneous channels	20	20
Directional Earth-to-space transmission		
– Bandwidth	56 kHz	1 MHz
– Max. Ant. beamwidth	10°	10°
– e.i.r.p. per channel	25 dBW	7.8 dBW
– Simultaneous channels	1	4
Satellite space-to-Earth transmission		
– pfd (1) dB(W/m²/4 kHz)	-124	-160
– Bandwidth	7.2 kHz (2)	1 MHz

Notes: (1) Values given are for frequencies near 150 MHz.
To convert to another frequency, f, add 20 log(f/150 MHz).

(2) For FDMA techniques these are minimum values per channel.

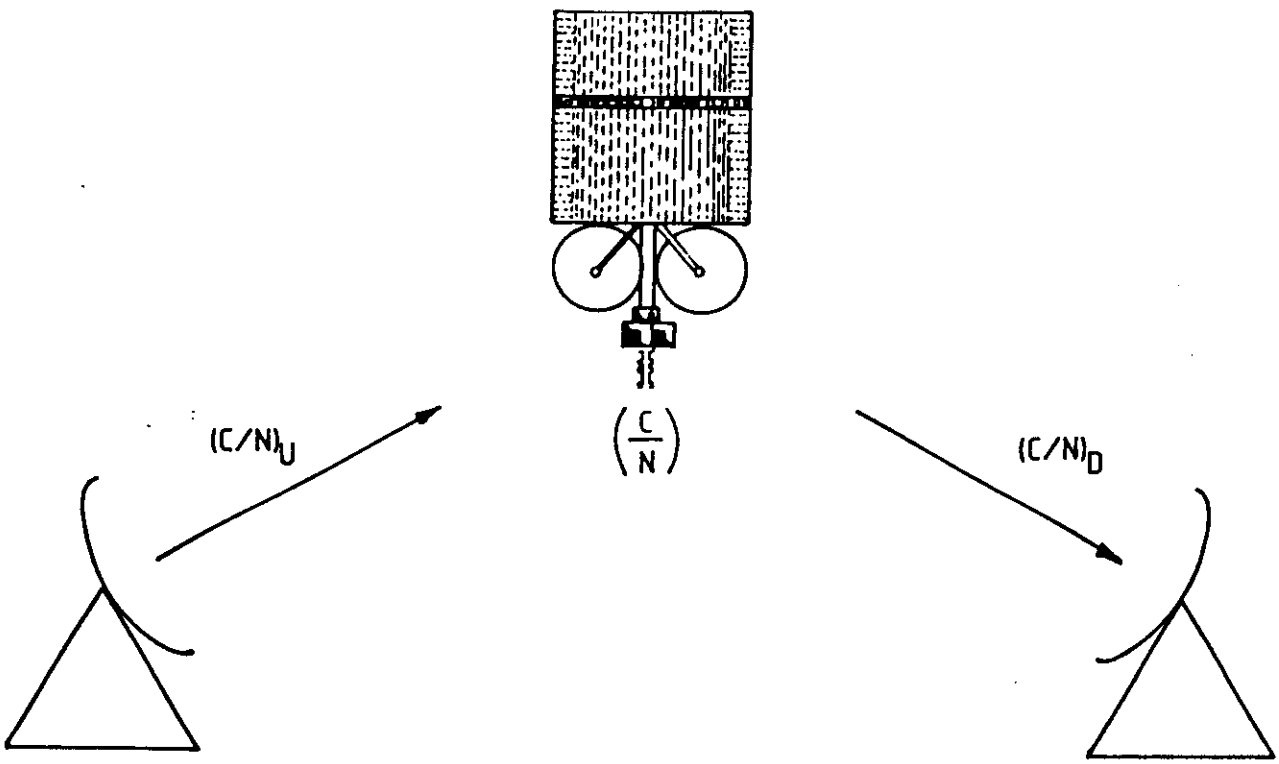

FIG 1 EARTH STATION TO EARTH STATION VIA SATELLITE

Fig 2

EVOLUTION OF INTELSAT SATELLITES

The improved design of INTELSAT satellites has yielded increased capacity and reduced costs for service.

INTELSAT Designation	I	II	III	IV	IV-A	V	V-A	VI
Year of First Launch	1965	1967	1968	1971	1975	1980	1985	1987
Prime Contractor	Hughes	Hughes	TRW	Hughes	Hughes	Ford Aerospace	Ford Aerospace	Hughes
Width Dimensions, m.(Undeployed)	0.7	1.4	1.4	2.4	2.4	2.0	2.0	3.6
Height Dimensions, m.(Undeployed)	0.6	0.7	1.0	5.3	6.8	6.4	6.4	6.4
Launch Vehicles	Thor Delta	Thor Delta	Thor Delta	Atlas Centaur	Atlas Centaur	Atlas Centaur or Ariane 1, 2	Atlas Centaur or Ariane 1, 2	NASA STS (Shuttle) or Ariane 4
Design Lifetime, Years	1.5	3	5	7	7	7	7	10
Bandwidth, MHz.	50	130	300	500	800	2,144	2,250	3,300
Capacity								
Voice Circuits	240	240	1,500	4,000	6,000	12,000	15,000	30,000
Television Channels	—	—	—	2	2	2	2	3

THE INTELSAT SPACE SEGMENT

The space segment of the INTELSAT network currently consists of 16 satellites in geosynchronous orbit over the Atlantic, Indian, and Pacific Ocean regions at an altitude of approximately 35,780 kilometers or 22,240 miles.

At present, global services are provided by a combination of IV-A, V, and V-A satellites.

The next generation of satellites, INTELSAT VI, will have a capacity of 30,000 voice circuits, plus three television channels. The first INTELSAT VI is scheduled for launch in 1987.

INTELSAT maintains eight telemetry, tracking, command and monitoring stations around the world. These stations track the satellites' orbits, check their positions and constantly relay vital information on their operations. Information received at these stations is relayed to the INTELSAT Operations Center and Spacecraft Control Center in Washington, D.C.

The Operations Center is manned 24-hours a day. Requests for services are received here from all over the world. Full-time TV leases are also available.

The Spacecraft Control Center is responsible for the satellites' position and orientation and the operation of the satellites' subsystems in space.

DEPLOYMENT OF INTELSAT SATELLITES

As of 31 December 1985

Satellite	Operational Role	Location
Atlantic Ocean Region		
INTELSAT V (F-3)	INTELSAT Business Service and Domestic Lease Services	307°E
INTELSAT IV (F-1)	Domestic Lease Services	310°E
INTELSAT V (F-4)	International and Domestic Lease Services	325.5°E
INTELSAT IV-A (F-1)	Domestic Lease Services	329°E
INTELSAT V-A (F-11)	Domestic and International Lease Services	332.5°E
INTELSAT V-A (F-10)	International Services	335.5°E
INTELSAT IV-A (F-4)	Domestic Lease Services	338.5°E
INTELSAT V (F-6)	International and Maritime Services	341.5°E
INTELSAT V (F-2)	International and Domestic Lease Services	359°E
Indian Ocean Region		
INTELSAT V (F-1)	Domestic Lease Services	57°E
INTELSAT V-A (F-12)	International Services	60°E
INTELSAT V (F-5)	International and Maritime Services	63°E
INTELSAT V (F-7)	Domestic Lease Services	66°E
Pacific Ocean Region		
INTELSAT IV-A (F-6)	International Services	174°E
INTELSAT IV-A (F-3)	International and Domestic Lease Services	179°E
INTELSAT V (F-8)	Maritime Services	180°E

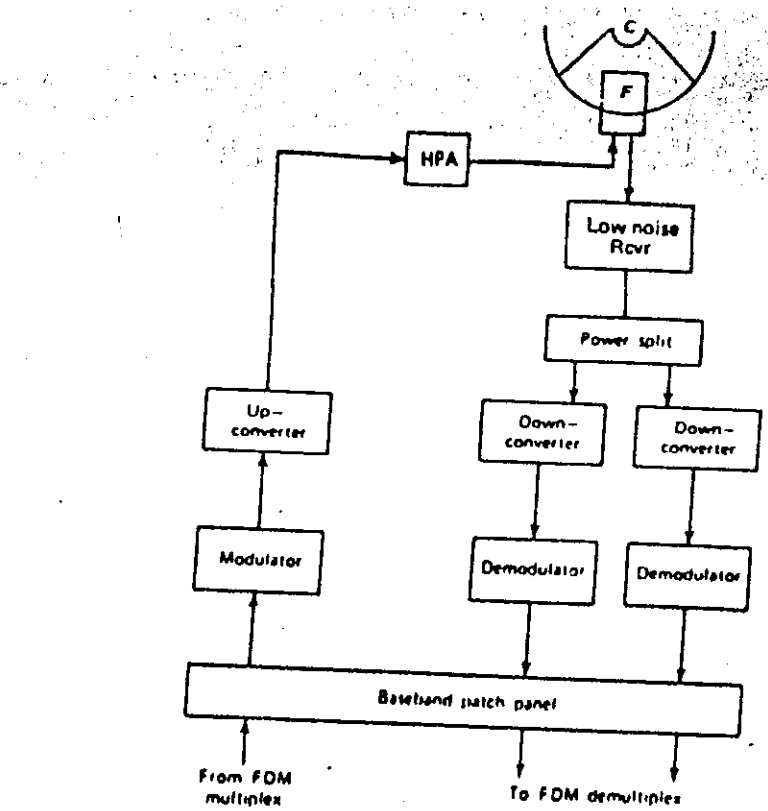

Figure 3 Simplified functional block diagram of an earth station communication subsystem. *F* = feed, HPA = high-power amplifier, *C* = Cassegrain subreflector.

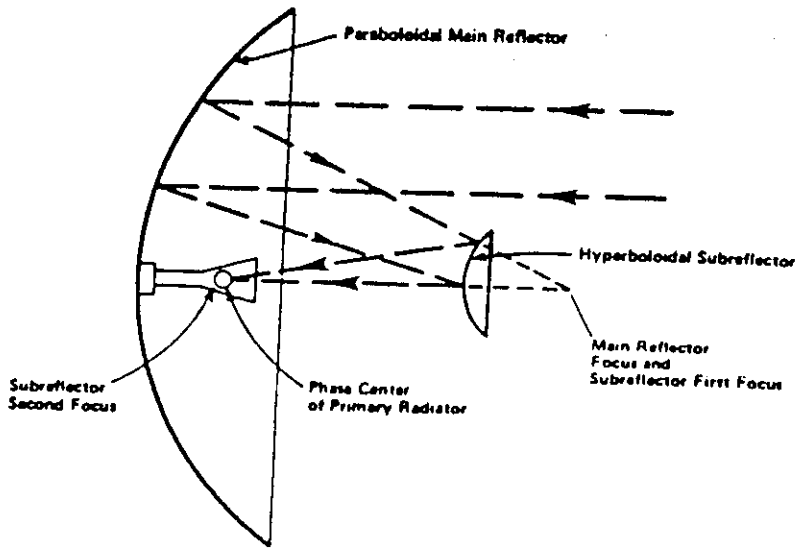

Figure 4 Cassegrain antenna functional operation

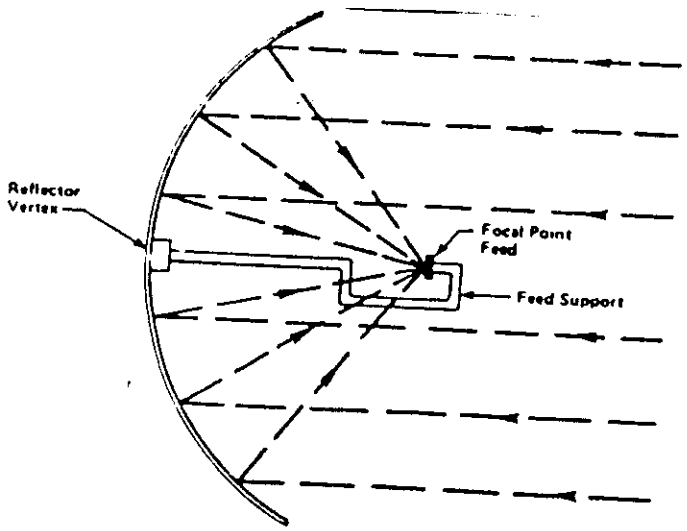

Figure 5 Prime focus antenna, functional operation.

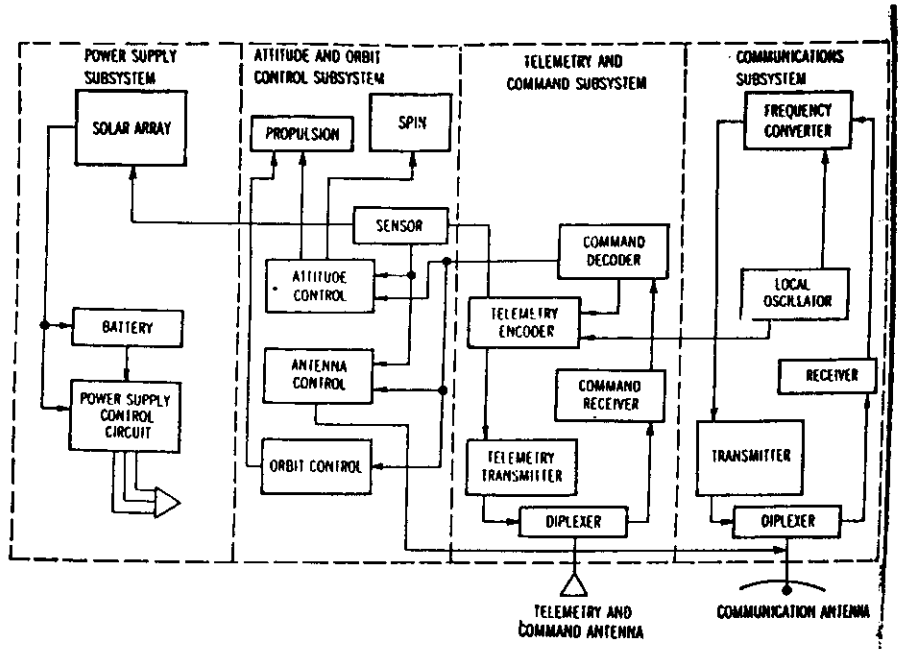

Fig. 6 Communication satellite configuration

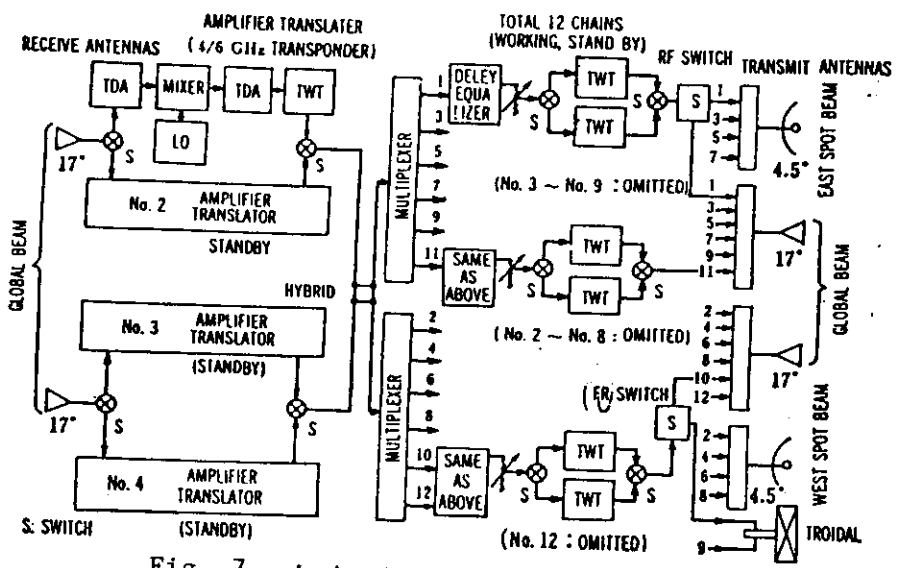

Fig. 7 Intelsat-IV communications subsystem

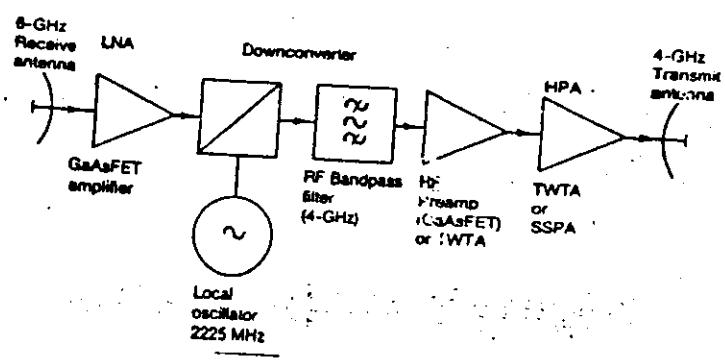

Fig 8: Single conversion
Transponder for 6/4 GHZ

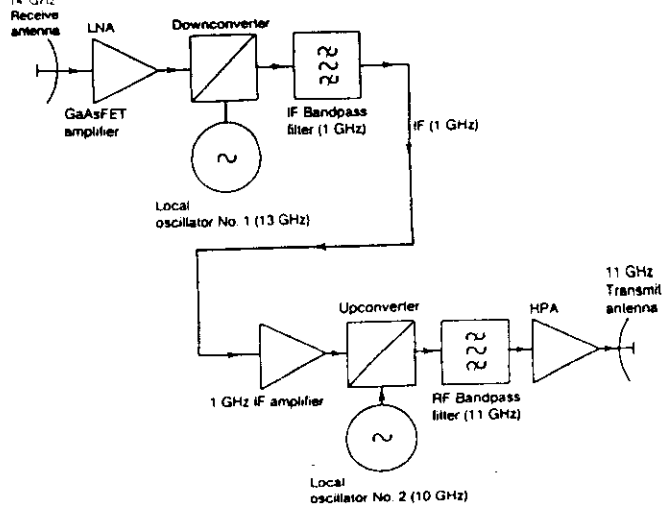

Fig. 9 Simplified double conversion transponder for 14/11 GHz.

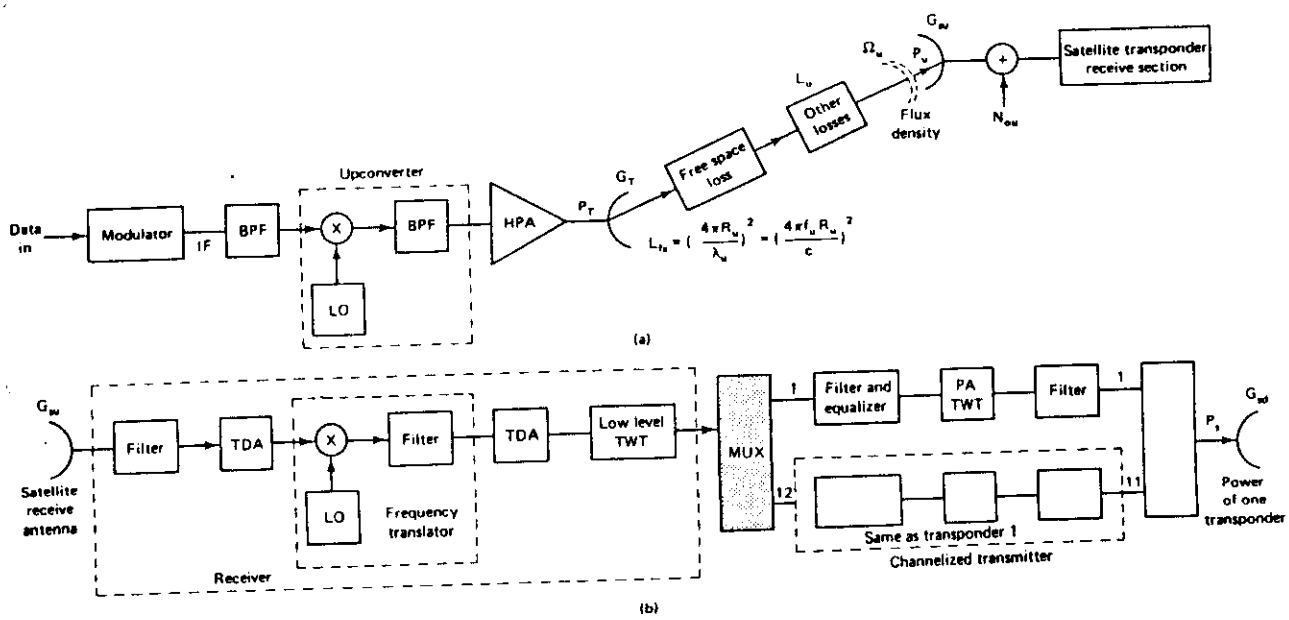

Fig 10 (a)(a) Uplink model. (b) Satellite transponder. (c) Downlink model. (d) Abbreviations used in (a)–(c).

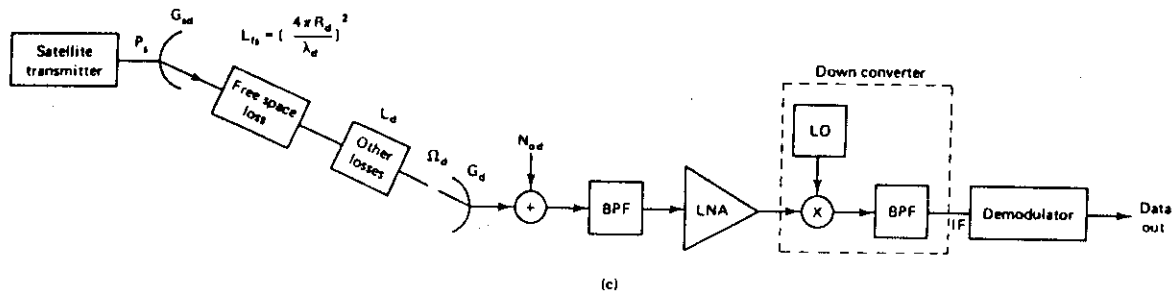

A_{su}	= effective area of the satellite receive (uplink) antenna
BPF	= bandpass filter
c	= 2.99 × 10^8 m/s speed of light
f_u	= uplink carrier frequency
G_d	= receive earth station antenna gain
G_{sd}	= satellite (transmit) antenna gain (downlink)
G_{su}	= satellite (receive) antenna gain (uplink)
G_T	= transmit earth station antenna gain
HPA	= high-power amplifier
IF	= intermediate frequency (typically 70 MHz ± Δf or 140 MHz ± Δf)
L_{fs}	= space path loss (spreading factor)
LO	= local oscillator
L_u, L_d	= other uplink (downlink) losses (such as antenna efficiency factor, atmospheric loss)
MUX	= multiplexing network (in this case a radio-frequency network)
N_{ou}	= uplink noise spectral density
P_u	= signal power received at satellite
PA	= power amplifier
P_s	= transmitted power of one satellite transponder
P_T	= transmitted power of the earth station high-power amplifier
R_u	= uplink range distance in meters. Geosynchronous satellites are at a height of 35,930 kilometers (19,400 nautical miles)
TDA	= tunnel diode amplifier (a frequently used preamplifier)
TWT	= traveling-wave-tube amplifier
λ_u, λ_d	= uplink (downlink) wavelength $\boxed{\lambda = c/f}$
Ω_u	= flux density of satellite receiver
π	= 3.1415

(d)

Fig 10 (b) *(Continued)*

Fig. 11 **THREE BASIC ORBITS**

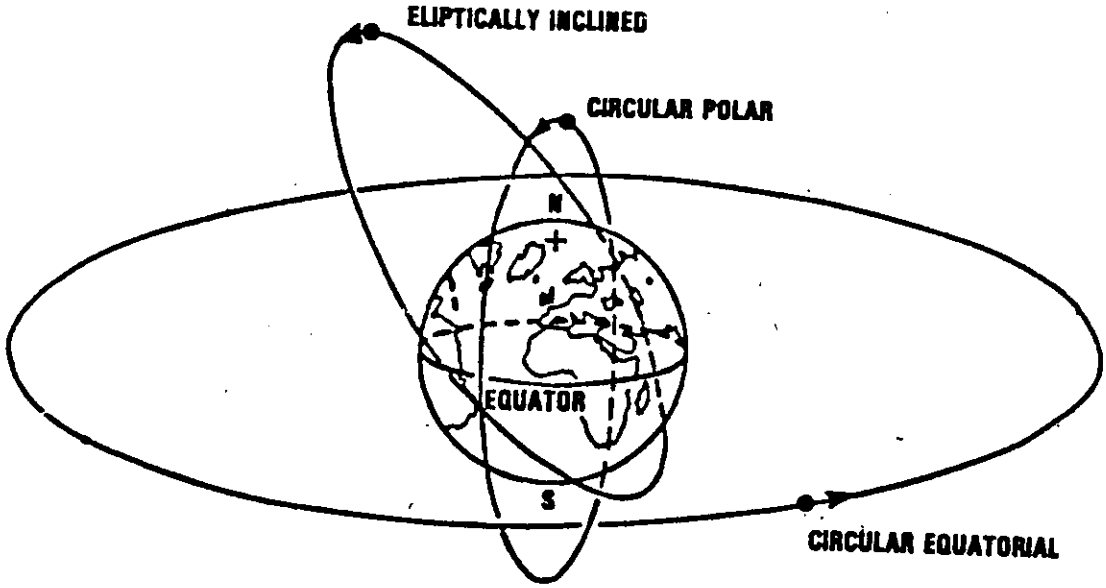

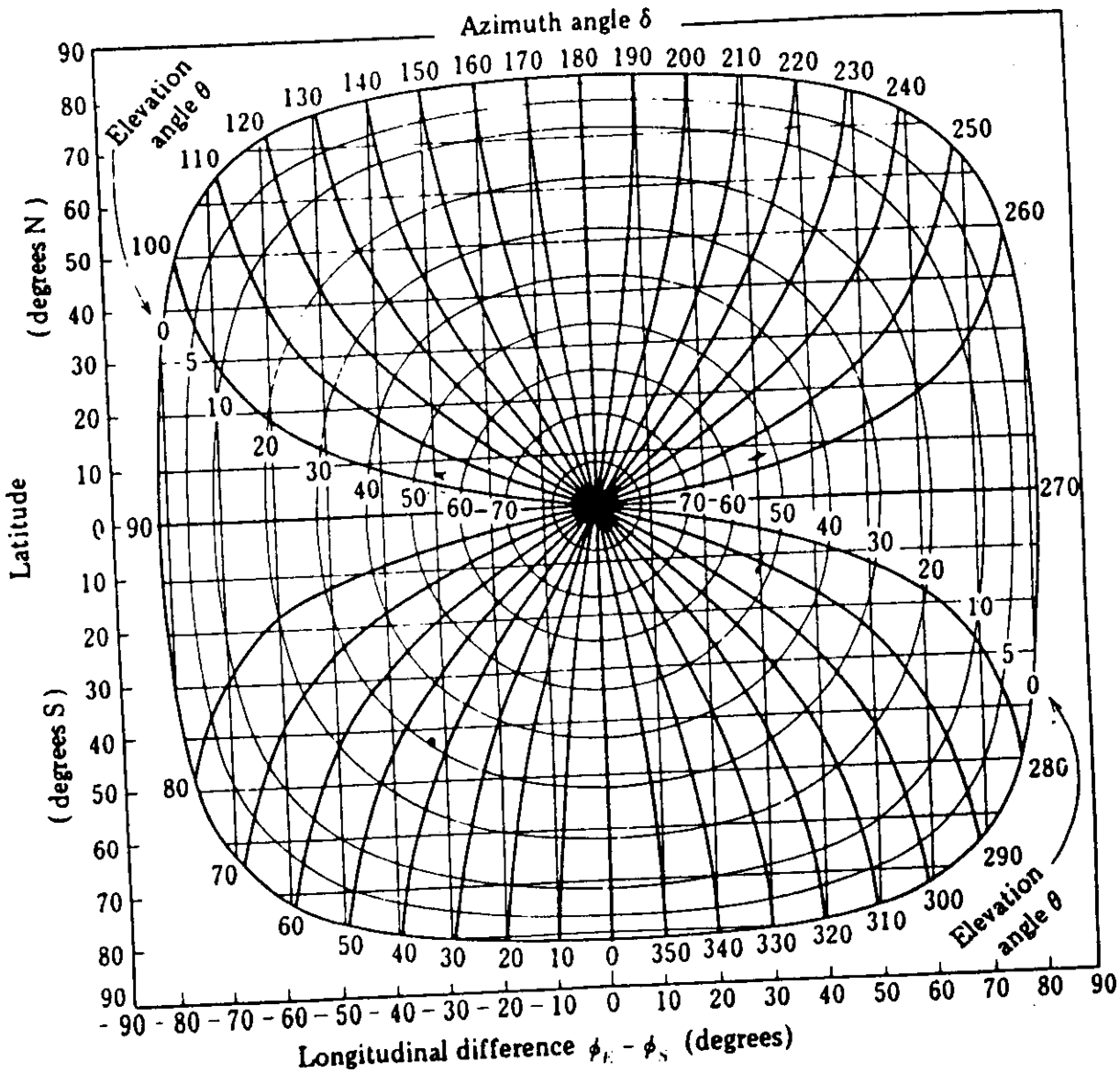

Fig. 12 Relationship between the locations of earth station and geostationary satellite

Planned IRIDIUM Constellation

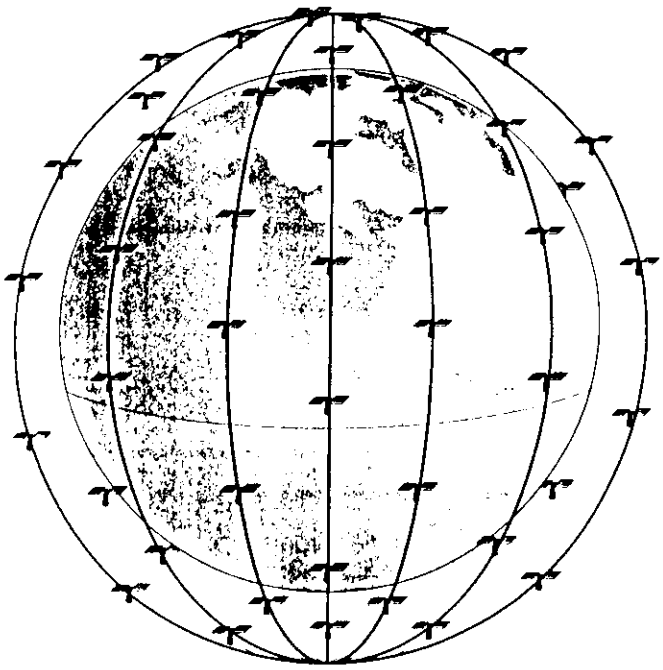

Fig. 13(a) **Low Earth Orbit Satellites**

- Polar orbit at approximately 420 nautical miles
- Full earth coverage at equator

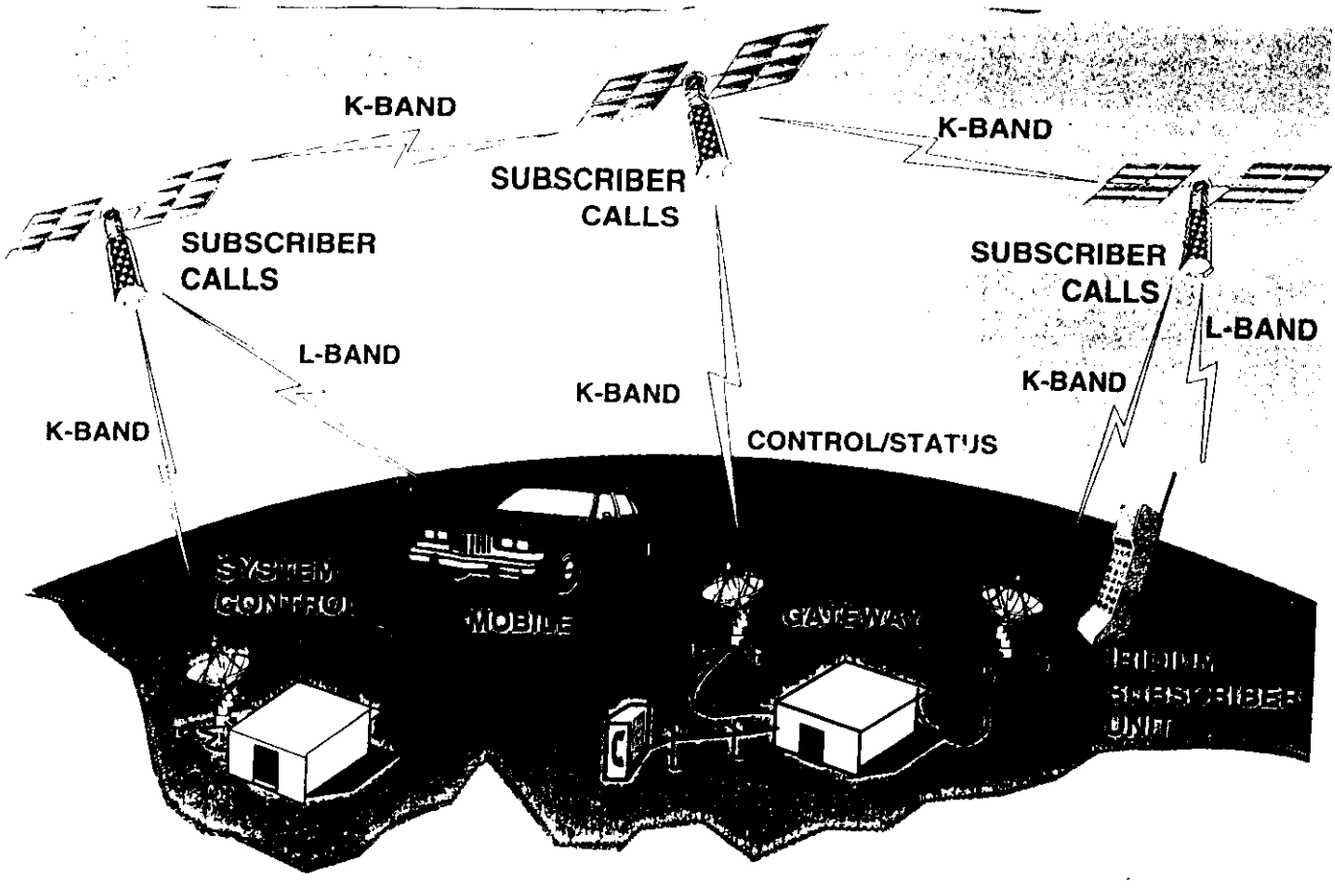

Fig. 13 (b) IRIDIUM System Overview.

INTERNATIONAL ATOMIC ENERGY AGENCY

AND

UNITED NATIONS EDUCATIONAL SCIENTIFIC AND CULTURAL ORGANIZATION

INTERNATIONAL CENTRE FOR THEORETICAL PHYSICS

CLIMATIC INFORMATION FOR SATELLITE COMMUNICATION PLANNING.

PART 2: CLEAR SKY PROPAGATION PHENOMENA

Prof. G.O. Ajayi
Department of Electronic & Electrical Engineering
Obafemi Awolowo University,
Ile-Ife, Nigeria.

FOURTH ICTP-URSI-ITU (BDT) COLLEGE ON RADIOPROPAGATION:
Propagation, Informatics and Radiocommunication System Planning.

30 January - 3 March, 1995.

1. THE NEUTRAL ATMOSPHERE

Although the geostationary satellite is at an altitude of 35,780 km from the earth, it is necessary to examine the effect of some regions of the atmosphere on the radiowave signals on the Earth-satellite path.

Fig. 1(a) shows the various regions of the atmosphere with conventional names describing levels, physical regimes, and characteristic constituents. Fig. 1(b) gives a pictorial view of some of the activities in the atmosphere as well as the pressure and temperature distributions. Fig. 1(c) gives more information about the vertical distribution of pressure P, density, ρ temperature, T and mean molecular mass M up to 300 km.

Fig. 1(a) shows the following regions of the atmosphere in ascending order: the troposphere, stratosphere, the mesosphere, thermosphere, exosphere and magnetosphere. In terms of electron concentration, the regions are ozonosphere, ionosphere, heliosphere and protonosphere.

For satellite communication, the effect of the ionosphere and troposphere on the radio signal will be considered, because of the major role played by the two regions.

1.1 Troposphere

The troposphere is the lower part of the Earth's atmosphere extending to an altitude of about 9 km at the earth's poles and 17 km at the equator. The temperature in the troposphere gradually decreases with height at the rate of approximately 6°C per km. The troposphere plays a major role in satellite communication.

1.2 Ionosphere

This is the region of the earth's upper atmosphere where ions and electrons are present in quantities sufficient to affect the propagation of radiowaves. The lower layer, the D layer extends down to about 50 km. The other layers in ascending order are E, F1 and F2.

2. PROPAGATION IMPAIRMENT

In the design of Earth-space links for communication systems, several effects must be considered. Effects of the non-ionized atmosphere need to be considered at all frequencies, but become critical above about 1 GHz and for low elevation angles. These effects include (ITU-R PN-618):

(i) absorption in atmospheric gases; absorption, scattering and depolarization by hydrometeors (water and ice droplets in precipitation, clouds, etc.); and emission

noise from absorbing media; all of which are especially important at frequencies above about 10 GHz;

(ii) loss of signal due to beam-divergence of the earth-station antenna, due to the normal refraction in the atmosphere;

(iii) a decrease in effective antenna gain, due to phase decorrelation across the antenna aperture, caused by irregularities in the refractive index structure;

(iv) relatively slow fading due to beam-bending caused by large-scale changes in refractive index; more rapid fading (scintillation) and variations in angle of arrival, due to small-scale variations in refractive index;

(v) possible limitations in bandwidth due to multiple scattering or multipath effects, especially in high-capacity digital systems;

(vi) attenuation by the local environment of the ground terminal (buildings, trees, etc.);

(vii) short-term variations of the ratio of attenuations at the up- and down-link frequencies, which may affect the accuracy of adaptive fade countermeasures.

Effects of the Earth's ionosphere and of extra-terrestrial ionized media which may need to be considered for systems operation include:

(i) rotation of the plane of polarization (Faraday rotation), particularly if frequency re-use and linear polarization are employed;

(ii) dispersion, which results in a differential time delay across the bandwidth of the transmitted signal;

(iii) excess time delay;

(iv) scintillation, which affects amplitude, phase and angle-of-arrival of the received signal.

Interference aspects to be considered include:

(i) interference between earth stations and terrestrial stations.

(ii) interference from and to space stations

(iii) bidirectional coordination of earth stations

Fig.2 shows a schematic representation of the various impairment that can occur on Earth-space path. Furthermore the impairments occur mostly in the troposphere and ionosphere. Some of the impairments can occur simultaneously e.g. ionospheric scintillation and rain depolarisation.

3. IONOSPHERIC EFFECTS

Fig. 3 shows a typical variation of the number of electrons/m^3 with height in the ionosphere during the day and at night. The frequencies of operation for satellite communication are much higher than the critical frequency of the ionosphere, hence satellite signals are not reflected from the ionosphere. However, there are other impacts of the ionosphere on satellite signals. From a knowledge of the total electron content (TEC), the other relevant parameters can be evaluated.

3.1 Faraday Rotation

A linearly polarised wave propagating in a plasma will generally suffer a rotation of the plane of polarisation due to the anisotropy of the medium. This effect is called Faraday Rotation (ϕ) given by

$$\phi = (c/f^2) \times \text{TEC radians} \qquad (1)$$

where $C = 2.36 \times 10^4 B_{av}$

where B_{av} is average value of earth's magnetic field in Wb/m^2.

Fig. 4 shows the Faraday rotation as a function of TEC and frequency. The diurnal, seasonal and annual variations of Faraday rotation are more relevant in satellite communications.

The effects of Faraday rotation on wideband signals can be of significance to system performance. Signal components separated in frequency may be expected to be subject to frequency and phase selective distortion.

3.2 Group Delay

The delay assuming a single frequency such as a ranging pulse, will cause the signal to arrive later than it would have done if transmitted in vacuo. Consequently, the inferred range R, will be greater than the true range since the velocity of light in vacuo C would have been assumed in calculating the range. The ranging error is given by

$$\Delta R = (40.3/f^2) \times \text{TEC metres} \qquad (2)$$

For a 4 GHz signal and an average TEC of 10^{17} electrons/m^2, the ranging error is 2.5m. For geostationary communications satellites,

where it is required to maintain station keeping to within 0.1 of a given position, the maximum ranging error should be about 3m (Allnutt, 1989).

3.3 Dispersion

The rate of change of the time delay with frequency, dt/df, is the dispersion of the signal due to time delay.

The difference in the time delay between two signals at the extreme ends of the bandwidth is

$$|\Delta t| = \frac{(2.68 \times 10^{-7})}{f^3} \times df \times TEC \text{ seconds} \qquad (3)$$

for df = 36MHz, TEC = 10^{17} electrons/m^2 and f = 4GHz, Δt is 15ps. The difference in the phase delay between two signals at the extreme ends of the bandwidth is

$$|\Delta \phi| = \frac{(8.44 \times 10^{-7})}{f^2} \times df \times TEC \text{ radians} \qquad (4)$$

for df = 36MHz, TEC = 10^{17} electrons/m^2 and f = 4GHz, Δt is 15ps.

The phase-dispersion for the example given above is 0.19 rad, approximately 11 .

Ionospheric dispersion can reduce the coherence bandwidth, which for digital systems lead to reduction in the upper limit of bit rate.

3.4 Ionospheric Scintillation

Scintillations are marked fluctuations in amplitude and phase imposed on satellite or radio-star signals in their passage through the ionosphere. Night-time scintillation is imposed by F-region irregularities. Scintillation activity is common in the auroral and equatorial regions. Scintillation can cause severe degradation on Earth-space communications near the equator. The degree of degradation depends on the depth and rate or duration of fading.

Equatorial scintillation is found within the equatorial spread-F belt. 1.7 GHz scintillation does not exceed 4dB, whereas near the crest of the equatorial anomaly, peak to peak scintillations of up to 31 dB at 1.5 GHz and 14 dB at 4 GHz have been observed. Gigahertz ionospheric scintillations of any significant amplitude only occur within approximately 30 of the magnetic equator for geostationary communications satellite links. Peak daily scintillation activity occurs approximately one hour after sunset at the ionospheric height. Fig. 5 shows the power spectrum of combined tropospheric and ionospheric scintillations as observed at Hong Kong earth station. (Allnutt, 1989). At frequencies around 4 -

6 GHz, peak-to-peak fading of around 10dB has been frequently reported, hence satellite signals at L (1.6/1.5 GHz) and C (6/4 GHz) bands can therefore be severely affected.

Tables 1(a) & (b) (ITU-R PN 680) show typical estimates of maximum ionospheric effects in the U.S.A. on paths with elevation angles of about 30 .

Characteristics of Ionospheric Scintillation (ref. 2) can be summarised as follows:

(a) Sun-spot number dependence

(i) No strong correlation between individual scintillation event occurrences and daily sun-spot number.

(ii) Strong correlation between annual scintillation occurrence and the annual sun-spot number.

(iii) Strong correlation between the amplitude of the scintillations and the monthly sun-spot number.

(b) Temporal dependence

(i) Annual scintillation activity varies in an 11-year cycle in concert with solar sun-spot cycle.

(ii) Peak annual scintillation activity occurs at or just after the equinox periods.

(iii) Peak daily scintillation activity occurs approximately one hour after sunset at the ionospheric height.

(c) Geographical dependence

GHz ionospheric scintillations of any significant amplitude only occur within approximately 30° of the magnetic equator for geostationary communications satellite links.

(d) Frequency dependence

(i) The scintillation frequency or fading rate is below 1Hz with a corner frequency of about 0.1Hz.

(ii) The period of the scintillations is generally less than 15s.

(iii) The power spectra of the scintillations generally roll off as f^{-3}.

(iv) The frequency dependence varies as f^{-n} for GHz frequencies. n has been found experimentally to be

1.5 between 4 and 6 GHz, although weak scattering theory predicts n to be 2. A value of n of 1 has been found for severe ionospheric disturbances between 1.5 and 4 GHz.

Fig.6 (Allnutt, 1989) shows the INTELSAT ionospheric predictive model flow diagram.

Fig. 7(a) shows a set of contours of the diurnal characteristics of ionospheric scintillation, under which the Earth can be considered to rotate from left to right (sunset to sunrise). As an equatorial point on the surface of the Earth moves from the sunset rim, there is a rapid increase in the likelihood of intense scintillation occurring followed by a gradual decrease in both the probability and the severity of the scintillation (Allnutt, 1989). The contours in Fig. 7(b) enclose equiprobable points for a given level of amplitude scintillations, which is 2dB in this example. The higher probabilities occur closer to sunset than to sunrise, and the equinoctal characteristics are also shown.

4. TROPOSPHERIC EFFECTS

The tropospheric effect on Earth-satellite propagation path can be considered in terms of clear air effects and effects due to hydrometeors.

4.1 Clear Air Effects

The atmospheric radio refractive index, n is very close to unity (typically 1.00035), hence it is more convenient to talk of the refractivity, N given by

$$N = (n - 1) \times 10^6 = \frac{77.6}{T} \left(p + 4810 \frac{e}{T}\right) \qquad (5)$$

where

p = atmospheric pressure (hPa)
e = water vapour pressure (hPa)
T = absolute temperature (K)

(hPa is numerically identical to mb).

For frequencies up to 100 GHz, the error is less than 0.5%. The relationship between water vapour pressure e and relative humidity is given by

$$e = \frac{He_s}{100} \qquad 6(a)$$

with

$$e_s = a \exp\left(\frac{bt}{t + c}\right) \qquad 6(b)$$

where H = relative humidity in %
t = celsius temperature in °C
e_s = saturation vapour pressure in hPa at the temperature t in C and the coefficients a, b and c are for water;

a = 6.1121, b = 17.502 and c = 240.97

Valid between -20 and +50 with accuracy of 0.20%. Vapour pressure e is obtained from the water vapour density ρ using the equation.

$$e = \frac{\rho\, T}{216.7} \qquad hPa \qquad (7)$$

where ρ is given in g/m^3

The world-wide contours of water vapour density are shown in Figs. 8 (a) & (b) for February and August respectively.

Pressure, temperature and water vapour contents all decrease with height above the earth's surface in the troposphere on the average, except in temperature inversion layers where temperature increases with height.

For clean dry air in the lower atmosphere, the radio refractivity is given as

$$N_{dry} = 77.6\ P/T \qquad (10)$$

This term is fairly constant with geographical location and with height, at least up to 50km. The "wet" term of radio refractivity is given by

$$N_{wet} = 77.6 \times 4810\ e/T^2 \qquad (11)$$

$$\simeq 373000\ e/T^2$$

N varies with height as

$$N(h) = N_s \exp(-\frac{h}{H}) \quad (12)$$

where N(h) is refractivity at a height h above which the refractivity is N_s, H is scale height.

For the ITU-R model atmosphere

$$N(h) = 315 \exp(-0.136h) \quad (13)$$

where 315 is the average surface refractivity and the scale height is 7.353 km. h is in km.

4.2 Sea Level Refractivity

For prediction of some propagation effects, the surface refractivity is useful. To remove surface height variations (topography of location) surface refractivity can be reduced to sea-level values N_o using

$$N_s = N_o \exp(-0.136h) \quad (14)$$

The scale height in the locality can be used if available.

The ITU-R has produced world map of N_o (Figs. 9(a) and (b)). Figs. 10 (a) and (b) Kolawole & Owonubi, 1982 show the surface refractivity variation in Africa.

4.3 Vertical refractivity gradients

The lapse in radio refractivity over a 1km layer from the surface is given by

$$\Delta N = N_s - N_1$$

where N_1 = radio refractivity at a height of 1km above the surface of the Earth.

Refractivity gradient statistics for the lowest 100m from the surface of the Earth are used to estimate the probability of occurrence of ducting and multi-path conditions.

4.4 Ray Bending

A radio ray passing through the lower (non-ionized) layer of the atmosphere undergoes bending caused by the gradient of the refractive index.

The curvature of the ray path is given by

$$\frac{1}{\rho} = \frac{-Cos\psi}{n} \frac{dn}{dh} \qquad (15)$$

where

ρ : radius of curvature of the ray path.

$\frac{dn}{dh}$: vertical gradient of refractive index

h : height of the point above the Earth's surface.

ψ : angle of the ray path with the horizontal at the point considered.

In the troposphere, n ~ 1 and for small values of angle ψ, we have

$$\frac{1}{\rho} = \frac{-dn}{dh} = \frac{-dN}{dh} \times 10^{-6} \qquad (16)$$

R is determined by the lapse rate of refractive index with height and not by its absolute value. For middle latitudes, average dN/dh for standard atmosphere is -40N units/km and K is 4/3, where K is the effective earth radius factor. There is a large variation in the median values of K near the equator (Ajayi, 1989). In the equatorial regions of India, K varies between 1.3 and 1.8, whilst in the equatorial regions of Africa, K is 1.5 (Kolawole & Owonubi). K was also found to be 1.43 and 1.22 for the rainy and dry seasons, respectively.

Super-refraction occurs when $\frac{dN}{dh} < -40$ and ducting takes place for $\frac{dN}{dh} < -157$.

A radiowave transmitted from a point on the surface of the earth to an earth satellite encounters successively lower values of N as it traverses upwards through the atmosphere and it will bend in decreasing amounts on its way up. The reverse takes place for a radio wave from the satellite to a point on the surface of the earth. For most satellite-to-ground applications, ducting will not occur unless the elevation angle is at or below 1 . Significant bending can occur for elevation angles below 10^{o} . Ray bending is independent of frequency. The ray bending τ can be obtained from the surface refractivity N_s from the equation:

$$\tau = a + (b \times N_s) \text{ millidegrees} \qquad (17)$$

where a and b are constants given in Table 2.

4.5 Scintillation and Multipath Effects

Small scale irregularities in the atmospheric refractive index cause rapid signal variations. In the absence of precipitation, tropospheric effects are unlikely to produce serious fading in space telecommunication systems operating below 10GHz and at elevation angles above 10^{c}. At low elevation angles and at frequencies above about 10 GHz, tropospheric scintillations can on occasion cause serious degradations in performance.

The magnitude of tropospheric scintillations depends on the magnitude and structure of the refractive index variations, increasing with frequency and with the path length through the medium, and decreasing as the antenna beamwidth decreases because of aperture averaging.

Monthly-averaged r.m.s fluctuations are well-correlated with the wet term N_{wet} of radio refractivity. N_{wet} depends on the water vapour content and can be estimated from surface meteorological data. Measurements at high latitudes showed that the cold, less humid climate greatly reduced the tropospheric scintillation effects.

Experiments have shown that rain along the path produced no net reduction in the amplitude of the scintillations, at least until the mean path attenuations were in excess of 5 dB or of their characteristics. Fig. 11 shows the separation of atmospheric scintillation and rain attenuation. The height of the turbulence causing the scintillations has been observed to be between 1.5 and 4km.

Tropospheric scintillation characteristics can be summarised as follows (ref. 2)

(a) Meteorological dependence

(i) Strong correlation of amplitude with temperature and humidity.

(ii) Amplitude increases with wind velocity, but weak correlation with wind direction.

(iii) Presence of rain does not significantly affect the amplitude of the scintillations until the path attenuations exceed about 5 dB.

(b) Temporal dependence

Strong correlation with the seasonal cycle and weak correlation with the diurnal cycle coinciding with the hottest and most humid parts of the period in question. Peaks of activity are in the early afternoon and in mid-summar for

temperate latitudes; tropical and sub-tropical climates show peaks of activity corresponding to their wet seasons.

(c) Geographic dependence

Major correlation is with high temperatures and humidities, so there is a concomitant dependence on latitude; the higher the latitude, the colder is the average temperature of the atmosphere and so the lower the amplitude of scintillations over a given path will be. For a given latitude, there does not appear to be a longitude dependence.

(d) Frequency dependence

When the same antenna is used to measure the tropospheric scintillations at two, or more, frequencies that have been derived from a common source (i.e. the signals are coherently derived), high correlation exists over very large bandwidths. The frequency dependence for the amplitude of the scintillations is approximately the ratio of the frequencies raised to the power 7/12.

(ii) A lack of frequency dependence generally signifies that multipath effects are dominant on that particular path.

(iii) The rate of change of amplitude is slower than that for ionospheric scintillations, the corner frequency is lower, and the roll-off is less steep. The power spectra rolls off as $f^{-8/3}$, generally independent of the elevation angle and frequency. The corner frequency and rate of change of amplitude vary with elevation angle.

(e) Systematic dependence

As the elevation angle goes down for a given location:

(i) Scintillation amplitude increases on the average
(ii) Period of the scintillations increases
(iii) Corner frequency decreases
(iv) There is an increasing tendency for non-symmetrical scintillation distribution (i.e. an increasing impact of multipath).

4.6 Calculation of Monthly and Long-term Statistics of Amplitude Scintillations at Elevation Angles greater than 4° (ITU-R PN 618-2)

The prediction is based on monthly or longer averages of temperature t(C) and relative humidity H and reflects the specific climatic conditions of the site. Seasonal variation in the

distributions of scintillation fade depth is predicted using seasonal averages of t and H. The procedure is applicable up to 20GHz.

Parameters required for the method include:

t : average surface ambient temperature (°C) at the site for a period of one month or longer.
H : average surface relative humidity (%) at the site for a period of one month or longer.
f : frequency (GHz), where 4 GHz ≤ f ≤ 20 GHz
Θ : path elevation angle, where $\Theta \geq 4°$
D : physical diameter (m) of the earth-station antenna
η : antenna efficiency, if unknown, $\eta = 0.5$ is a conservative estimate.

Step 1: For the value of t, calculate the saturation water vapour pressure, e_s, (kPa) as in equation (6)(b).

Step 2: Compute the wet term of the radio refractivity, N_{wet}, corresponding to e_s, t and H as in equation (11).

Step 3: Calculate the standard deviation of the signal amplitude, σ_{ref}:

$$\sigma_{ref} = 3.6 \times 10^{-3} + 10^{-4} \times N_{wet} \quad dB \qquad (18)$$

Step 4: Calculate the effective path length L according to:

$$L = \frac{2h_L}{\sqrt{\sin^2\theta + 2.35 \times 10^{-4} + \sin\theta}} \quad m \qquad (19)$$

where h_L is the height of the turbulent layer; the value to be used is $h_L = 1000$ m.

Step 5: Estimate the effective antenna diameter, D_{eff}, from the geometrical diameter D, and the antenna efficiency η:

$$D_{eff} = \sqrt{\eta}\, D \quad m \qquad (20)$$

Step 6: Calculate the antenna averaging factor from:

$$g(x) = \sqrt{3.86(x^2 + 1)^{11/12} \cdot \sin\left[\frac{11}{6} \arctan\frac{1}{x}\right] - 7.08\, x^{5/6}} \qquad (21)$$

with:

$$x = 1.22\, D_{eff}^2\, (f/L)$$

where f is the carrier frequency (GHz)

Step 7: Calculate the standard deviation of the signal for the considered period and propagation path:

$$\sigma = \sigma_{ref} \cdot f^{7/12} \frac{g(x)}{(\sin\theta)^{1.2}} \qquad (22)$$

Step 8: Calculate the time percentage factor a(p) for the time percentage, p, of concern in the range $0.01 < p \leq 50$:

$$a(p) = 0.061\, (\log_{10} p)^3 + 0.072\, (\log_{10} p)^2 - 1.71 \log_{10} p + 3.0 \qquad (23)$$

Step 9: Calculate the scintillation fade depth for the time percentage p by:

$$x(p) = a(p).\sigma \quad \text{dB} \qquad (24)$$

4.7 Signal variations at elevation angles lower than about 4°

Amplitude scintillation increases rapidly with decreasing elevation angle. At elevation angles below about 2 to 4 , large-scale fading due to the effect of tropospheric stratification becomes important.

4.8 Signal fading mixed with rain attenuation and scintillation

Although rain attenuation is the dominant effect at frequencies above 10 GHz, the effect of scintillation is by no means negligible, particularly at elevation angles lower than 10°. In this case, overall signal fading is estimated by:

$$A(p) = \sqrt{A_R^2(p) + A_S^2(p)} \quad dB \qquad (25)$$

where:

A: total attenuation excluding gaseous absorption (dB)

A_R: rain attenuation (dB)

A_s: signal fade due to scintillation (dB).

4.9 Defocusing Loss

The regular decrease of refractive index with height causes ray bending and hence a defocusing effect at low angles of elevation. The magnitude of the defocusing loss of the antenna beam is independent of frequency, and is less than 0.4 dB at 3° elevation, even for high values of refractivity at ground level. Coastal areas would generally exhibit a high loss owing to their generally high humidity, and dry climates a lower loss.

4.10 Decrease in Antenna Gain due to Wavefront Incoherence

Incoherence of the wavefront of a wave incident on a receiving antenna is caused by small-scale irregularities in the refractive index structure of the atmosphere. This leads to antenna - to medium coupling loss that can be described as a decrease of the antenna gain.

This effect increases both with increasing frequency and decreasing elevation angle, and is a function of antenna diameter. In practice, the effect will likely be significant for narrow-beam width antennas, high frequencies and elevation angles below 5°.

4.11 Angle of Arrival Effect

Refractive effects give rise to error in the elevation angle and this constitutes a variation in the angle of arrival of the signal. Angle of arrival fluctuations are independent of frequency between 1 and 100 GHz. Angle of arrival fluctuations can be considered to be a single ray that is being deviated from its normal path. Table 3 shows angular deviation values for propagation through the total atmosphere. Fig. 11 shows the median standard deviation in angle of arrival fluctuations.

5. REFERENCES

1. Ajayi G. O.: Physics of the Troposheric Radiopropagation, ICTP Internal Report IC/89/23, Feb. 1989 54pp.

2. Allnut J. E.: Satellite-toground radiowave propagation, Peter Peregrims Ltd. IEE Electromagnetic Waves Series 29, 1989.

3. ITU-R REC PN 680: Propagation data required for the design of Earth-space Maritime Mobile Telecommunication Systems; 1992.

4. ITU-R REC. PN-618-2: Propagation data and prediction methods required for the design of Earth-space telecommunications Systems, 1994.

5. Kolawole L. B. and J. J. Owonubi: The surface radio refractivity over Africa, Nigerian Journal of Science, 16, 441-454, 1982.

TABLE 1 (a)

Estimated maximum* ionospheric effects for elevation angles of about 30° one-way traversal (derived from Recommendation 531)**

Effect	Frequency dependence	0.1 GHz	0.25 GHz	0.5 GHz	1 GHz	3 GHz	10 GHz
Faraday rotation	$1/f^2$	30 rotations	4.8 rotations	1.2 rotations	108°	12°	1.1°
Propagation delay (μs)	$1/f^2$	25 μs	4 μs	1 μs	0.25 μs	0.028 μs	0.0025 μs
Refraction	$1/f^2$	< 1°	< 0.16°	< 2.4′	< 0.6′	< 4.2″	< 0.36″
Variation in the direction of arrival (r.m.s.)	$1/f^2$	20′	3.2′	48″	12″	1.32″	0.12″
Absorption (auroral/and polar cap) (dB)	$\approx 1/f^2$	5 dB	0.8 dB	0.2 dB	0.05 dB	6×10^{-3} dB	5×10^{-4} dB
Absorption (mid-latitude) (dB)	$1/f^2$	< 1 dB	< 0.16 dB	< 0.04 dB	< 0.01 dB	< 0.001 dB	$< 10^{-4}$ dB
Dispersion (ps/Hz)	$1/f^3$	0.4 ps/Hz	0.026 ps/Hz	0.0032 ps/Hz	0.0004 ps/Hz	1.5×10^{-3} ps/Hz	4×10^{-7} ps/Hz
Scintillation (1)					> 20 dB peak-to-peak	≈ 10 dB peak-to-peak	≈ 4 dB peak-to-peak

* This estimate is based on a total electron content (TEC) of 10^{18} electrons/m², which is a high value of TEC encountered at low latitudes in day-time with high solar activity.

** Effects above 10 GHz are negligible.

(1) Values observed near the geomagnetic equator during the early night-time hours (local time) at equinox under conditions of maximum sunspot number.

TABLE 1 (b)

Distribution of mid-latitude fade depths due to ionospheric scintillation (dB)

Percentage of time (%)	Frequency (GHz)			
	0.1	0.2	0.5	1
1.0	5.9	1.5	0.2	0.1
0.5	9.3	2.3	0.4	0.1
0.2	16.6	4.2	0.7	0.2
0.1	25.0	6.2	1.0	0.3

(Ref. 3)

Table 2 *Regression parameters for estimating the bending angle through the atmosphere given surface refractivity (from Table 2 of Reference 13)*

Elevation angle (deg)	a (mdeg)	b (mdeg/N unit)	Correlation coefficient	RMS error (mdeg)	95% deviation (mdeg)
0·1	−1112·8	5·778	0·81	89·0	151·0
0·2	−889·2	4·951	0·85	64·0	119·0
0·5	−512·3	3·473	0·94	26·0	58·0
1·0	−268·3	2·372	0·97	12·0	28·0
2·0	−95·9	1·409	0·99	5·0	11·0
3·0	−41·0	0·985	0·99	3·1	6·6
5·0	−10·2	0·610	0·99	1·9	3·8
10·0	−0·3	0·309	0·99	0.99	1·8
20·0	+0·6	0·151	0·99	0·49	0·88
50·0	+0·2	0·046	0·99	0·15	0·27

(Ref. 2)

TABLE 3

Angular deviation values for propagation through the total atmosphere

Elevation angle θ (degrees)	Average total angular deviation, Δθ (degrees)			
	Polar continental air	Temperate Continental air	Temperate maritime air	Tropical maritime air
1	0.45	-	-	0.65
2	0.32	0.36	0.38	0.47
4	0.21	0.25	0.26	0.27
10	0.10	0.11	0.12	0.14
20		0.05	0.06	
30		0.03	0.04	
	Day-to-day variation in Δθ (for columns 1 and 4 only)			
1	0.1 r.m.s.			
10	0.007 r.m.s.			

Ref (CCIR DOC 5/5
5/BL/3-E)

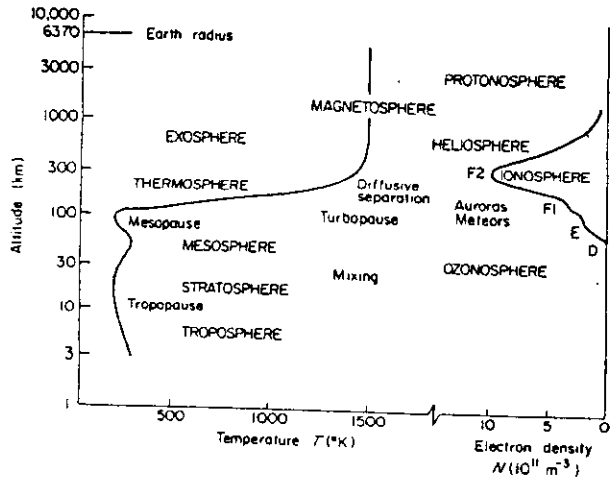

Fig 1(a) Regions of the atmosphere, showing conventional names describing levels, physical regimes, and characteristic constituents. The temperature profile is taken from the U.S. Standard Atmosphere, and the profile of electron density (or electron concentration) represents average daytime conditions for mid-latitudes, high solar activity.

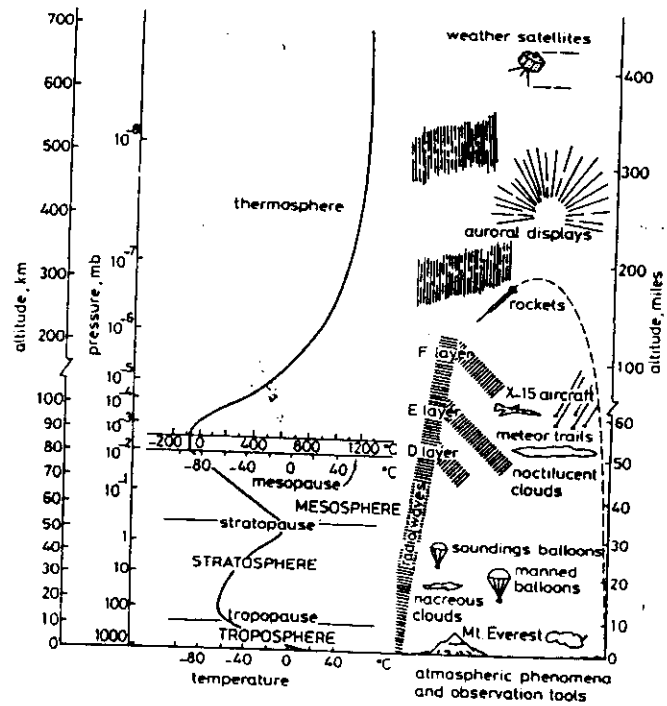

Fig 1(b) *Pressure and temperature distribution of the Earth's atmosphere*

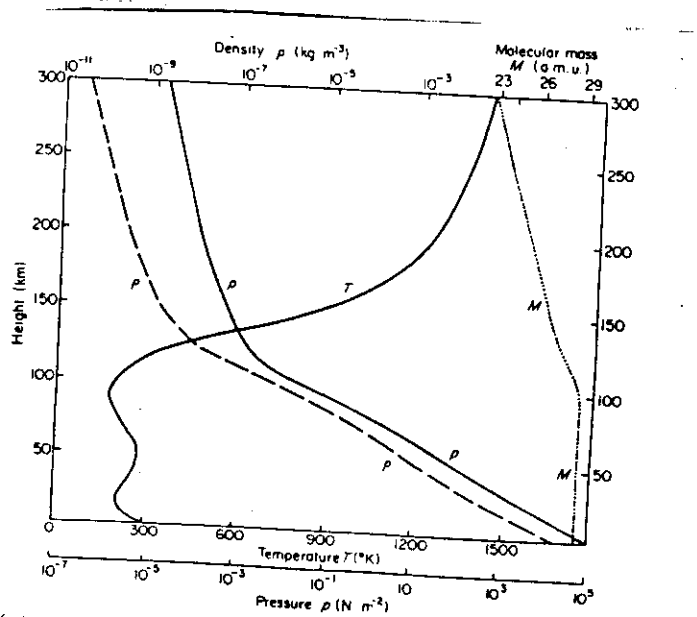

Fig 1(c) U.S. Standard Atmosphere (Government Printing Office, Washington, D.C., 1962). Vertical distribution of pressure p, density ρ, temperature T, and mean molecular mass M to 300 km. The composition is assumed constant up to 100 km.

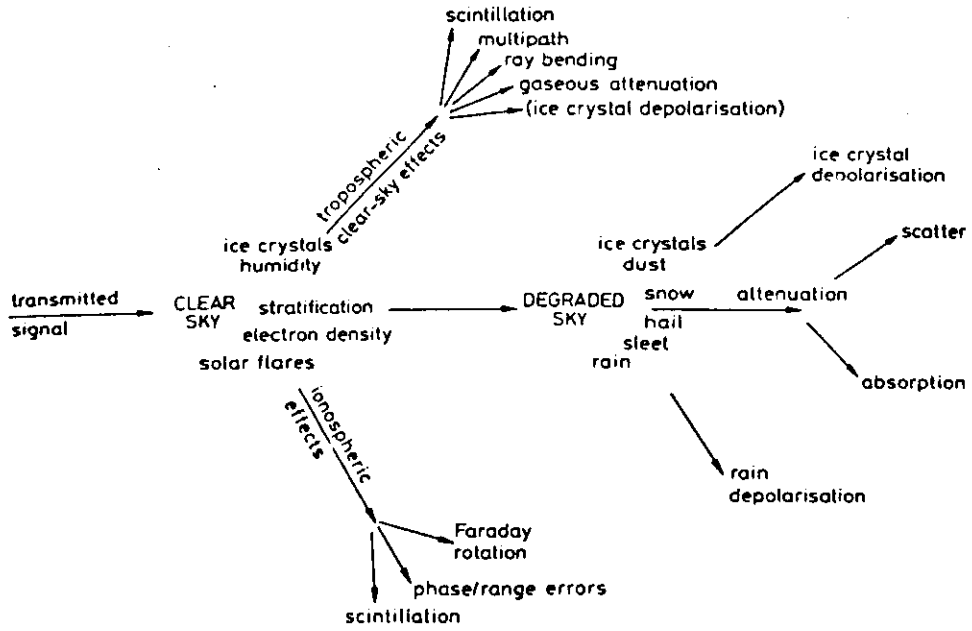

Fig 2 *Schematic presentation of propagation impairment mechanisms* (Ref. 2)

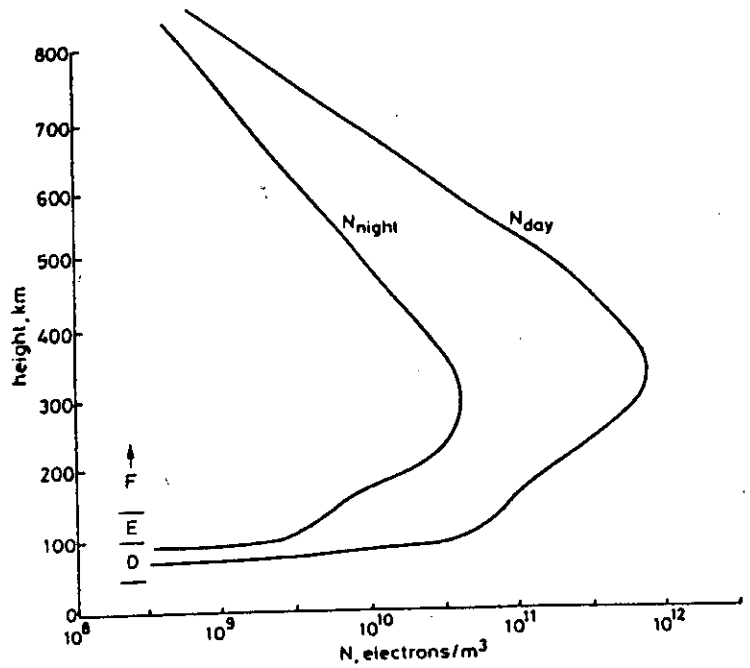

Fig 3 *Number of electrons/m³ versus the height above the Earth during an average day and night*
The approximate range of the three regions, D, E and F, is indicated (Ref. 2)

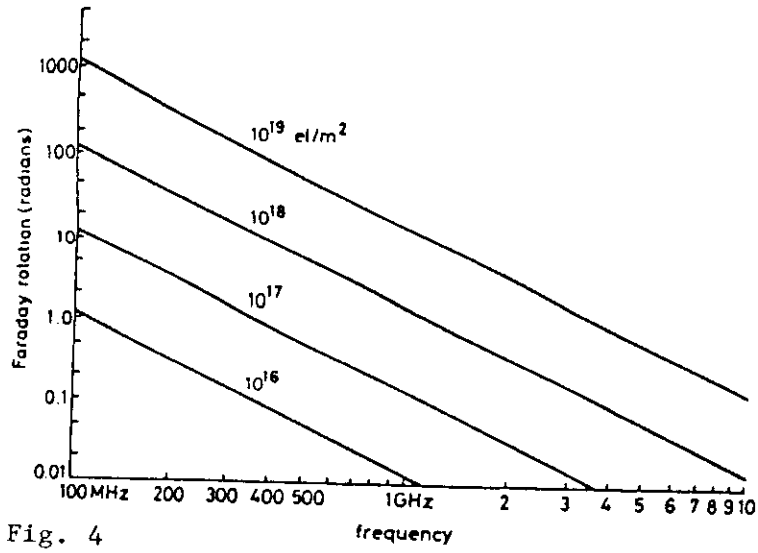

Fig. 4 *Faraday rotation as a function of TEC and frequency* (Ref. 2)

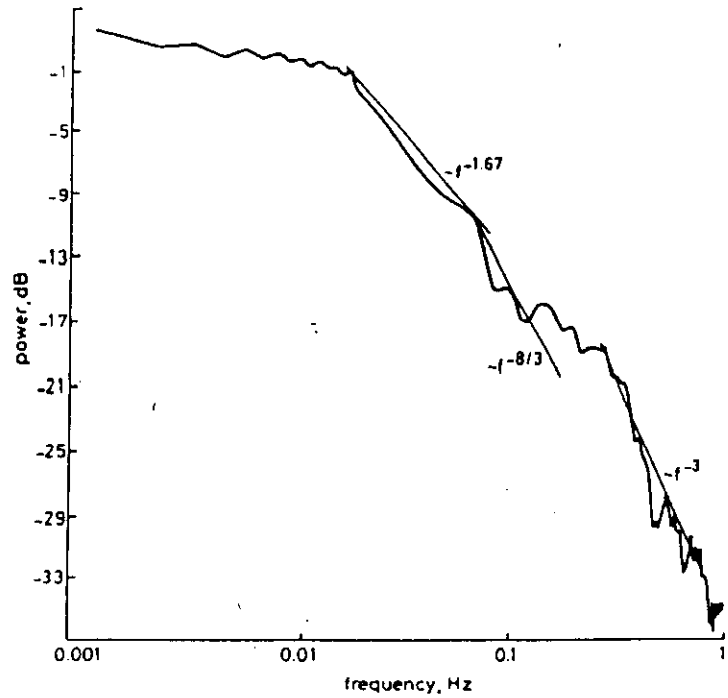

Fig. 5 *Power spectrum of combined tropospheric and ionospheric scintillation as observed at Hong Kong earth station (D. J. Fang, private communication)* (Ref. 2)

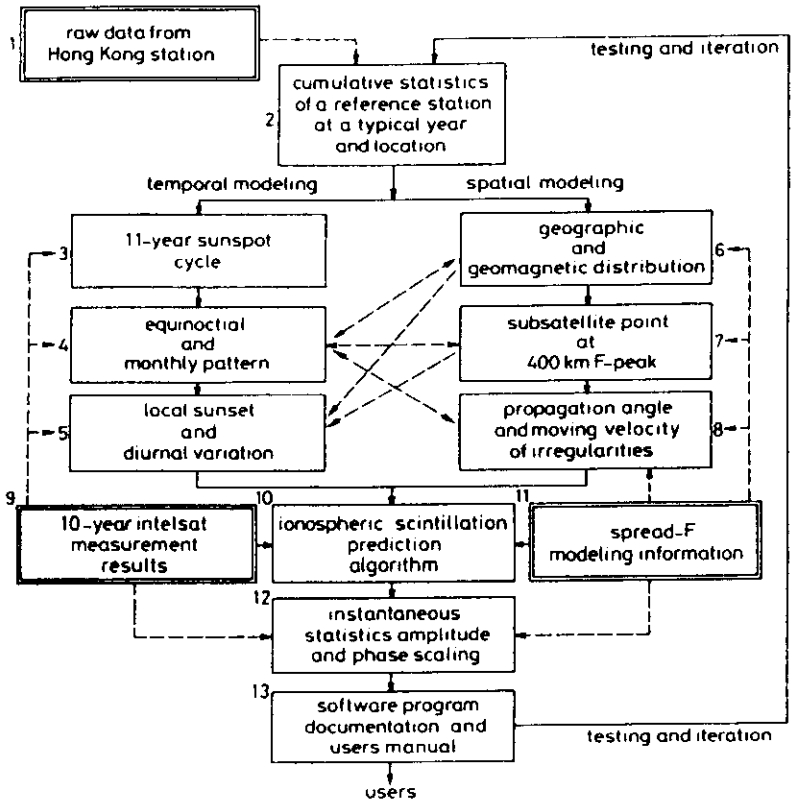

Fig. 6. INTELSAT ionospheric predictive model flow diagram (Allnutt , 1989)

⟶ Modelling sequence

---→ Database input path

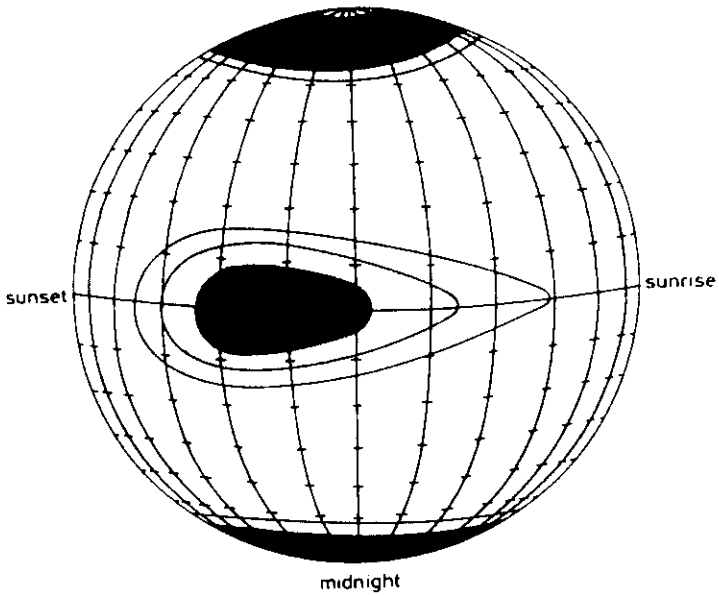

Fig 7(a): Night-time picture of scintillation occurrence. The density of hatching is proportional to the occurrence of deep fading. (Allnutt, 1989)

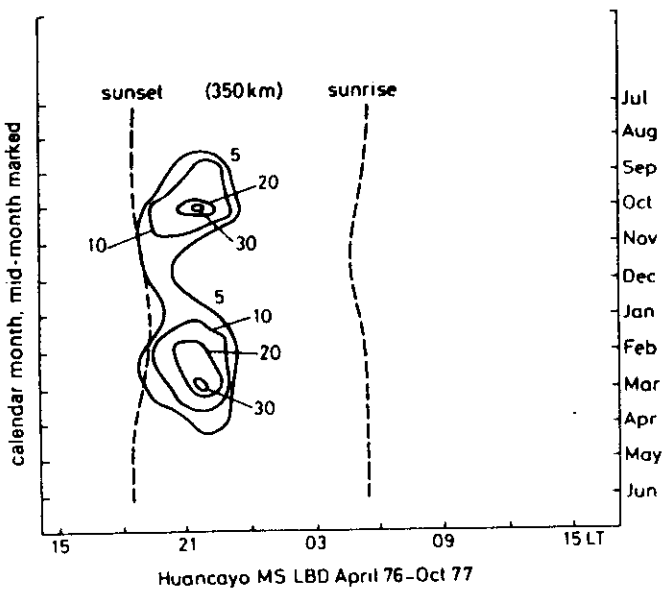

Fig 7 (b): Monthly percentage occurrence of 1.54 GHz scintillations $\geq$ 2dB at Huancayo, S4=0.13 (Allnutt, 1989).

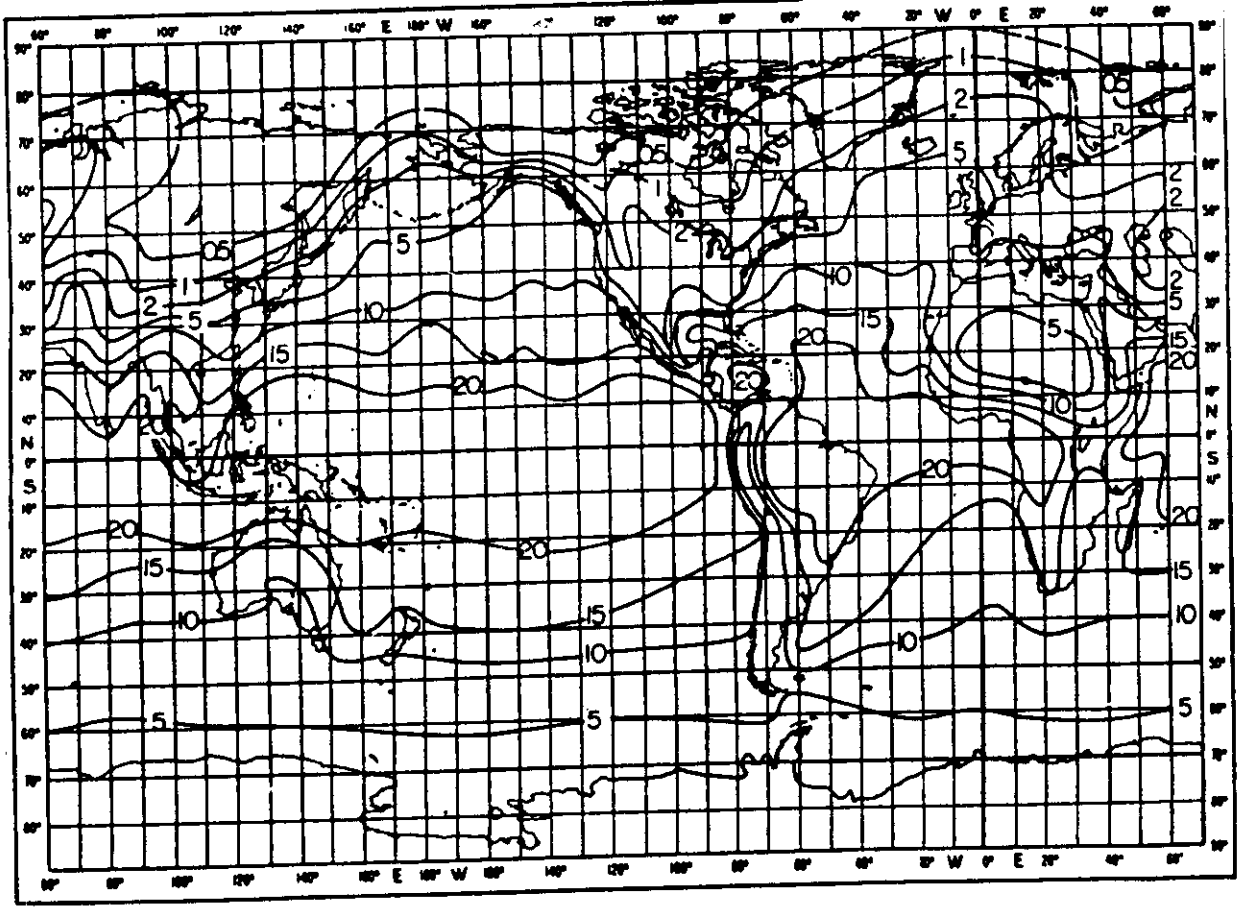

Fig 8(a) – *Water vapour concentration (g/m³), February*

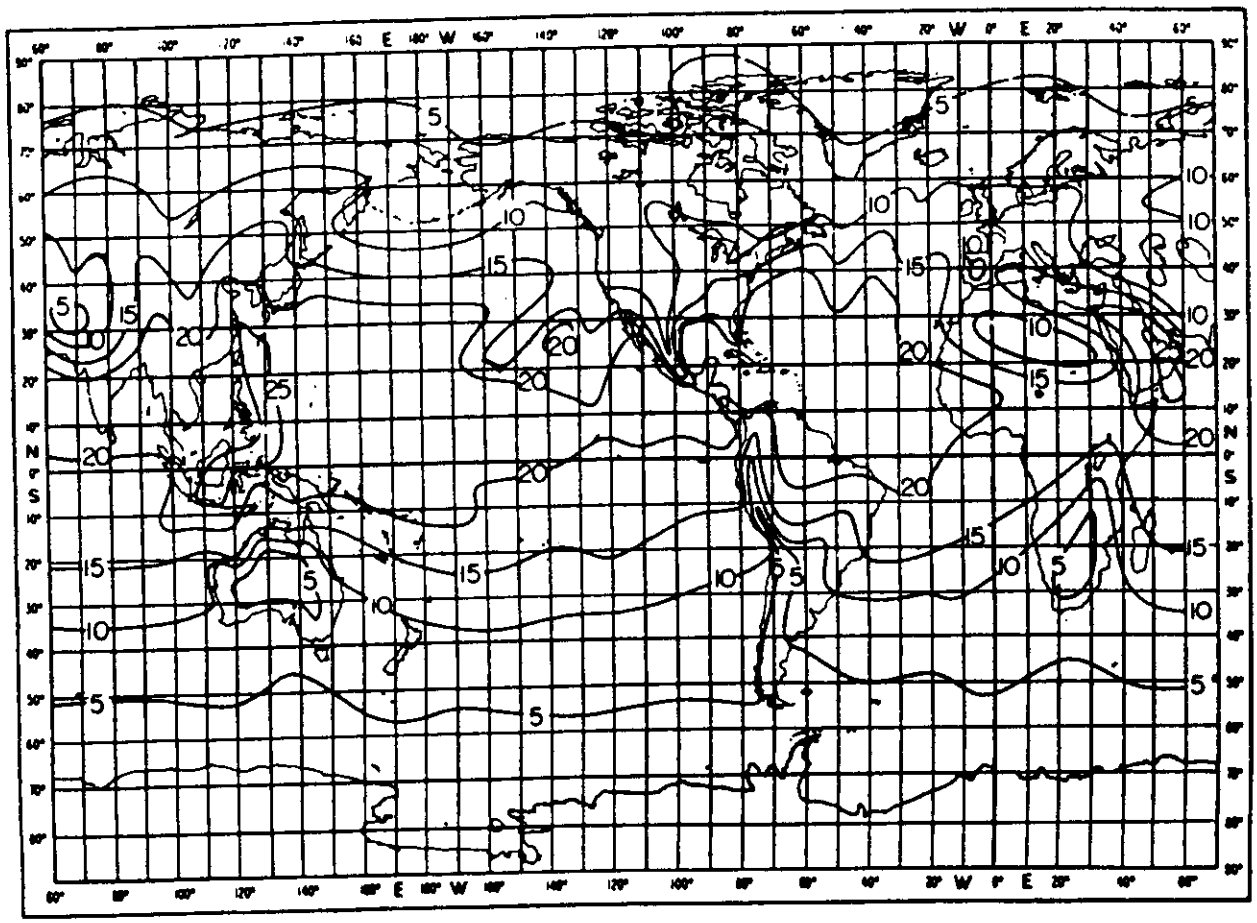

Fig 8 (b) – *Water vapour concentration (g/m³), August*

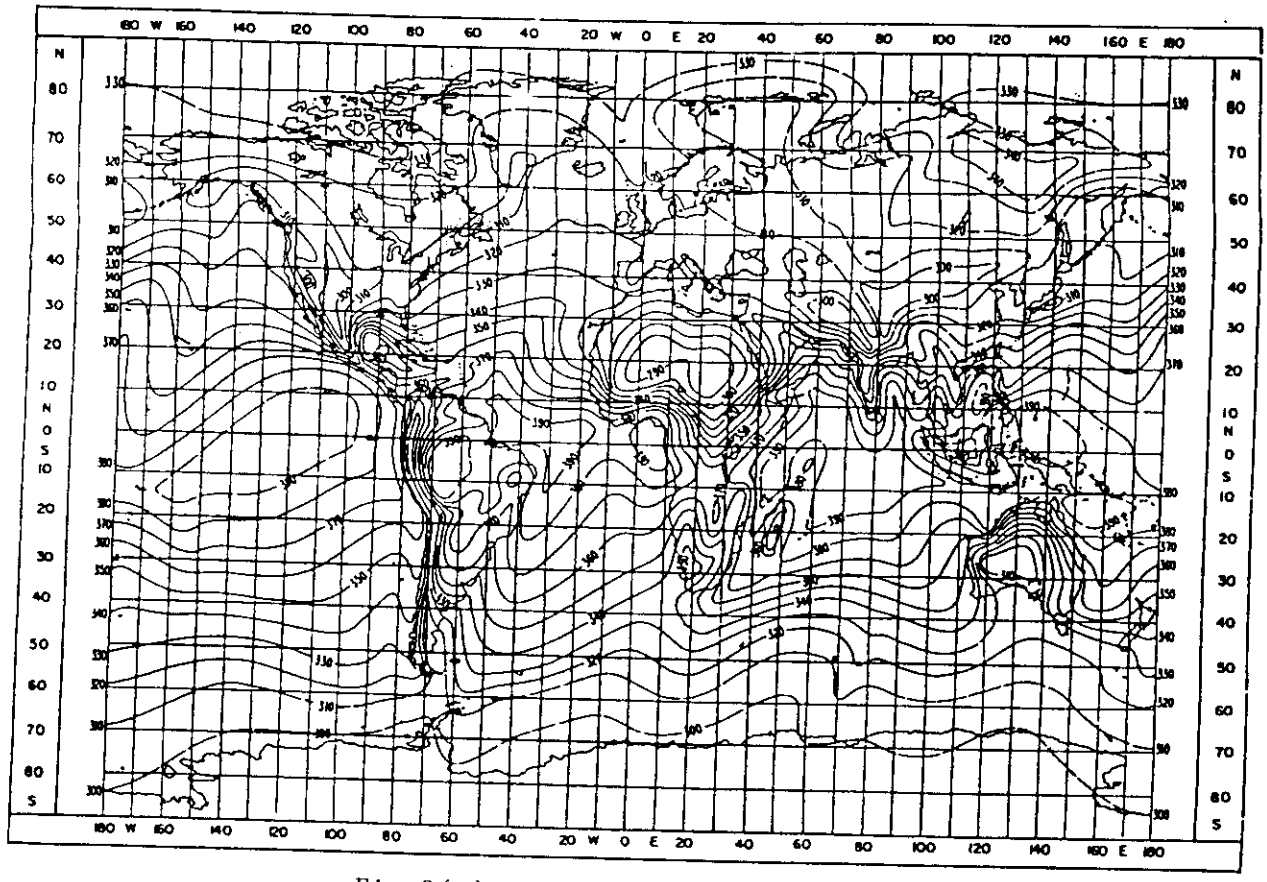

Fig 9(a) – *World-wide mean value of N_0 : February*

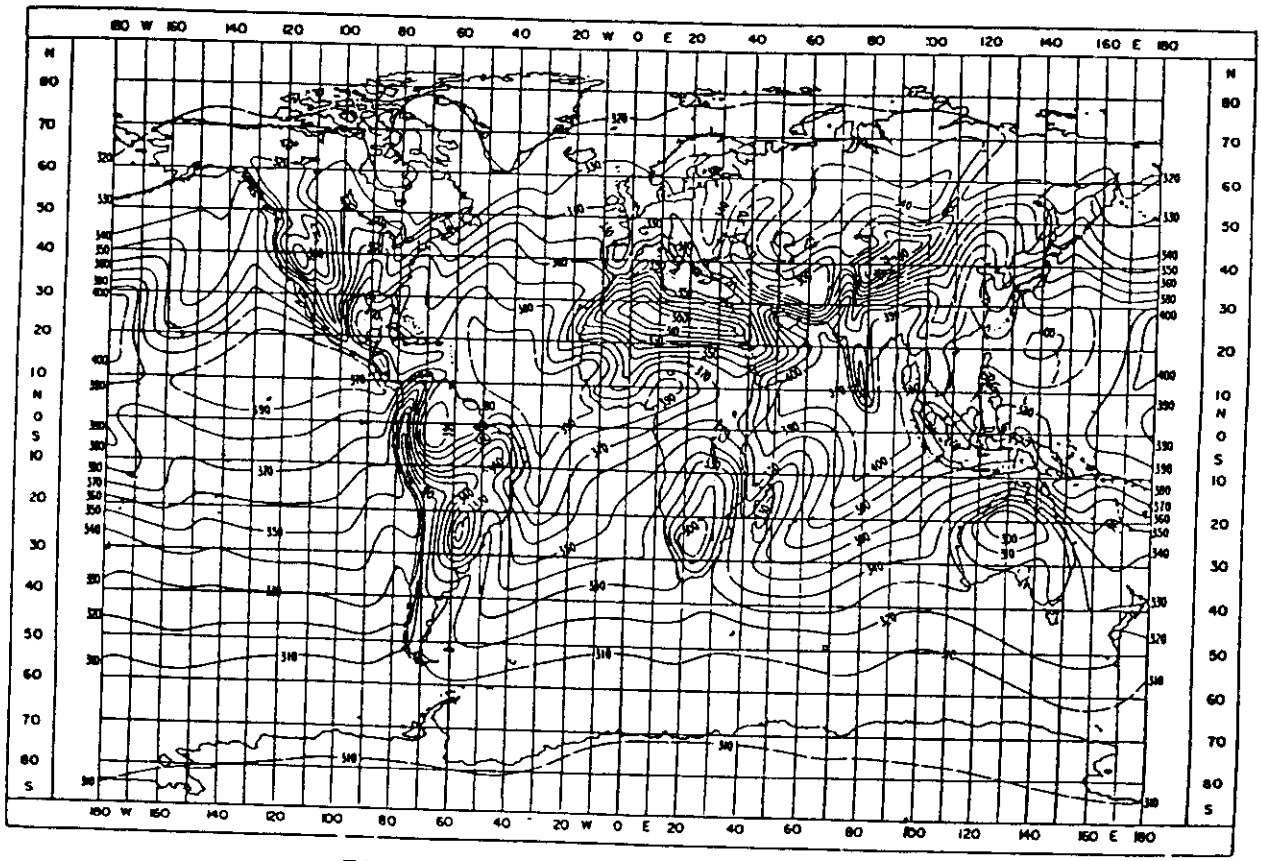

Fig 9 (b) – *World-wide mean value of N_0 : August*

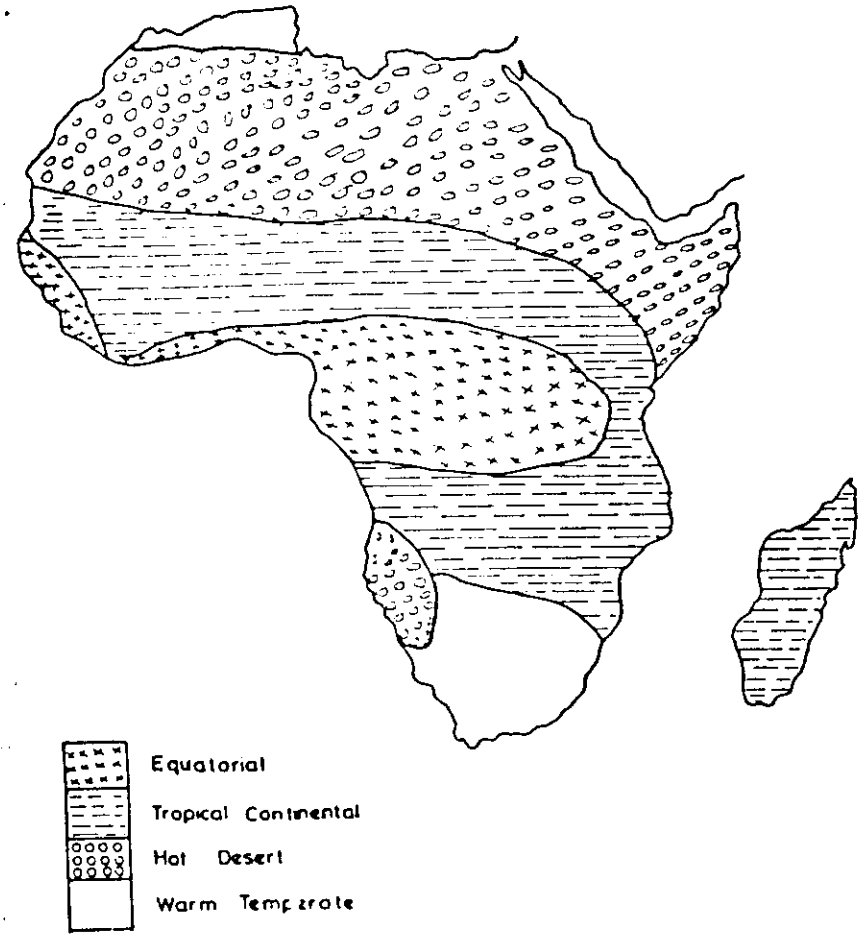

Figure 10(a) Main climatic Regions of Africa. (Ref. 5)

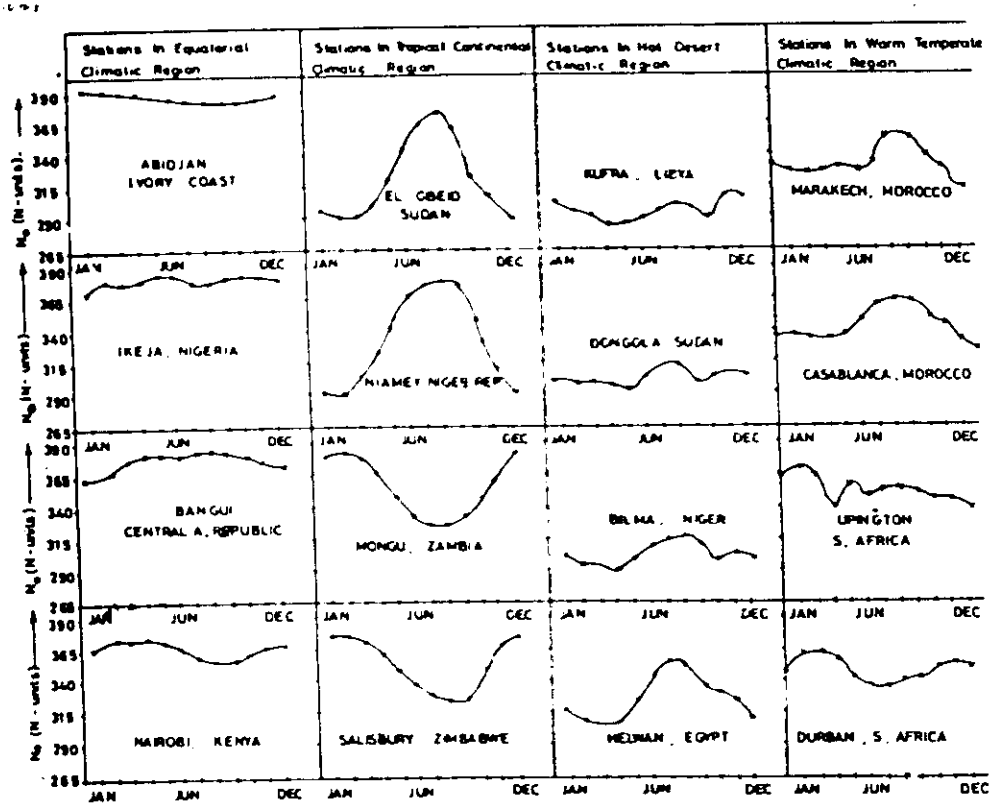

Figure 10(b) N_o patterns in the different climatic regions of Africa. (Ref. 5)

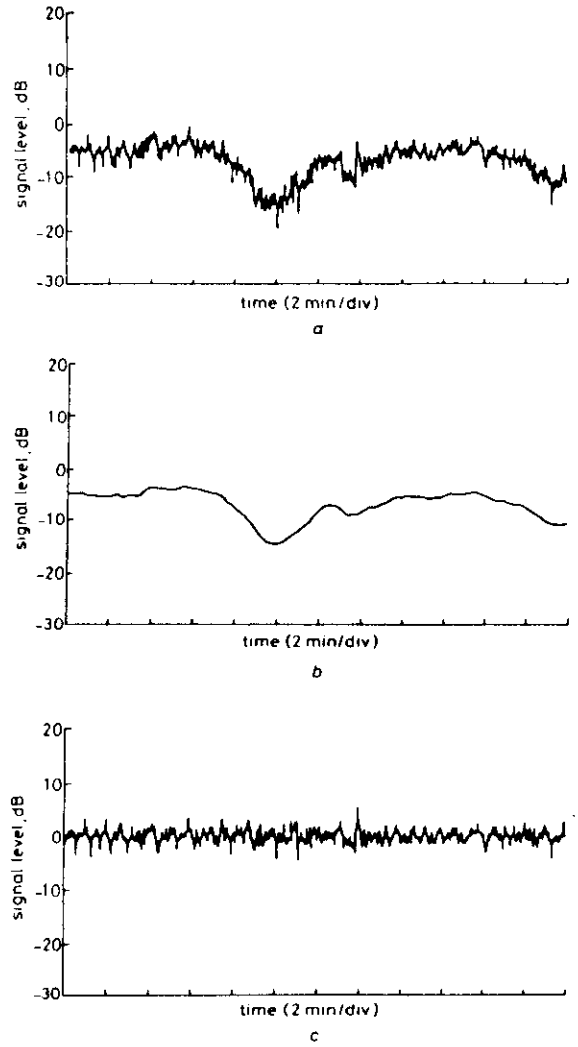

Fig. 11 *Separation of atmospheric scintillation and rain attenuation using a moving 1 min averaging technique, 29 July 1982*
a original 11 GHz data at Yamaguchi
b Data smoothed by the moving average procedure at 1 min intervals (11 GHz attenuatio
c Difference between original and smoothed data (11 GHz scintillation)
(Ref. 2)

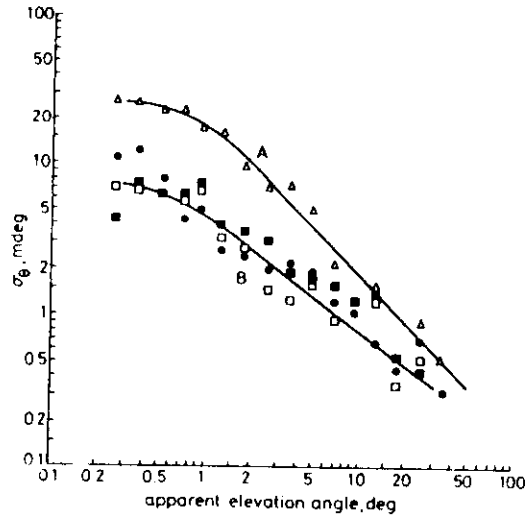

Fig 12 *Median standard deviation in elevation angle scintillation*
● spring A: summer
△ summer B: rest of year
□ fall f = 7·3 GHz
■ winter D = 36·6 m
(Ref. 2)

INTERNATIONAL ATOMIC ENERGY AGENCY

AND

UNITED NATIONS EDUCATIONAL SCIENTIFIC AND CULTURAL ORGANIZATION

INTERNATIONAL CENTRE FOR THEORETICAL PHYSICS

CLIMATIC INFORMATION FOR SATELLITE COMMUNICATION PLANNING.

PART 3: CLEAR SKY ABSORPTIVE EFFECTS - ATTENUATION BY ATMOSPHERIC GASES.

Prof. G.O. Ajayi
Department of Electronic & Electrical Engineering
Obafemi Awolowo University,
Ile-Ife, Nigeria.

FOURTH ICTP-URSI-ITU (BDT) COLLEGE ON RADIOPROPAGATION:
Propagation, Informatics and Radiocommunication System Planning.

30 January - 3 March, 1995.

1. INTRODUCTION

Molecular absorption at centimeter and millimeter wavelengths is primarily due to atmospheric water vapour and oxygen. The oxygen molecule has a small magnetic moment and absorption is produced by magnetic interaction with the incident field. The interaction produces a series of very close lines between about 50 and 70 GHz and an isolated line at 118.74 GHz. The electric dipole associated with the water vapour molecule interacts with the electromagnetic radiation to produce rotation absorption lines at 22.2, 183.3 and 325 GHz.

The total gaseous absorption in the atmosphere A_a (dB) over a path length r_o(km) is given by

$$A_a = \int_0^{r_o} \gamma_a(r)\,dr \qquad (1)$$

where

$$\gamma_a(r) = \gamma_o(r) + \gamma_w(r) \qquad (2)$$

$\gamma_a(r)$ is the specific attenuation (dB/km) made up of $\gamma_o(r)$ and $\gamma_w(r)$, the contributions by oxygen and water vapour respectively.

2. SPECIFIC ATTENUATION

The specific attenuation due to dry air at ground level (pressure = 1013 hPa) and at a temperature of 15°C is given by the following equations, which are based on curve-fitting to the line-by-line calculations (ITU-R Rec. 676).

$$\gamma_o = \left[7.19x10^{-3} + \frac{6.09}{f^2 + 0.227} + \frac{4.81}{(f-57)^2 + 1.50} \right] f^2 \; x \; 10^{-3} \; dB/km \qquad (3a)$$

for f < 57 GHz

$$\gamma_o = \left[3.79 \; x10^{-7} \; f + \frac{0.265}{(f - 63)^2 + 1.59} + \frac{0.028}{(f - 118)^2 + 1.47} \right] (f + 198)^2 \; x \; 10^{-3} \; dB/km \qquad (3b)$$

for 63 GHz < f < 350 GHz

where f is the frequency (GHz).

Figure 1 shows the dry-air specific attenuation at 15 C from 1 to 350 GHz. Between 57 and 63 GHz, the specific attenuation may

be obtained from the 0 km curve in Figure 2.

The temperature dependence of dry-air specific attenuation in the window regions (away from the peaks in attenuation) may be taken into account by a correction factor of -1% per °C from 15°C (attenuation increasing with decreasing temperature).

The specific attenuation due to water vapour at ground level (pressure = 1013 hPa) and at a temperature of 15°C is given by the following equation, which is based on curve fitting to the line-by-line calculation described in Annex 1:

$$\gamma_w = \left[0.050 + 0.0021\rho + \frac{3.6}{(f-22.2)^2 + 8.5} + \frac{10.6}{(f-183.3)^2 + 9.0} + \frac{8.9}{(f-325.4)^2 + 26.3} \right] f^2 \rho \, 10^{-4} \quad dB/km \qquad (4)$$

for f < 350 GHz

where f is the frequency expressed in GHz, and ρ is the water vapour density expressed in g/m^3.

Water-vapour specific attenuation is shown in Figure 1 for a water-vapour density of 7.5 g/m^3 and at 15°C.

The temperature dependence of water-vapour specific attenuation in the window regions (away from the peaks in attenuation) may be taken into account by a correction factor of -0.6% per °C from 15°C (attenuation increasing with decreasing temperature).

Note that water-vapour densities may not exceed the saturation value at the temperature considered. In equation (2), at a temperature of 15°C, the saturation density is approximately 12 g/m^3. For higher water-vapour densities, equation (2) must be corrected for the higher temperature necessary to sustain such densities.

Ranges of Validity of equations (1) & (2) are:

(i) Pressure: 1013 50 hPa
(ii) Temperature: -20°C to 40°C with accuracy of 15%
(iii) Water-vapour density: 0 to 50 g/m^3.

For greater accuracy, the line by line calculation is required.

3. REFERENCE STANDARD ATMOSPHERE FOR GASEOUS ATTENUATION

3.1 Temperature and Pressure

This is based on the U.S. Standard Atmosphere, 1976. The

atmosphere is divided into 7 successive layers showing linear variation with temperature as in Fig. 3 (ITU-R PN 835).

The temperature T at height h is given by (ref. 2):

$$T(h) = T_i + L_i\ (h-H_i) \qquad K \tag{5}$$

where $T_i = T(H_i)$

and L_i is the temperature gradient starting at altitude H_i and is given in Table 1.

When the temperature gradient $L_i \neq 0$, pressure is given by the equation:

$$P(h) = P_i \left[\frac{T_i}{T_i + L_i(h - H_i)}\right]^{\left[\frac{34.163}{L_i}\right]} \qquad hPa \tag{5}$$

(6a)

and when the temperature gradient $L_i = 0$, pressure is obtained from the equation:

$$P(h) = P_i \exp\left[\frac{-34.163(h - H_i)}{T_i}\right] \qquad hPa \tag{6}$$

(6b)

The ground-level standard temperature and pressure are:

$$T_o = 288.15 \quad K \tag{7}$$

$$P_o = 1013.25 \quad hPa$$

Note that above about 85 km altitude, local thermodynamic equilibrium of the atmosphere starts to break down, and the hydrostatic equation, on which the above equations are based, is no longer valid.

3.2 Water-vapour pressure

The distribution of water vapour in the atmosphere is generally highly variable, but may be approximated by the equation:

$$\rho(h) = \rho_o \exp(-0.5h) \qquad g/m^3 \tag{8}$$

and the standard ground-level water-vapour density is

$$\rho_o = 7.5 \quad g/m^3 \tag{9}$$

Vapour pressure is obtained from the density using the equation

$$e(h) = \frac{\rho(h)T(h)}{216.7} \quad hPa \tag{10}$$

Water-vapour density decreases exponentially with increasing altitude, up to an altitude where the mixing ratio $e(h)/P(h) = 2 \times 10^{-6}$. Above this altitude, the mixing ratio is assumed to be constant.

4. SLANT PATH ATTENUATION

The zenith path attenuation from sea level is obtained approximately from the product of the specific attenuation and the respective equivalent heights for dry air and water vapour.

Equivalent heights are given for

(i) dry air:

$$h_o = 6\text{km} \quad \text{for } f < 57 \text{ GHz} \tag{11a}$$

$$h_o = 6 + \frac{40}{(f-118.7)^2 + 1} \quad km \quad for\ 63 < f < 350\ GHz \tag{11b}$$

(ii) water-vapour:

$$h_w = h_{wo}\left[1 + \frac{3.0}{(f-22.2)^2 + 5} + \frac{5.0}{f-183.3)^2 + 6} + \frac{2.5}{(f-325.4)^2 + 4}\right] \quad km \tag{12}$$

for f < 350 GHz

where:

h_{wo} : water vapour equivalent height in the window regions

= 1.6 km in clear weather

= 2.1 km in rain.

The total zenith attenuation is then

$$A_g = \gamma_o h_o + \gamma_w h_w \quad dB \tag{13}$$

Figure 4 shows the total zenith attenuation at sea level for two cases:

(A) the dry reference standard atmosphere (B) including the water-

vapour model atmosphere. Between 50 and 70 GHz greater accuracy can be obtained from a more detailed figure.

(i) For elevation angles between 10° and 90°, the path attenuation is obtained using the cosecant law.

For stations at sea level.

$$A_g = \frac{h_o\gamma_o + h_w\gamma_w}{\sin\theta} \quad dB \tag{14}$$

where θ is the elevation angle.

(ii) For elevation angles between 0° and 10°, the real length of the atmospheric path must be taken into consideration.

$$A_g = \frac{\sqrt{R_e}}{\cos\theta}\left[\gamma_o\sqrt{h_o}\ F\left(\tan\theta\frac{\sqrt{R_e}}{h_o}\right) + \gamma_w\sqrt{h_w}\ F\left(\tan\theta\frac{\sqrt{R_e}}{h_w}\right)\right] dB \tag{15}$$

where:

R_e: effective Earth radius including refraction, expressed in km (a value of 8500 km is generally acceptable for the immediate vicinity of the Earth's surface);

θ: elevation angle;

F: function defined by:

$$F(x) = \frac{1}{0.661x + 0.339\sqrt{x^2 + 5.51}} \tag{16}$$

The formula (15) is applicable to cases of inclined paths between a satellite and an earth station situated at sea level.

Total slant path gaseous attenuation for a station at an altitude, h_s is given by (ref. 2)

(i) For $\theta > 10^{\circ}$

$$A_g = \frac{\gamma_o h_o e^{-h_s/h_o} + \gamma_w h_w}{\sin\theta} \quad dB \tag{17}$$

(ii) For $\theta < 10$

$$A_g = \frac{\gamma_o h_o e^{-h_s / h_o}}{g(h_o)} + \frac{\gamma_w h_w}{g(h_w)} \quad dB \qquad (18)$$

with

$$g(h) = 0.661x + 0.339\sqrt{x^2 + 5.5(h/R_e)}$$

$$x = \sqrt{Sin^2\theta + 2\ (h_s/R_e)}$$

where h is h_o or h_w as appropriate

R_e = 8500 km for $h_s \leq$ 1km

Equation (18) is an engineering approximation. Contribution by oxygen is relatively constant, but that due to water vapour varies since both water vapour density and its vertical profile are variable. Maximum gaseous attenuation occurs during the season of maximum rainfall.

5. GASEOUS ATTENUATION BY LINE-BY-LINE SUMMATION

Appendix 1 (ref. 2) outlines the procedure for accurate calculation of gaseous attenuation by line-by-line summation.

6. RANGES OF SPECIFIC ATTENUATION AT THE WINDOWS (Ref. Ajayi and Kolawole, 1984)

Spectra Window	Freq. Range (GHz)	Attenuation (dB)	
		Tropical	Temperate
W_1	24 - 48	0.10 - 0.15	0.06 - 0.15
W_2	70 - 110	0.20 - 0.50	0.08 - 0.20
W_3	120 - 155	0.60 - 1.00	0.20 - 0.40
W_4	190 - 300	2.00 - 5.00	0.70 - 2.00
W_5	335 - 350	13.00	5.00 - 6.00

Figure 5 (Ajayi and Kolawole, 1984) shows the comparison between the specific attenuation due to oxygen and water vapour at Ile-Ife

(geog. lat. 7.3 N, geog. long. 4.3 E) in Nigeria and a typical temperate station. Figure 6 (ref. 1) also shows the computed total zenith attenuation due to oxygen and water vapour as well as the total slant path attenuation at elevation angles of 55° and 23°, which correspond to the elevation angle at Ile-Ife for the INTELSAT AOR (Atlantic Ocean Region) and IOR (Indian Ocean Region) Satellites respectively.

Figs. 7 and 8 show respectively measured slant-path attenuation at 31.65 GHz measured in Beijing and slant-path attenuation as a function of elevation angle at 20.6 GHz in Beijing (ref. 5).

7. REFERENCES

1. Ajayi G. O. and Kolawole L. B.: Centimeter and millimeter wave attenuation by atmospheric gases and rainfall at a tropical station. Int. J. of Infrared and Millimeter Waves, 5(7), 919 -935, 1984.

2. ITU-R Rec. 676: Attenuation by atmospheric gases in the frequency range 1 - 350GHz, DOC. 5/13, 1992.

3. ITU-R PN 835: Reference standard atmosphere for gaseous attenuation; DOC. 5A/TEMP/26, 1993.

4. ITU-R Rec. PN 818-2: Propagation data and prediction methods required for the design of Earth - space telecommunications systems.

5. Li, L. and C. Y. Jiang: Investigation on attenuation by atmospheric gases in China - Private Commuincation, 1994.

6. Rogers D. V.: Propagation Considerations for Satellite Broadcasting at Frequencies above 10GHz, IEEE J. SAC-3, 100 -110, 1985.

CALCULATION OF GASEOUS ATTENUATION BY LINE-BY-LINE SUMMATION

In this Annex are given details of a Microwave Propagation Model using a reduced line base. This model enables the calculation of gaseous attenuation at frequencies up to 350 GHz at any temperature, pressure and humidity. For frequencies higher than 350 GHz, the full line base should be employed.

The specific gaseous attenuation is given by:

$$\gamma = 0.1820\, f\, N''(f) \qquad \text{dB/km} \tag{21}$$

when f is the frequency in GHz and N″(f) is the imaginary part of the frequency-dependent complex refractivity:

$$N''(f) = \sum_i S_i F_i + N''_D(f) + N''_W(f) \tag{22}$$

S_i is the strength of the i^{th} line, F_i is the line shape factor and the sum extends over all the lines; $N''_D(f)$ and $N''_W(f)$ are dry and wet continuum spectra.

The line strength is given by:

$$\begin{aligned} S_i &= a_1 p \theta^3 \exp[a_2(1-\theta)] && \textit{for oxygen lines} \\ &= b_1 e \theta^{3.5} \exp[b_2(1-\theta)] && \textit{for water-vapour lines} \end{aligned} \tag{23}$$

p: dry air pressure in hPa

e: water vapour partial pressure in hPa (total barometric pressure P = p + e)

θ = 300/T, T: temperature (Kelvin).

The coefficients a_1, a_2 are given in Table 1 for oxygen, those for water vapour, b_1 and b_2, are given in Table 2.

The line-shape factor is given by:

$$F_i = \frac{f}{f_i}\left[\frac{\Delta f - \delta(f_i - f)}{(f_i - f)^2 + \Delta f^2} + \frac{\Delta f - \delta(f_i + f)}{(f_i + f)^2 + \Delta f^2}\right] \tag{24}$$

where f_i is the line frequency and Δf is the width of the line:

$$\begin{aligned} \Delta f &= a_3(p\theta^{0.8} + 1.1 e\theta) && \textit{for oxygen} \\ &= b_3(p\theta^{0.6} + 4.80 e\theta^{1.1}) && \textit{for water vapour} \end{aligned} \tag{25}$$

and δ is a correction factor which arises due to interference effects in oxygen lines:

$$\delta = a_4 p \theta^{a_5} \qquad \textit{for oxygen}$$
$$= 0 \qquad \textit{for water vapour} \tag{26}$$

The spectroscopic coefficients are given in Tables 1 and 2.

TABLE 1

Spectroscopic parameters for oxygen lines

f_i (GHz)	a_1 (kHz/hPa)	a_2	a_3 (GHz/hPa)	a_4 (1/hPa)	a_5
51.5034	6.08 E-7	7.74	8.90 E-4	6.60 E-4	1.8
52.0214	14.14 E-7	6.84	9.20 E-4	5.50 E-4	1.8
52.5424	31.02 E-7	6.00	9.40 E-4	5.70 E-4	1.8
53.0669	64.10 E-7	5.22	9.70 E-4	5.30 E-4	1.9
53.5957	124.70 E-7	4.48	10.00 E-4	5.40 E-4	1.8
54.1300	228.00 E-7	3.81	10.20 E-4	4.80 E-4	2.0
54.6712	391.80 E-7	3.19	10.60 E-4	4.80 E-4	1.9
55.2214	631.60 E-7	2.62	10.79 E-4	4.17 E-4	2.1
55.7838	953.50 E-7	2.12	11.10 E-4	3.75 E-4	2.1
56.2648	548.90 E-7	0.01	16.46 E-4	7.74 E-4	0.9
56.3634	1344.00 E-7	1.66	11.44 E-4	2.97 E-4	2.3
56.9682	1763.00 E-7	1.26	11.81 E-4	2.12 E-4	2.5
57.6125	2141.00 E-7	0.91	12.21 E-4	0.94 E-4	3.7
58.3239	2386.00 E-7	0.62	12.66 E-4	- 0.55 E-4	- 3.1
58.4466	1457.00 E-7	0.08	14.49 E-4	5.97 E-4	0.8
59.1642	2404.00 E-7	0.39	13.19 E-4	- 2.44 E-4	0.1
59.5910	2112.00 E-7	0.21	13.60 E-4	3.44 E-4	0.5
60.3061	2124.00 E-7	0.21	13.82 E-4	- 4.13 E-4	0.7
60.4348	2461.00 E-7	0.39	12.97 E-4	1.32 E-4	- 1.0
61.1506	2504.00 E-7	0.62	12.48 E-4	- 0.36 E-4	5.8
61.8002	2298.00 E-7	0.91	12.07 E-4	- 1.59 E-4	2.9
62.4112	1933.00 E-7	1.26	11.71 E-4	- 2.66 E-4	2.3
62.4863	1517.00 E-7	0.08	14.68 E-4	- 4.77 E-4	0.9
62.9980	1503.00 E-7	1.66	11.39 E-4	- 3.34 E-4	2.2
63.5685	1087.00 E-7	2.11	11.08 E-4	- 4.17 E-4	2.0
64.1278	733.50 E-7	2.62	10.78 E-4	- 4.48 E-4	2.0
64.6789	463.50 E-7	3.19	10.50 E-4	- 5.10 E-4	1.8
65.2241	274.80 E-7	3.81	10.20 E-4	- 5.10 E-4	1.9
65.7648	153.00 E-7	4.48	10.00 E-4	- 5.70 E-4	1.8
66.3021	80.09 E-7	5.22	9.70 E-4	- 5.50 E-4	1.8
66.8368	39.46 E-7	6.00	9.40 E-4	- 5.90 E-4	1.7
67.3696	18.32 E-7	6.84	9.20 E-4	- 5.60 E-4	1.8
67.9009	8.01 E-7	7.74	8.90 E-4	- 5.80 E-4	1.7
118.7503	945.00 E-7	0.00	15.92 E-4	- 0.13 E-4	0.8

TABLE 2

Spectroscopic parameters for water-vapour lines

f_i (GHz)	b_1 (kHz/hPa)	b_2	b_3 (GHz/hPa)
22.235	0.0109	2.143	27.84 E-4
183.310	0.2300	0.653	31.64 E-4
325.153	0.1540	1.515	26.70 E-4

The dry air continuum arises from the non-resonant Debye spectrum of oxygen below 10 GHz and a pressure-induced nitrogen attenuation above 100 GHz.

$$N''_D(f) = fp\theta^2\left[\frac{6.14 \times 10^{-5}}{d\left[1+\left(\frac{f}{d}\right)^2\right]\left[1+\left(\frac{f}{60}\right)^2\right]} + 1.4 \times 10^{-11}(1 - 1.2 \times 10^{-5} f^{1.5})p\theta^{1.5}\right] \quad (27)$$

where d is the width parameter for the Debye spectrum:

$$d = 5.6 \times 10^{-4}(p + 1.1e)\theta^{0.8} \quad (28)$$

The wet continuum, N"w(f), is included to account for the fact that measurements of water vapour attenuation are generally in excess of those predicted using the theory described by equations (4) to (8), plus a term to include the effects of higher-frequency water-vapour lines not included in the reduced line base.

$$N''_W(f) = 1.18 \times 10^{-6}[p + 30.3e\theta^{6.2}]fe\theta^{3.0} + 2.3 \times 10^{-10} pe^{1.1}\theta^2 f^{1.5} \quad (29)$$

Note that if the full line base is employed, the second term in (29) is not required.

To calculate gaseous attenuation along a vertical path through the atmosphere, it generally suffices to divide the atmosphere into horizontal layers 1 km thick, assigning to each layer a pressure, temperature and water-vapour partial pressure, for example from the reference standard atmosphere in draft new Recommendation [Document 5/9], and to sum the attenuations for each layer.

For elevation angles other than the zenith, the total one-way attenuation through the atmosphere is considered by means of a path extension factor, s, by which the attenuation is multiplied.

For a stable, spherically-symmetric and horizontally-stratified atmosphere, and at elevation angles, ψ, between 10° and 90° , the increase in pathlength through the atmosphere follows a cosecant law, i.e.

$$s = (\sin \psi)^{-1} \qquad (30)$$

At elevation angles below about 10°, however, the refractive index of the atmosphere and the curvature of the Earth's surface must be considered, and the pathlength extension factor for each layer of the atmosphere should be determined from:

$$s = \left\{ 1 - \left[\frac{n_i(a + h_i)}{n_j(a + h_j)} \cos \psi \right]^2 \right\}^{-\frac{1}{2}} \qquad (31)$$

where n_i is the index of refraction at altitude h_i, n_j is the index of refraction at altitude h_j and a is the radius of the Earth (6 370 km).

To take account properly of refractive bending at very low elevation angles, ψ should be recalculated along the path, according to

$$\cos \psi_{j_i} = \frac{n_i(a + h_i)}{n_j(a + h_j)} \cos \psi_i \qquad (32)$$

Note that there will also be a small contribution to the index of refraction, n, from the frequency-dependent refractive dispersion, although this is generally less than 1% of the frequency-independent index as given in Recommendation 453, at frequencies below 350 GHz.

TABLE 1

Subscript i	Altitude, H_i (km)	Temperature gradient, L_i (K/km)
0	0	-6.5
1	11	0.0
2	20	+1.0
3	32	+2.8
4	47	0.0
5	51	-2.8
6	71	-2.0
7	85	

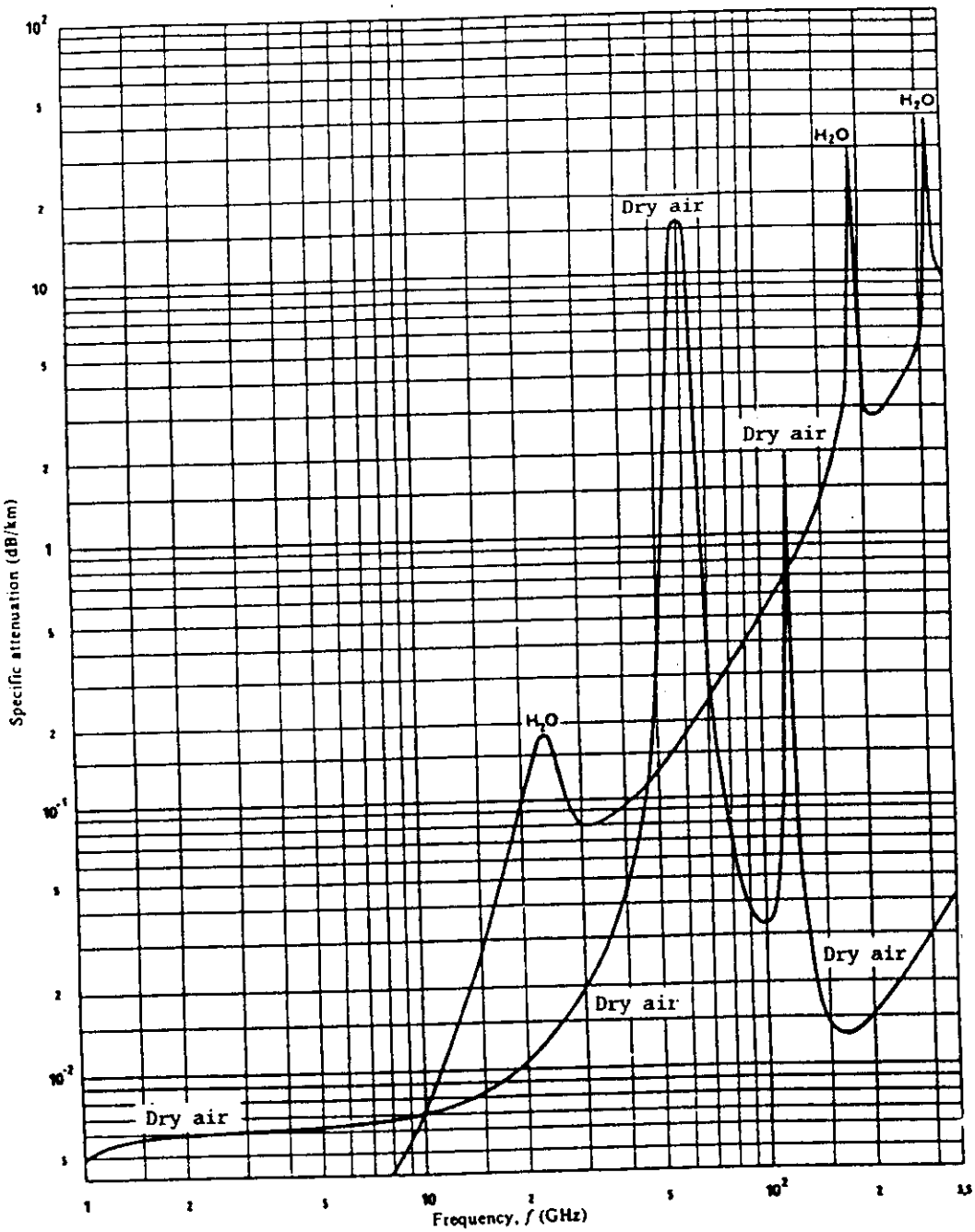

FIGURE 1 – *Specific attenuation due to atmospheric gases*

Pressure: 1013 hPa
Temperature: 15 °C
Water vapour: 7.5 g/m³

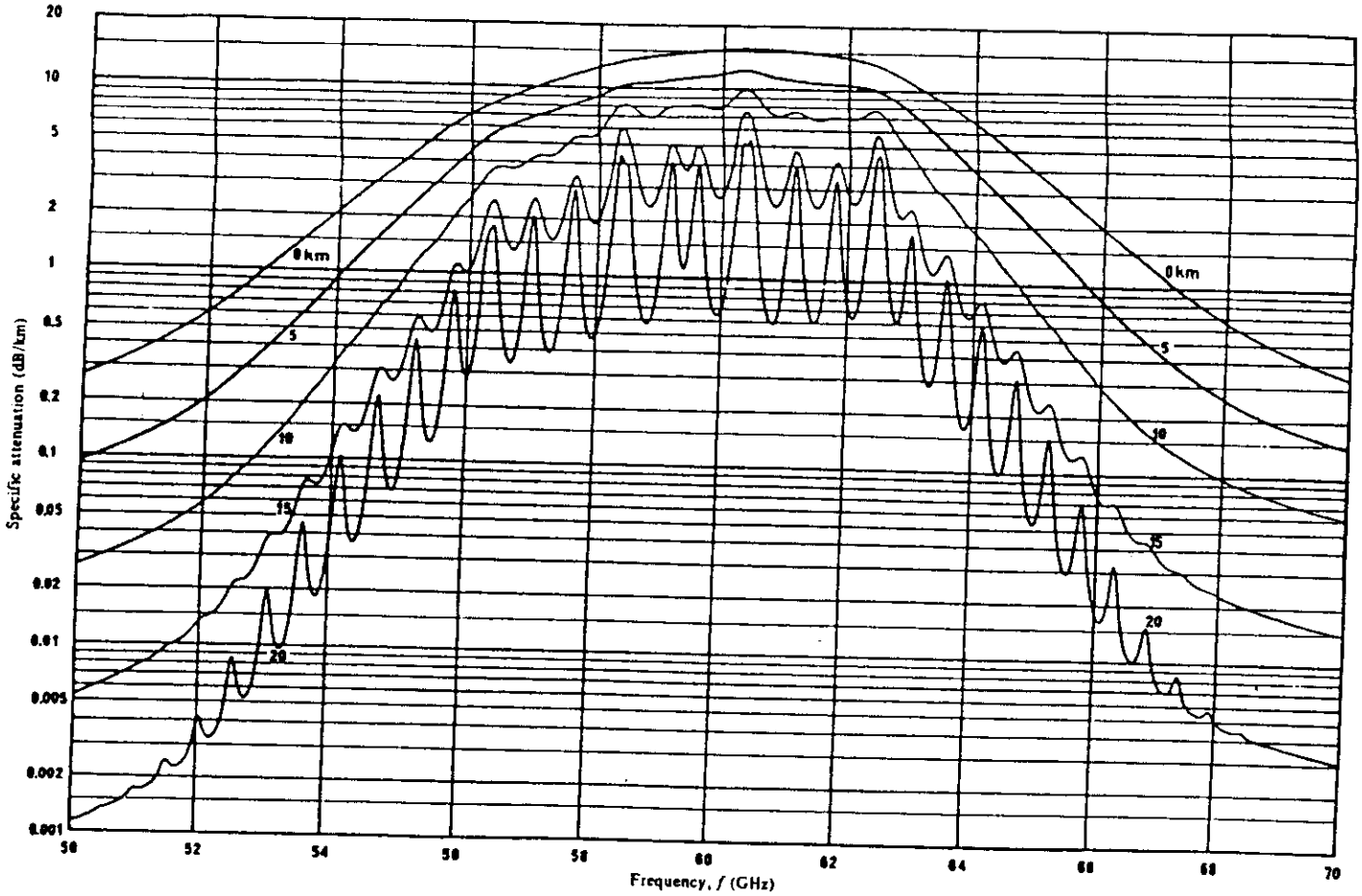

FIGURE 2 – *Specific attenuation in the range 50-70 GHz at the altitudes indicated*

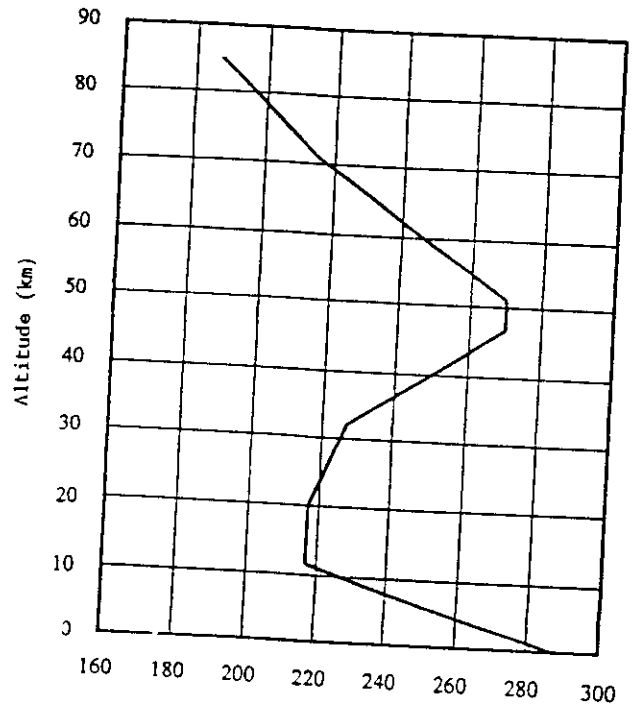

FIGURE 3

Reference profile of atmospheric temperature

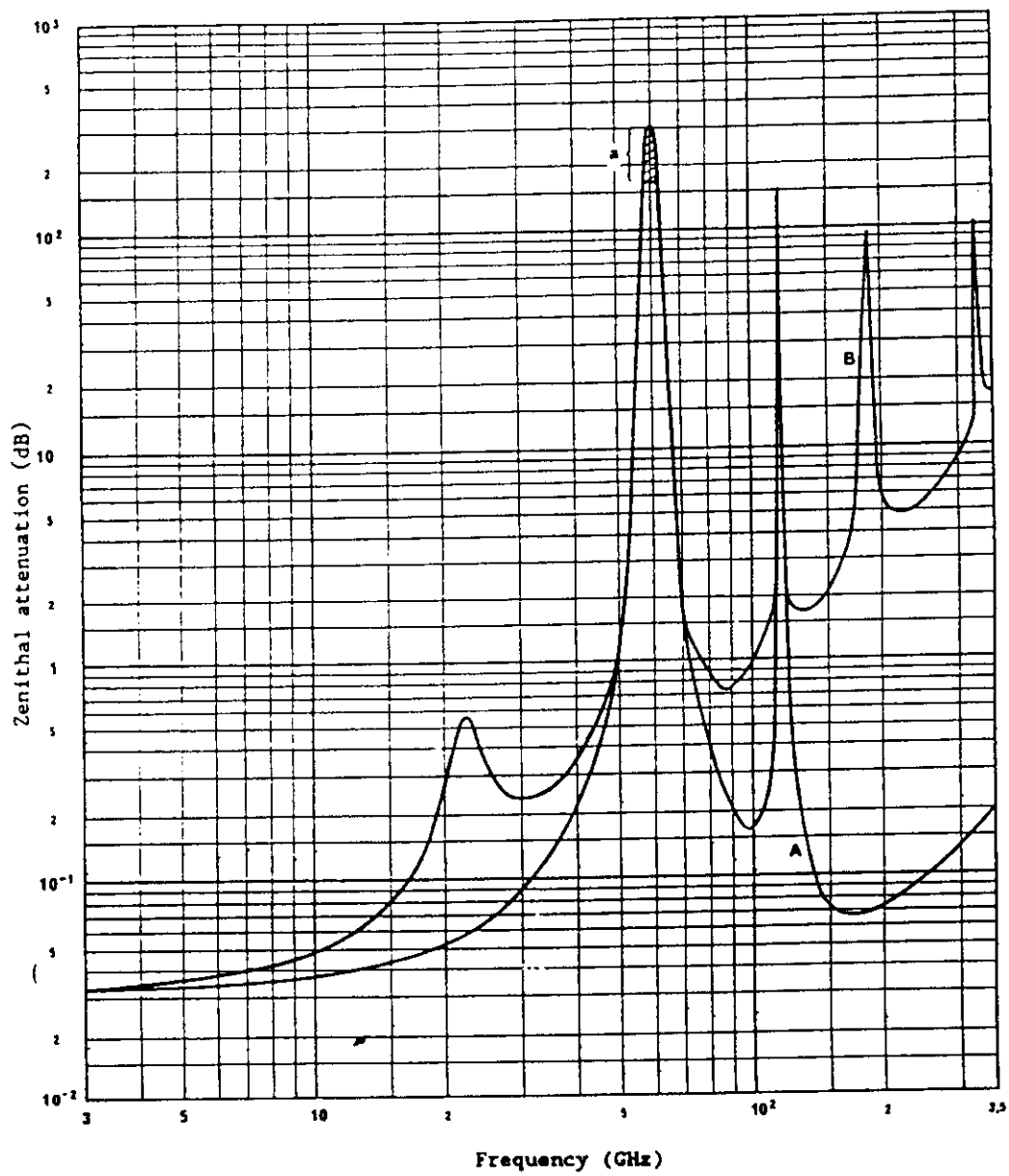

FIGURE 4

Total zenithal attenuation at ground level

Pressure: 1013 hPa
Temperature: 15°C
a): range of values (see Figure 4)

A: for a dry atmosphere

B: with an exponential water-vapour atmosphere of 7.5 g/m³ at ground level, and a scale height of 2 km

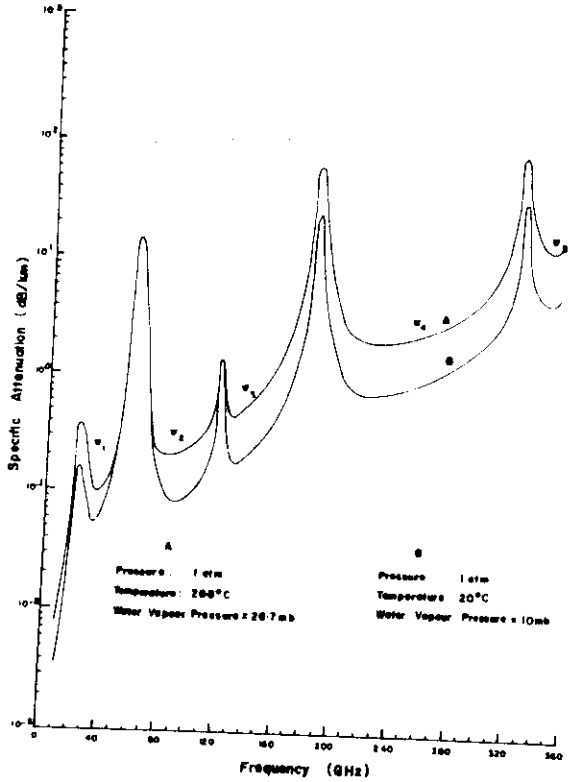

Figure 5 Specific attenuation due to oxygen and water vapour.

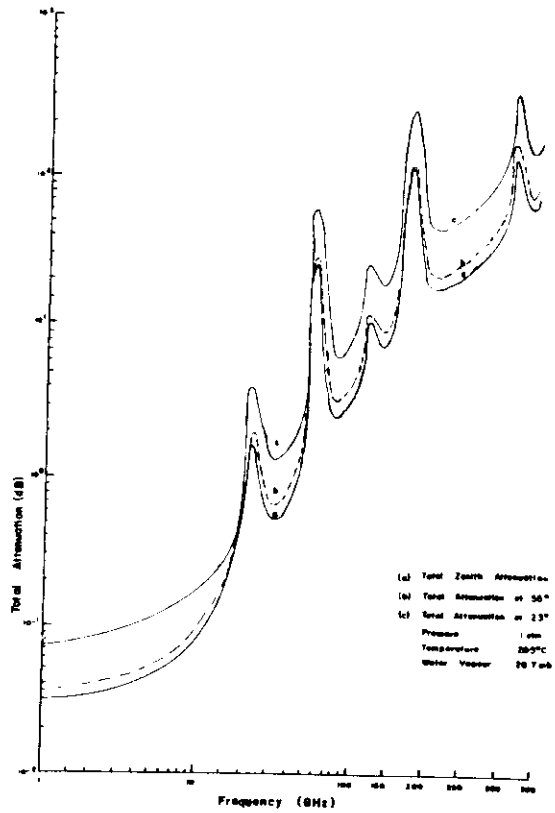

Figure 6. (a) Total zenith attenuation due to oxygen and water vapour (b) Total slant path attenuation at elevation angle of 55^{0} and (c) Total slant path attenuation at elevation angle of 23^{0}.

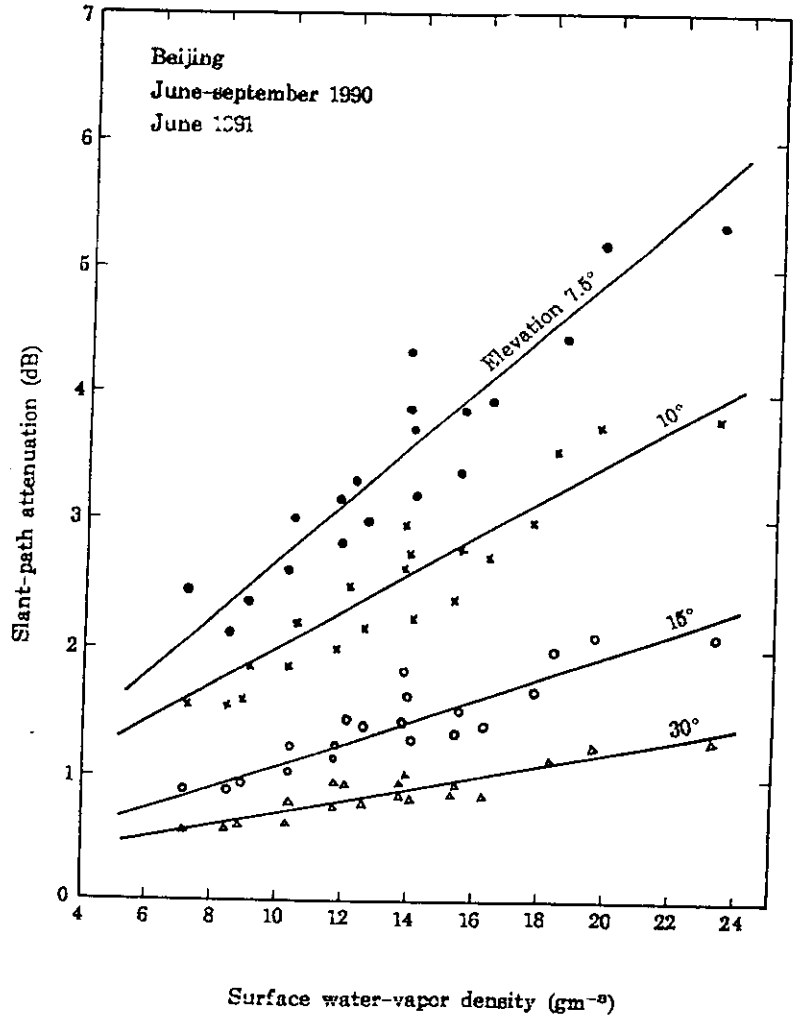

Figure 7 : Slant-path attenuation at 31.65 GHz

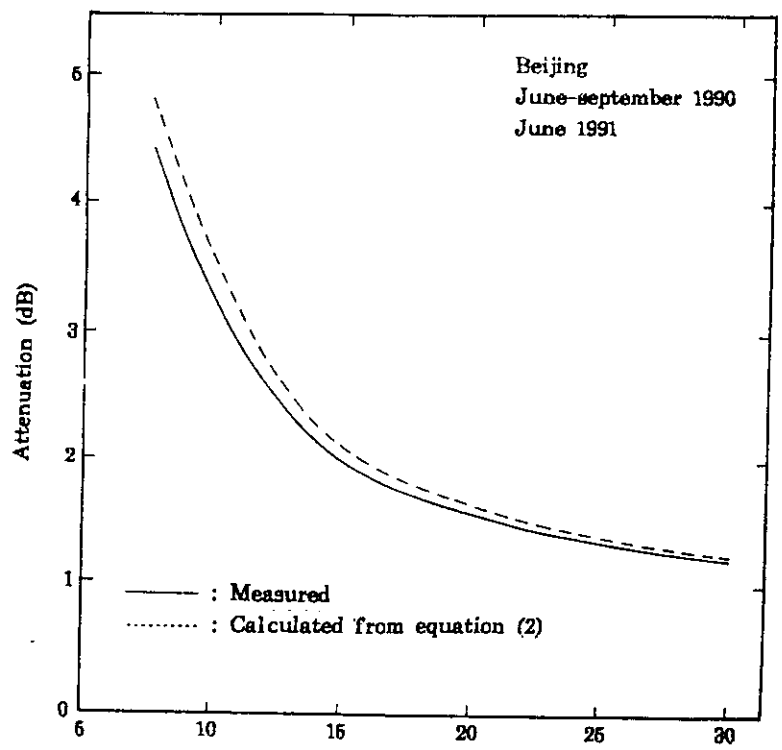

Figure 8 : Atmospheric attenuation versus path elevation at 20.6 GHz

INTERNATIONAL ATOMIC ENERGY AGENCY

AND

UNITED NATIONS EDUCATIONAL SCIENTIFIC AND CULTURAL ORGANIZATION

INTERNATIONAL CENTRE FOR THEORETICAL PHYSICS

CLIMATIC INFORMATION FOR SATELLITE COMMUNICATION PLANNING.

PART IV: RAIN EFFECTS

Prof. G.O. Ajayi
Department of Electronic & Electrical Engineering
Obafemi Awolowo University,
Ile-Ife, Nigeria.

FOURTH ICTP-URSI-ITU (BDT) COLLEGE ON RADIOPROPAGATION:
Propagation, Informatics and Radiocommunication System Planning.

30 January - 3 March, 1995.

1. INTRODUCTION

Hydrometeors such as rain, hail, fog, ice, cloud and snow attenuate radio waves above 5 GHz and cause other impairments to communication systems. The most important effects of hydrometeors on microwave propagation are (Ippolito, 1981):

(a) attenuation caused by dissipation of radio wave energy as heat.

(b) scatter resulting in loss in the desired direction and consequently causing interference to other systems.

(c) depolarization due to non-spherical nature of raindrops.

(d) rapid amplitude and phase scintillations caused by equivalent multipath propagation.

(e) antenna gain degradation due to phase dispersion of ray paths reaching the antenna.

(f) bandwidth coherence reduction especially in digital systems involving carriers spanning over large channel bandwidths.

2. ATTENUATION DUE TO RAIN

The specific attenuation γ in dB/km due to precipitation can be evaluated on the basis of the classical Mie scattering theory. The evaluation depends on the knowledge of the complex refractive index of water at the raindrop temperature as well as the terminal velocity and the size distribution of the raindrops [see ITU-R Report 721-1].

$$\gamma = 4.343 \int_0^\infty Q_t(D)\, N(D)\ \ dB \qquad (1(a)$$

where $Q_t(D)$ is the extinction cross-section and N(D) dD is the number density of raindrops with equivalent diameter D in the interval dD.

$$Q_t(D) = Q_s(D) + Q_A(D) \qquad (1(b))$$

where Q_s and Q_A are scattering and absorption cross sections respectively.

$Q_t(D)$ is a function of dropsize diameter, wavelength and complex refractive index m of the water drops.

The rain rate is related to the drop size distribution by

$$R = 6\pi \times 10^{-4} \int_0^\infty D^3 \; N(D) \; V \; (D) \; dD \qquad (2)$$

where V(D) is the terminal velocity of drops in ms^{-1} and N(D) is in $mm^{-1}\ m^{-3}$.

The specific attenuation has been found to be related to rainfall rate R as

$$\gamma = aR^b \qquad (3)$$

where a and b are dependent on the frequency, polarization and the raindrop characteristics.

Table 1 (Ajayi, 1990) shows the comparison between the values of a and b recommended by the ITU-R and those obtained making use of the tropical raindrop size distribution.

2.1 Rain Rate Distribution

The specific attenuation can be predicted from a knowledge of rain rate distribution and raindrop size distribution. Fig. 1 shows the ITU-R rain rate climatic zones and Table 2 shows the rain rate for each zone. In areas where measured data of rain rate distribution are not available, then Fig. 1 is adequate.

A model for rain rate distribution is given by Moupfouma, 1987 as

$$P(R \geq r) = \frac{ae^{-ur}}{r^b} \quad r \geq 2mm/h \qquad (4)$$

where a and b are derived from the rain rate $R_{0.01}$ exceeded 0.01% of the time and u is the parameter depending on climate and geographical features.

$$a = 10^{-4} \; R^b_{0.01} \quad \exp \; (U \; R_{0.01}) \qquad (5)$$

$$b = 8.22 \; R_{0.01}^{-0.584} \qquad (6)$$

for tropical regions, U = 0.042 for coastal and mountainous areas and U = 0.025 for average rolling terrain (Moupfouma, 1987).

In the modified version of the model, Moupfouma expressed the

parameter U as a function of the rain rate

$$U = \lambda R^{-s} \qquad (7)$$

where λ and s are parameters representing the ITU-R rain climatic zones. The values of λ and s are given below.

ITU-R Climatic Zones	λ	s
D	0.18	0.33
E	0.05	0.29
F	0.07	0.32
G	0.14	0.28
H	0.06	0.19
J	0.07	0.18
K	0.05	0.17
L	0.05	0.22
M	0.05	0.09
N	0.033	0.06
P	0.035	0.10

A modified form of equation (7) in CCIR DOC 5A/40-E is under consideration for universal application. Fig. 2(a) shows the climatic dependence of the parameter U. Figs.2(b), (c), (d) show comparison of predicted and measured rainfall rate for a number of localities.

2.2 Raindrop Size Distribution

The ITU-R currently recommends the Laws and Parsons (L-P) raindrop size distribution for scattering applications. This distribution is similar to that of the negative exponential distribution of Marshall and Palmer given by

$$N(D) = N_o \, e^{-\Lambda D} \qquad (8(a))$$

where

$$\Lambda = A \, R^{-0.21} \qquad (8(b))$$

and N(D) = number of drops per mm diameter interval per cubic metre, $N_o = 8000 m^{-3} \, mm^{-1}$ and A = 4.1.

Making use of the raindrop size distribution measured in Nigeria, Ajayi and Olsen, 1985 proposed the following model for tropical regions

$$N(D) = \frac{N_T}{\sigma D\sqrt{2\pi}} \left(\exp -\frac{1}{2} \left(\frac{\ln D - \mu}{\sigma}\right)^2\right) \quad (9)$$

$$N_T = 108R^{0.363} \quad (10(a))$$

$$\mu = -0.195 + 0.199 \ln R \quad (10(b))$$

$$\sigma^2 = 0.137 - 0.013 \ln R \quad (10(c))$$

Fig. 3 shows the comparison between the M-P and the Ajayi-Olsen (A-O) distributions. The M-P overestimates both the small and the large diameter drop number for the tropical region.

Fig. 4 (Ajayi and Adimula) also shows a comparison of the tropical raindrop size models with the Marshall-Palmer and Joss, et. al. models for (a) shower rain and (b) thunderstorm rain.

3. EARTH-SATELLITE PATH

Figure 5 shows an Earth-satellite radio path. If the rain rates were uniform over a radio path of length L (km), the path rain attenuation A_p would simply be the product of the specific attenuation γ for the rain rate R and the length, L, between the earth and the satellite. In practice the variation of precipitation in both horizontal and vertical directions makes the calculation of attenuation along an earth-space path a complex matter.

3.1 Horizontal Structure of Rain

Rainfall is inhomogeneous in the horizontal plane. For example convective cells embedded in stratiform rain render the distribution of rain non-uniform in the horizontal direction. The horizontal structure is known to depend on the rainfall type, the topography and the composition of the convective cells.

The concept of the horizontal reduction factor has been employed to account for the non-uniform nature of rain in computing the attenuation due to rain on terrestrial paths. The effective path length assuming uniform rain rate is obtained by multiplying the

physical path length, L by the reduction factor r, given by

$$r = \frac{1}{1 + \frac{L}{L_o}} \qquad (11)$$

where for $R_{0.01} \leq 100$mm/h

$$L_o = 35 \exp(-0.015 R_{0.01}) \qquad (12)$$

For $R_{0.01} > 100$mm/h, the value 100mm/h is used in place of $R_{0.01}$. As shown later, the CCIR currently adopts the concept of the reduction factor to account for the horizontal variation of rainfall in the estimation of attenuation along Earth-satellite path.

3.2 Vertical Structure of Precipitation

A vertically homogeneous and cylindrical model of a raincell extending from the earth's surface to the 0°C isotherm height has been assumed in prediction models for attenuation. Although the simple raincell model has given good results for the temperate latitudes, it overestimates the attenuation in the tropical regions because of the heavy rainfall, different characteristics of tropical rain with different horizontal and vertical structures and/or different drop size distributions.

Below the 0°C isotherm liquid particles exist, that attenuate the signals and above the 0°C isotherm, there are only freezing particles with negligible attenuation on the radio waves.

3.2.1 ITU-R and the Rain Height

The vertical profile of rain and its height in particular have been taken into careful consideration by the ITU-R in the prediction of rain attenuation along Earth-satellite paths.

The current ITU-R slant path attenuation procedure uses an effective rain height, h_R given by

$$h_R = 3.0 + 0.028\varphi \quad km \qquad 0 \leq \varphi < 36 \qquad (13)$$

$$h_R = 4.0 - 0.075\,(\varphi - 36) \text{ km} \qquad \varphi \geq 36 \qquad (14)$$

where φ is the latitude of the site, which is taken as positive in the southern and northern hemispheres.

The height of the 0°C isotherm in rain, h_{FR} in the ITU-R

meteorological texts is given by

h_{FR} = 5 km $0 \leq \varphi < 23$ (15)

h_{FR} = 5 - 0.075 (φ - 23) km $\varphi \geq 23$ (16)

The draft new recommendation for h_{FR} is given as (CCIR DOC. 5/15)

$$h_{FR} = \begin{cases} 5 - 0.075\,(\varphi - 23) & \varphi > 23 \quad \text{Northern Hemisphere} \\ 5 & 0 \leq \varphi \leq 23 \quad \text{Northern Hemisphere} \\ 5 & 0 \geq \varphi \geq -21 \quad \text{Southern Hemisphere} \\ 5 + 0.1\,(\varphi + 21) & -71 \leq \varphi < -21 \quad \text{Southern Hemisphere} \\ 0 & \varphi < -71 \quad \text{Southern Hemisphere} \end{cases} \qquad (17)$$

Ajayi and Barbaliscia, 1990 making use of radiosonde data obtained the following equations for h_{FR}.

(i) Variation with rain threshold

(a) Italian locations: $h_{FR} = 2.125 + 0.009R$

(b) Nigerian locations: $h_{FR} = 4.67 + 0.006R$

where R in rainfall rate in mm/2h.

(ii) Variation with ground temperature for summer months.

(a) Northern hemisphere: $h_{FR} = -0.171 + 0.174\ T$ (°C) (18)

T > 1, hence h_{FR} is non-negative

(b) Southern hemisphere: $h_{FR} = 0.68 - 0.155\ T$ (°C) (19)

3.3 Calculation of Long-term Rain Attenuation Statistics from Point Rainfall Rate.

The following parameters are required.

$R_{0.01}$ = point rainfall rate for the location for 0.01% of an average year (mm/h)

h_s = height above mean seal level of the earth station (km)

θ = elevation angle (degrees)

φ = latitude of the earth station (degrees)

f = frequency (GHz).

The current CCIR prediction method consists of the following steps 1 to 7 to predict the attenuation for 0.01% of the time and step 8 for other time percentages between 0.001 and 1% of an average year.

Step 1: The effective height, h_R is calculated from the latitude of the station φ using equations (13) and (14).

Step 2: For $\theta > 5$, which applies in tropical regions.

$$L_s = \frac{h_R - h_s}{Sin\theta} \quad km \tag{20}$$

For $\theta < 5$

$$L_s = \frac{2(h_R - h_s)}{(Sin^2\theta + 2\frac{h_R - h_s}{R_e})^{\frac{1}{2}} + Sin\theta} \quad km \tag{21}$$

R_e is the effective radius of the earth (8500 km).

Step 3: The horizontal projection, L_G of the slant path in figure 1 is given by

$$L_G = L_s \cos\theta \quad km \tag{22}$$

Step 4: $R_{0.01}$, the rain intensity exceeded for 0.01% of the time, with an integration time of 1 minute. If this information is not available from local data sources, it is obtained from the CCIR rain climatic map (Fig. 6).

Step 5: The reduction factor $r_{0.01}$ for 0.01% of the time is obtained from

$$r_{0.01} = \frac{1}{1 + \frac{L_G}{L_o}} \tag{23}$$

where $L_o = 35 \exp(-0.015R_{0.01})$ (24)

Step 6: Obtain the specific attenuation from

$$\gamma_R = aR_{0.01}^{\ b} \text{ dB/km} \tag{25}$$

Step 7: The attenuation exceeded for 0.01% of an average year is obtained from

$$A_{0.01} = \gamma_R L_S r_{0.01} \quad \text{dB} \tag{26}$$

Step 8: The attenuation to be exceeded for other percentages of an average year, in the range of 0.001% to 1.0% may be estimated from

$$\frac{A_p}{A_{0.01}} = 0.12 p^{-(0.546 + 0.043 \log p)} \tag{27}$$

The current CCIR prediction model in Steps 1 to 8 had been found not to be suitable for tropical stations due to the nature of the rainfall in the region. As a result of the availability of more slant path rain attenuation data globally available especially in the tropical regions, the ITU-R is considering a modification of the prediction model as follows. (Report 564): Reference is made to figure 7 (CCIR Doc. WP5C/26E).

Step 1: The height of the freezing level during rain, h_{FR} is calculated using:-

$$h_{FR} = 5.0 \text{ km} \qquad 0 \le \varphi < 23 \tag{28}$$

$$h_{FR} = 5.0 - 0.075\,(\varphi - 23) \text{ km} \qquad \varphi \ge 23 \tag{29}$$

Step 2, 3 and 4 remain unchanged

Step 5: The ~~vertical~~ horizontal reduction factor, $rh_{0.01}$ for 0.01% of the time can be calculated from:

$$rh_{0.01} = \frac{1}{1 + L_G^{0.002}\,(R_{0.01})^{1.01}} \tag{30}$$

Step 6: The vertical reduction factor, $rv_{0.01}$, for 0.01% of the time can be calculated from:

$$rv_{0.01} = \frac{1}{1 + \dfrac{h_{FR}}{(5 + 0.4\varphi^{1.5})}} \tag{31}$$

Step 7: The effective path-length through the rain, Le, can be calculated from:

$$Le = \frac{(L_G rh_{0.01})}{\cos\theta} \qquad \xi > \theta \tag{32}$$

$$Le = \frac{(h_{FR} rv_{0.01})}{\sin\theta} \quad \xi \leq \theta \tag{33}$$

In steps 8, 9 and 10, γ_R, $A_{0.01}$ and A_p are calculated as in equations 25, 26 and 27 respectively, with Le substituted for L_s in equation (26).

$$where\ \xi = \tan^{-1}\left(\frac{h_{FR}\, rv_{0.01}}{L_G\, rh_{0.01}}\right) \tag{34}$$

The modification to Report 564 is expected to take care of the vertical inhomogeneity of rain as well as the "roll over" problem. (Fig. 8), Assis (1990).

4. MEASUREMENT OF EARTH-SPACE RAIN ATTENUATION

4.1 Direct Measurement

Beacon signals from satellites provide the most direct method of measuring attenuation due to rain on Earth-space paths. However, such transmissions are not available for all locations, frequencies and elevation angles of interest. Indirect methods such as radar and radiometric have been widely used for such measurements.

4.1.1 Olympus Satellite Propagation Experiment

Beacon signals from experimental satellites are most suitable for measurement of slant path rain attenuation. The parameters are usually well known and tailored towards the experiment. Most of the available satellite signals cover mainly the temperate and high latitude regions. Unfortunately these beacon signals are not readily available in the tropical regions especially Africa.

The European Space Agency (ESA) Olumpus satellite experiment OPEX could have afforded a unique opportunity for beacon satellite measurement in Africa because of the coverage of the 12.5GHz beacon shown in Fig. 9. Collaboration with the Italian PTT and Fondazione Ugo Bordoni (FUB) by our Research Group at the Obafemi Awolowo University, Ile-Ife, Nigeria and another research group in Brazil was to have resulted in the TROPEX (Tropical Olympus Propagation Experiment). Under this arrangement, the Italian collaborators were to supply Nigeria and Brazil with the beacon receiver and Data Acquisition System (DAS) for measurement of Earth-space rain attenuation at 12.5GHz. Unfortunately the Olympus satellite lost orbit early in its mission and it took a unique effort to put it back in orbit and eventually its reduced life expectancy and its inclined orbit aborted the OPEX experiment.

4.2 Radiometric Measurements

Two types of radiometers are used for measuring attenuation on

Earth-Satellite links:

(i) Solar radiometer - Absorption type;

(ii) Sky noise radiometer - Emission type.

4.2.1. Solar radiometer

The solar radiometer measurement (active radiometer measurement) makes use of the sun as the signal source. That is, attenuation is obtained directly from an extinction measurement using the sun as the source. This type of radiometer can measure earth-space attenuation with sufficient accuracy and over a wide dynamic range.

The validity of the solar radiometric measurement is limited by the motion of the sun and the solar diurnal effects. The elevation angle dependence of attenuation cannot be obtained from solar radiometers.

4.2.2 Passive Radiometer Measurements

With this type of radiometer, the attenuation is evaluated from a measurement of atmospheric emission. An absorbing medium in thermal equilibrium with its surroundings acts as a source of noise radiation for which the brightness temperature is determined by the absorbing properties of the medium and its kinetic temperature.

The effective noise temperature measured by the sky noise radiometer consists of absorption by the gaseous atmospheric constitutents and the absorption and scattering by precipitation. At frequencies below the water vapour absorption band, the precipitation effect is dominant. The radiometer makes use of only the radiated temperature T_r of the intervening medium to calculate the attenuation induced by the medium.

The slant path attenuation A can be obtained from the expression

$$T_r = T_m \ (1 - e^{-A/4.34}) \quad \text{degrees K} \tag{35}$$

hence

$$A = 10\log\frac{T_m}{(T_m - T_r)} \quad dB \tag{36}$$

where T_m is the physical temperature of the absorbing medium and T_r is the radiated temperature. For cosmic background temperature, T_c,

we have

$$A = 10\log\frac{(T_m - T_c)}{(T_m - T_r)} \quad dB \tag{37}$$

It has been shown that the medium temperature, T_m can be evaluated from the equation

$$T_m = (1.12T_g - 50)\ K \tag{38}$$

where T_g = ground temperature measured at the site. Although there has not been a test of the validity of equation (38) for the tropical region, it can be used tentatively for the evaluation of T_m.

A constant value of 260K for T_m has been found to give good results from ESA data at 11GHz. However a value of T_m of 285K was used for the radiometer experiment at the three sites in Africa.

4.3 RECENT SLANT PATH ATTENUATION MEASUREMENTS

Fig. 10 shows the CCIR Radiowave Propagation Campaign in Africa, which culminated in the radiometric measurement of slant path rain attenuation for two years at three locations in Africa, described in Table 3 (Ajayi, 1994).

Figures 11, 12, 13, (McCarthy et al, 1994a, b, c) show the cumulative distributions for both the rainfall rate and slant path attenuation of Douala, Nairobi and Ile-Ife, the three measurement sites in Africa. Figs. 14(a) & (b) show (Migliora et al, 1990) the slant path attenuation cumulative distributions in Rio de Janeiro and Belem respectively in Brazil. Figs. 15 & 16 (Lekkla et al, 1994) show the rainfall rate and radiometer measurement results in Bangkok, Si Racha and Singapore in South East Asia. The results at the three sites in Africa showed that the ITU-R prediction underestimates the slant path attenuation at the tropical stations. Similar observations exist for results from other tropical locations, for example Bangkok, Si Racha and Singapore in Fig. 16.

4.4 LONG TERM FREQUENCY SCALING OF RAIN ATTENUATION

For the same path in the frequency range 7 to 50GHz (ITU-R PN. 618-2)

$$A_2 = A_1(\varphi_2/\varphi_1)^{1-H(\varphi_1, \varphi_2, A_1)} \tag{39}$$

where

$$\varphi(f) = f^2/(1 + 10^{-4} f^2) \tag{40}$$

$$H(\varphi_1, \varphi_2, A_1) = 1.12 \times 10^{-3} (\varphi_2/\varphi_1)^{0.5} (\varphi_1 A_1)^{0.55} \tag{41}$$

A_1 and A_2 are equiprobable values of the excess rain attenuation of frequencies f_1 and f_2 (GHz) respectively.

Frequency scaling from reliable attenuation data is preferred to prediction methods starting from rain data. Two main applications of frequency scaling of attenuation are:

(i) to allow the statistics of attenuation measured at one frequency to be scaled to a different frequency.

(ii) to allow the power transmitted to a satellite to be adjusted to compensate for increased path loss by scaling from real time attenuation data obtained at a different frequency (up-path power control). This is used for fade counter measures for satellite links.

The constant attenuation ratio is given by

$$\frac{A_2}{A_1} = \frac{g(f_2)}{g(f_1)} \qquad (42)$$

$$where \quad g(f) = \frac{f^{1.72}}{1 + 3 \times 10^{-7} f^{3.44}} \qquad (43)$$

4.4.1 Instantaneous frequency scaling

This is required for adaptive fade counter-measure for satellite links. The up-link attenuation calculated from down-link attenuation measurement can be used to control uplink transmitter power or adaptive coding. Adaptive control requires real time frequency scaling.

Hysteresis effects have been observed in instantaneous frequency scaling of attenuation on 20 and 30 GHz satellite links especially during severe thunderstorm rain. (Sweeney et al, 1992). This effect has been attributed to inadequate rain dropsize distribution utilised. At high frequencies the contribution of small raindrops is significant and their distribution is not well known Error in frequency scaling can lead to loss of service or waste of the countermeasure resource.

4.4.2 Site Diversity

Intense rain cells causing large attenuation on Earth-satellite link often have horizontal dimensions of at least several kilometres. Diversity systems able to re-route traffic to alternate earth stations, or with access to a satellite with extra on-board resources available for temporary allocation, can improve the

system reliability considerably.

For frequencies between 10 and 30GHz and for time percentages less than 0.1% we have the following:

(i) Diversity improvement factor, I or Diversity Advantage.

$$I(A) = P_m(A)/P_{div}(A)$$

where P_m and P_{div} are single-path and diversity time percentages respectively for a specified rain attenuation A.

I is shown in Fig. 17.

$$I = \frac{P_1}{P_2} = \frac{1}{(1 + \beta^2)} \left[1 + \frac{100\beta^2}{P_1}\right] \approx 1 + \frac{100\ \beta^2}{P_1} \qquad (44)$$

where P_1 and P_2 are the respective single-site and diversity time percentages.

β = parameter depending on link characteristics.

$\beta^2 << 1$.

For measurements in the 10 - 20 GHz

β^2 is only slightly dependent on elevation angle and the frequency.

$$\beta^2 = 10^{-4}\ d^{1.33} \qquad (45)$$

where d = distance between the stations.

Fig. 18 shows P_2 versus P_1.

(ii) Diversity Gain, G

$$G(P) = A_m(P) - A_{div}(P) \qquad (46)$$

where G(P) is the dB difference between the single site and diversity attenuation values for the same time percentage P. G is shown in Fig. 17.

Parameters required for calculating G are (ITU-R PN. 618-2)

d: separation (km) between the two sites
A: path rain attenuation (dB) for a single site
f: frequency (GHz)
θ: path elevation angle (degrees)
ψ: angle (degrees) made by the azimuth of the propagation

path with respect to the baseline between sites, chosen such that $\psi \leq 90$.

Step 1: Calculate the gain contributed by the spatial separation from:

$$G_d = a(1 - e^{-bd}) \quad (47)$$

where:

$$a = 0.78\ A-1.94\ (1 - e^{-0.11A})$$

$$b = 0.59\ (1 - e^{-0.1A})$$

Step 2: Calculate the frequency-dependent gain from:

$$G_f = e^{-0.025f} \quad (48)$$

Step 3: Calculate the gain term dependent on elevation angle from:

$$G_\theta = 1 + 0.006\ \theta \quad (49)$$

Step 4: Calculate the baseline-dependent term from the expression:

$$G_\psi = 1 + 0.002\psi \quad (50)$$

Step 5: Compute the net diversity gain as the product:

$$G = G_d \cdot G_f \cdot G_\theta \cdot G_\psi \text{ dB} \quad (51)$$

When the above method was tested against the Study Group 5 site diversity data bank, the arithmetic mean and standard deviation were found to be 0.14 dB and 0.96 dB, respectively, with an r.m.s. error of 0.97 dB.

4.4.3 Factors affecting diversity performance are: (Allnut, 1989)

(i) Terminal Separation, D.

Diversity gain G increases rapidly as D increases from zero until the separation exceeds 10 -15km, when further increases in D gives small benefit. The value of D for which 95% of available G is achieved ranges from about 15 to 30 km.

(ii) Path Geometry (elevation angle θ and azimuth ϕ) and orientation of baseline joining the sites.

Maximum horizontal path separation is achieved by

orienting the diversity baseline perpendicular to the path azimuth. Baseline orientation normal to the radio path, and also to the direction of travel of convective weather fronts would give best diversity advantage.

For low elevation angles, the diversity gain appears to decrease with decreasing elevation angle.

(iii) Frequency, f

Diversity performance is expected to decrease with increasing frequency because the impact of widespread, low rainfall rate structures on the single-path statistics will increase. Weak frequency dependence has been reported, although frequency effects are expected to be important for low elevation angles especially above 30GHz.

(iv) Local meteorological and topographic effects.

Diversity performance can be influenced by local terrain, since topographic features often modify rainfall characteristics.

4.5 Fade Duration Statistics

This is due to variations of the atmospheric medium and it is of great importance to design of future telecommunication systems above 10GHz, such as

(i) ISDN connections via satellite (requires data on contribution of attenuation events shorter than 10 seconds to the total fading time).

(ii) Systems adopting fading counter measures to cope with severe rain induced effects.

(iii) multiple access systems.

(iv) commercial low-power margin systems.

The fade duration statistics can be further considered as follows (Paraboni and Riva, 1993).

(i) the availability of ISDN connections via satellite is specified in terms of cumulative exceedance time composed of intervals longer than 10s for synchronism; the design of these connections requires the knowledge of fade duration statistics down to the shortest values of the order of 1s in most cases.

(ii) the design of advanced systems using a shared resource on

board to assist earth terminals undergoing severe fading conditions requires to know the expected time the resource is likely to be engaged.

(iii) site diversity systems will have to face the problem of too frequent commutations between the terminals: any technique to avoid this inconvenience must account for the fade duration statistics.

(iv) The knowledge of the dynamic variation of the down link signal amplitude (including the fade duration statistics) will be required for the optimal design of up-link power control systems.

For fade durations longer than about 1 minute, durations of fades exceeding certain levels have lognormal distributions. Shorter durations (which may include tropospheric scintillations) follow a power law distribution.

Results indicate that the duration of fades exceeding a given level increases with decreasing elevation angle.

Paraboni and Riva, 1993 described the fade duration statistics by two different processes.

(i) Process A: characterized by a function $N_s(D)$ giving the total time (number of seconds) a threshold A is exceeded, composed by intervals (fades) longer than D; $N_s(D)$ can be regarded as the non-normalized cumulative distribution function of a statistical process whose samples are given a weight equal to D.

(ii) Process B: characterized by a function, $N_d(D)$ giving the number of individual fades longer than D; $N_d(D)$ is the non-normalized cumulative distribution function of the statistical process of the fades, with unit weight.

Figs. 19, 20, 21 (CCIR Rep. 564-4) show some experimental results of fade duration statistics.

4.6 Rates of Change of Attenuation

Up-link power control and/or diversity operation may become mandatory with increasing frequency. Criteria for power control or re-routing of traffic will have to be derived from down-link signals. Fade slope can be one of these criteria, providing estimates of the time available for a given increase of attenuation.

The distributions of positive and negative slopes are lognormal and very similar to each other. As the fade rate increases, the apparent difference between the fade slope and the reocvery slope (negative going) tends to increase with the fade slope always being

greater. The explanation could be that the higher fading rates (both positive and negative) are associated with thunderstorms and that the leading edges of thunderstorms contain higher rainfall rates than the trailing edges. The average fade slope does not appear to depend significantly on the fade level, with a maximum fade rate of about 1dB/s in the frequency range 10-14 GHz for integration time of the order of 10s. Higher fading rates are observed with integration times below 10s. (Allnutt, 1989).

4.7 Seasonal variations - Worst month

The worst month statistics for a given link are obtained by compiling a composite curve using, at each threshold level, the highest exceedance probability obtained in any calendar month. Figs. 22 (a) and (b) show an example of such a process from the radiometric slant path attenuation measurement at Ile-Ife.

Some communications services, for example broadcasting (TV) require the link to operate with a specified outage in the worst month. An outage of 1% is usually tolerated in the worst month.

$$Q = A\ Y^{-\beta}$$

where Q is the average annual-worst-month probability divided by the average annual probability, Y.

A and β are constants

A is between 1.20 and 3.30

β is between 0.167 and 0.074

For global planning purposes

$$A = 2.85,\ \beta = 0.13$$

ie

$$Q = 2.85Y^{-0.13} \qquad (52)$$

This leads by inversion to the relationship

$$P = 0.30\ P_w^{1.15}\ \% \qquad (53)$$

where P_w is the average annual worst month probability and P is the average annual probability P.

$$Q = P_w/P \text{ and } Y = P \qquad (54)$$

Equations 52 and 53 seem adequate for both rainfall rate and path attenuation statistics.

For slant path rain effect

USA - $A = 2.7$, $\beta = 0.15$
Japan - $A = 2.7$, $\beta = 0.15$
Europe (West and Mediterran):- $A = 3.1$, $\beta = 0.16$

Fig. 23(a) (Allnut, 1989) shows the variation of Q with Y for several locations, and Fig. 23(b) (CCIR-DOC. 5/12) the variation of Q with P for $A = 2.85$, $\beta = 0.13$.

In system planning the following procedure can be used to estimate the attenuation exceeded for a specified percentage of the worst month.

(i) Obtain the annual percentage, P, corresponding to the desired worst-month time percentage P_w by using the equation 53.

(ii) For the path of interest obtain the attenuation, A(dB) exceeded for the annual time percentage P, or from measured or frequency scaled attenuation statistics. A is the estimated attenuation for P_w percent of the worst month.

5. CROSS-POLARIZATION DUE TO THE ATMOSPHERE

In order to increase channel capacity without increasing bandwidth, orthogonal polarizations (linear or circular) may be independently used for transmission at the same frequency over the same path. "Frequency re-use" may be impaired by the possibility of some energy transmitted in one polarization state can be transferred to the orthogonal polarization state, thus causing interference between the two channels.

Cross-polarization may be caused

(i) by rain due to non-spherical raindrop shape

(ii) by other hydrometeors

(iii) during periods of multipath propagation.

Cross-polarization may arise due to the characteristics of the antenna systems at each terminal. Frequency reuse by means of orthogonal polarizations is often used to increase the capacity of space telecommunication systems.

5.1 Cross-polarisation Discrimination (XPD) and Cross-polarisation Isolation (XPI).

With reference to fig. 24

$$XPD = 20 \log_{10} \frac{ac}{ax} \; dB \qquad (55)$$

$$XPI = 20 \log_{10} \frac{ac}{bx} \; dB \qquad (56)$$

For a rain medium, XPD and XPI are equivalent.

If the differential attenuation and differential phase induced by the propagation medium can be measured, XPD can be obtained as:

$$XPD = 20 \log_{10} \left| \frac{\exp(-(\alpha + j\beta)) + 1}{\exp(-(\alpha + j\beta)) - 1} \right| \; dB \qquad (57)$$

where α = differential attenuation nepers
β = differential phase, rad.

Figs. (25) and (26) (Ajayi, 1990) show respectively variation of differential phase shift and differential attenuation with frequency using the Ajayi-Olsen and Laws and Parsons raindrop size distributions for a frequency of 1 to 300 GHz.

5.2 Cross-polarization due to rain

As the size of the raindrops increases, their shape departs from spherical and is similar to that of oblate spheroids with an increasingly pronounced flat base in which a concave depression develops for every large drops sizes. A commonly accepted model for a falling raindrop is an oblate spheroid with its major axis canted to the horizontal and with deformation dependent upon the radius of a sphere of equal volume. The raindrop canting angles vary randomly in space and time.

5.3 Calculation of long-term statistics of hydrometeor-induced cross-polarization (ITU-R PN.618-2, 1994).

The following parameters are required;

A_p: rain attenuation(dB) exceeded for the required percentage of time, p, for the path in question, commonly called co-polar attenuation, CPA.

τ: tilt angle of the linearly polarized electric field vector with respect to the horizontal (for circular polarization use $\tau = 45$)

f: frequency (GHz)

θ: path elevation angle.

The method described below to claculate cross-polar discrimination (XPD) statistics from rain attenuation statistics for the same path is valid for 8 GHz $\leq f \leq$ 35 GHz and $\theta \leq 60$.

Step 1: Calculate the frequency-dependent term:

$$C_f = 30 \log f \quad \text{for } 8 \leq f \leq 35 \text{ GHz} \tag{58}$$

Step 2: Calculate the rain attenuation dependent term:

$$C_A = V(f) \log (A_p) \tag{59}$$

where:

$$V(f) = 12.8\ f^{0.19} \quad \text{for } 8 \leq f \leq 20 \text{ GHz}$$

$$V(f) = 226 \quad \text{for } 20 < f \leq 35 \text{ GHz}$$

Step 3: Calculate the polarization improvement factor:

$$C_\tau = -10 \log [1 - 0.484\ (1 + \cos (4\tau))] \tag{60}$$

The improvement factor $C_\tau = 0$ for $\tau = 45$ and reaches a maximum value of 15 dB for $\tau = 0$ or 90 .

Step 4: Calculate the elevation angle-dependent term:

$$C_\theta = -40 \log (\cos \theta) \text{ for } \theta \leq 60 \tag{61}$$

Step 5: Calculate the canting angle dependent term:

$$C_\sigma = 0.0052\ \sigma^2 \tag{62}$$

σ is the effective standard deviation of the raindrop canting angle distribution, expressed in degrees; σ takes the value 0 , 5 , 10 and 15 for 1%, 0.1%, 0.01% and 0.001% of the time, respectively.

Step 6: Calculate rain XPD not exceeded for p% of the time:

$$XPD_{rain} = C_f - C_A + C_\tau + C_\theta + C_\sigma \text{ dB} \tag{63}$$

Step 7: Calculate the ice crystal dependent term:

$$C_{ice} = XPD_{rain} \times (0.3 + 0.1 \log p) / 2 \quad \text{dB} \tag{64}$$

Step 8: Calculate the XPD not exceeded for p% of the time, including the effects of ice:

$$XPD_p = XPD_{rain} - C_{ice} \text{ dB} \quad (65)$$

In this prediction method in the frequency band 4 to 6 GHz where path attenuation is low, A_p statistics are not very useful for predicting XPD statistics. For frequencies below 8 GHz, the frequency-scaling formula can be used to scale cross-polarization statistics calculated for 8 GHz down to the 6/4 GHz band.

5.4 Typical XPD Chracteristics

Fig. 27 (Ref. 7) shows measured XPD versus co-polar attenuation.

Fig. 28 (Ref. 7) shows variability from year to year of annual XPD statistics at 11.6 GHz.

Fig. 29 (Ref. 2) shows the effect of raindrop shape on XPD.

Fig. 30 (Ref. 7) shows XPD event duration statistics for the severe depolarising events with XPD values of 5 or 10 dB, the trend is log-normal. For the events with smaller depolarisation (15 to 20 dB), the log-normal trend is only for the long duration times.

5.5 Long-term frequency and polarization scaling of statistics of hydrometeor-induced cross-polarization (ITU-R PN 618-2, 1994).

Long-term XPD statistics obtained at one frequency and polarization tilt angle can be scaled to another frequency and polarization tilt angle using the semi-empirical formula:

$$XPD_2 = XPD_1 - 20 \log \left[\frac{f_2 \sqrt{1 - 0.484 \ (1 + \cos 4\tau_2)}}{f_1 \sqrt{1 - 0.484 \ (1 + \cos 4\tau_1)}} \right] \quad (66)$$

$$for \ 4 \leq f_1, f_2 \leq 30 \ GHz$$

where XPD_1 and XPD_2 are the XPD values not exceeded for the same percentage of time at frequencies f_1 and f_2 and polarization tilt angles, τ_1 and τ_2, respectively.

5.6 Data relevant to cross-polarization cancellation

Experiments have shown that a strong correlation exists between rain depolarization at 6 and 4 GHz on Earth-space paths, both on the long term and on an event basis, and up-link depolarization compensation utilizing concurrent down-link depolarization measurements appears feasible. Only differential phase effects were apparent, even for severe rain events, and single-parameter compensation (i.e. for differential phase) appears sufficient at 6

and 4 GHz.

Measurements at 6 and 4 GHz have also shown that 99% of the XPD variations are slower than 4dB/s, or equivalently, less than 1.5 in the mean path differential phase shift. Therefore, the time constant of a depolarization compensation system at these frequencies need only be about 1 s.

6. SYSTEM IMPACT

6.1 Noise Temperature

As attenuation increases, the emission noise increases. For earth stations with low-noise front-ends, this increase of noise temperature may have a greater impact on the resulting S/N than the attenuation itself.

The atmospheric contribution to antenna noise in a ground station is given by

$$T_s = T_m \ (1 - 10^{-A/10}) + T_c \ x \ 10^{-A/10} \ deg. \ K \qquad (67)$$

where

T_s = sky noise temperature (K) as seen by antenna
A = path attenuation (dB) and
T_m = effective temperature (K) of the medium
T_c = background sky noise due to cosmic radiation.

T_m is dependent on

(a) the contribution of scattering to attenuation
(b) the physical extent of clouds and rain cells
(c) the vertical variation of the physical temperature of the scatterers.
(d) the antenna beamwidth to a lesser extent.

T_m varies from 260 to 285k for rain and clouds along the path between 10 and 30 GHz.

In practice, for clear sky T_s is relatively small unless the antenna illuminates the sun, moon or certain radio nebulae such as Cassiopeia A, Taurus A, and Cygnus A and X.

For engineering application, since T_c is very small (about 2.7K), T_s can be estimated from

$$T_s = T_m \ (1 - 10^{-A/10}) \qquad (68)$$

Fig. 31 shows the extra-terrestrial noise sources .

6.2 SYSTEM PERFORMANCE

The performance of most digital communication systems is specified in terms of Bit Error Rate (BER) for a given Carrier-to-noise (C/N).

C/N is usually converted to E_b/N_o

where E_b = Energy per bit

N_o = Noise power density

Fig. 32 shows a typical BER versus E_b/N_o

When BER $\leq 10^{-8}$ - normal performance
BER $\geq 10^{-6}$ - outage
$10^{-8} \leq$ BER $\leq 10^{-6}$ - degraded performance.

For a given system bandwidth, the E_b/N_o can be converted to C/N for link budget calculation. Fig. 33 (ref. 7) shows a synopsis of an Earth station link margin calculation procedure.

Fig. 34 (ref. 7) also shows the impact of propagation parameters on the determination of earth station design.

6.3 UPLINK FADE MARGIN

(i) For f $\geq$ 10 GHz.

The up-link fade margin is determined principally by the predicted rain attenuation at the specified % of time, frequency, polarisation, site and path elevation angle.

(ii) For f < 10 GHz, ionospheric scintillation could be the major amplitude effect on the margin.

For availability, the predicted fade margin $\leq$ calculated net link budget margin.

When anticipated rain fade > calculated net budget margin, system experiences more outage for the specified availability.

6.4 DOWN-LINK DEGRADATION

The satellite receiver will observe an essentially constant, high temperature emitted from the Earth except in the case of a global beam antenna. Hence additional noise contribution due to thermal emission from rain in the up link is a relatively small contribution to the receiving system noise temperature.

Conversely, an earth station receiver has a lower noise temperature

than an equivalent satellite receiver. The antenna is also usually directed towards a "cool" sky. In rain, there will be signal attenuation, as well as a significant increase in noise temperature. The two constitute the down-link degradation.

T_{sys}, the system noise temperature has to be calculated for both clear sky and in the rain fade.

In Fig. 35, T_{sys} referenced to plane PP' is given by

$$T_{sys} = T_R + (1 - \sigma_f)\ T_f + \sigma_f\ T_A \quad deg.\ K \tag{69}$$

where T_f = feed temperature
T_A = noise temperature incident on antenna
σ_f = feed transmissivity
T_R = receiver noise temperature.

In clear sky, attenuation = Ag (gaseous attenuation)
In rain condition, attenuation = A (rain + gaseous attenuation)

$$T_{ACS} = T_m\ (1 - 10^{-Ag/10}) + T_c \times 10^{-Ag/10} \text{ deg K} \tag{70}$$

where $T_{ACS} = T_A$ for clear sky.

$$T_{Arain} = T_m\ (1 - 10^{-A/10}) + T_c \times 10^{-A/10} \text{ deg. K} \tag{71}$$

(Note $10^{-x/10} = e^{-x/4.34}$)

$$DND = A + 10 \log (T_{sys/rain}/T_{sys/clear\ sky}) \text{ dB} \tag{72}$$

where DND is downlink degradation.
For Ag = 0.5 dB, T_c = 2.7K, T_m = 280K, A = 5.0dB, σ_f = 0.95, T_f = 280k and T_R = 200K

T_{ACS} = 32.9K

T_{Arain} = 192.3K

Therefore

$T_{sys/clear\ sky}$ = 245.3K

$T_{sys/rain}$ = 396.7K

DND = 5 + 2.1 = 7.1 dB.

In effect, a 5dB rain fade has led to a 7.1dB down-link degradation. Hence DND must be taken into consideration in link budget and not just rain fade.

7. REFERENCES

(1). Ajayi, G.O.: Some aspects of tropical rainfall and their effect on microwave propagation, Int. Journ. of Satellite Communications, 8, 1990, 163-172.

(2) Ajayi, G.O.: Slant Path Rain Attenuation Measurements in Africa, ITU/ICTP Seminar on Radiowave Propagation in Tropical Regions, Trieste, Nov / Dec. 1993;

(3) Ajayi, G.O.: Rain Intensity and Raindrop Size Measurements in Nigeria, ITU/ICTP Seminar on Radiowave Propagation in Tropical Regions, Trieste, Nov/Dec., 1994.

(4) Ajayi, G.O. And R.L. Olsen: Modelling of tropical raindrop size distribution for microwave and millimetre wave applications, Radio Science, 20, 1985, 183 - 202.

(5) Ajayi, G.O. and A. Adimula: Variation in raindrop size distribution and specific attenuation in a tropical environment, URSI Comm. F Symposium, La Londe-les-Maures, France, Sept. 1989, 8.1.1 - 8.1.4.

(6) Ajayi, G.O. and F. Barbaliscia: Prediction of attenuation due to rain: Characteristics of the O C isotherm in temperate and tropical climates, Int. Journ. of Satellite Communications, 8, 1990, 187 - 196.

(7) Allnut, J.E. Satellite-to-ground radiowave propagation, Peter Peregrinus Ltd., IEE Electromagnetic Waves Series 29, 1989.

(8) Allnut, J.E. and B. Arbesser-Rastburg: Low elevation angle propagation modelling consideration for the INTELSAT Business Service, IEE Conf. Publ. 248, 1985, 57 - 61.

(9) Assis, M.S.: Path length reduction factor for tropical regions, URSI Open Symp. on Regional Factors in Predicting Radiowave Attenuation due to Rain, Rio de Janeiro, Brazil, Dec. 1990, 69 - 71.

(10) CCIR Study Group 5: Proposed Revisions to Report 564 - 3 (MOD 1) Interim Working Party IWP 5/2, Doc. 89/44, 1989.

(11) CCIR (ITU-R) Report 563-4: Radiometeorological Data, Propagation in non-ionized media, ITU, 1990.

(12) CCIR Document WP 5C/26-E: INTELSAT Contribution to the Path Attenuation Prediction Procedure: Proposed Modification to Recommendation 618, Oct. 1991.

(13) CCIR Doc. 5/12: Conversion of annual statistics to worst-mouth statistics - Draft new recommendation, 1991.

(14) CCIR DOC.5A/40-E: A probability law model for the prediction of point rainfall rate cumulative distribution for various locations in the world, 1993.

(15) Ippolito, L.J.: Radio propagation for space communication systems, Proc. IEEE 69, 1981.

(16) ITU-R Recommendation PN 618-2: Propagation data and prediction methods required for the design of Earth-space telecommunications systems, 1994.

(17) Joss, J., J.C. Thams and A. Waldvogel: The variation of raindrop size distribution at Locarino, Proc. Int. Conf. Cloud Phys. Toronto, Canada, 1968, 369 - 373.

(18) Laws, J.D. and D.A. Parsons: The relation of raindrop size to intensity, EOS Trans. AGU, 24, 1943, 452 - 460.

(19) Lekkla, R., S.L. Lim, J. Wachja and K.S. McCormick Rain attenuation measurements in South-East Asia. Preprints of URSI Open Symposium, CLIMPARA '94, June 1994, 5.12.1 - 5.12.4.

(20) Marshall, J.S. and W.M. Palmer,: The distribution of raindrops with size, J. Meteor., 5, 198, 165 - 166.

(21) McCarthy, D.K., J.E. Allnutt, W. Salazar, E.C. Omeata, B.R. Owolabi, T. Oladiran, E.B. Ojeba, G.O. Ajayi, T.Raji and C. Zaks: Results of 11.6 GHz radiometric experiment in Nigeria: Second Year Electronics Letters, 30,(17) 1452 - 1453, 1994(c)

(22) McCarthy, D.K., J.E. Allnutt, W.E. Salazar, F. Wanmi, M. Tchinda, T.D.G. Ndinayi and C. Zaks: Results of an 11.6 GHz radiometric experiment in Cameroon: Second year, Electronics Letters, 30, (17), 1449 - 1450,1994(a).

(23) McCarthy, D.K., J.E. Allnutt, W.E. Salazar, R.W. Sitati, M-. Okoth, M.J. Mutungi, C.D. Odhiambo, and C. Zaks: Results of an 11.6 GHz radiometric experiment in Kenya: Second year, electronics Letters, 30, (17), 1450-1452, 1994(b).

(24) Migliora, C.G.S., M.S. Pontes, L.A.R. Silva Mello: Rain rate and attenuation measurements in Brazil, Preprints of URSI Open Symposium, Rio de Janeiro, Brazil, 1990, 8 - 13.

(25) Moupfouma, F.: More about rainfall rates and their prediction for radio systems engineering, Proc. IEE, Part H, 134, 527 - 539, 1987.

(26) Paraboni, A. and C. Riva: A new method for the prediction of fade duration statistics in satellite links beyond 10 Ghz - Personal Communications, 1994.

(27) Sweeney, D.G., T. Pratt and C.W. Bostian: Hysteresis effects in instantaneous frequency scaling of attenuation on 20 and 30 Ghz satellite links. Eletron. Lett. 28 (1), 76 - 78, 1992.

(28) Ortgies, G.: Results of fade duration analysis, Proc. of 20th Meeting of Olympus Propagation Experimenters, Darmstadt, 257 - 261, 1993.

distribution with CCIR values[*]

Frequency (GHz)	a				b			
	HP		VP		HP		VP	
	Ajayi*	CCIR	Ajayi*	CCIR	Ajayi*	CCIR	Ajayi*	CCIR
1	0·3521(−4)	0·3867(−4)	0·3110(−4)	0·3516(−4)	0·9273	0·9116	0·8940	0·8802
2	0·1417(−3)	0·1539(−3)	0·1240(−3)	0·1384(−3)	0·9627	0·9632	0·9323	0·9234
4	0·6506(−3)	0·6499(−3)	0·5732(−3)	0·5910(−3)	1·072	1·121	1·043	1·075
6	0·1848(−2)	0·1745(−2)	0·1634(−2)	0·1547(−2)	1·214	1·307	1·177	1·265
8	0·4724(−2)	0·4536(−2)	0·4102(−2)	0·3946(−2)	1·273	1·327	1·253	1·310
10	0·1063(−1)	0·1010(−1)	0·9238(−2)	0·8870(−2)	1·252	1·276	1·242	1·264
12	0·2015(−1)	0·1882(−1)	0·1774(−1)	0·1681(−1)	1·204	1·217	1·195	1·200
15	0·4007(−1)	0·3668(−1)	0·3599(−1)	0·3347(−1)	1·139	1·154	1·126	1·128
20	0·8195(−1)	0·7508(−1)	0·7477(−1)	0·6906(−1)	1·083	1·099	1·057	1·065
25	0·1333	0·1244	0·1206	0·1130	1·055	1·061	1·026	1·030
30	0·1977	0·1871	0·1761	0·1674	1·024	1·020	1·001	0·9997
35	0·2764	0·2629	0·2438	0·2334	0·9860	0·9789	0·9697	0·9633
40	0·3672	0·3495	0·3228	0·3098	0·9437	0·9391	0·9335	0·9287
45	0·4648	0·4424	0·4097	0·3932	0·9022	0·9032	0·8963	0·8965
50	0·5618	0·5362	0·4984	0·4793	0·8649	0·8725	0·8617	0·8683
55	0·6507	0·6253	0·5823	0·5632	0·8338	0·8471	0·8321	0·8443
60	0·7268	0·7069	0·6569	0·6419	0·8089	0·8621	0·8078	0·8243
65	0·7912	0·7816	0·7213	0·7149	0·7885	0·8083	0·7880	0·8073
70	0·8474	0·8514	0·7779	0·7836	0·7712	0·7930	0·7713	0·7925
75	0·8970	0·9167	0·8281	0·8477	0·7563	0·7798	0·7570	0·7799
80	0·9392	0·9758	0·8714	0·9063	0·7441	0·7687	0·7453	0·7693
85	0·9718	1·025	0·9064	0·9572	0·7346	0·7598	0·7360	0·7606
90	0·9940	1·064	0·9321	0·9992	0·7279	0·7528	0·7293	0·7537
95	1·007	1·094	0·9490	1·033	0·7235	0·7476	0·7248	0·7483
100	1·011	1·116	0·9583	1·059	0·7209	0·7434	0·7221	0·7441
120	0·9883	1·177	0·9517	1·132	0·7209	0·7313	0·7215	0·7320
150	0·9677	1·310	0·9387	1·267	0·7168	0·7095	0·7187	0·7112
200	0·9544	1·448	0·9382	1·420	0·7092	0·6887	0·7104	0·6899
300	0·8948	1·364	0·8862	1·349	0·7096	0·6876	0·7110	0·6890
400	0·8617	1·318	0·8554	1·309	0·7060	0·6827	0·7080	0·6841

*Tropical raindrop-size distribution values: HP—horizontal polarization; VP—vertical polarization

TABLE 2 *Rain climatic zones*

Rainfall intensity exceeded (mm/h) (Reference :.

Percentage of time (%)	A	B	C	D	E	F	G	H	J	K	L	M	N	P	Q
1.0	<0.1	0.5	0.7	2.1	0.6	1.7	3	2	8	1.5	2	4	5	12	24
0.3	0.8	2.0	2.8	4.5	2.4	4.5	7	4	13	4.2	7	11	15	34	49
0.1	2	3	5	8	6	8	12	10	20	12	15	22	35	65	72
0.03	5	6	9	13	12	15	20	18	28	23	33	40	65	105	96
0.01	8	12	15	19	22	28	30	32	35	42	60	63	95	145	115
0.003	14	21	26	29	41	54	45	55	45	70	105	95	140	200	142
0.001	22	32	42	42	70	78	65	83	55	100	150	120	180	250	170

Country	Location	Latitude	Longitude	Altitude(m)	Elevation	Azimuth
Cameroun	Douala	4°.03'N	9°42'E	15	47.0°	263.6°
Kenya	Nairobi	1° 18'S	36° 45'E	1800	56.9°	83.8°
Nigeria	Ile-Ife	7° 33'N	4° 34'E	274	48.3°	257.25°

Location	Annual Total Precipitation (mm)	Convective Factor	CCIR Climatic Region	T_m	Antenna Factor H	Observation Time %	
						Rain	Radio-meter
Douala	3213	0.43	Q	285	0.9	99.08	84.15
Nairobi	1042.4	0.23	K	285	0.9	99.76	99.62
Ile-Ife	1703.6	0.6	N & P	285K	0.9	99.90	99.79

Table 3 - Comparison of some factors at the 3 radiometer sites in Africa.

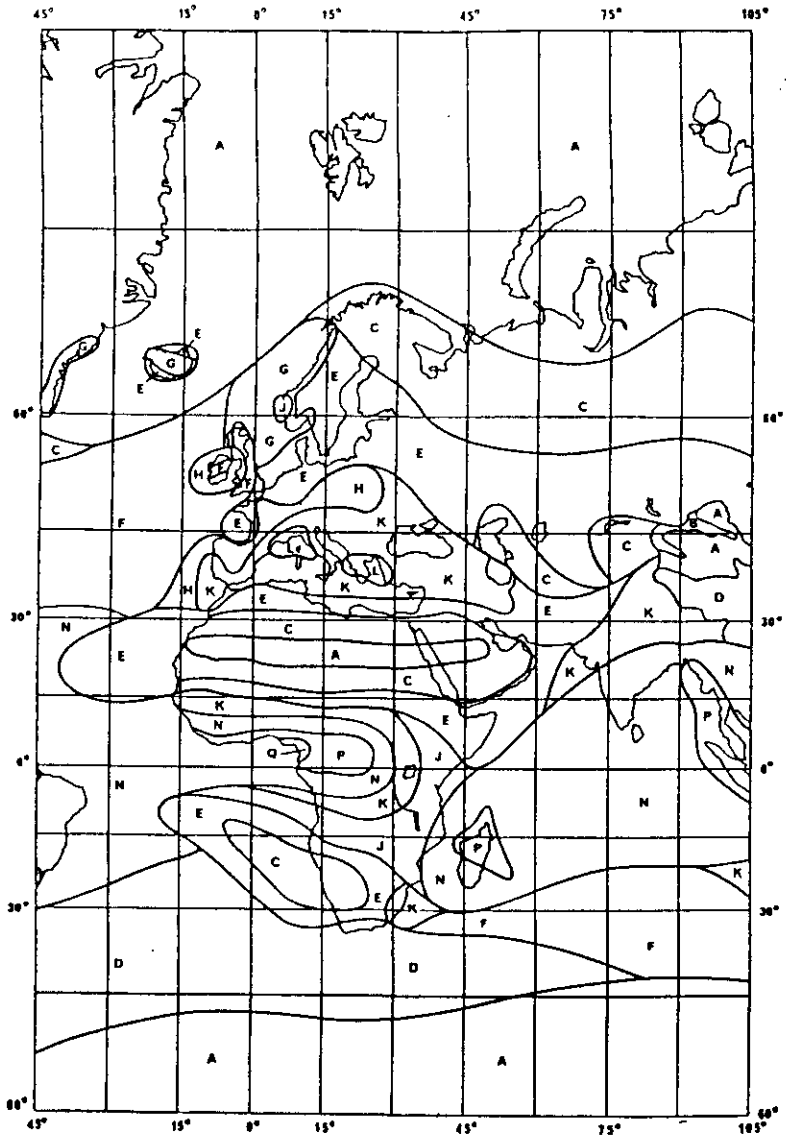

Fig. 1

(See Table 2)

Fig. 2(a) Parameter 'u' behaviour according to the climate

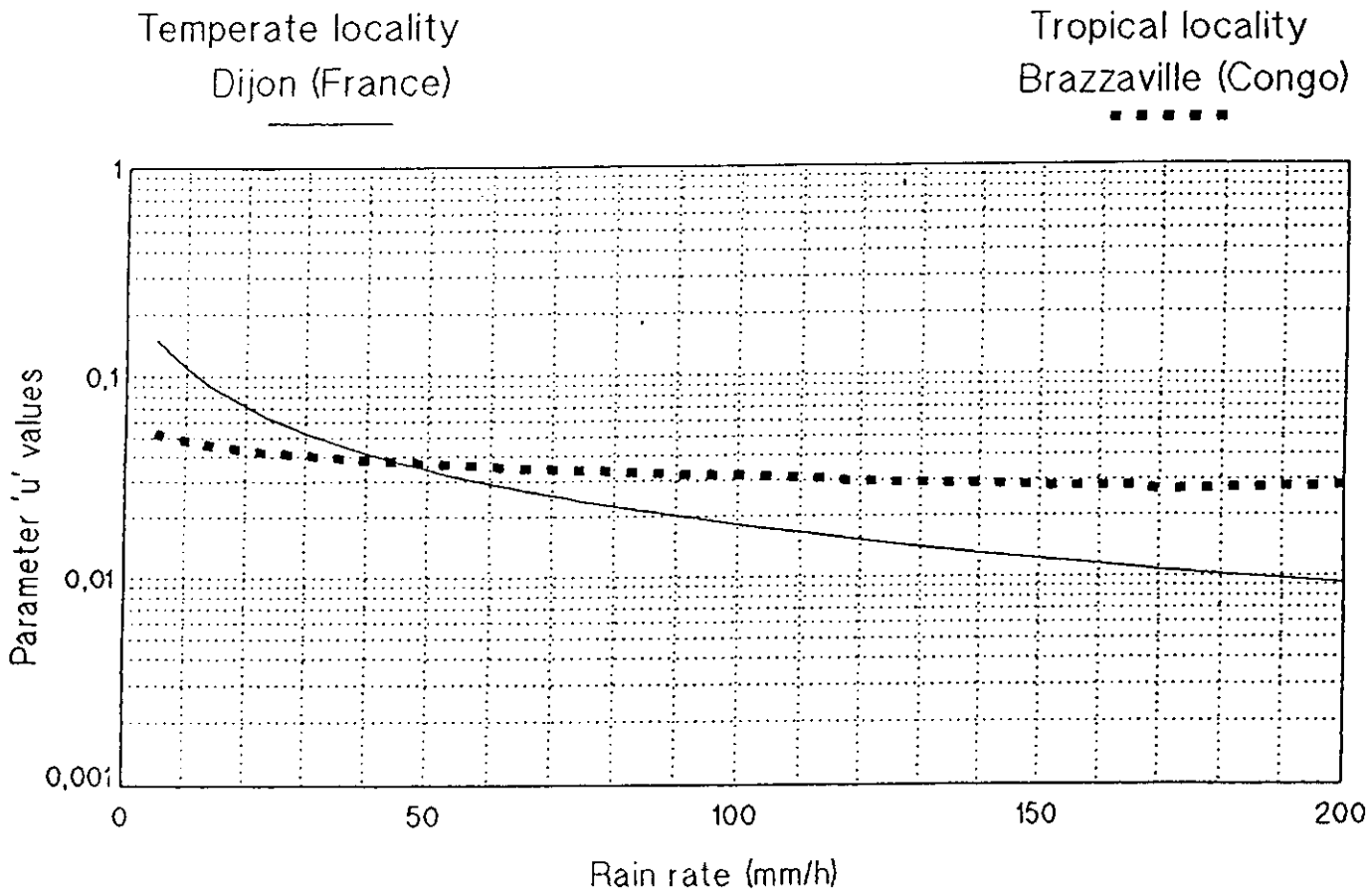

Fig. 2(b) Rainfall rate cumulative distributions in african tropical localities
Comparison between predictions and measured data

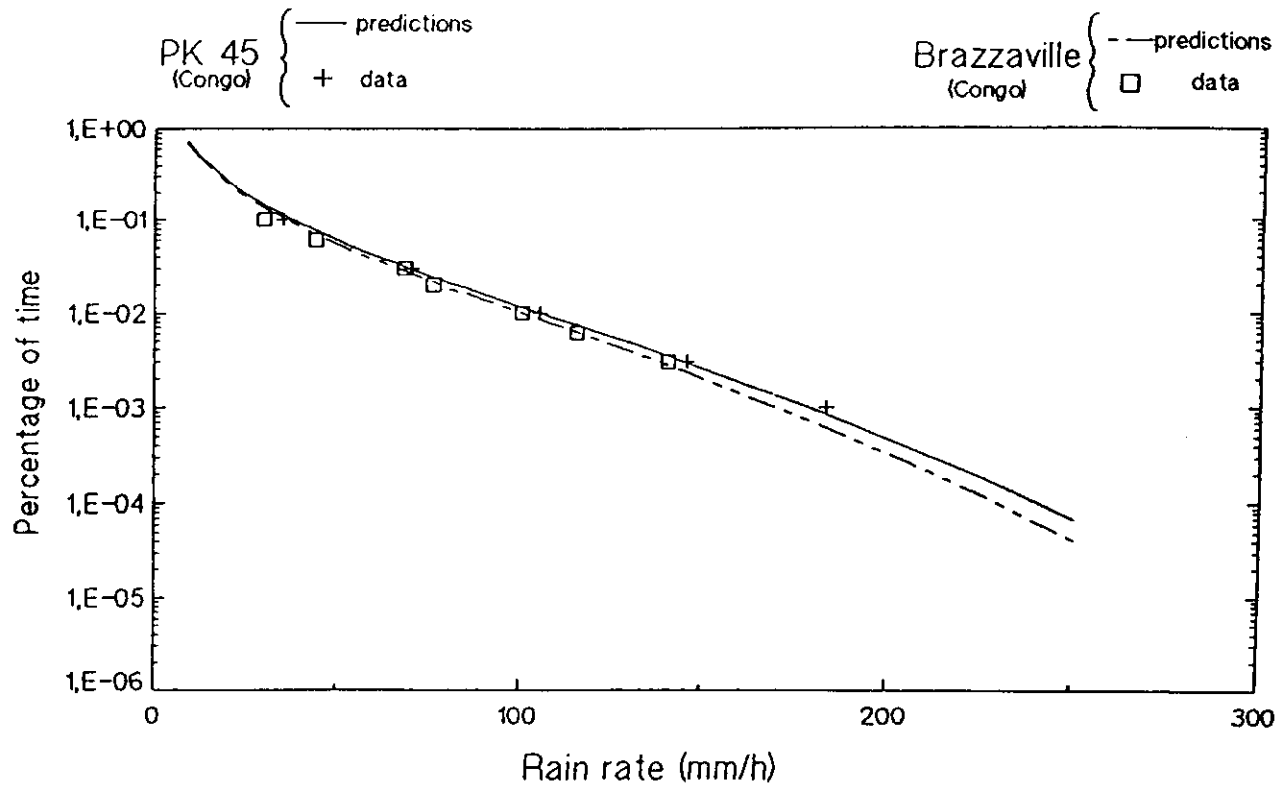

Fig. 2(c) Rainfall rate cumulative distribution in an african tropical locality
Comparison between predictions and measured data

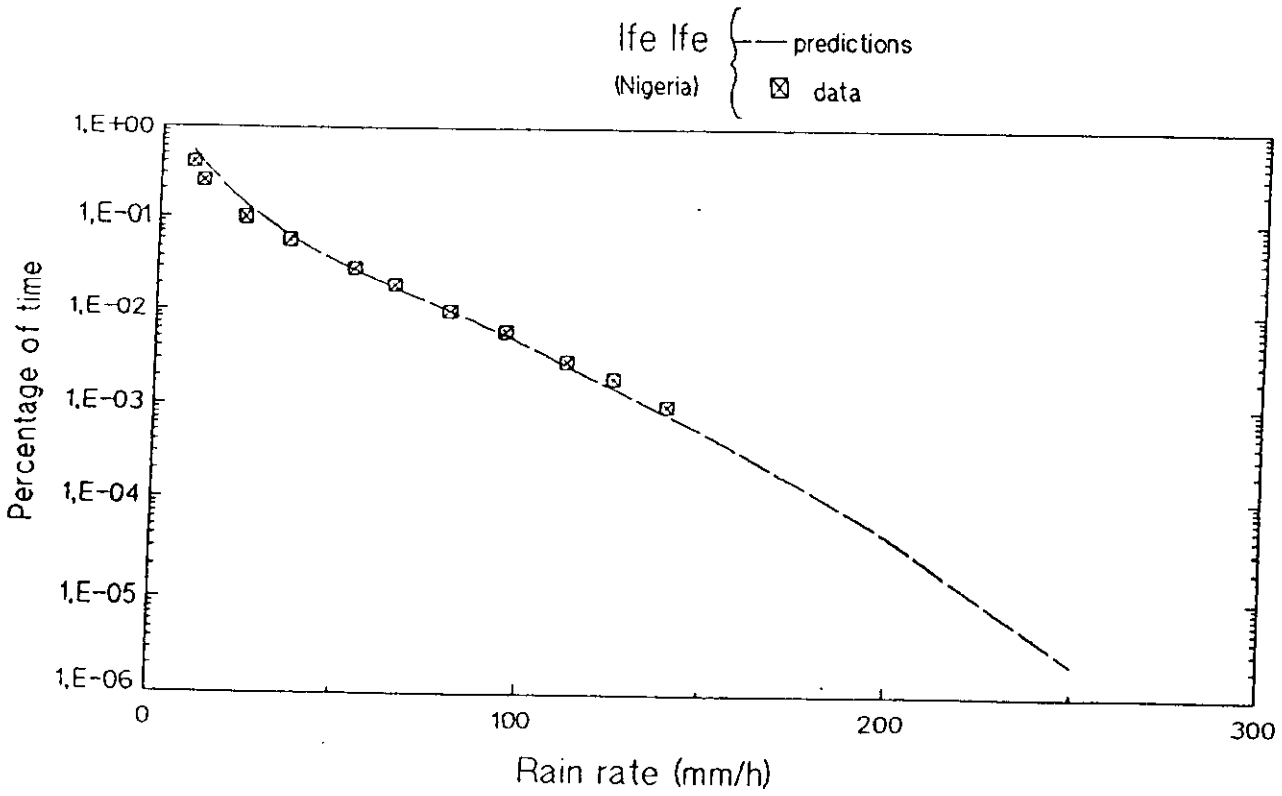

Fig. 2d Rainfall rate cumulative distributions in european localities
Comparison between predictions and measured data

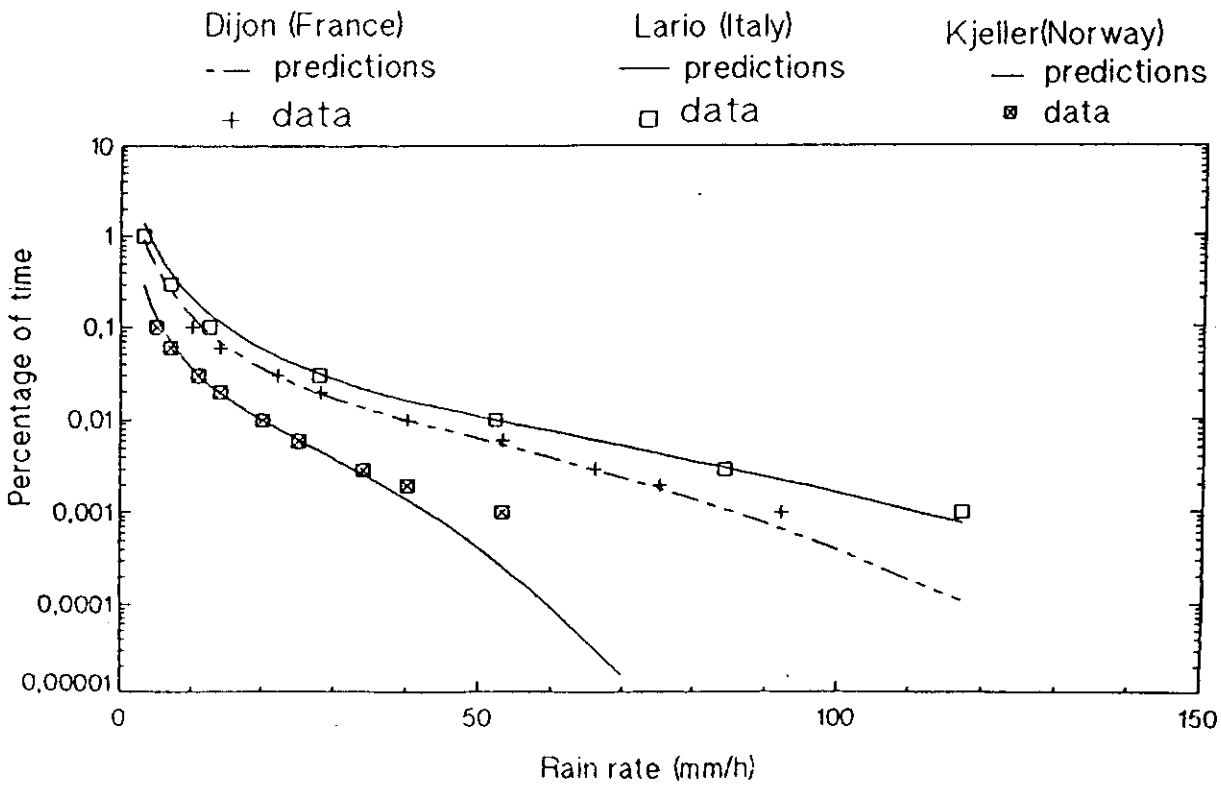

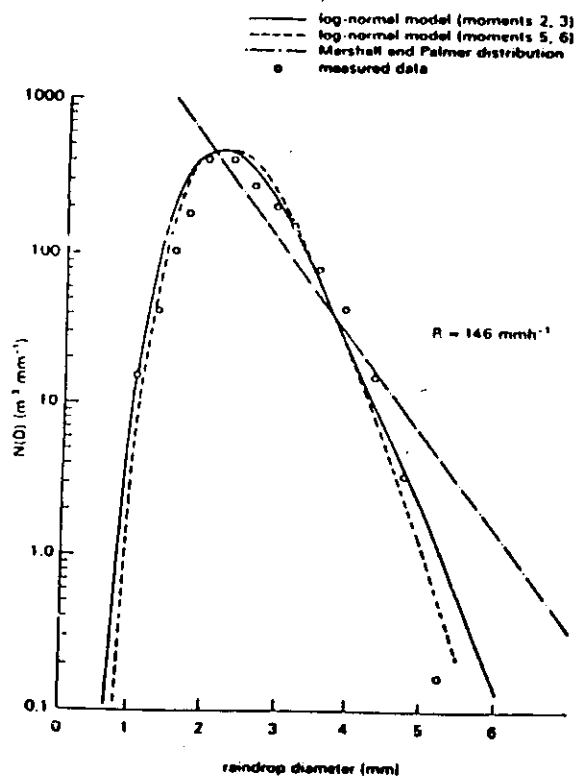

Fig. 3

Comparison of Ajayi-Olsen raindrop size lognormal model with the Marshall and Palmer distribution (after Ref. 4).

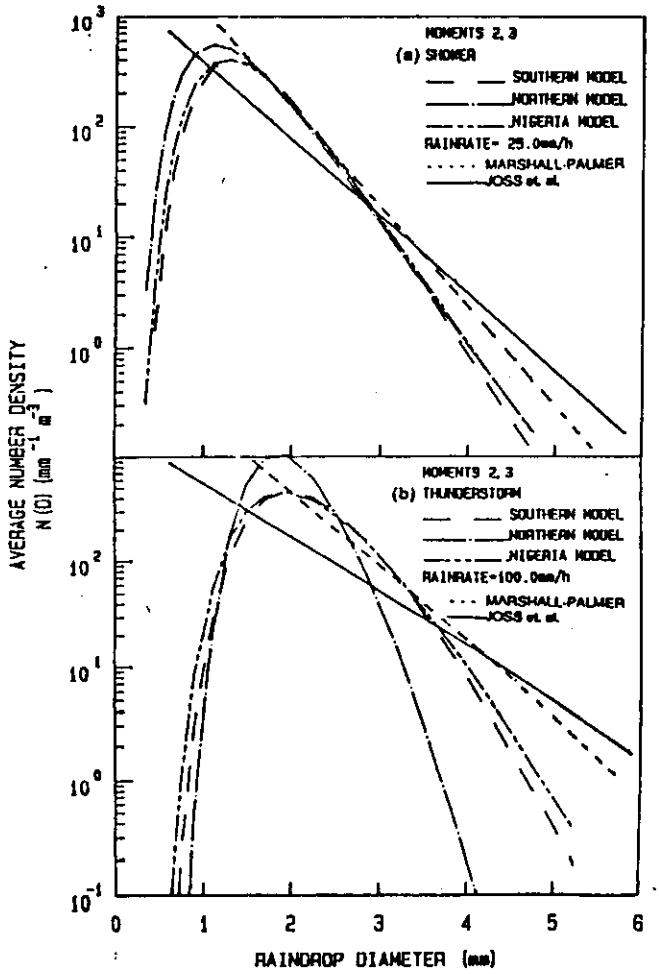

Fig. 4 Comparison of tropical raindrop size models with the Marshall-Palmer and Joss et al. models for

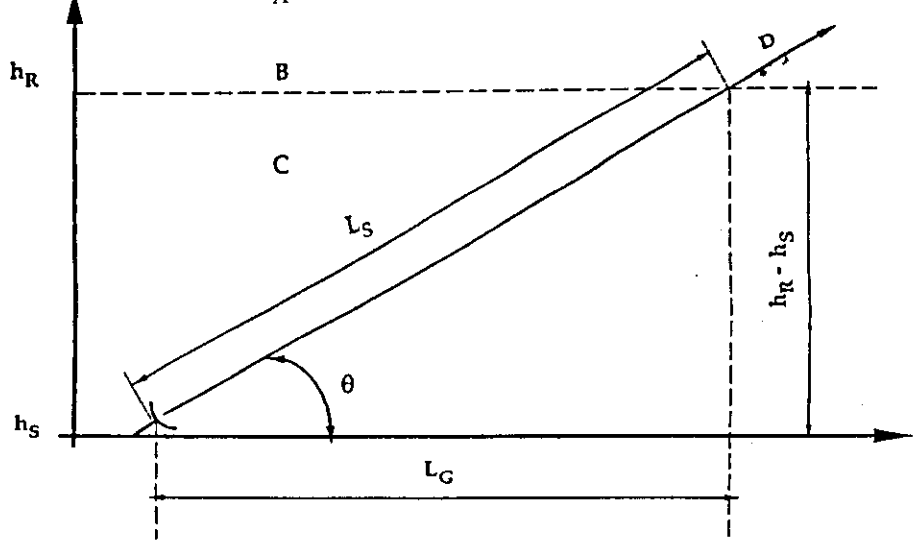

Fig. 5 Schematic representation of an earth-space path

A: Frozen precipitation
B: Rain height
C: Liquid precipitation
D: Earth-space path

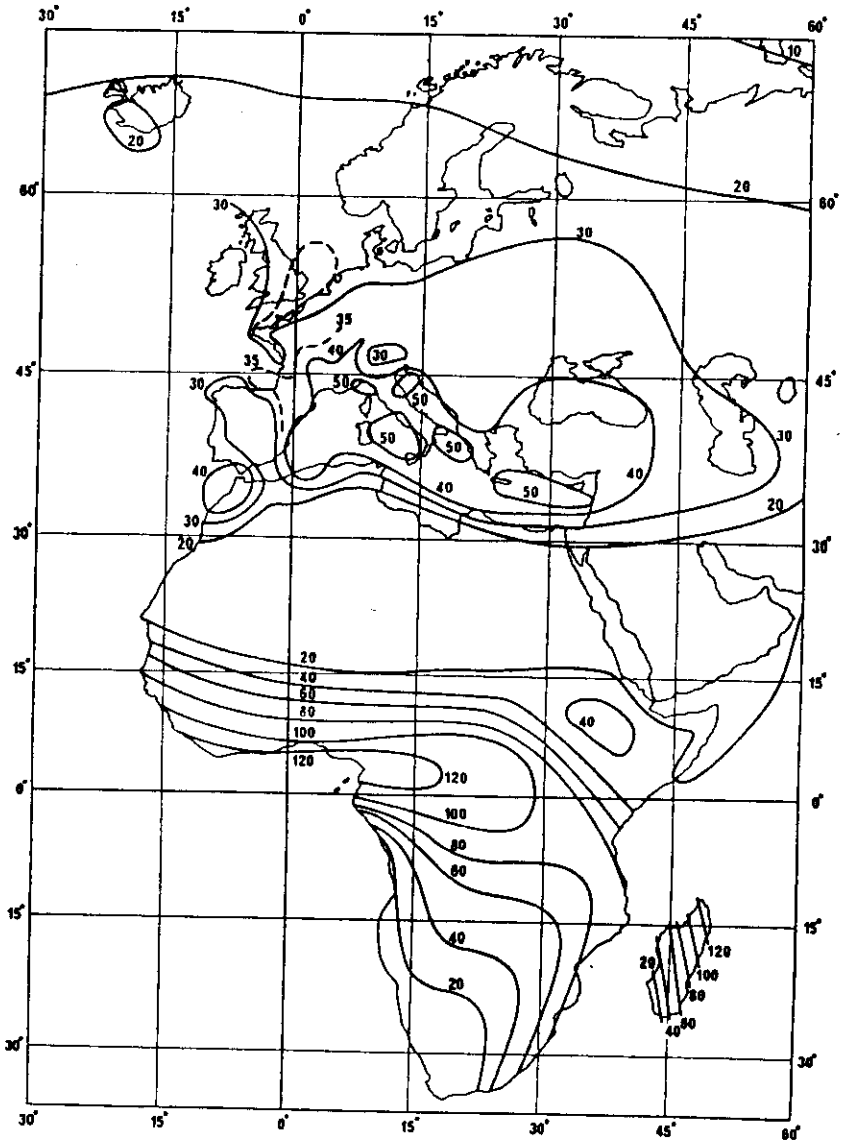

Fig. 6 – *Rainfall contours for 0.01% of the time*

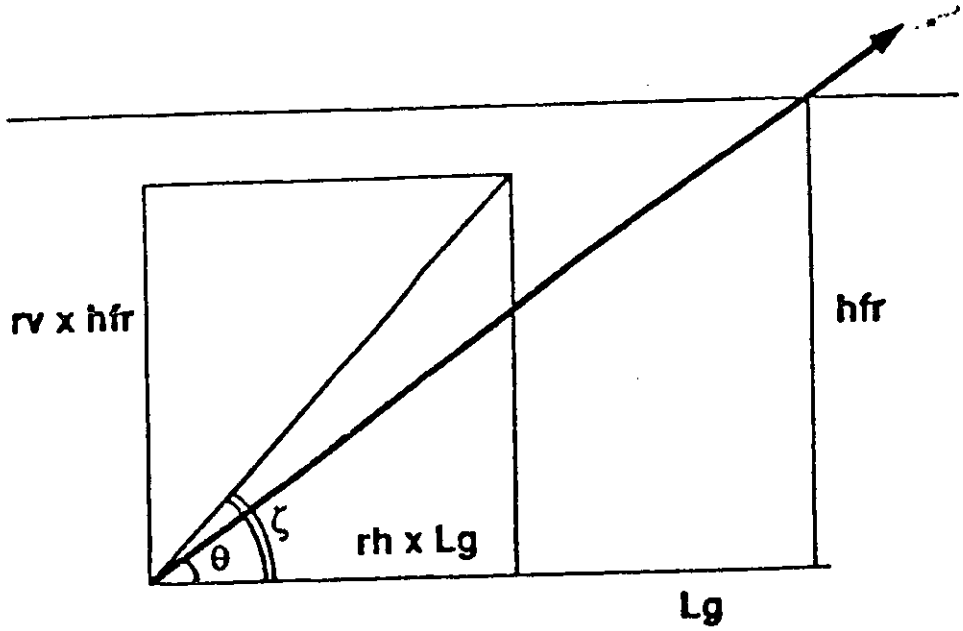

Fig. 7 - Slant-path geometry

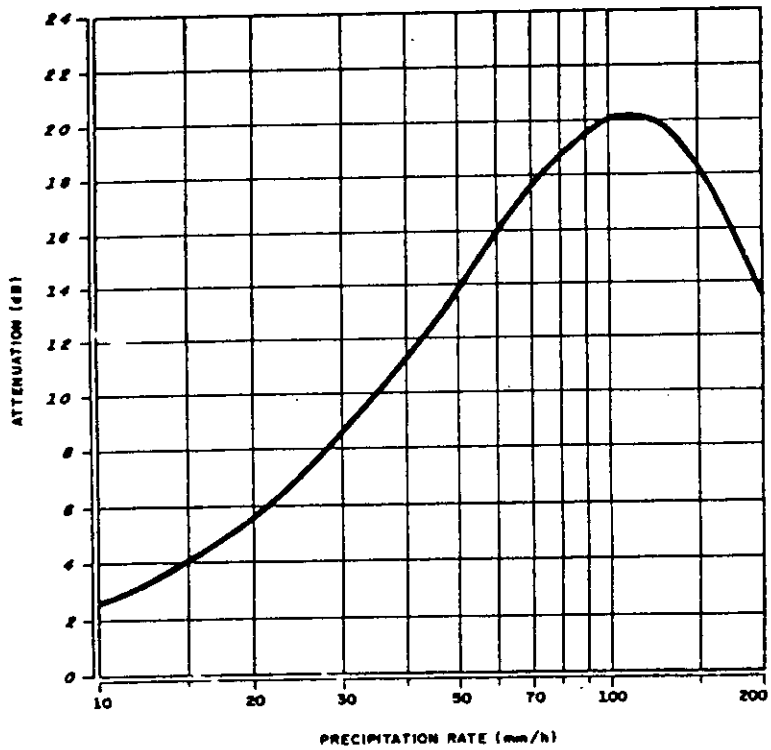

Fig. 8 - Rain attenuation - CCIR model
f = 11 GHz ; d = 20km; vertical polarization

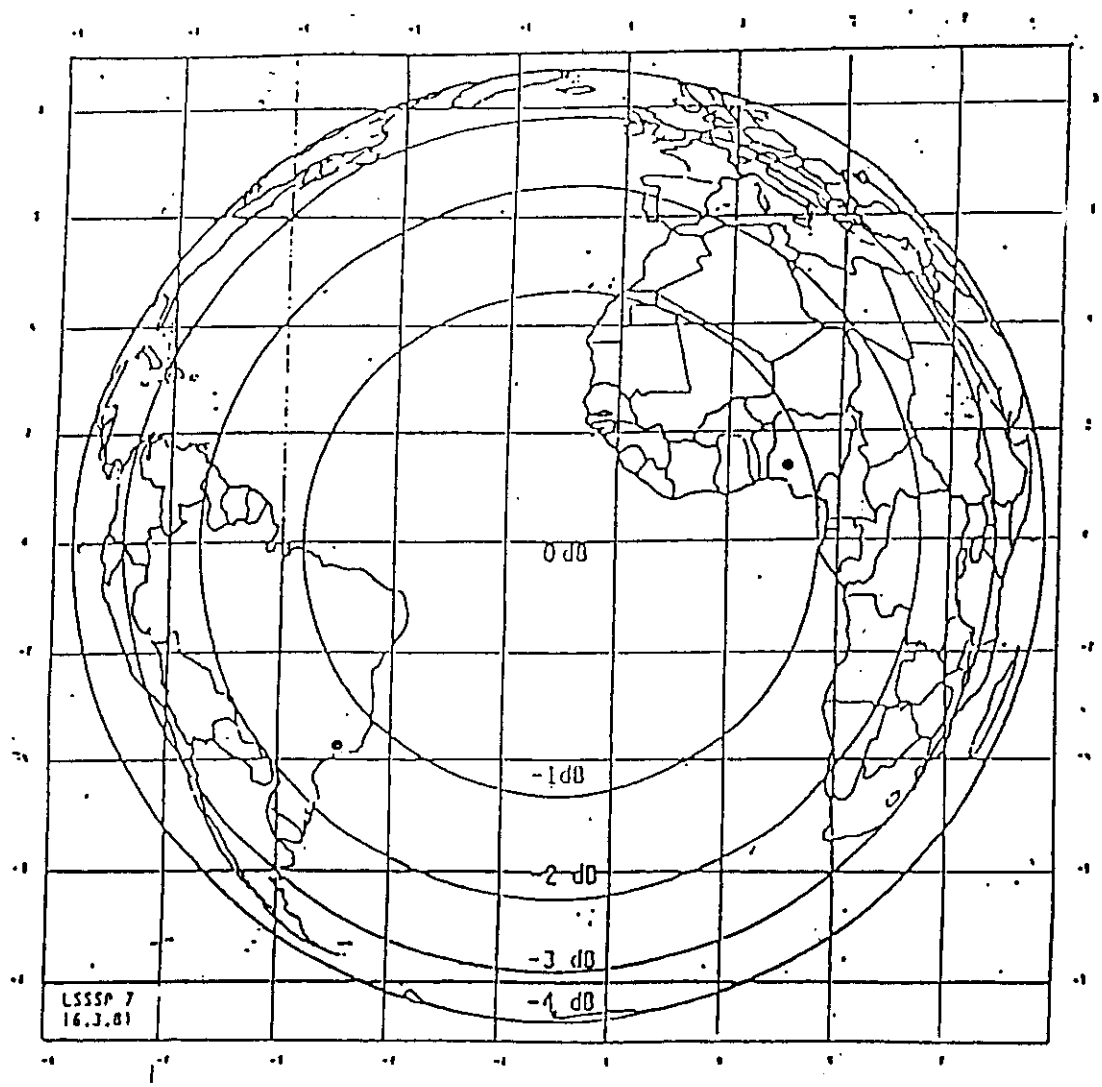

Fig. 9 Coverage of OLYMPUS B0 beacon (EIRP profiles are referred to the maximum value)

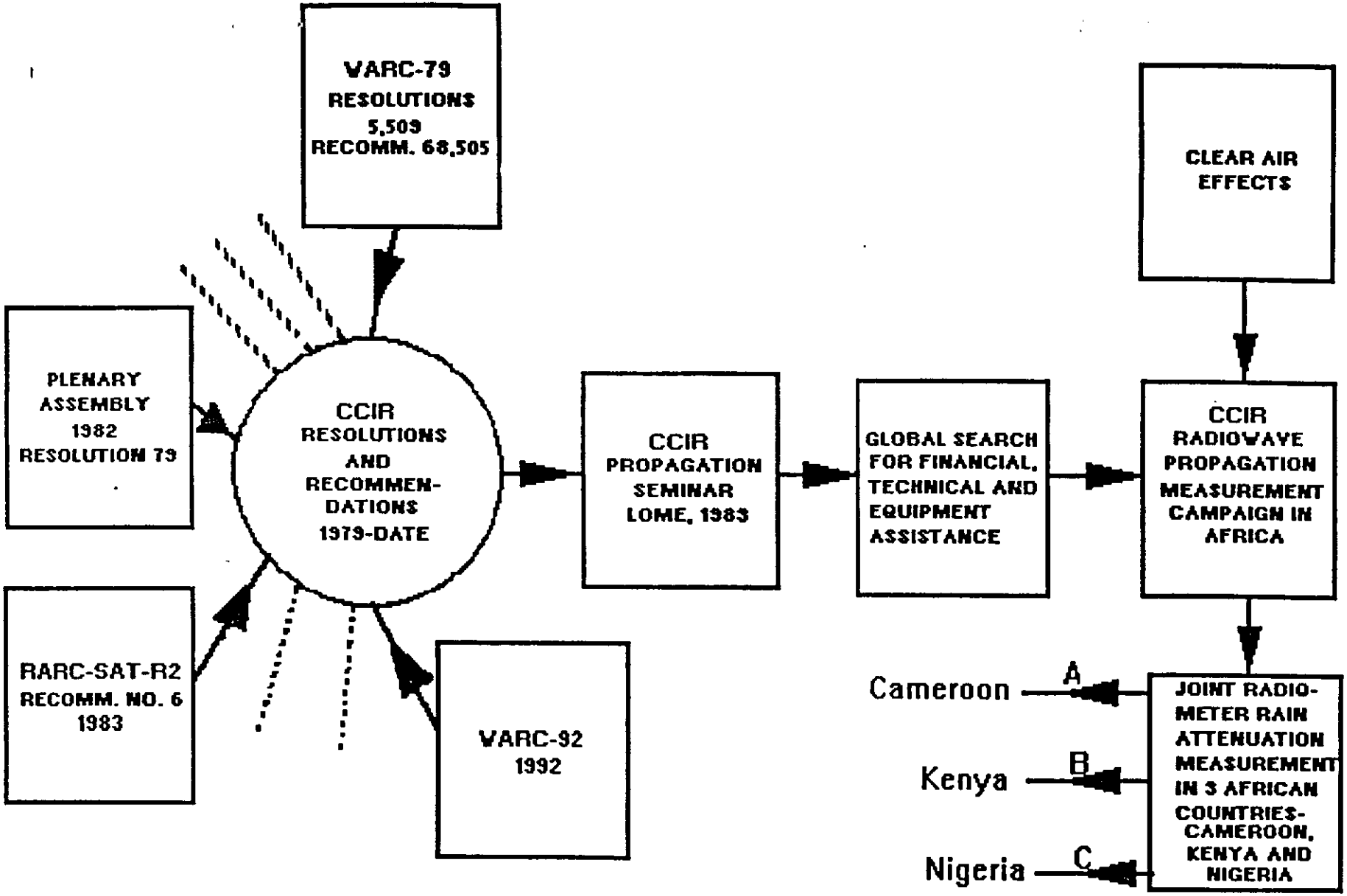

Fig. 10 (a) CCIR RADIO PROPAGATION MEASUREMENT CAMPAIGN IN AFRICA

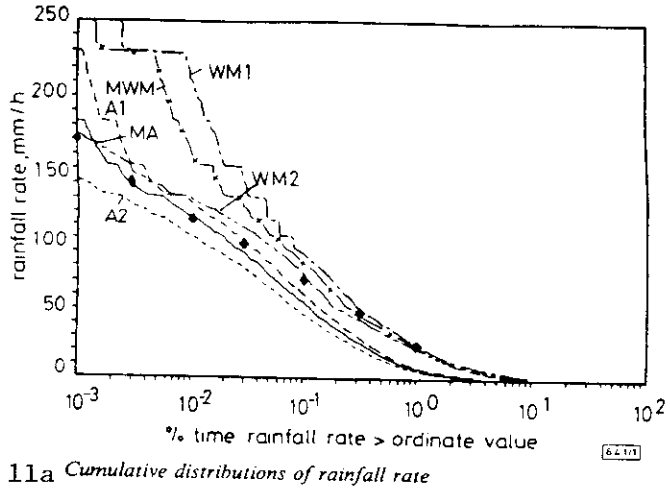

Fig 11a *Cumulative distributions of rainfall rate*

A1 : Annual cumulative distribution, first year
A2 : Annual cumulative distribution, second year
MA : Mean annual cumulative distribution
WM1 : Worst-month cumulative distribution, first year
WM2 : Worst-month cumulative distribution, second year
MWM : Mean worst-month cumulative distribution
◆ ITU-R annual cumulative distribution for rain zone Q

Fig. 11(a) DOUALA

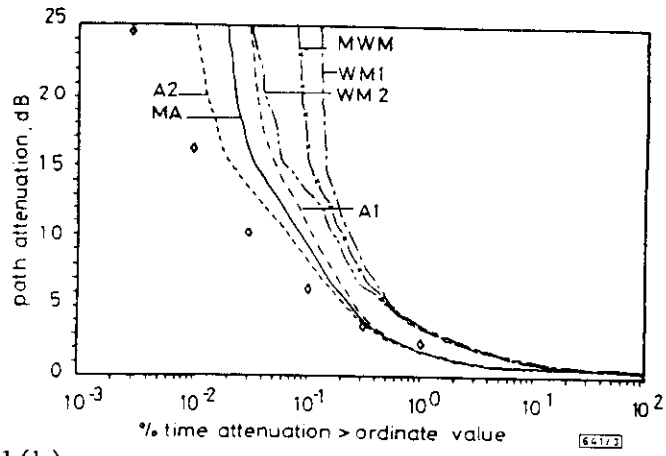

Fig.11(b) *Cumulative distributions of path attenuation*

A1 : Annual cumulative distribution, first year
A2 : Annual cumulative distribution, second year
MA : Mean annual cumulative distribution
WM1 : Worst-month cumulative distribution, first year
WM2 : Worst-month cumulative distribution, second year
MWM : Mean worst-month cumulative distribution
◊ ITU-R prediction from Rec. 618

DOUALA

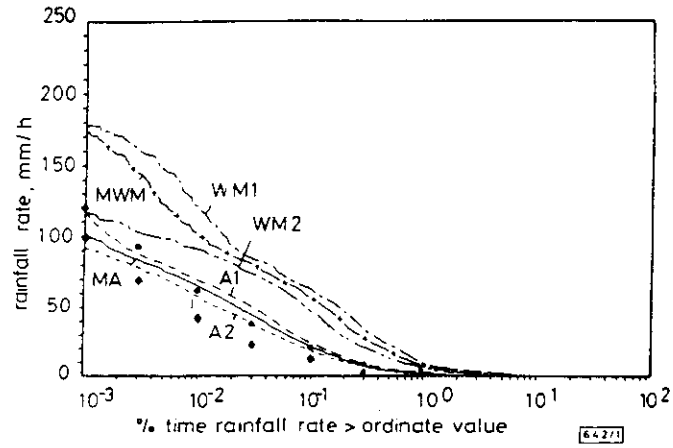

Cumulative distributions of rainfall rate

A1 : Annual cumulative distribution, first year
A2 : Annual cumulative distribution, second year
MA : Mean annual cumulative distribution
WM1 : Worst-month cumulative distribution, first year
WM2 : Worst-month cumulative distribution, second year
MWM : Mean worst-month cumulative distribution
× ITU-R annual cumulative distribution for rain zone K
● ITU-R annual cumulative distribution for rain zone M

Fig 12(a) NAIROBI

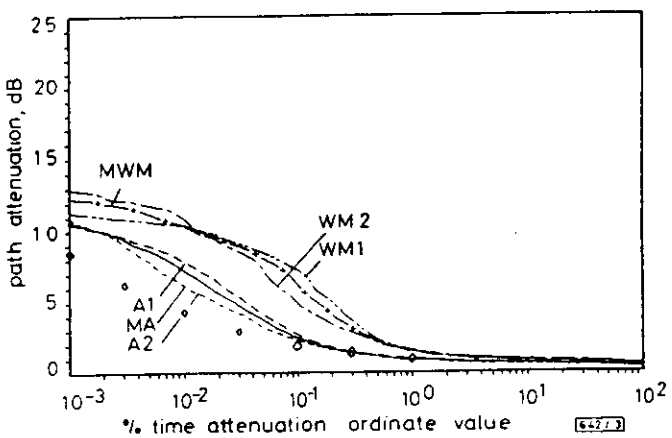

Cumulative distributions of path attenuation

A1 : Annual cumulative distribution, first year
A2 : Annual cumulative distribution, second year
MA : Mean annual cumulative distribution
WM1 : Worst-month cumulative distribution, first year
WM2 : Worst-month cumulative distribution, second year
MWM : Mean worst-month cumulative distribution
× ITU-R prediction from Rec. 618

Fig. 12(b) Nairobi

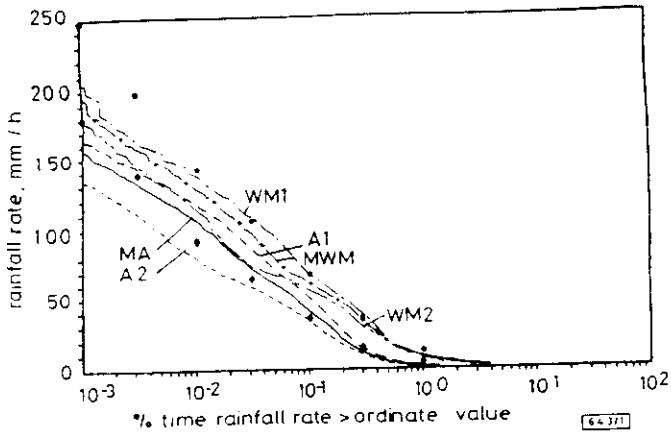

Cumulative distributions of rainfall rate

A1 : Annual cumulative distribution, first year
A2 : Annual cumulative distribution, second year
MA : Mean annual cumulative distribution
WM1 : Worst-month cumulative distribution, first year
WM2 : Worst-month cumulative distribution, second year
MWM : Mean worst-month cumulative distribution
◆ ITU-R annual cumulative distirbution for rain zone N
● ITU-R annual cumulative distribution for rain zone P

Fig. 13(a)

ILE-IFE

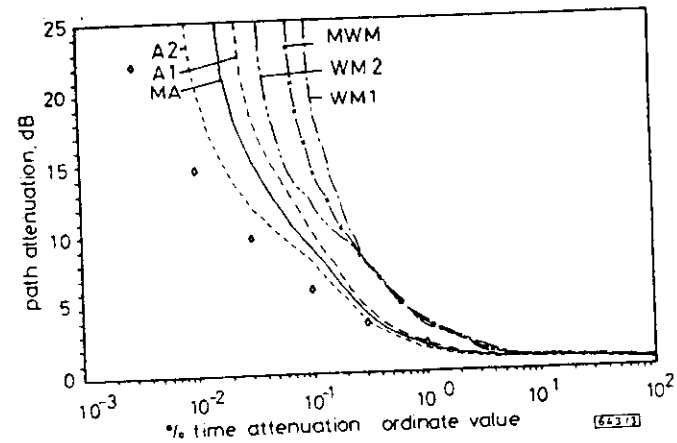

Cumulative distributions of path attenuation

A1 : Annual cumulative distribution, first year
A2 : Annual cumulative distribution, second year
MA : Mean annual cumulative distribution
WM1 : Worst-month cumulative distribution, first year
WM2 : Worst-month cumulative distribution, second year
MWM : Mean worst-month cumulative distribution
◆ ITU-R prediction from Rec. 618

Fig. 13(b) Ile-Ife.

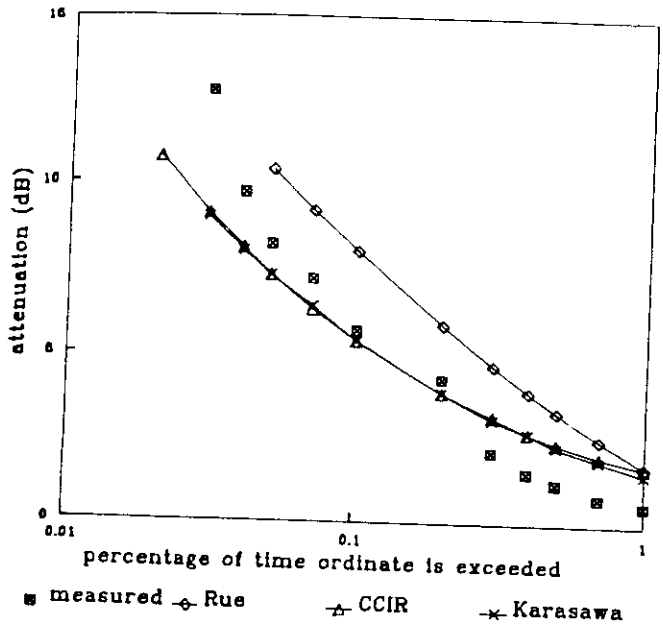

Fig. 14(a) Measured and predicted cumulative distributions from radiometric measurements at Rio de Janeiro

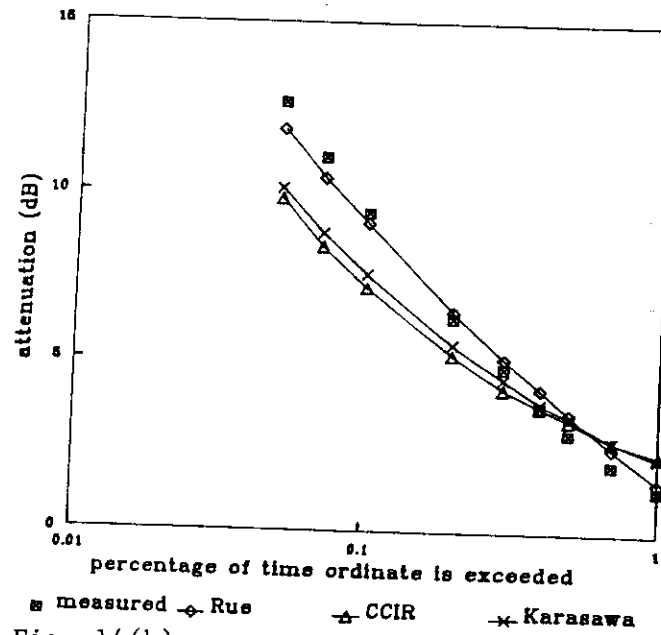

Fig. 14(b) Measured and predicted cumulative distributions from radiometric measurements at Belém

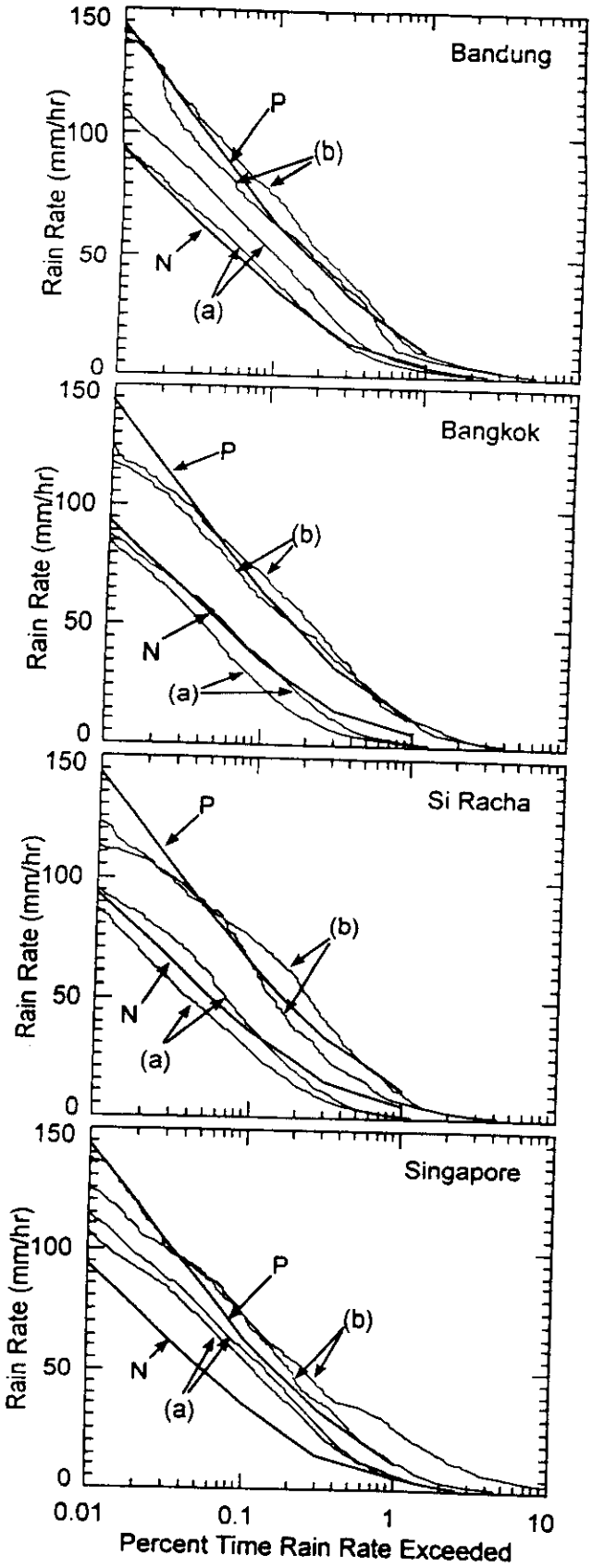

Fig 15 *Measured rainfall rate distributions for each of the four experimental locations.*

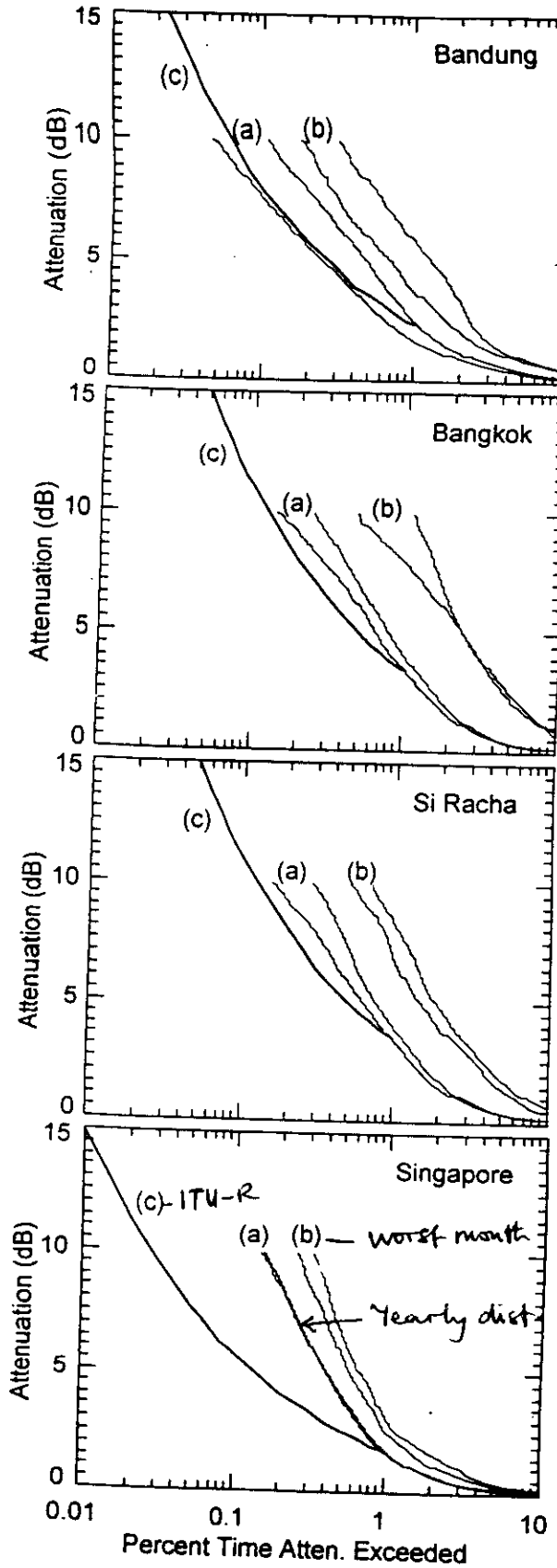

Fig. 16 *Distributions of attenuation at 12 GHz inferred from radiometer measurements at each of the four experimental locations.*

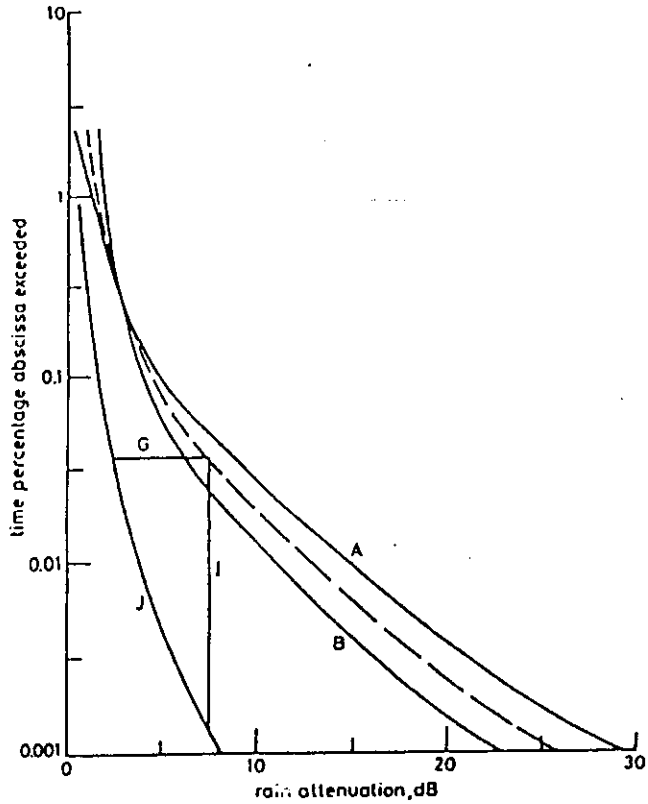

Fig. 17: Diversity Gain and Improvement

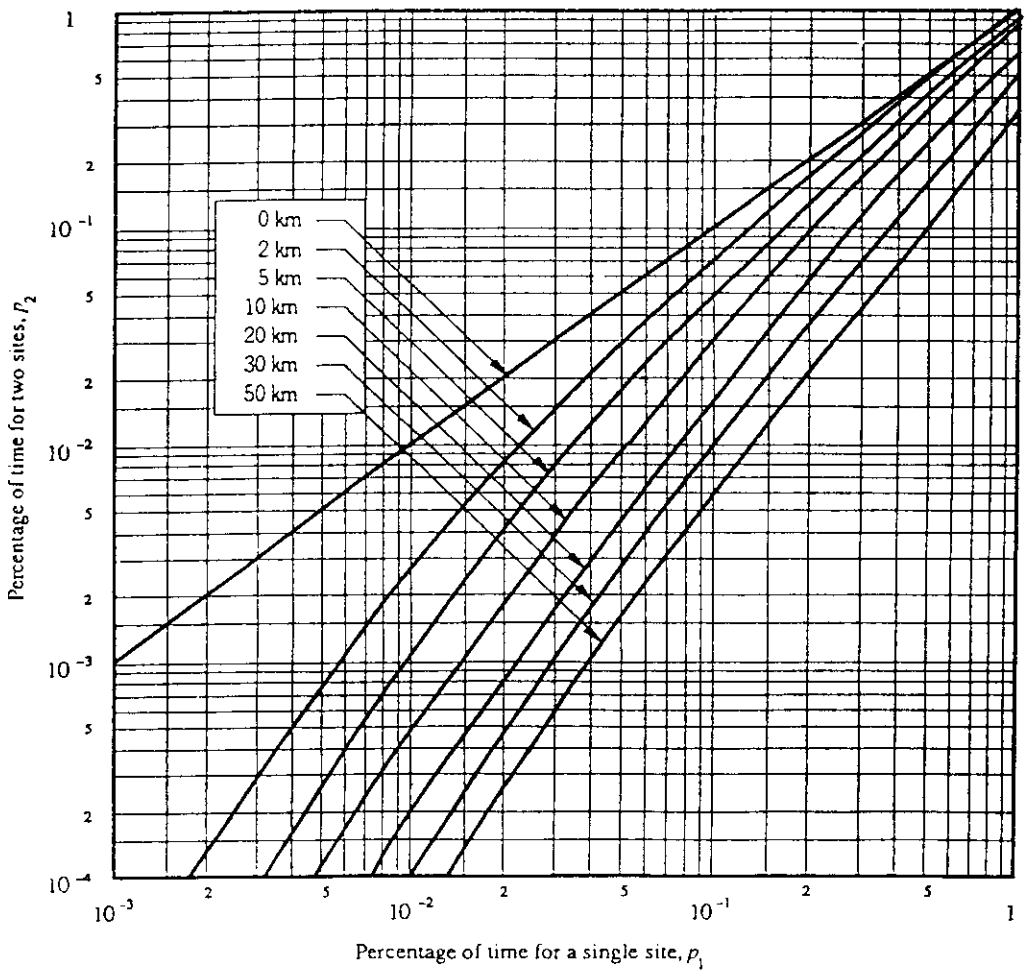

Fig 18: Relationship between percentages of time with and without diversity for the same attenuation (Earth-satellite paths)

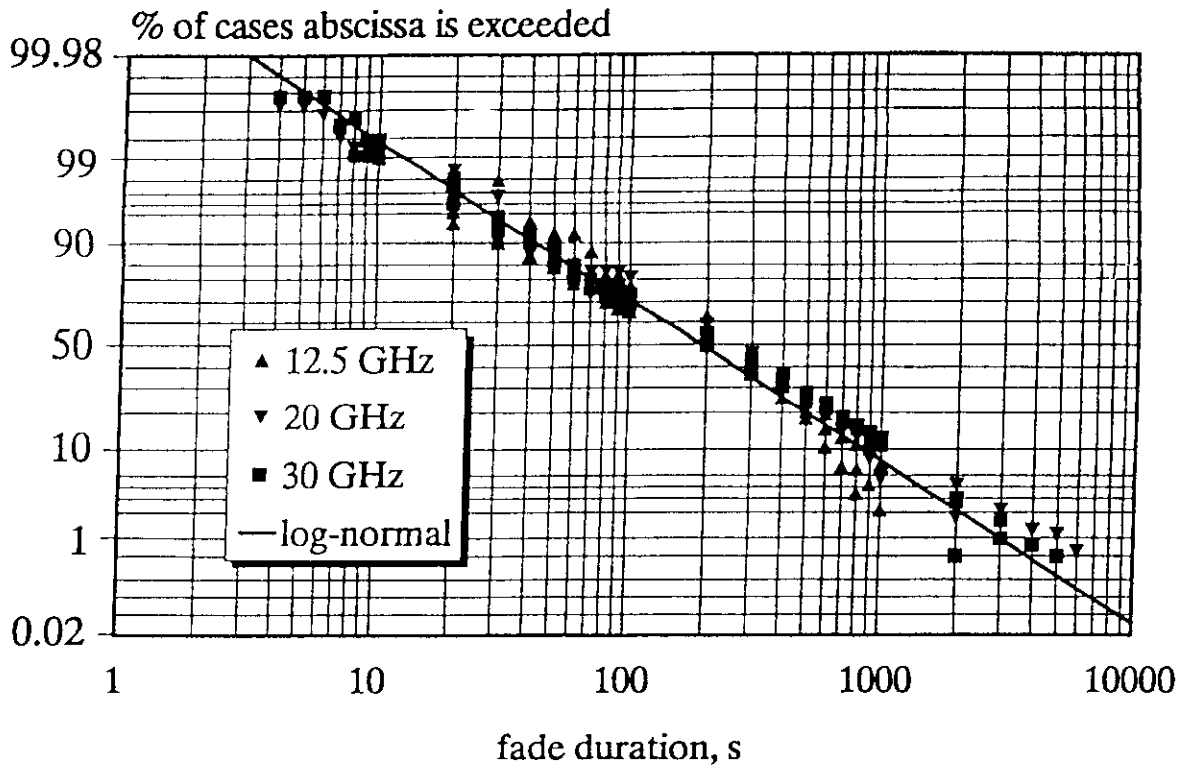

Fig. 19(a) *Cumulative distribution of fade duration events at 12.5, 20 and 30 GHz for attenuation thresholds in the range 4 to 10 dB.*

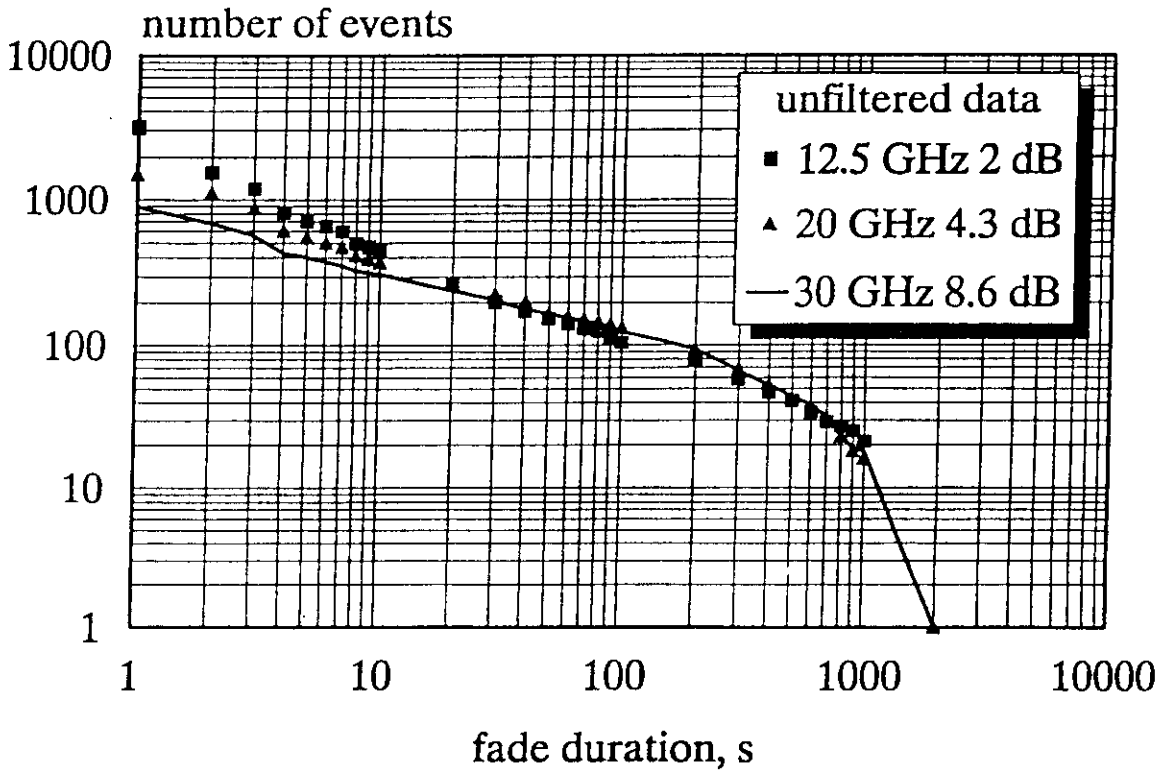

Fig. 19(b) *Cumulative distributions of absolute number of fade duration events at 12.5, 20 and 30 GHz with attenuation thresholds following the rules of long-term rain attenuation frequency scaling (unfiltered data).*

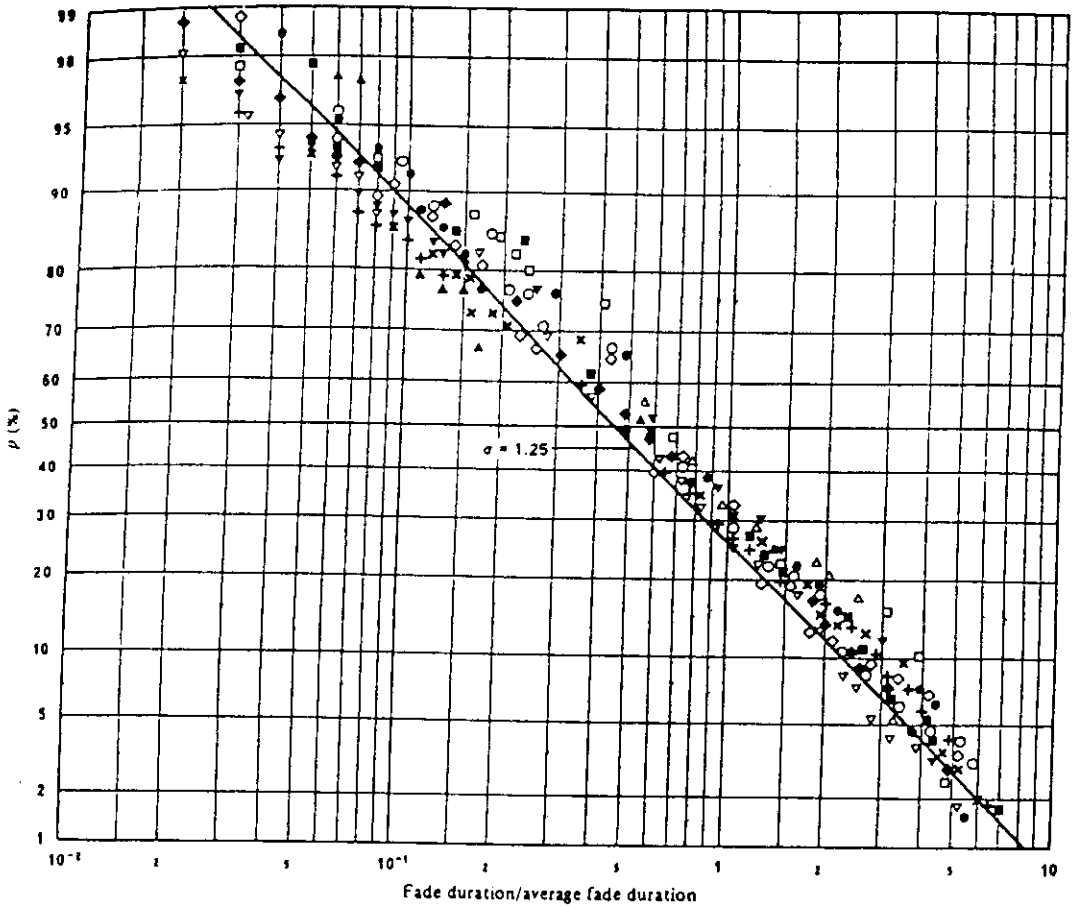

Fig. 20 – *Log-normal distribution of normalized fade duration*

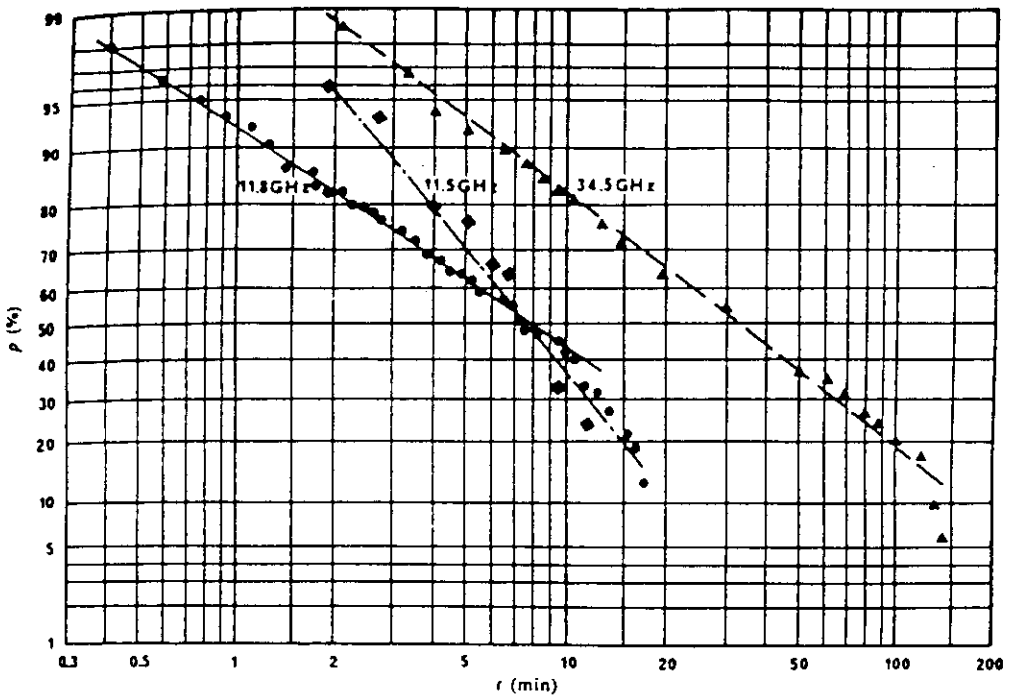

Fig. 21 – *Cumulative distribution of duration of co-polar attenuation exceeding 5 dB*

t: duration of CPA events ≥ 5 dB

p: conditional probability (percentage of total 5 dB fading time)

▲ ■ : ETS – II, measured in Japan, May 1977 – April 1978

● : OTS, measured in W. Europe, July 1978 – December 1980 (7 stations)

Nigeria
JUL-88 to JUN-89 Uptime: 99.85%

Frequency: 11.6 GHz
Elevation Angle: 48.2 degrees

Fig. 22(a) Cumulative Distribution of Rainfall Rates (Worst Month)

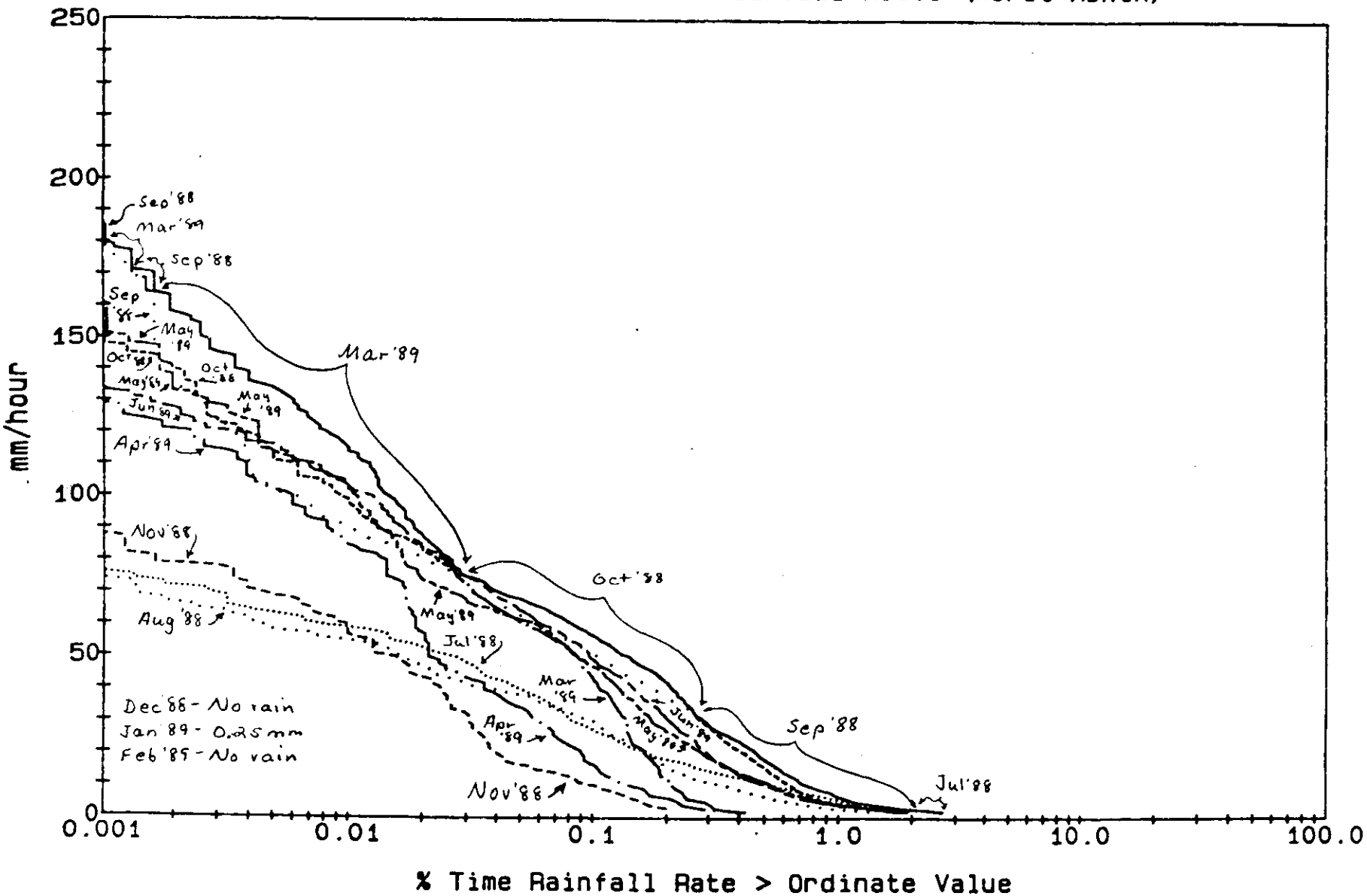

Nigeria
JUL-88 to JUN-89 Uptime: 99.83% Frequency: 11.6 GHz
Elevation Angle: 48.2 degrees

Fig. 22(b) Cumulative Distribution of Attenuation (Worst Month)

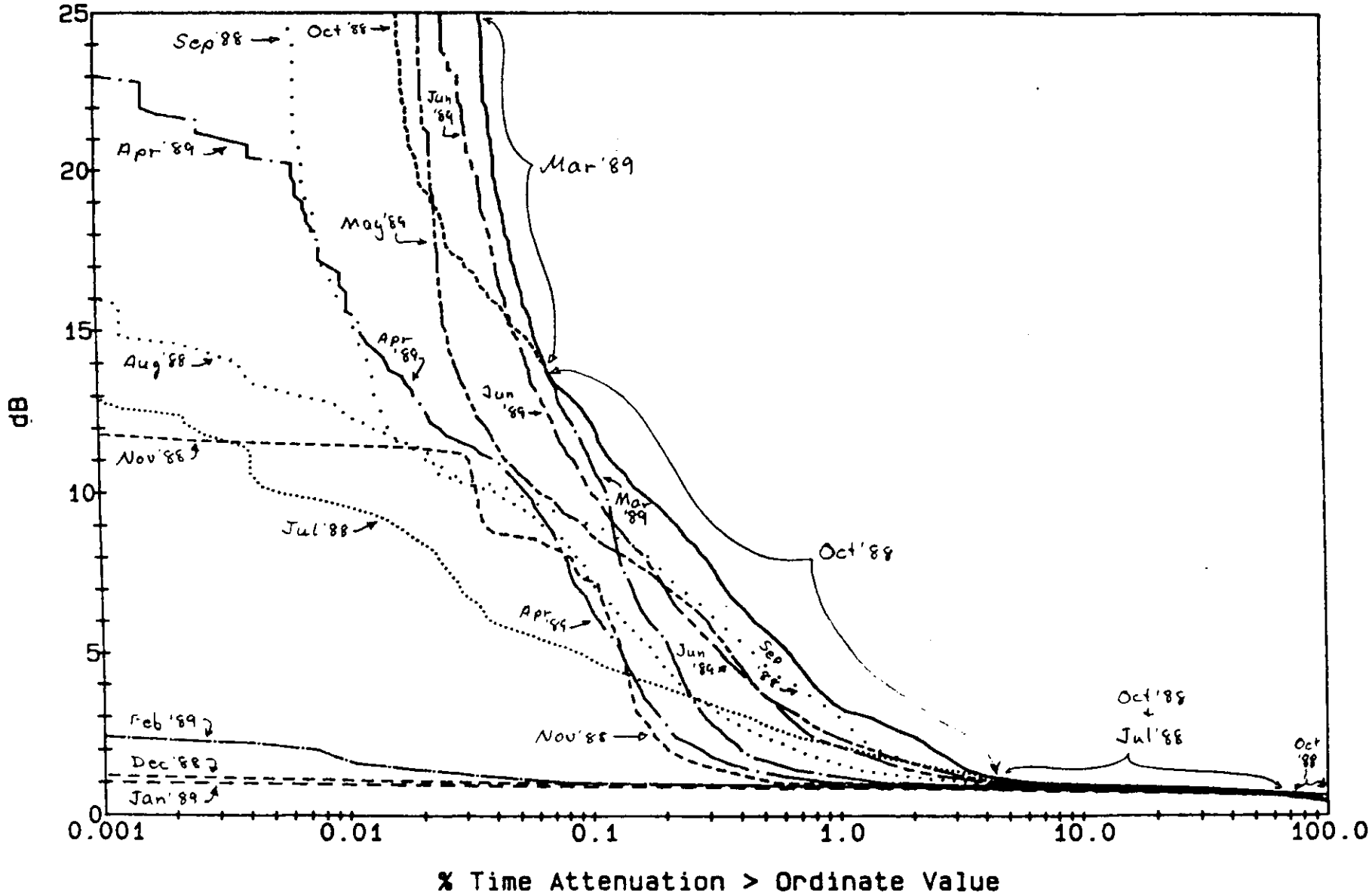

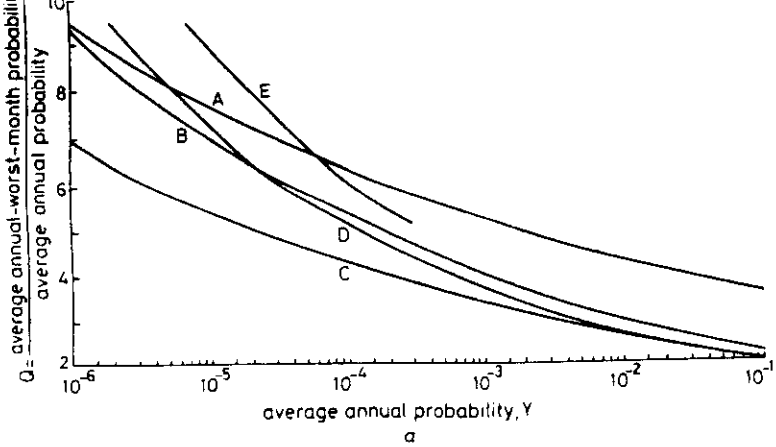

Fig. 23a *Ratio of annual-worst-month to average annual probability, Q, as a function of average annual probability Y*

A: Prairie + Northern
B: Central + Mountain } Rain rate, Canada
C: Coastal + Great Lakes
D: Rain rate and rain attenuation, Europe
E: Rain rate, Sweden

(Ref. Allnutt, 1989).

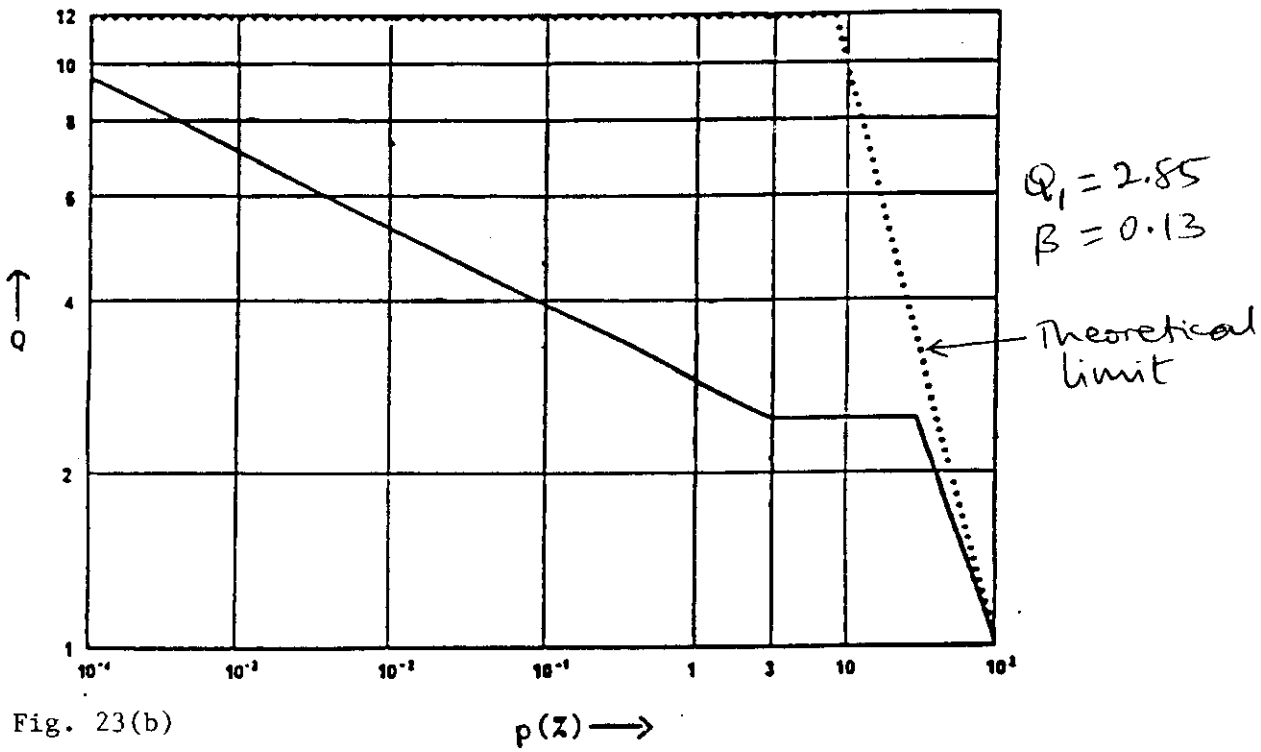

Fig. 23(b)

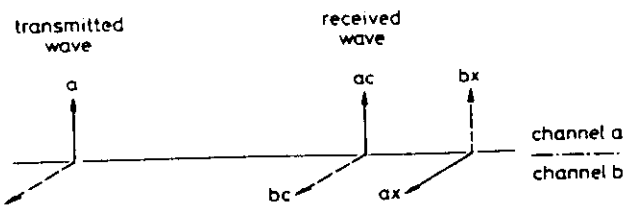

Fig. 24 *Terms used to define the difference between XPD and XPI*

ac and *bc* are the co-polarised components of signals transmitted in channels *a* and *b*, respectively. *ax* and *bx* are the cross-polarised components of signals transmitted in channels *a* and *b*, respectively.

A dual-polarised receiver that is designed to receive orthogonal channels simultaneously will detect both the wanted, or co-polarised, signals *ac* and *bc* and the unwanted, or cross-polarised signals *bx* and *ax*. The isolation in channel *a* will be the ratio of *ac*/*bx*. In general, experiments use only mono-polarised transmissions and so what is measured is the discrimination ratio *ac*/*ax* or *bc*/*bx*.

(Ref. Allnutt, 1989)

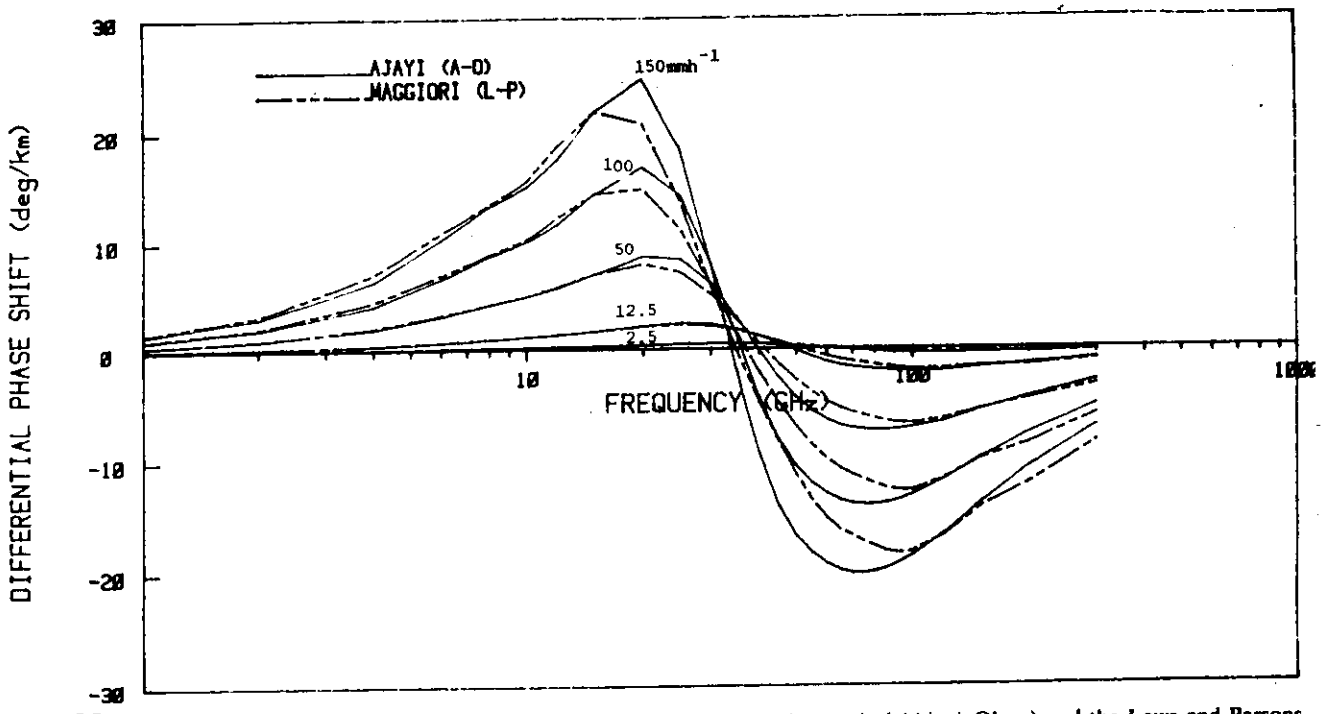

Fig. 25 Effect of raindrop size distribution on differential phase shift using the tropical (Ajayi–Olsen) and the Laws and Parsons (L–P) drop-size distributions

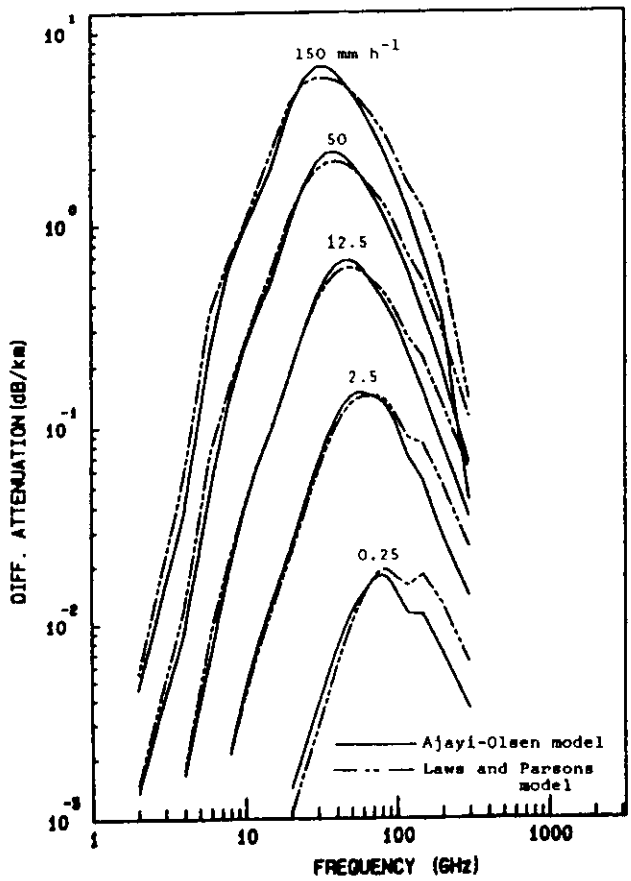

Fig. 26 Differential attenuation for oblate spheroidal drops using the tropical (Ajayi–Olsen, A–O) and the Laws–Parsons (L–P) drop size distribution

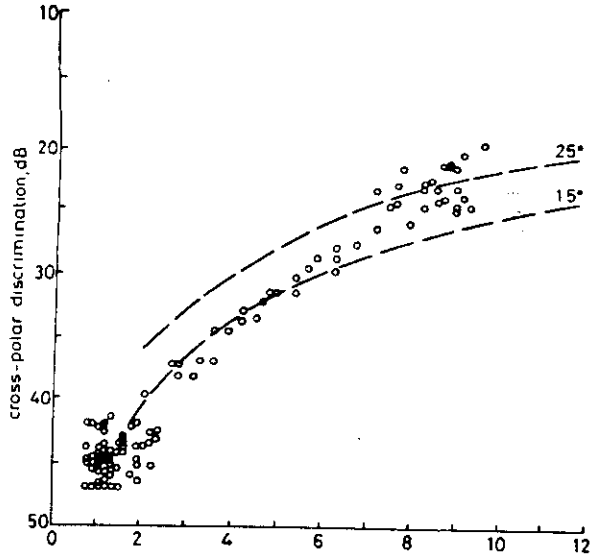

Fig. 27

Measured cross-polarisation discrimination versus co-polarised signal attenuation on a satellite-to-ground link from ATS-6 at a frequency of 30 GHz

The broken lines refer to theoretical curves of depolarisation versus attenuation for the given canting angles

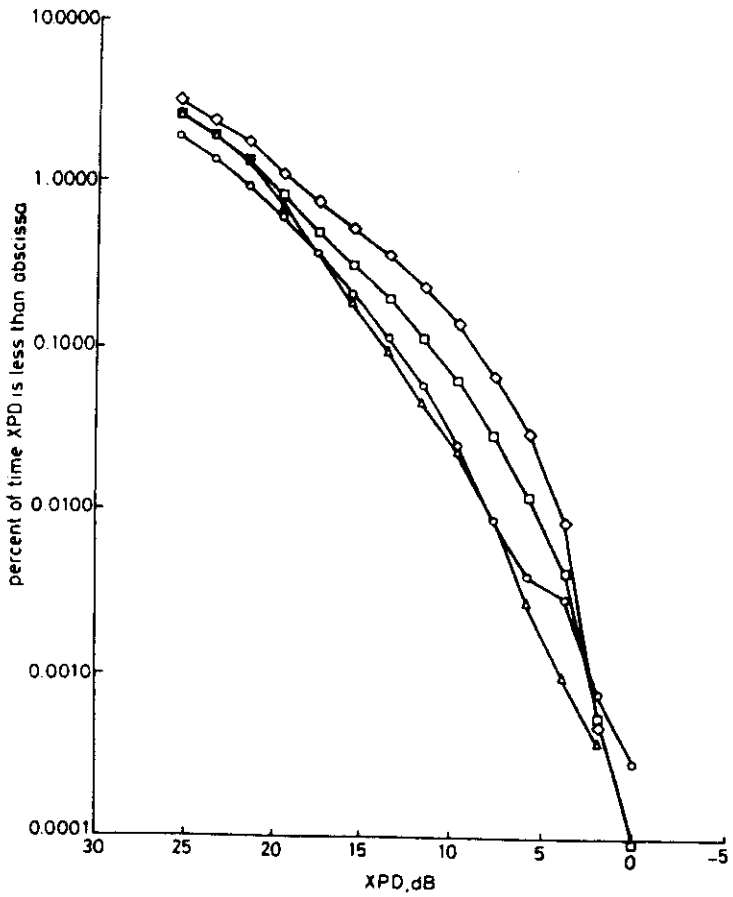

Fig. 28 *Variability from year to year of annual XPD statistics*

□ Combined
○ 1979
△ 1980
◇ 1981

The data were taken at an elevation angle of 10·7° using a circularly polarised 11·6 GHz beacon from the SIRIO satellite

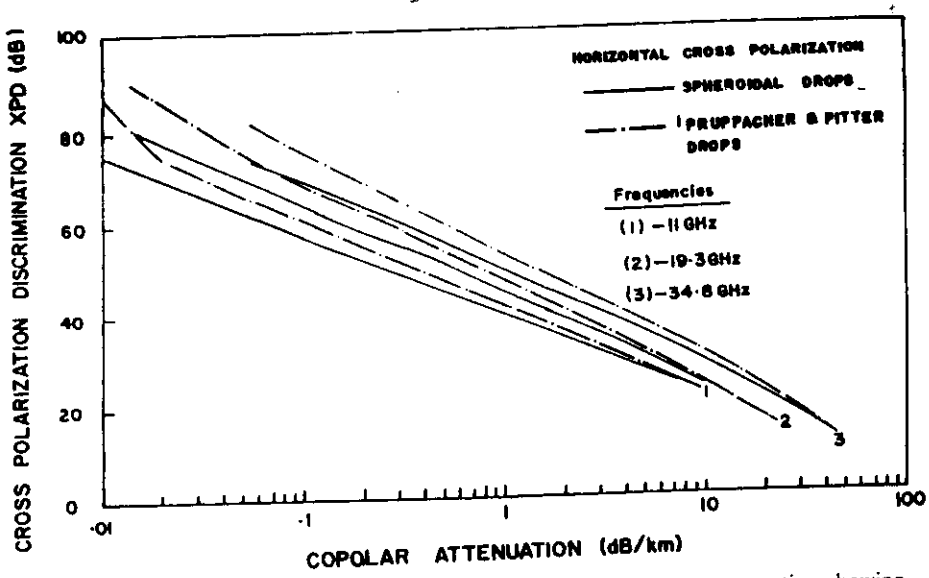

Fig. 29 Variation of cross-polarization discrimination with copolar attenuation showing the effect of raindrop shape (Reference)

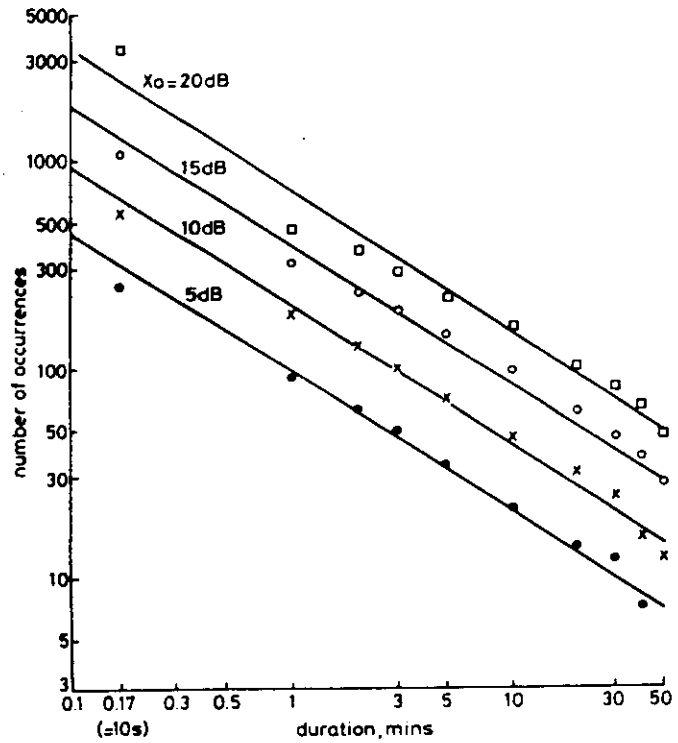

Fig. 30 *XPD event duration statistics* (Ref. 7)
Yamaguchi
11·452 GHz (CP)
Jan.–Dec. 1983
Elev. angle; 6·5°
The data thresholds were 5, 10, 15 and 20 dB as shown

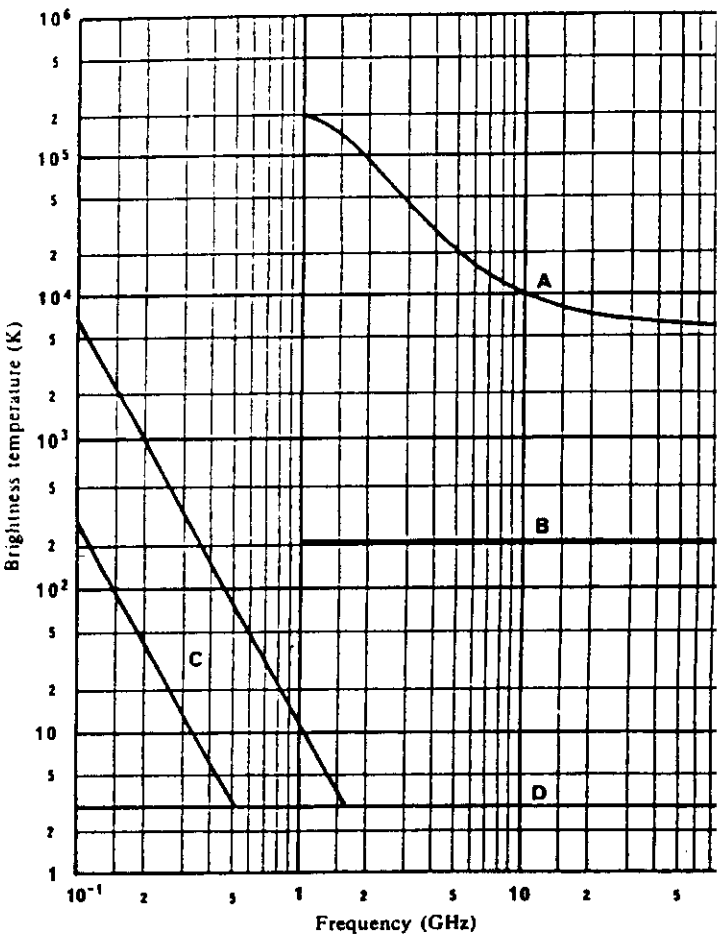

Fig. 31 – *Extra-terrestrial noise sources*

A: quiet Sun
B: Moon
} diameter ~ 0.5°
C: range of galactic noise
D: cosmic background

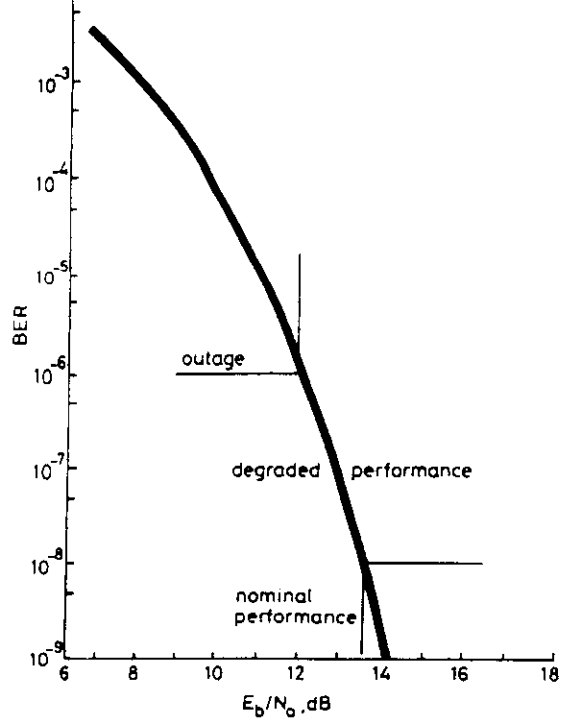

Fig. 32 *Typical uncoded coherent QPSK performance including implementation losses*

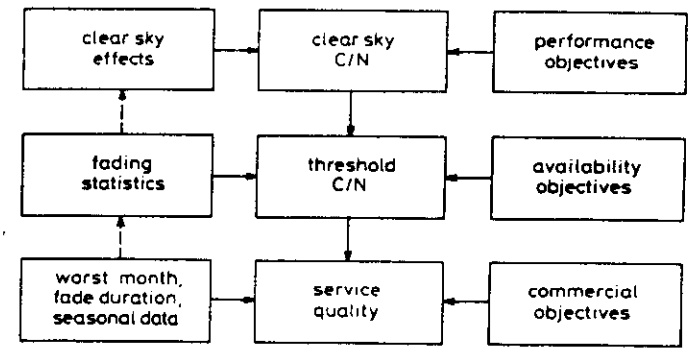

Fig. 33 *Synopsis of an earth station link margin calculation procedure*

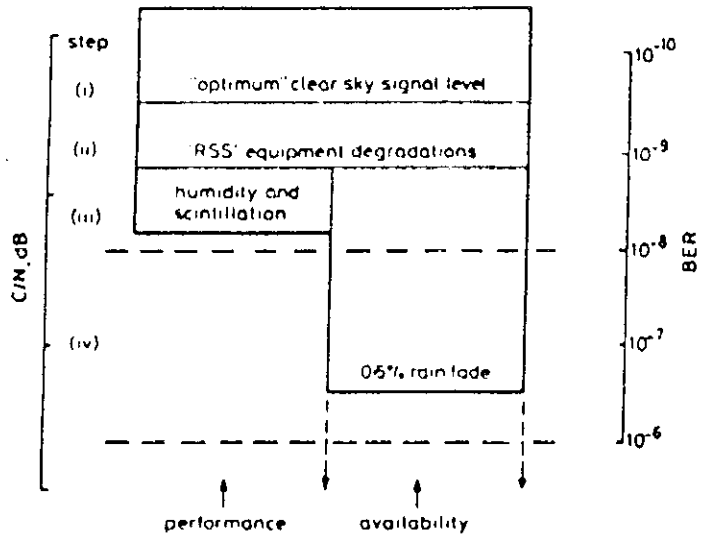

RSS - Root Sum Squ

Fig 34 *Schematic of the impact of propagation parameters on the determination of earth station design* (Ref. 8)

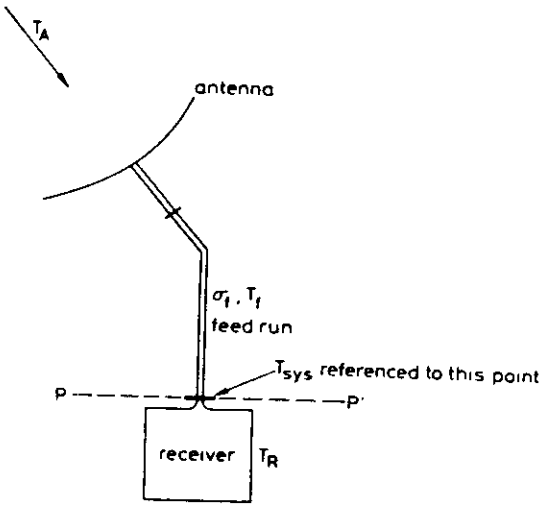

Fig. 35 *Simple schematic of an earth station giving the principal components for determining the system noise temperature T_{sys}*
Incident upon the plane *P–P'*, at which point the system noise temperature is calculated, is the modified antenna temperature $\sigma_f T_A$. Plane *P–P'* is usually taken to be the flange connecting the feed run to the receiver. The physical temperature of the feed run is T_f while T_R is the equivalent noise temperature of the receiver. The fractional transmissivity of the feed run is σ_f (Ref. 7)

INTERNATIONAL ATOMIC ENERGY AGENCY

AND

UNITED NATIONS EDUCATIONAL SCIENTIFIC AND CULTURAL ORGANIZATION

INTERNATIONAL CENTRE FOR THEORETICAL PHYSICS

CLIMATIC INFORMATION FOR SATELLITE COMMUNICATION PLANNING.

PART V: PROPAGATION PARAMETERS FOR SPECIAL TYPES OF EARTH-SAPCE TELECOMMUNICATION SYSTEMS

Prof. G.O. Ajayi
Department of Electronic & Electrical Engineering
Obafemi Awolowo University,
Ile-Ife, Nigeria.

FOURTH ICTP-URSI-ITU (BDT) COLLEGE ON RADIOPROPAGATION:
Propagation, Informatics and Radiocommunication System Planning.

30 January - 3 March, 1995.

SECTION A

RADIOPROPAGATION PARAMETERS FOR DESIGN OF BROADCASTING - SATELLITE SYSTEMS

1. INTRODUCTION

In earlier parts, the general radiopropagation requirements for fixed-satellite services (FSS) were considered. The requirements for broadcasting-satellite systems differ in some areas. The feeder links to broadcasting satellites are considered as part of fixed-satellite services.

For the case of space-to-Earth paths, propagation effects to be considered include:

(i) Tropospheric effects - gaseous absorption, attenuation and depolarization by rain and other hydrometeors.

(ii) Ionospheric effects - Scintillation and Faraday rotation.

(iii) Local environmental effects - attenuation by buildings and vegetation.

2. TROPOSPHERIC EFFECTS

(i) For $f < 1GHz$ and $\theta > 10^{o}$ - Signal impairment is negligible.

(ii) For $f > 1GHz$ and/or $\theta < 10^{o}$ - Signal amplitude and angle of arrival fluctuations can be significant, especially for high latitudes.

where θ = angle of elevation.

(iii) Reduction in C/N due to increase in sky noise temperature due to precipitation.

(iv) Snow and ice accumulations on reflector and feed surfaces of antenna can degrade antenna pointing, gain and cross-polar characteristics.

2.1 Attenuation By Atmospheric Gases.

In the 22GHz band allocated to the broadcasting-satellite service in some regions, water vapour absorption can be large. For example, at a location where the 22.75GHz path attenuation exceeds 9.5dB for 1% of the worst month, about 3dB of the attenuation is contributed by gaseous attenuation.

2.2 Precipitation and Cloud Attenuation -

As for fixed-satellite service.

2.3 Rain attenuation for worst month

For satellite broadcast, rain attenuation exceeded for 1% of the worst month is usually of greatest importance. Prediction is similar to that of fixed-satellite.

2.4 Diurnal variation of fading

For broadcasting-satellite services, the diurnal variation of fading is important.

For many regions, large fades tend to occur in the afternoon and early evening hours.

Increased probability of deep fade occurrence is associated with time of maximum local thunderstorm activity. The diurnal variation of attenuation due to rain at Ile-Ife for the period July 1987 to June 1988 and July 1988 to June 1989 are shown in Figs. 1(a) and (b) respectively.

Figs. 1(a) and (b) show that low-level fading is more evenly distributed unlike the deep fading.

2.5 Scintillation fading

For $f < 10GHz$ and $\theta > 10^{o}$ - scintillation effect is small.

where θ = angle of elevation.

Prediction method is similar to that of fixed-satellite service.

3. DEPOLARIZATION - as for fixed-satellite service.

4. IONOSPHERIC EFFECTS

For $f < 3$ GHz, ionospheric effects are important on some paths and some locations. Estimated maximum values of ionospheric effects are as in Table 1 of Part 2.

5. EFFECTS OF LOCAL ENVIRONMENT

Effects of local structures and vegetation may be important in specific locations.

6. STATISTICAL DISTRIBUTION OF SIGNAL LEVEL FOR LARGE AREAS

A broadcasting satellite must serve a large area, preferably

with the same quality of service throughout for the same time percentage.

Available data show that the joint probability of occurrence of rainy conditions at different locations is several per cent for separations up to 500 km and that statistical independence cannot be assumed for separations less than about 800km. For pairs of sites separated by 200km, the joint probability for rainfall rates in excess of 5 mm/h can be about five times the probability obtained by assuming statistical independence.

7. REFERENCE

ITU-R Rec. PN-679-1: Propagation data required for the design of Broadcasting-Satellite Systems, 1992.

Nigeria
JUL-87 to JUN-88

Uptime: 99.79%

Frequency: 11.6 GHz
Elevation Angle: 48.2 degrees

Fig. 1(a): Diurnal Distribution of Attenuation

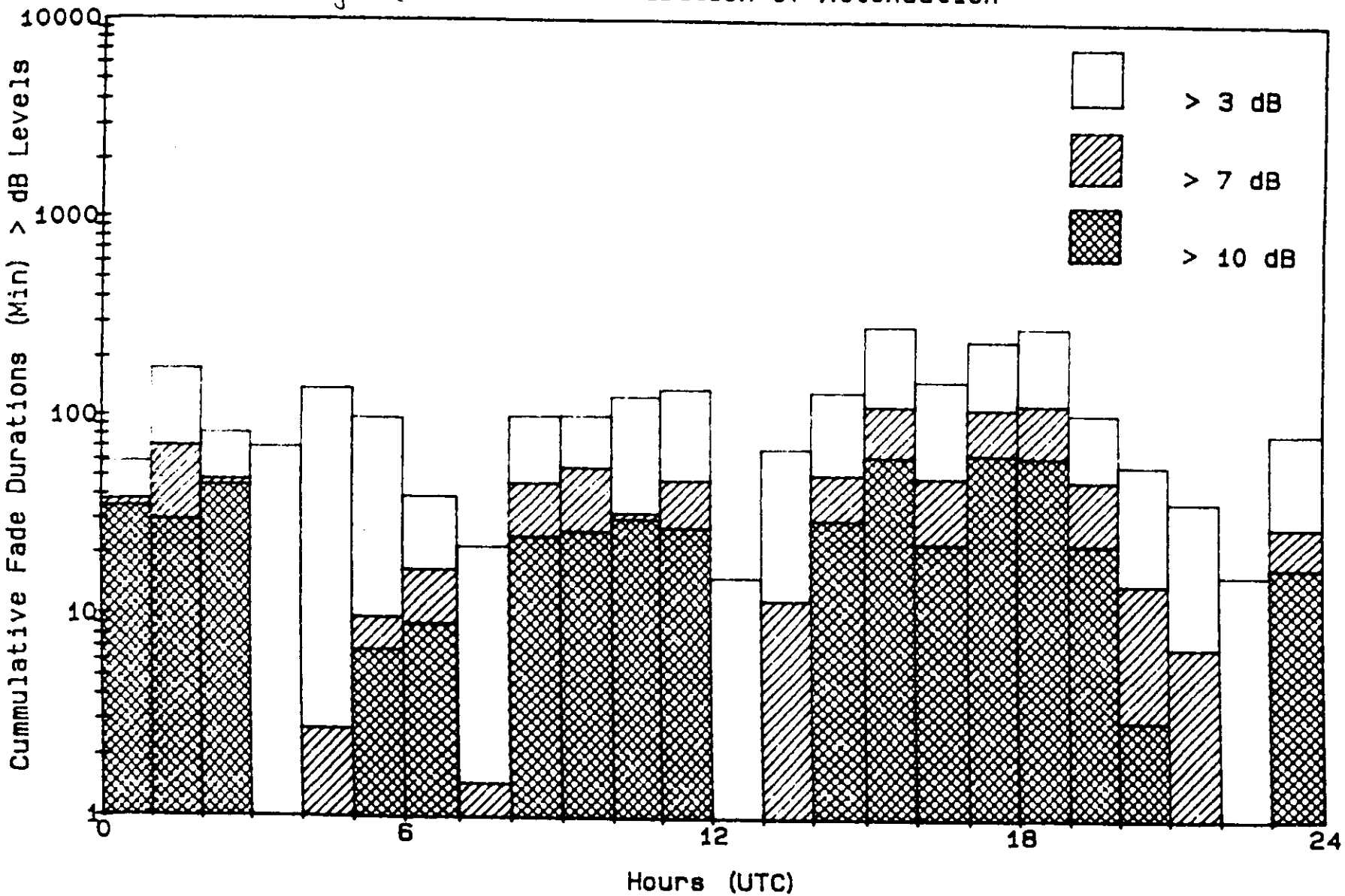

Nigeria
JUL-88 to JUN-89

Uptime: 99.83%

Frequency: 11.6 GHz
Elevation Angle: 48.2 degrees

Fig. 16: Diurnal Distribution of Attenuation

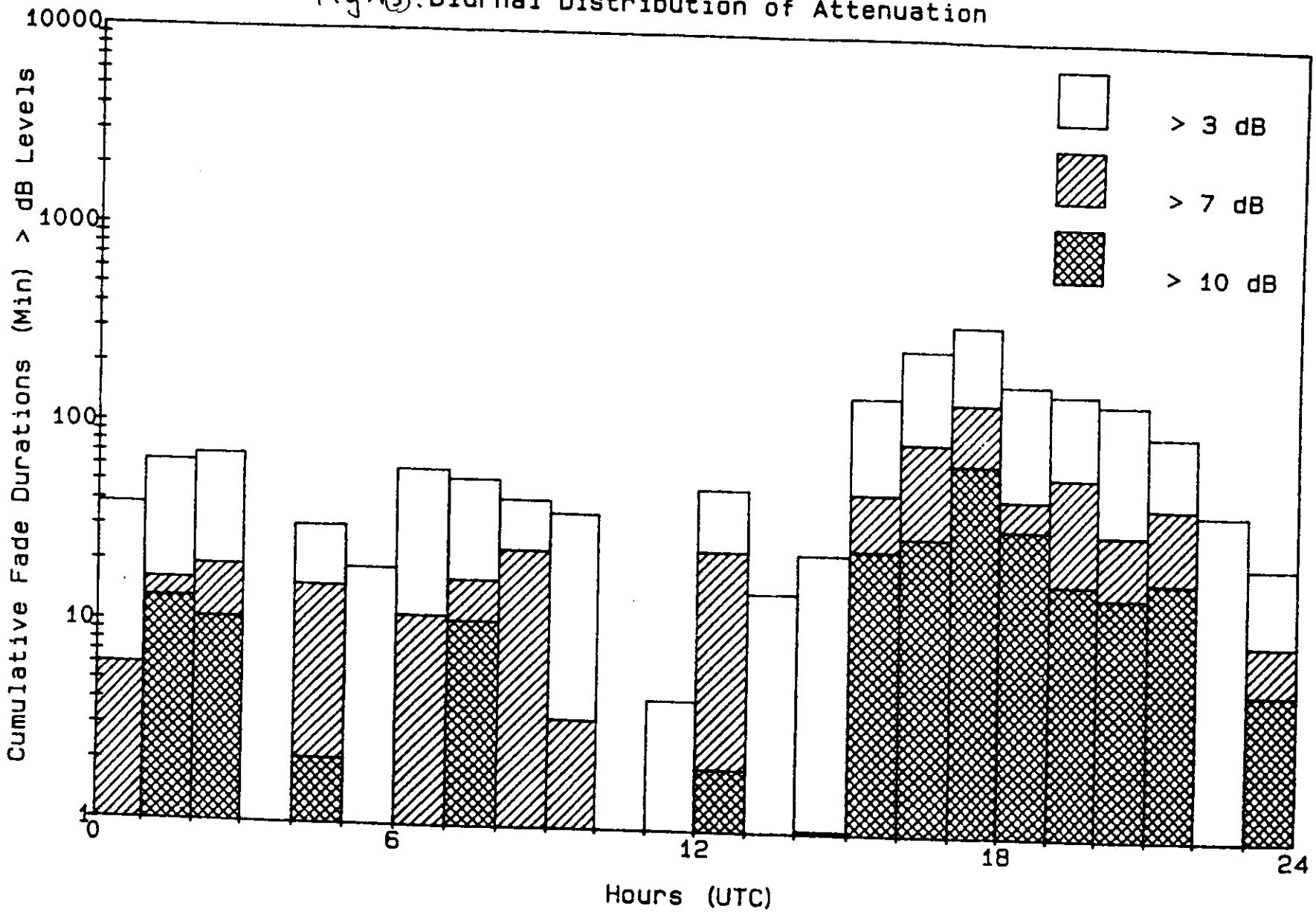

SECTION B

LAND MOBILE SATELLITE SYSTEMS (LMSS)

1. INTRODUCTION

In Fixed-Satellite Service (FSS), it is possible to discriminate against multi-path, shadowing and blockage by using highly directive antennas placed at unobstructed sites. Terrain effects play a greater importance in Land-Mobile-Satellite Service (LMSS) than in FSS. Lower link availability of 80% to 99% applies in LMSS.

2. TROPOSPHERIC EFFECTS

2.1 Attenuation

(i) Atmospheric gases and rain

for f < 1 GHz	negligible
1 < f < 10 GHz	small

except at low elevation angles.

For f > 10 GHz - prediction methods are as for FSS.

Fog and cloud attenuation

for f < 10GHz - negligible

2.2 Scintillation

Causes: Tropospheric turbulence and atmospheric multipath.

Effects: Irregular variations in received signal level and angle-of-arrival.
Magnitudes of the effects increase with increasing frequency and decreasing elevation angle.

Angle-of-arrival fluctuations caused by turbulence are independent of frequency.

Antenna beamwidth affects the scintillation magnitude.

Prediction: As for FSS.

3. IONOSPHERIC EFFECTS

As for the FSS.

4. MULTIPATH MODELS FOR CLEAR LINE-OF-SIGHT CONDITIONS.

There is negligible shadowing in many cases with clear line-of-sight from the mobile terminal to the satellite. Terrain induced multipath can still lead to signal degradation. Constructive or destructive addition of direct line-of-sight signal and several multipath signals lead to signal enhancement or fade. The multipath signal characteristics depend on the following parameters:

(i) scattering cross-sections of the multipath reflectors

(ii) the number

(iii) distances to the receiving antenna

(iv) field polarizations

(v) receiving antenna gain pattern.

The following multipath degradation models are based on measurements with an antenna with the following characteristics:

(a) omnidirectional in azimuth
(b) gain variation between 15 and 75 degrees elevation less than 3 dB.
(c) below the horizon (negative elevation angles) the antenna gain was reduced by at least 10 dB.

4.1 Multipath in a Mountain Environment

In a mountainous terrain, the multipath distribution fade depth is given by

$$P = aA^{-b} \qquad \text{for } 1\% < P < 10\%$$

where P is % of distance over which the fade is exceeded
A is fade exceeded in dB
a and b are curve fit parameters in Table 1
for L-band and UHF frequencies.

Fig. 1 shows the cumulative fade distributions for path elevation angles of 30 and 45 at L-band and UHF.

Freq.(GHz)	Elevation = 30		Elevation = 45	
	a	b	a	b
0.870	34.52	1.855	31.64	2.464
1.5	33.19	1.710	39.95	2.321

Table 1: Parameters for best fit cumulative fade

distribution for multipath in mountainous terrain.

4.2 MULTIPATH IN A ROADSIDE TREE ENVIRONMENT

In the U.S.A., experiments conducted along tree-lined roads showed that multipath fading is relatively insensitive to path elevation over the range 30 to 60 . The following model was obtained assuming negligible shadowing:

$$P = U \exp(-VA) \quad \text{for } 1\% < P < 50\%$$

where P is % of distance over which fade is exceeded.

A is the fade exceeded in dB.

U and V are curve fit parameters in Table 2.

Fig. 2 shows the cumulative fade distributions for 1.5GHz (L-band) and 870MHz (UHF). Enhanced multipath fading can occur at lower elevation angles (5 to 30) where forward scattering from relatively smooth rolling terrain can be received from larger distances.

Freq. (GHz)	U	V	Fade Range (dB)
0.870	125.6	1.1160	1 - 4.5
1.500	127.7	0.8573	1 - 6.0

Table 2: Parameters for best exponential fit cumulative fade distributions for multipath for tree-lined roads.

5. REFERENCE

ITU-R Rec. PN 681: Propagation data required for the design of Earth-Space mobile telecommunication systems, 1993.

FIGURE 1

Best fit cumulative fade distributions for multipath fading in mountainous terrain

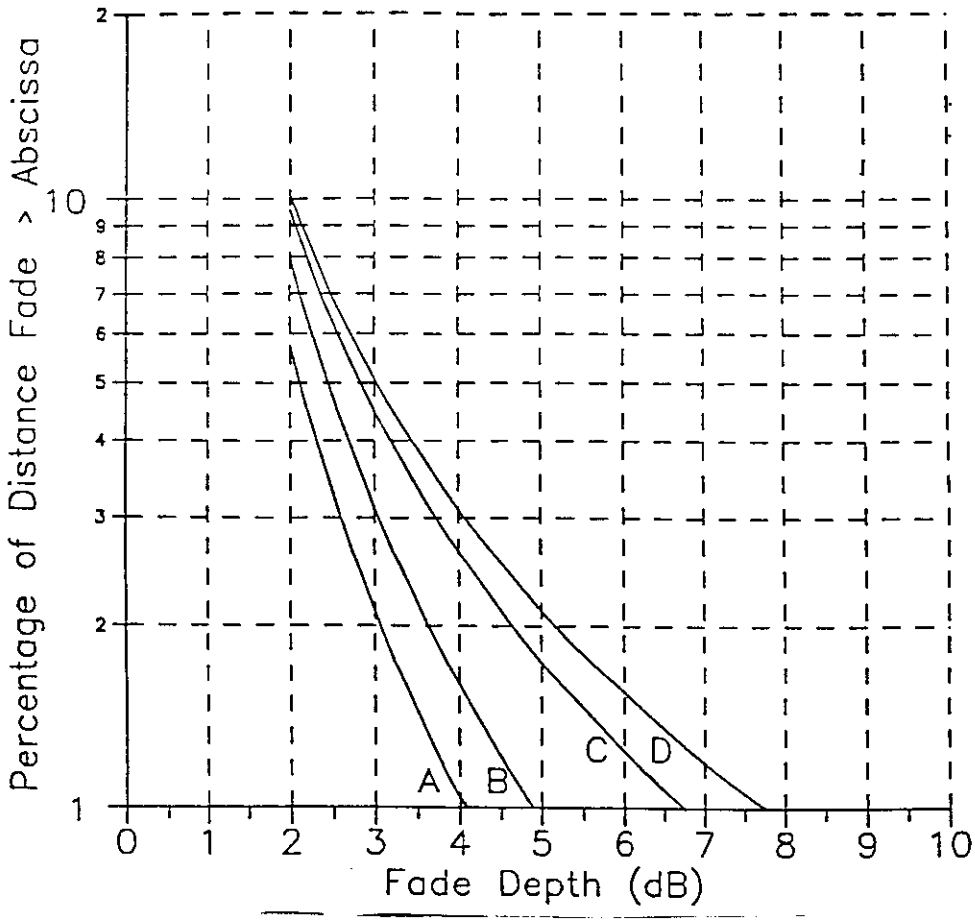

A: 870 MHz, 45 degrees
B: 1.5 GHz, 45 degrees
C: 870 MHz, 30 degrees
D: 1.5 GHz, 30 degrees

FIGURE 2

Best fit cumulative fade distributions for multipath fading on tree-lined roads

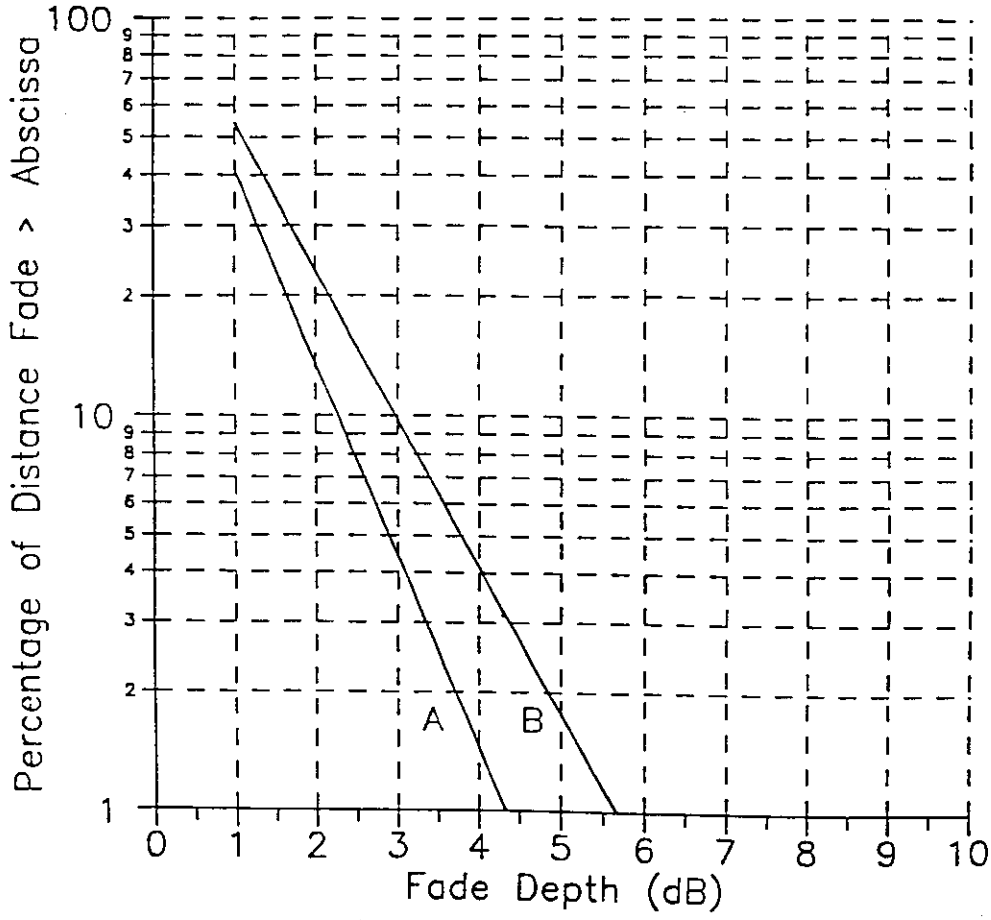

A: 870 MHz
B: 1.5 GHz

7a

SECTION C

EARTH-SPACE MARITIME MOBILE SATELLITE SYSTEMS (MMSS)

1. INTRODUCTION

Propagation problems are different from those of FSS due to

(i) effects of reflections and scattering by the sea surface, which can be severe for wide beamwidth antennas.

(ii) world-wide operation of maritime mobile-satellite systems, which may include paths of low elevation angles.

Sea-space radio path impairments include:

(i) tropospheric effects, including rain attenuation, gaseous absorption, refraction, scintillation and anomalous propagation occurring at low elevation angles;

(ii) ionospheric effects such as scintillation and Faraday rotation;

(iii) surface reflection effects (multipath due to secondary paths arising from the reflection of radio waves from the sea surface);

(iv) local environment effects (ship motion and sea conditions);

(v) interference effects due to differential fading between a desired signal and an interference signal, both affected by multipath fading.

Tropospheric (attenuation and scintillation) and ionospheric effects were treated in the FSS and are applicable to MMSS. The effects are similar to those of Land Mobile Satellite System.

2. FADING DUE TO SEA REFLECTION

2.1 Fading depth.

The following simple method provides approximate estimates of multipath power or fading depth suitable for many engineering applications.

Applicable conditions:

Frequency range: 1 - 2 GHz

elevation angle: $\theta_i \geq 3$, and $G(1.5\theta_i) \geq -10$ dB

where $G(\theta)$ is the antenna radiation pattern of the main lobe given by:

$$G(\theta) = -4 \times 10^{-4} \ (10^{Gm/10} - 1)\theta^2 \qquad \text{dB} \qquad (1)$$

where:

G_m: value of the maximum antenna gain (dB) and
θ: angle measured from boresight (degrees).

Polarization: circular and horizontal polarizations; vertical polarization for $\theta_i \geq 8$

Sea condition: wave height of 1 - 3m (incoherent component fully developed).

Step 1: Find the relative antenna gain G in the direction midway between the point of specular reflection and the horizon. The relative antenna gain is approximated by equation (1).
where $\theta = 1.5\ \theta_i$ (degrees).

Step 2: Calculate the Fresnel reflection coefficient of the sea:

$$R_H = \frac{\sin\theta_i - \sqrt{\eta - \cos^2\theta_i}}{\sin\theta_i + \sqrt{\eta - \cos^2\theta_i}} \quad (\textit{horizontal polarization}) \qquad (2a)$$

$$R_v = \frac{\sin\theta_i - \sqrt{(\eta - \cos^2\theta_i)/\eta^2}}{\sin\theta_i + \sqrt{\eta - \cos^2\theta_i)/\eta^2}} \quad (\textit{vertical polarization}) \qquad (2b)$$

$$R_c = \frac{R_H + R_v}{2} \quad (\textit{Circular polarization}) \qquad (2c)$$

$$\eta = \varepsilon_r(f) - j60\lambda\sigma(f)$$

where:

$\varepsilon_r(f)$: relative permittivity of the surface at frequency f
$\sigma(f)$: conductivity (S/m) of the surface at frequency f
λ: free space wavelength (m)

Step 3: Calculate the correction factor C_θ (dB):

$$C_\theta = 0 \qquad \text{for } \theta_i \geq 7 \tag{3}$$

$$= (\theta_i - 7)/2 \qquad \text{for } \theta_i < 7$$

Step 4: The mean incoherent power of sea reflected waves relative to the direct wave, P_r, is given by:

$$P_r = G + R + C_\theta \qquad \text{(dB)} \tag{4}$$

where:

$R = 20 \log | R_i |$, with $R_i = R_H$, R_V, or R_c from equation (2).

Step 5: Assuming the Nakagami-Rice distribution, fading depth is estimated from

$$A + 10 \log (1 + 10^{Pr/10}) \tag{5}$$

where:

A: amplitude (dB) read from the ordinate of Figure 1.

Fig. 2 shows the computed relationship between multipath power and elevation angle for different antenna gains.

3. INTERFERENCE FROM ADJACENT SATELLITE SYSTEMS

In mobile-satellite communication systems, amplitudes of the desired signal from the satellite and an interfering signal from an adjacent satellite experience independent level fluctuations due to multipath fading, requiring a different treatment from that of fixed-satellite systems. A main point to be considered is the statistics of differential fading, which is the difference between amplitudes of the direct wave and interference wave, both affected by multipath fading.

A practical prediction method for the statistics of signal-to-interference ratio where the effect of thermal noise and time-variant interference is taken into account is given in Appendix 1.

4. REFERENCE

ITU-R Rec. 680: Propagation Data required for the Design of Earth-Space Maritime Mobile Telecommunication Systems., 1992.

APPENDIX 1

Prediction Method for Interference from adjacent Satellite Systems

Prediction method

In general there are two kinds of interference between adjacent satellite systems. One is "down-link interference" on the mobile earth station side, and the other is "up-link interference" on the satellite side. Another situation is interference between beams in multi-spot-beam operation, where the same frequency is allocated repeatedly. The method is applicable to such cases.

Input parameters (in units of power, not dB) are:

D: power of the direct wave component of desired signal

M: average power of the reflected component (i.e. incoherent component) of desired signal

N: average power of system noise

I_D: power of the direct wave component of interference signal

I_M: average power of reflected component of interference signal

(I: average power of interference: $I = I_D + I_M$).

Output parameters (in units of power, not dB) are:

[c/n](p): ratio of desired signal power to system noise power as a function of time percentage p

[c/i](p): ratio of desired signal power to interfering signal power

[c/(i + n)](p): ratio of desired signal power to system noise plus interfering signal power.

Signal-to-noise ratio as a function of p is given by:

$$[c/n](p) = (\eta_c)^2(p)\ D/N \tag{6}$$

where η_c is the normalized time-percentage-dependent factor of desired signal power having a probability density function of a Nakagami-Rice distribution with constant direct power given in Figure 1, in which

$$20 \log \eta_c = A + 10 \log(D + M) \tag{7}$$

where A is amplitude (dB) read from the ordinate of Figure 1. The parameter in the figure for this application is M/(D + M).

The signal-to-interference ratio as a function of p is given by:

$$[c/i](p) = (\eta_{c/i})^2(p)\ D/I_{50} \tag{8}$$

where I_{50} is the median value (i.e. value for 50% of the time) of power variations of the interference signal:

$$I_{50} = (\eta_{i,50})^2\ I \tag{9}$$

and $\eta_{c/i}$ is the normalized time-percentage-dependent factor of [c/i] variations approximately given by:

$$\{\log \eta_{c/i}(p)\}^2 = \{\log \eta_c(p)\}^2 + \{\log \eta_i(100-p)\}^2 \tag{10}$$

where η_I is the normalized time-percentage-dependent factor of interference signal power. A solution where $\eta_{C/I} < 1$ should be selected for the time percentage satisfying $\eta_C <$ and $\eta_i > 1$. By setting $I_D/I = b$, $\eta_{I,50}$ and η_I (both in dB) as a function of b are given in Table I

Finally,

$$[c/(i + n)](p) = \{1/[c/n](p) + 1/[c/i](p)\}^{-1} \quad (11)$$

Prediction accuracy of the method for [c/i] and [c/(n+i)] is within 1 dB for all cases within the following parameter range:

$$N \leq -5 \text{ dB}; \quad M \leq -5 \text{ dB}; \quad I \leq -10 \text{ dB}; \quad 0.5 \leq b \leq 1 \quad (12)$$

where all quantities are relative to D.

TABLE I

Values of η_I and $\eta_{I,50}$ as functions of time percentage (p) and b [= $I_D/(I_D+I_M)$]

b	I_M/I_D (dB)	$\eta_{I,50}$ (dB)	η_I (dB)							
			P (%) 50	20	10	5	1	0.5	0.1	0.01
0	∞	−1.59	0.00	3.66	5.21	6.36	8.22	8.83	9.98	11.25
0.5	0	−1.12	0.00	3.16	4.48	5.44	7.03	7.54	8.52	9.60
0.6	−1.8	−0.91	0.00	2.88	4.09	4.99	6.46	6.95	7.87	8.90
0.7	−3.7	−0.68	0.00	2.53	3.62	4.43	5.78	6.22	7.08	8.03
0.8	−6.0	−0.45	0.00	2.10	3.03	3.72	4.90	5.30	6.07	6.92
0.9	−9.5	−0.22	0.00	1.52	2.21	2.76	3.69	4.00	4.62	5.32
0.95	−12.8	−0.11	0.00	1.09	1.61	2.02	2.74	2.99	3.48	4.02
1.0	−∞	0.00	0.00	0.00	0.00	0.00	0.00	0.00	0.00	0.00

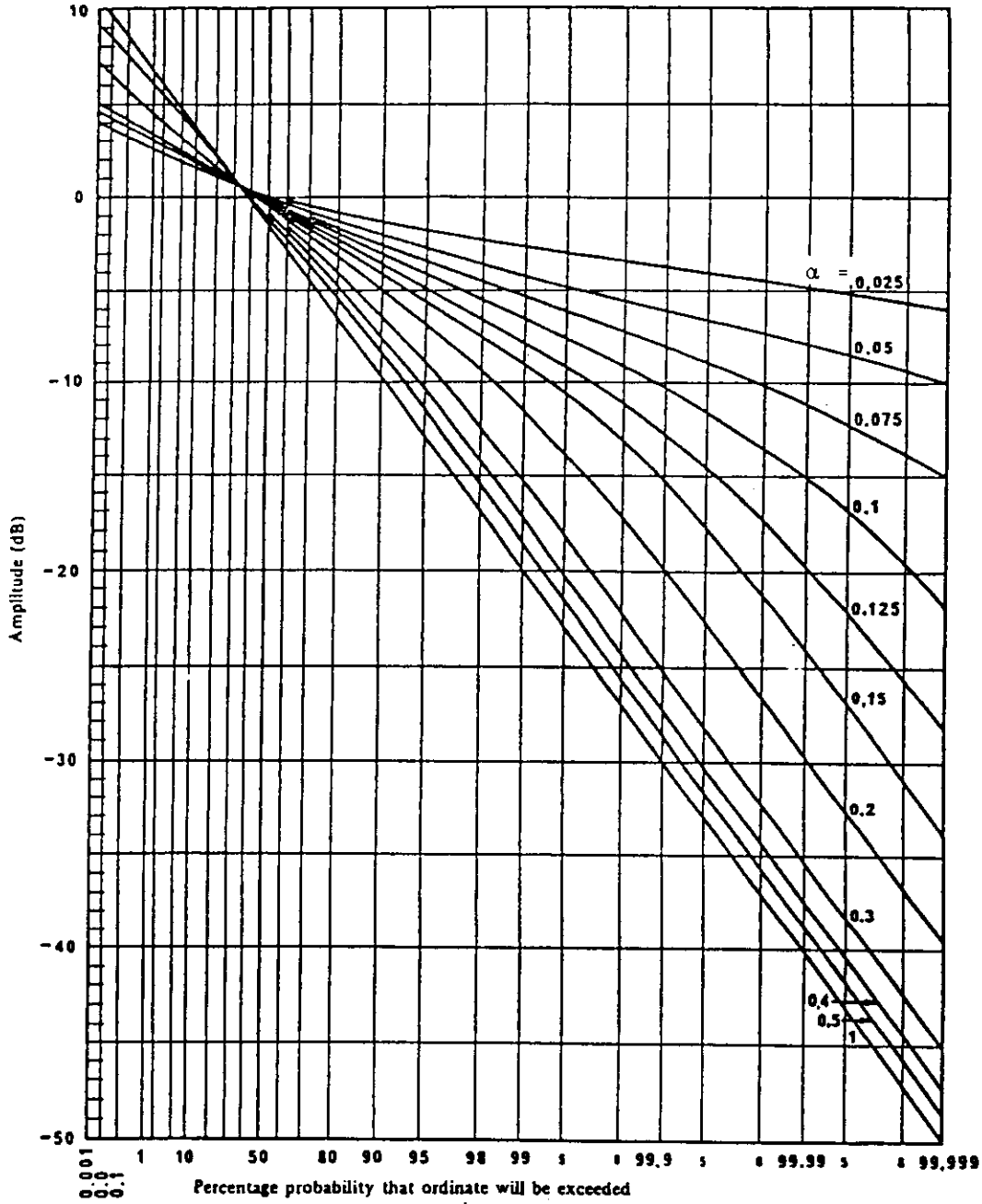

FIGURE 1

Nakagami-Rice distribution for a constant total power
(with the fraction $\alpha = \frac{\text{multipath power}}{\text{total power}}$ as parameter

For this case, $\alpha = \frac{10^{P_r/10}}{1 + 10^{P_r/10}}$

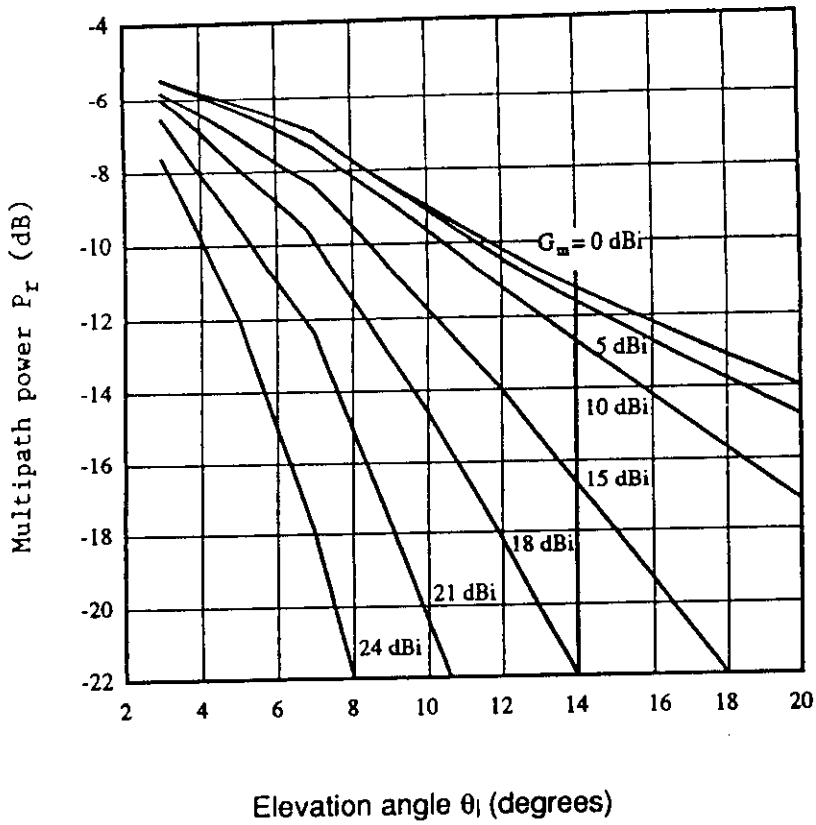

FIGURE 2

Multipath power relative to direct signal power as a function of elevation angle calculated by the prediction method

Frequency = 1.5 GHz

Circular polarization

SECTION D

AERONAUTICAL MOBILE - SATELLITE SYSTEMS (AMSS)

1. INTRODUCTION

Characteristics differ from FSS and LMSS because:

(i) small antennas are used on aircraft, and the aircraft body may affect the performance of the antenna;

(ii) high aircraft speeds cause large Doppler spreads;

(iii) aircraft terminals must accommodate a large dynamic range in transmission and reception;

(iv) aircraft safety considerations require a high integrity of communications, making even short-term propagation impairments very important, and communications reliability must be maintained in spite of banking manoeuvres and three-dimensional operations.

The path impairments are due to factors including:

(i) tropospheric effects, including gaseous attenuation, cloud and rain attenuation, fog attenuation, refraction and scintillation;

(ii) ionospheric effects such as scintillation;

(iii) surface reflection (multipath) effects;

(iv) environmental effects (aircraft motion, sea state, land surface type).

Frequencies near 1.5GHz are of current interest for AMSS.

2. TROPOSPHERIC EFFECTS

The altitude of the mobile antenna becomes an important parameter. Tropospheric attenuation can be estimated as for the FSS.

The received signal may be affected both by larger scale refraction and by scintillations induced by atmospheric turbulence. These effects will diminish for aircraft at high altitudes.

3. IONOSPHERIC EFFECTS

Important for slant paths at $f < 10$GHz, especially within 15° of the geomagnetic equator, but to a lesser extent within the auroral zones and polar caps. Ionospheric effects peak near the

solar sunspot maximum.

At typical aircraft altitudes, the ionospheric impairments will still be as in Table 1 of Part 2 which is applicable to mobile satellite systems.

For most mobile-satellite communication signals (f < 2GHz) the most severe impairment will probably be ionospheric scintillation.

4. FADING DUE TO SURFACE REFLECTION AND SCATTERING

The aeronautical mobile satellite systems differ from other mobile systems due to the speeds and altitudes of aircraft.

The procedure for Maritime Mobile Satellite System can be adopted if earth sphericity is taken into consideration, especially for increasing antenna altitude above the reflecting surface.

4.1 Dependence on Antenna Height and Antenna Gain

The following engineering approximation based on a simple model provides estimates of multipath power or fading depth due to sea surface reflections.

Applicable range:

Frequency: 1 - 2 GHz
Elevation angle: $\theta_i \geq 3$, and $G(1.5\theta_i) \geq -10$ dB

where $G(\theta)$ is the main-lobe antenna pattern given by:

$$G(\theta) = -4 \times 10^{-4} (10G_m/10 - 1) \theta^2 \quad (1)$$

G_m: value of the maximum antenna gain (dB)

θ: angle measured from boresight (degrees).

Polarization: circular and horizontal polarizations; vertical polarization for $\theta_i \geq 8$

Sea condition: wave height of 1 - 3 m (incoherent component fully developed).

Step 1: Calculate the grazing angles of the specular reflection point (θ_{sp}) and the horizon (θ_{hr}) by

$$\theta_{sp} = 2\gamma_{sp} + \theta_i \quad \text{degrees} \quad (2a)$$

$$\theta_{hr} = \cos^{-1} \{R_e/(R_e + H_a)\} \quad (2b)$$

(R_e: radius of the Earth = 6371 km)

where:

$\gamma_{sp} = 7.2 \times 10^{-3} H_a/\tan\theta_i$ (H_a:antenna height in km)

Step 2: Find the relative antenna gain G in the direction midway between the specular point and the horizon. The relative antenna gain is approximated by equation (1) where $\theta = \theta_i + (\theta_{sp} + \theta_{hr})/2$ (degrees).

Step 3: Calculate the Fresnel reflection coefficient of the sea:

$$R_H = \frac{\sin\theta_i - \sqrt{\eta - \cos^2\theta_i}}{\sin\theta_i + \sqrt{\eta - \cos^2\theta_i}} \quad (horizontal\ polarization) \qquad (3a)$$

$$R_v = \frac{\sin\theta_i - \sqrt{(\eta - \cos^2\theta_i)/\eta^2}}{\sin\theta_i + \sqrt{(\eta - \cos^2\theta_i)/\eta^2}} \quad (vertical\ polarization) \qquad (3b)$$

$$R_c = \frac{R_H + R_v}{2} \quad (circular\ polarization) \qquad (3c)$$

$\eta = \varepsilon_r(f) - j60\lambda\sigma(f)$

where:

$\varepsilon_r(f)$: relative permittivity of the surface at frequency f.
$\sigma(f)$: conductivity (S/m) of the surface at frequency f.
λ: free space wavelength (m)

Step 4: Calculate the correction factor C_θ (dB):

$$C_\theta = 0 \quad \text{for } \theta_{sp} \geq 7 \qquad (4)$$

$$= (\theta_{sp} - 7)/2 \quad \text{for } \theta_{sp} < 7$$

Step 5: Calculate the divergence factor D (dB) due to the Earth's curvature:

$$D = -10 \log \left[1 + \frac{2 \sin\gamma_{sp}}{\cos\theta_{sp} \sin(\gamma_{sp} + \theta_i)} \right] \qquad (5)$$

Step 6: the mean incoherent power of sea reflected waves, relative to the direct wave, P_r, is given by:

$$P_r = G + R + C_\theta + D \qquad \text{dB} \qquad (6)$$

where:

$$R = 20 \log |R_i|$$

with $R_i = R_H$, R_v or R_c from equations (3).

Step 7: Assuming the Nakagami-Rice distribution, fading depth is estimated from:

$$A + 10 \log (1 + 10^{Pr/10}) \qquad (7)$$

where A is the amplitude (dB) read from the ordinate of Figure 1.

Figure 2 shows the mean multipath power of the incoherent component obtained by the above method as a function of the elevation angle for different gains. By comparing with the case of maritime mobile-satellite systems (Figure 2) it can be seen that the reflected wave power P_r for aeronautical mobile-satellite systems is reduced by 1 to 3 dB at low elevation angles.

4.2 Delay Time and Correlation Bandwidth

Due to the propagation delay between the direct and the reflected wave, the received signal may be subject to frequency-selective fading. Signal correlation decreases with increasing frequency separation. For gains below 15dB, the dependence of correlation on the antenna gain is small. Fig. 3 shows the relationship between antenna height and the correlation bandwidth, defined as the frequency separation for which the correlation coefficient between two radio waves equals 1/e. In Fig.3, at an altitude of 10km, the correlation bandwidth decreases to about 10 to 20 kHz (delay time of about 6 to 12μsec.).

Fig. 4 shows measured normalized oceanic multipath power against elevation angle at 1.6 GHz.

5. REFERENCE

1. CCIR-DOC. 5/BL/20-E: Recommendation 682, Propagation Data Required for the Design of Earth-Space Aeronautical Mobile Telecommunication Systems, 1992.

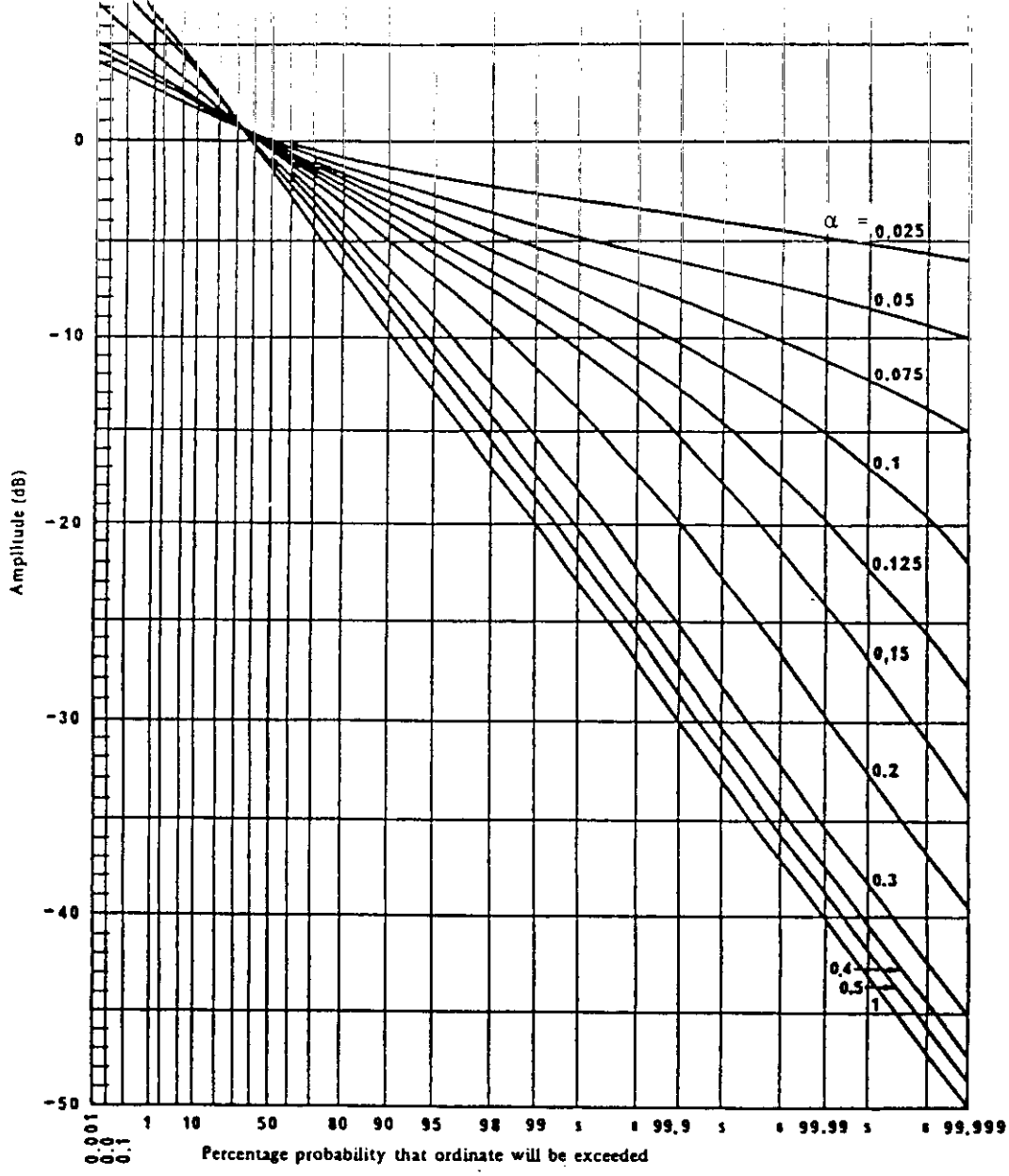

FIGURE 1

Nakagami-Rice distribution for a constant total power

(with the fraction $\alpha = \frac{\text{multipath power}}{\text{total power}}$ as parameter

For this case, $\alpha = \frac{10^{P_r/10}}{1 + 10^{P_r/10}}$

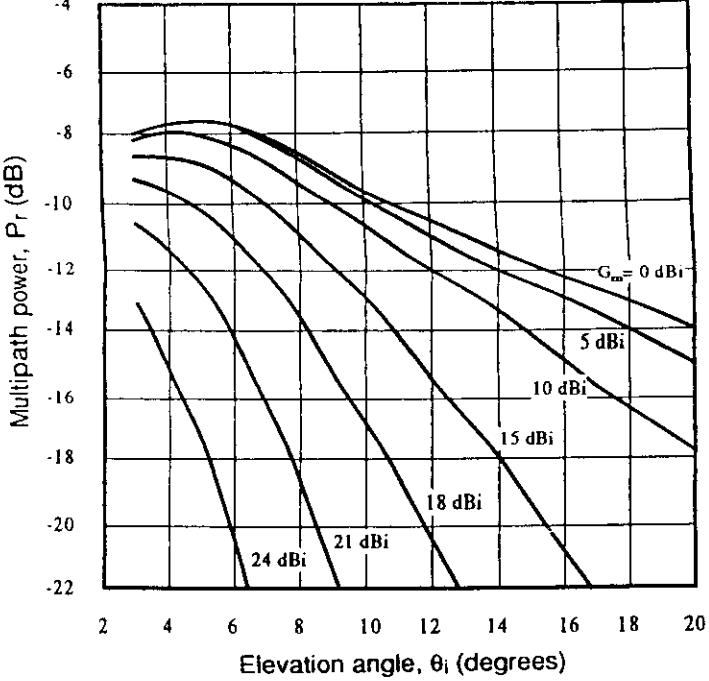

FIGURE 2

Mean multipath power relative to direct signal power as a function of elevation angle for different antenna gains

Frequency = 1.54 GHz
Circular polarization
H_a = 10 km

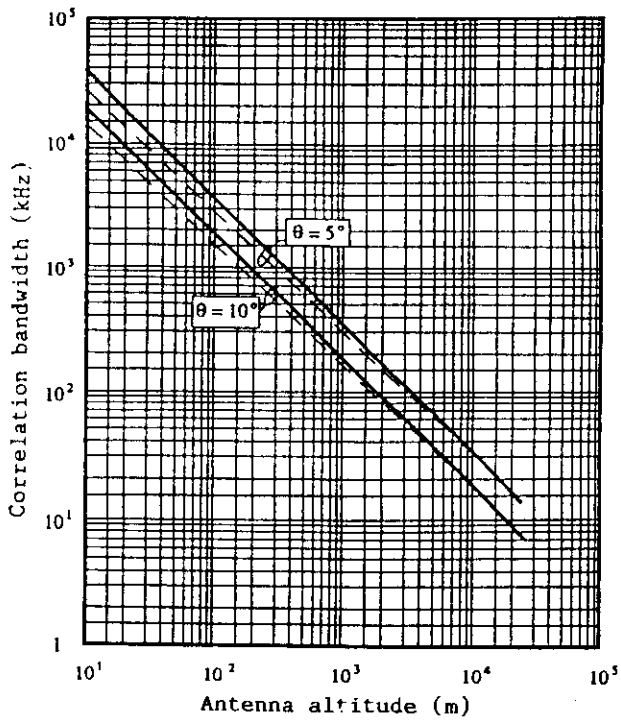

FIGURE 3

Correlation bandwidth vs antenna altitude for antenna gain of 10 dBi

——— coherent component
— — — incoherent component (rough sea conditions)
G_m = 10 dBi

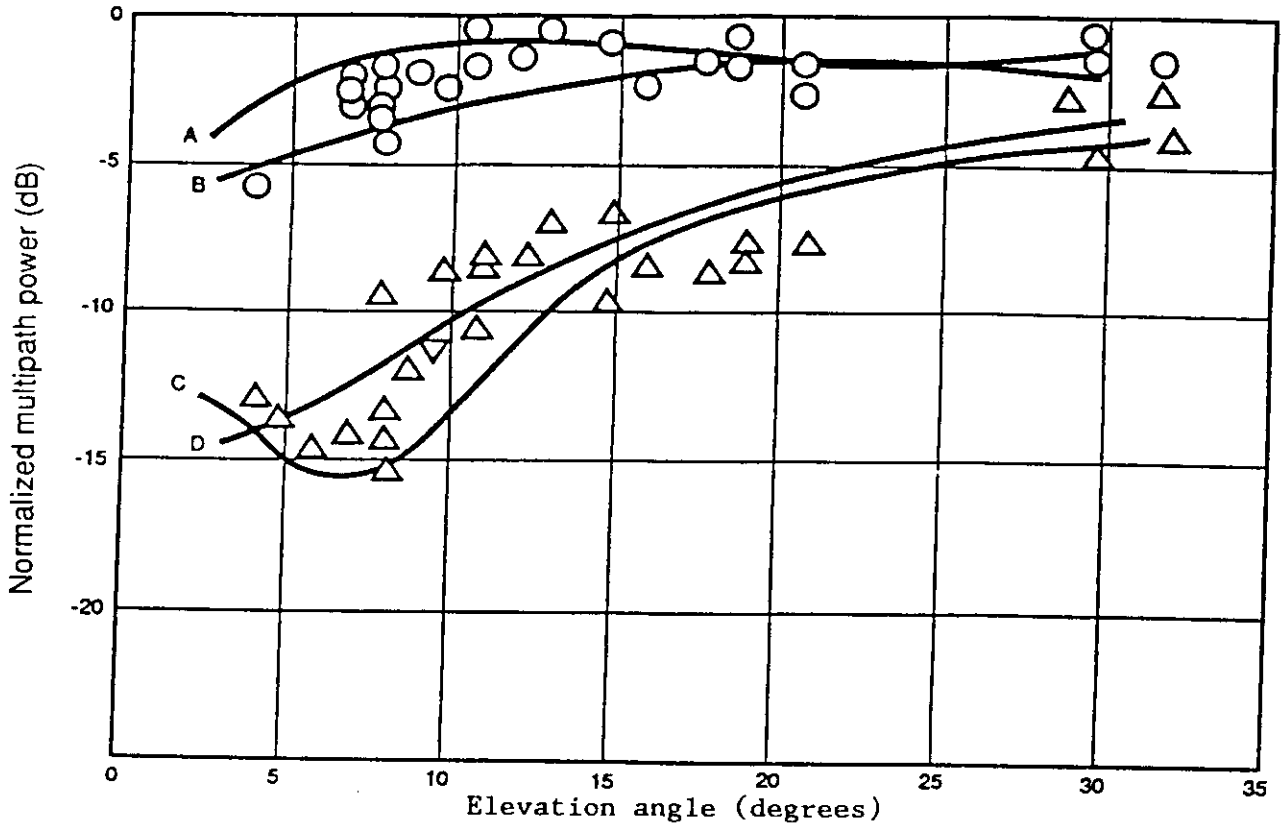

FIGURE 4

Oceanic normalized multipath power vs elevation angle at 1.6 GHz

○ horizontal polarization measurements
△ vertical polarization measurements

A: horizontal polarization prediction, calm sea
B: horizontal polarization prediction, rough sea
C: vertical polarization prediction, calm sea
D: vertical polarization prediction, rough sea

INTERNATIONAL ATOMIC ENERGY AGENCY

AND

UNITED NATIONS EDUCATIONAL SCIENTIFIC AND CULTURAL ORGANIZATION

INTERNATIONAL CENTRE FOR THEORETICAL PHYSICS

CLIMATIC INFORMATION FOR SATELLITE COMMUNICATION PLANNING.

PART VI: LOW AVAILABILITY SYSTEM (LAS)

Prof. G.O. Ajayi
Department of Electronic & Electrical Engineering
Obafemi Awolowo University,
Ile-Ife, Nigeria.

FOURTH ICTP-URSI-ITU (BDT) COLLEGE ON RADIOPROPAGATION:
Propagation, Informatics and Radiocommunication System Planning.

30 January - 3 March, 1995.

LOW AVAILABILITY SYSTEMS (LAS)

1. INTRODUCTION

High availability of about 99.99% is required for the conventional satellite communication systems, currently utilising C(6/4 GHz), Ku (14/11-12 GHz) and Ka (30/20 GHz) frequency bands. The availability of larger bandwidths has made the use of higher frequency bands attractive, especially in the light of the new competitors such as optical fibres. The use of higher frequencies offers advantage of small size and higher EIRP. However, at Ka, Q and V bands, the attenuation due to rain and other agents become excessive and it is no longer practical to provide the necessary fade margin required to maintain the conventional availability of 99.99%.

The low availability systems have been developed to provide availability of the order of 90-99% adequate for some services using the Ka, Q and V bands. The clear sky effects contribute a major part to the propagation impairment. The propagation factors to be considered include the non-rainy atmosphere, light rain, clouds and gases.

The future trends of satellite communication are for

(i) Use of higher bands: 40, 50, 90 GHz. Necessitating consideration for new atmospheric parameters.

(ii) Small terminals 30 - 90 cm antennas for

- (a) Commercial
- (b) Direct Broadcast (HDTV)
- (c) Low availability systems

(iii) High capacity systems utilizing up-link power control and non-conventional techniques.

(iv) Flexible systems such as:

- (a) On-board management
- (b) Large scale diversity.

2. FEATURES OF LAS

The services provided, include:

(i) data transmission
(ii) reduced availability telephony
(iii) dissemination of news
(iv) education
(v) electronic mail
(vi) business and commerce
(vii) emergency
(viii) medical

(ix) data relay systems (DRS).

The advantages include:

Transportability, flexibility and limited dimension and costs.

The disadvantages include:

Low fade margin (≤ 10dB)
Reduced availability 90 - 99%
Low priority

Some of the technical specifications are:

Antenna diameter:	0.3m - 2m
Power:	1 - 5 Watts
Frequency bands:	14/12, 30/20, 50/40 GHz
Configuration:	Star/Hub network for VSAT/USAT.

Meteorological factors affecting LAS are:

(i) Light rain (1 - 10% of time)
(ii) Clouds (20 - 80% of time)
(iii) Water Vapour (10 - 100% of time)
(iv) Oxygen (100% of time)

3. VSAT (VERY SMALL APERTURE TERMINAL)

VSAT is a low cost satellite terminal with a small antenna aperture, from 0.6 to 2.4m. VSATs usually operate in a star network topology with a hub at the centre. Typical VSAT star network topology is shown in Fig. 1, while VSAT network configurations are shown in Figs. 2(a) and (b). Although VSAT systems operate both in the 6/4 GHz and 14/12 GHz bands, the latter is preferred because higher power satellite EIRPs are permitted.

The hub compensates for the modest performance of the distant-end VSAT terminals.

VSATs have comparatively low G/Ts and EIRPs. The Hub has higher G/Ts and EIRPs as shown in Tables 1 A, B, C, D.

Some features of VSAT are:

(i) It is more cost-effective for data link connectivity than the conventional connectivity through the PSTN. The VSAT bypasses the PSTN.

(ii) VSAT can offer better performance in BER and availability than PSTN counterpart.

3.1 Applications

(i) Credit card verification
(ii) Banks
(iii) E-mail
(iv) Reservations: hotel, airline, car rental, etc.
(v) Telemetry and Control
(vi) Data Relay Systems.

3.2 Data Rate

VSAT to hub data rate varies from 600 bps to 64 kbps using random access TDMA.

Higher data rates are utilised for Hub to VSAT ranging from 64 - 256 kbps.

3.3 Rainfall Rate Statistics

Fig. 3 shows the ITU-R climatic zones approximate rainfall rate statistics for higher time percentages, illustrating typical VSAT outage range. Table 2 shows the % of time when the rainfall rate in the various CCIR climatic zones is zero.

CCIR Rain Zone	P_o (%)
A, B	2
C, D, E	3
F, G, H, J, K	5
L, M	7.5
N. P. Q*	10

*The new climate, Q, has yet to be assigned to this table by the CCIR, but is similar to climate P.

4. EARTH-SATELLITE LINK ATTENUATION PREDICTION FOR LAS

Availability 90 - 99% for frequencies ≥ 20 GHz.

Fade Margin ≤ 10 dB.

Impairment effects up to about 1% of the year can be disregarded as the LAS can be considered as blind during such period.

Atmospheric factors occurring for 1 - 10% of time to be considered are: light rains, clouds, water vapour, oxygen and clear air scintillations.

Salonen et al. (1992) considered predictions at 20 and 30GHz for

LAS (90% to 99% availability) taking into consideration the effects of cloud, water vapour, melting zone and scintillation effects along with rainfall. Fading components were added on equi-probability basis, which may not be adequate for all processes.

Watson and Hu, 1994 proposed an improvement on the prediction technique as follows:

The various fading processes for LAS can neither be regarded as entirely correlated or completely independent. Table 3 shows the combination of fading processes, as used by Watson and Hu.

The rain and non-rain processes are modelled as two disjoint sets, adding exceedances.

Table 3: Combination of Fading Processes

Rain processes	rain attenuation melting zone saturated water vapour (up to rain height) rain - cloud	added on an equi-probability basis	added as disjoint variables
Non-rain processes	cloud scintillation water vapour	added on an equi-probability basis	(adding exceedances for equal fade thresholds)

The two main parts to the total fading model are:

(i) rain-fading component
(ii) non-rain fading component.

$$P(A_T > a) = P\ (A_{non\text{-}rain} > a) + P(A_{rain} > a)$$

where A_T = Total attenuation

The non-rain component consists of attenuation due to water vapour, cloud and scintillation. Their effects are combined on equiprobable basis. Under non-rainy conditions, $A_T(P)$ is given by:

$$A_T(P) = A_{wv}(P) + A_{cloud}(P) + A_{scint}(P)$$

where A_{wv} = attenuation due to water vapour.

$$P = P(A_{non\text{-}rain} > a)$$

The improvement of the model described by Watson and Hu is based on the following:

(i) Rain and non-rain fading processes are combined as disjoint processes instead of adding equi-probability attenuations.

(ii) The vertical on-average profile of rain specific attenuation is taken into consideration.

(iii) The differing frequency dependencies of melting zone and rain components of attenuation are included.

(iv) Contributions from widespread and showery rain are included separately.

4.1 Absorption by the Non-rainy Atmosphere

The non-rainy "wet" atmospheric absorption is due to gases and small water droplets ($d < 50\mu m$).
Gases are oxygen and water vapour.
In the absence of water droplets, we have clear atmosphere due to gases only.
Oxygen absorption depends only on temperature and pressure and its calculation is simple up to about 50GHz. The microwave absorption spectrum of oxygen has a complex resonance around 60GHz, extending in range between 50 - 69 GHz and an isolated weaker line at 118.75 GHz.

Water vapour absorption resonance peaks occur at 22.235, 183.31, 325.4 GHz extending into the IR region.

The total atmospheric attenuation, A is given by

$$A = A_o + A_v + A_L$$

where A_o, A_v and A_L are attenuations due to oxygen, water vapour and liquid water respectively.

Barbaliscia et al 1993 used radiosonde data to obtain the latitudinal variation of total water vapour (mm) (Fig. 4) and the total liquid water (mm) employing the Salonen and Decker models (Figs. 5(a) and (b) respectively). Barbaliscia et al 1993 also computed the total clear sky attenuation (clouds i.e. liquid water not included) using radiosonde data as shown in Figs. 6(a) & (b) for temperate and tropical climates respectively. Comparison with dual channel radiometric measurements at 23.8 and 31.7 GHz seem encouraging.

4.2 Estimation of Atmospheric Water Contents

Liquid and water vapour contents can be obtained indirectly from a radiometer at 20 and 30 GHz by separating the two water phases.

The attenuation A measured by a radiometer and the two total heights V and L are related as:

$$A = A_o + a_v V + a_L L$$

where

V, L:	integrated vapour and water contents along the path (mm).
a_v, a_L:	mass absorption coefficients (dB/mm)
A_o :	attenuation due to oxygen (dB)

a_v and a_L are calculated for various frequencies for the main climatic regions using 10 years of radiosonde data and existing models.

A_o is total zenith attenuation and can be corrected for the slant path using the cosecant law.

V and L are available on a statistical basis using radiosonde soundings for world regions.

V and L can be obtained from radiometric data at appropriate frequencies.

For radiometric measurements at f_1 and f_2:

$$A_1 = A_{o1} + a_{v1} V + a_{L1} L$$

$$A_2 = A_{o2} + a_{v2} V + a_{L2} L$$

One frequency is more sensitive to the vapour and the other to the liquid.

The 20GHz band is usually selected for the vapour and the 31-36GHz window for the liquid.

V and L can be obtained by inversion as

$$V = C_{ov} + C_{1v} A_1 + C_{2v} A_2$$

$$L = C_{oL} + C_{1L} A_1 + C_{2L} A_2$$

where the C_{ij} : Inversion coefficients.

Figs 7 (a) & (b) (Barbaliscia) show the latitudinal variation of total water vapour content and total liquid content respectively.

4.3 Light Rain Attenuation

In LAS, the effect of light rain becomes important. The physical structure of light rain (about 5 - 10 mm/h) and drizzle

(about 1mm/h) differs from those of the heavy rainfalls that are considered for high availability systems. The light rain is usually widespread with large horizontal extent and a more predictable vertical structure.

Two approaches can be considered:

(i) Probability P(R > r) of exceeding rainfall rate r, which gives the outage time of the station.

(ii) The rain level R(P) exceeded for a given % of time P, which in effect represents the fade margin to be given to the system for required availability.

Various techniques are available for evaluating R exceeded for 1 - 10% of the time for example the ITU-R scaling, Rice-Holmberg/Dutton and Dougherty (R-H/DD) method using long term rain data and direct measurement.

5. REFERENCES

1. BarbalisciaF., M. Boumis and J. P. V. Poiares Bapista: Propagation modelling of non-rainy atmosphere by means of radiosonde data. FUB Report ID 02693., Proc. of Int. Symp. on Radio Propagation, Pechino, August 1993, pp. 214-217.

2. Dutton, E. J., H. T. Dougherty and R. F. Martin: Prediction of European rainfall and link performance coefficients at 8 to 30GCHz, Tech. Report ACC-ACO-16-74, Institute for Telecomm. Sc., U. S. A., Aug. 1974.

3. Rice, P. L. and N. R. Holmberg: Cumulative time statistics of surface point rainfall rates, IEEE Trans. Comms., COM-21 (10) 1973, 1131, 1131-1136.

4. Salonen, E., S. Karhu, P. Jokela, W. Zhang, S. Uppala, H. Aulamo, S. Sarkkula, and J. P. V. Poiares Bapista: Modelling and Calculation of atmospheric attenuation for low-fade-margin in satellite communications, ESA Journal 1992, 16, 3, pp. 299-317.

5. Watson, P. A. and Y. F. Hu: Prediction of attenuation on satellite-Earth links for systems operating with low fade margins, CLIMPARA '94, Moscow, June 1994, 12.2.1-12.2.6.

Table 1 A Some typical VSAT G/T values

Antenna Aperture		Antenna Gains		G/T Values	
(m)	(ft)	G_4 (dB)	G_{12} (dB)	G/T_4	G/T_{12}
1.2	3.94	31.85	41.39	+9.0 dB/K	+15.5 dB/K
1.5	4.92	33.78	43.32	+11.0 dB/K	+17.5 dB/K
1.8	5.90	35.36	44.90	+12.56 dB/K	+19.1 dB/K
2.0	6.56	36.28	45.82	+13.5 dB/K	+20.0 dB/K
2.4	7.87	37.86	47.40	+15.1 dB/K	+21.6 dB/K

[a] *Assumptions*: Transmission line losses: 1 dB
Sky noise: 15 K at 4 GHz; 180 K at 12 GHz
Receiver noise temperature: 80 K at 4 GHz; 180 K at 12 GHz

Table 1 B VSAT hub G/T values[a]

Antenna Aperture		Antenna Gains		G/T Values	
(m)	(ft)	G_4 (dB)	G_{12}	G/T_4	G/T_{12}
6	19.7	45.82	55.37	+21.1 dB/K	+29.3 dB/K
7	23.0	47.17	56.71	+22.5 dB/K	+30.7 dB/K
8	26.25	48.32	57.86	+23.6 dB/K	+31.9 dB/K
9	29.52	49.34	58.9	+24.6 dB/K	+32.9 dB/K
10	32.81	50.26	59.8	+25.6 dB/K	+33.8 dB/K

[a] *Assumptions*: Transmission line losses: 2 dB
Sky noise: 15 K at 4 GHz; 30 K at 12 GHz
Receiver noise temperature 75 K at 4 GHz; 120 K at 12 GHz

Table 1 C VSAT EIRP values[a]

Antenna Aperture		Antenna Gains (dB)		$EIRP_6$ (dBW)	$EIRP_{14}$ (dBW)
(m)	(ft)	G_6	G_{14}		
1.2	3.94	35.37	42.73	+37	+44
1.5	4.92	37.3	44.66	+39	+47
1.8	5.9	38.88	46.23	+41	+48
2.0	6.56	39.8	47.15	+42	+49
2.4	7.37	41.38	48.74	+43	+51

[a] *Assumptions*: Transmission line losses: 1 dB
Transmitter power output: 2 W (+3 dBW)

Table 1 D VSAT hub EIRP values[a,b]

Antenna Aperture		Antenna Gains (dB)		$EIRP_6$ (dBW)	$EIRP_{14}$ (dBW)
(m)	(ft)	G_6	G_{14}		
6	19.7	49.35	56.71	+74.35	+81.71
7	23.0	50.69	58.1	+75.69	+83.1
8	26.23	51.84	59.2	+76.84	+84.2
9	29.52	52.86	60.2	+77.86	+85.2
10	32.81	53.78	61.1	+78.78	+86.1

[a] *Assumptions*: Transmission line losses: 2 dB
Transmitter power output: 500 W (+27 dBW)
Antenna aperture efficiency: 60%
[b] If a VSAT hub terminal were to have 1-kW transmitter power output, then add 3 dB to the appropriate EIRP value.

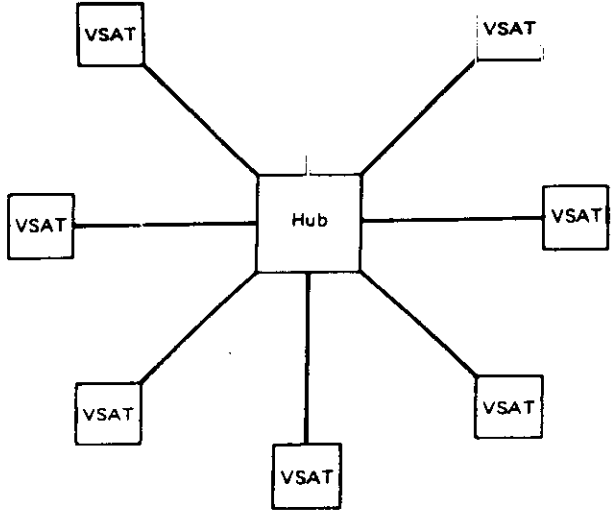

Figure 1 : VSAT star network topology.

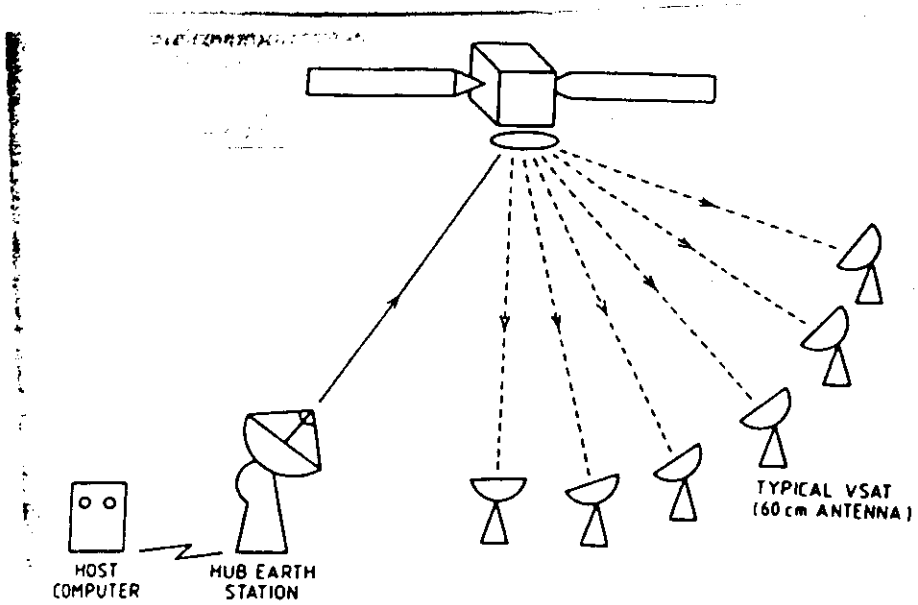

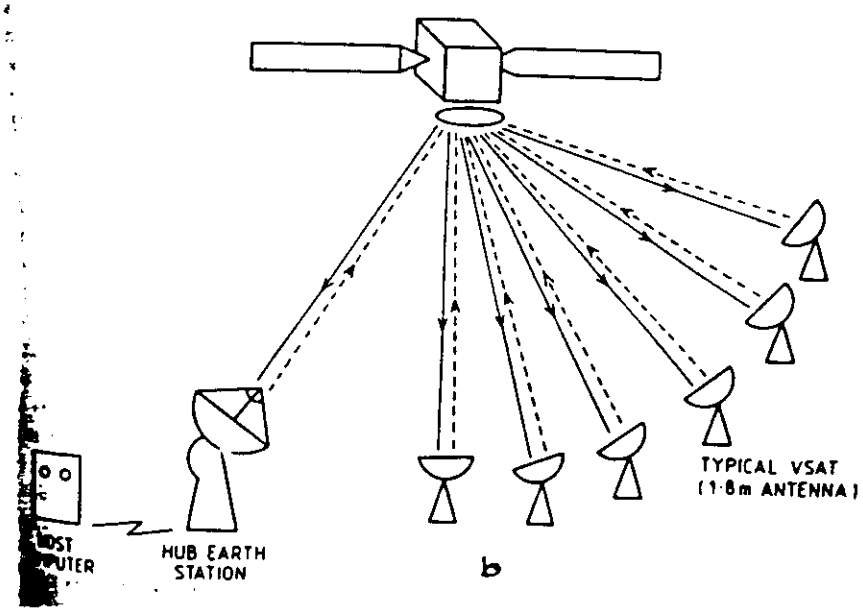

Fig. 2: VSAT Configuration.

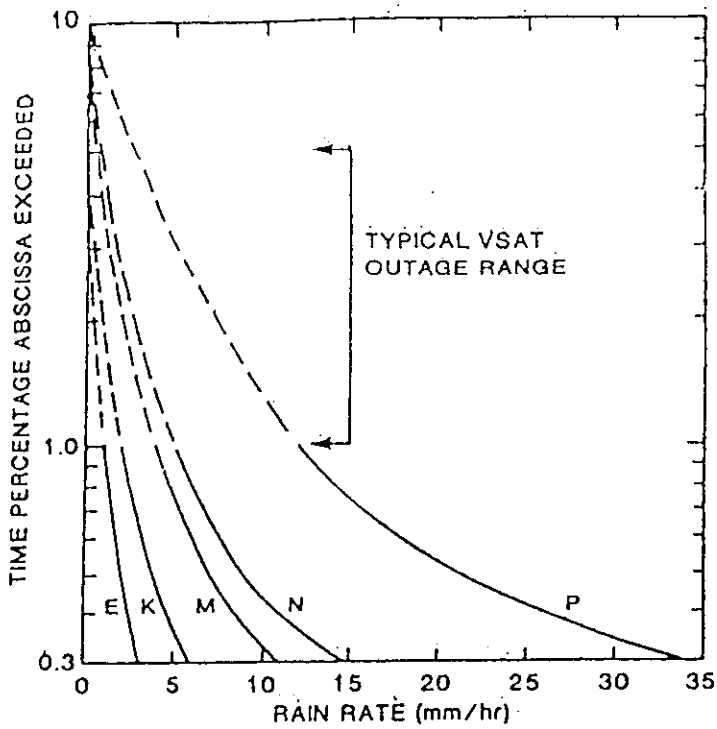

Fig. 3: Approximate rain rate statistics for several ITU-R rain climate zones

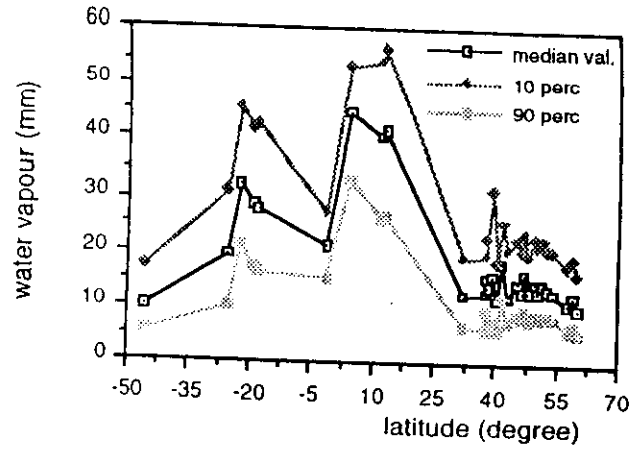

Fig. 4 - Total water vapour content versus latitude.

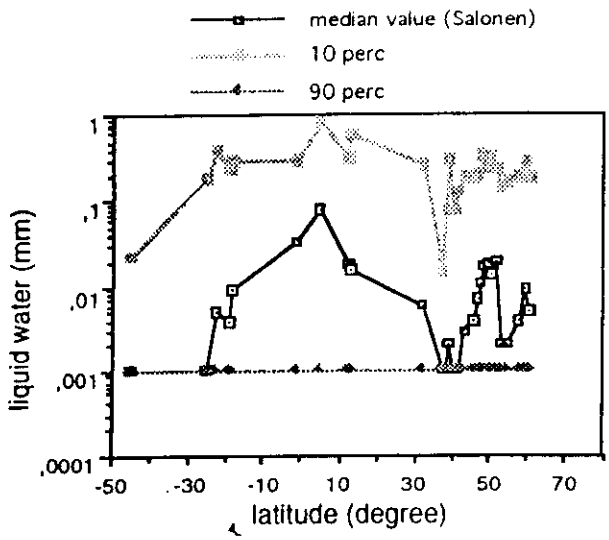

Fig. 5(a): Total liquid water content vs latitude (Salonen).

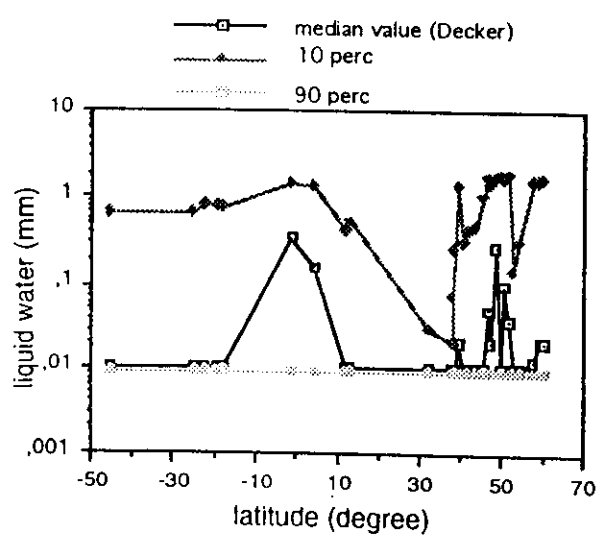

Fig. 5(b): Total liquid water content vs latitude (Decker).

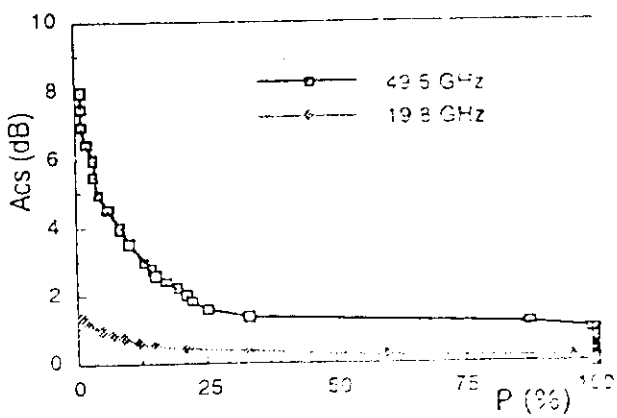

Fig. 6(a): Average CD of clear sky attenuation for two frequencies for temperate climates.

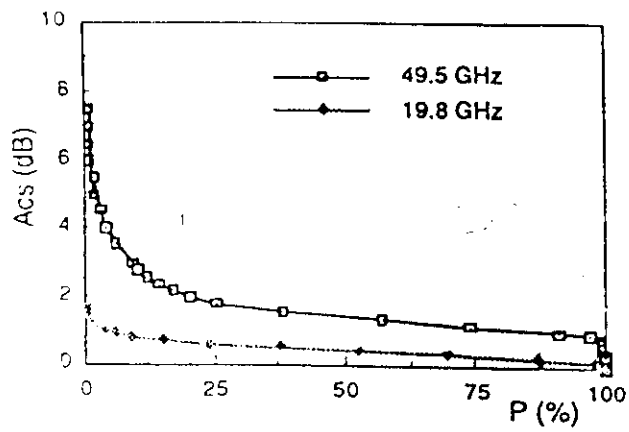

Fig. 6(b): Average CD of clear sky attenuation for two frequencies for tropical climates.

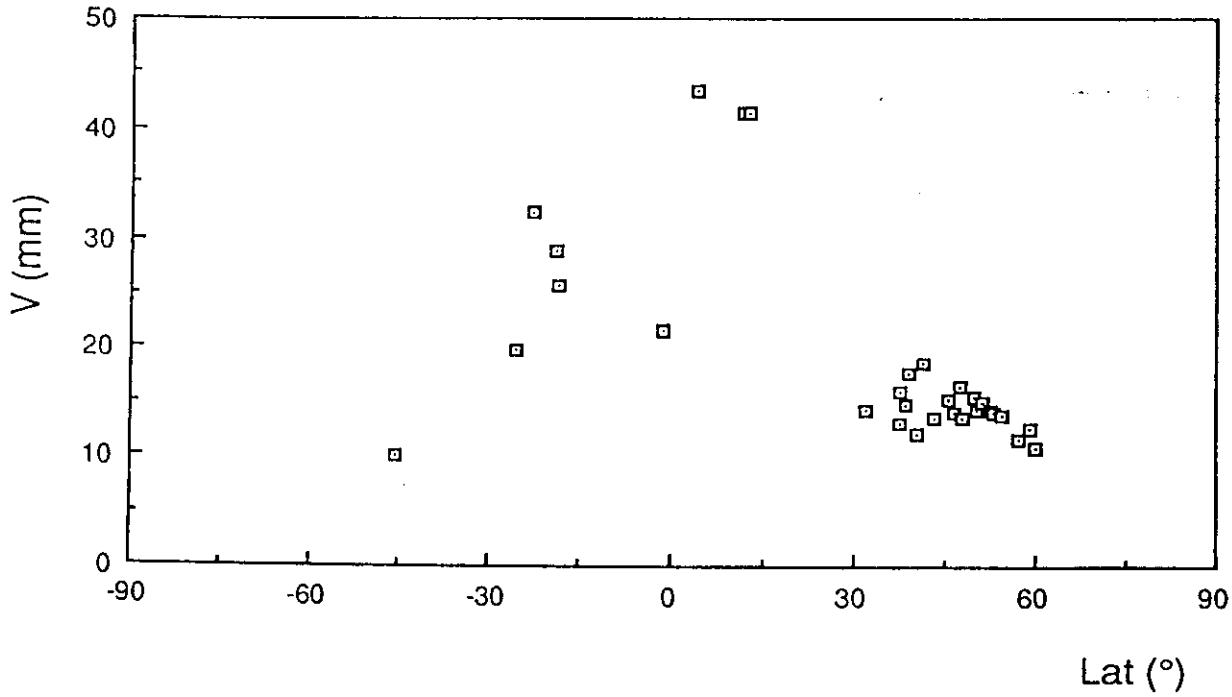

Fig. 7(a): Total water vapour content as a function of latitude

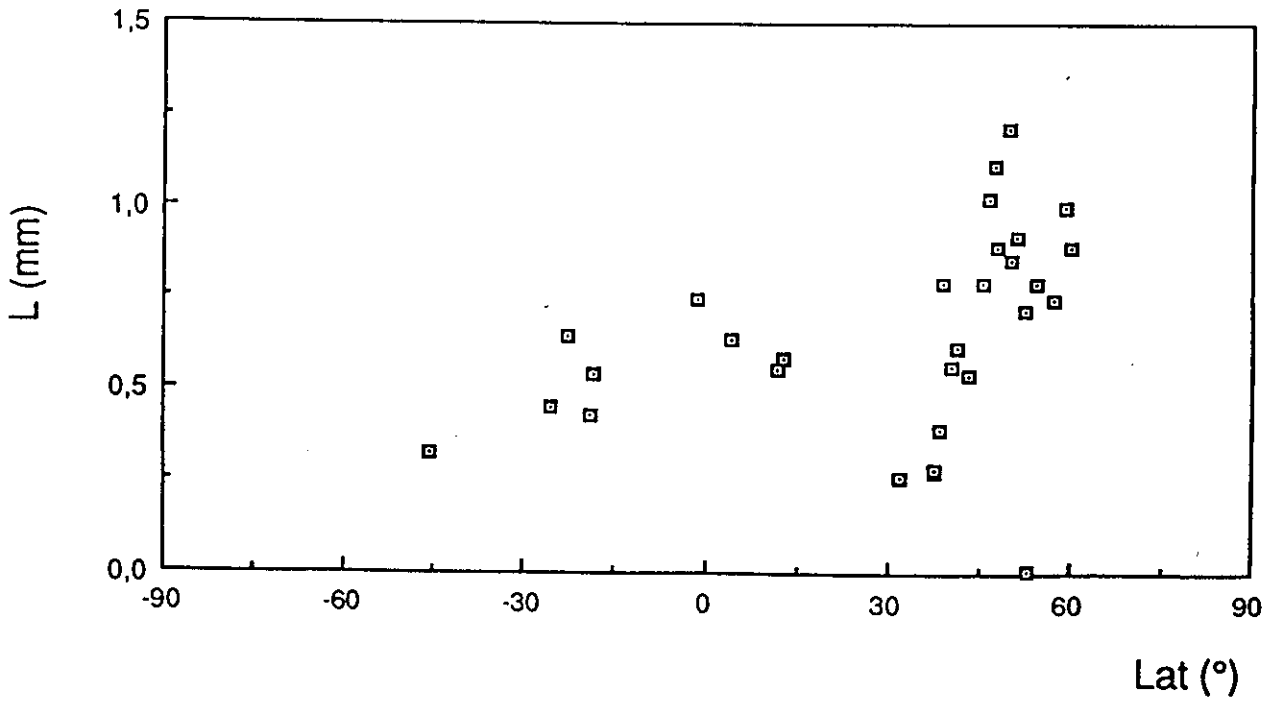

Fig. 7(b): Total liquid content as a function of latitude

INTERNATIONAL ATOMIC ENERGY AGENCY

AND

UNITED NATIONS EDUCATIONAL SCIENTIFIC AND CULTURAL ORGANIZATION

INTERNATIONAL CENTRE FOR THEORETICAL PHYSICS

CLIMATIC INFORMATION FOR SATELLITE COMMUNICATION PLANNING.

PART VII: CLIMATIC AND REGIONAL PARAMETERS FOR SLANT PATH RADIOPROPAGATION PREDICTION MODELS

Prof. G.O. Ajayi
Department of Electronic & Electrical Engineering
Obafemi Awolowo University,
Ile-Ife, Nigeria.

FOURTH ICTP-URSI-ITU (BDT) COLLEGE ON RADIOPROPAGATION:
Propagation, Informatics and Radiocommunication System Planning.

30 January - 3 March, 1995.

1. INTRODUCTION

Radiometeorological variables vary with climate. URSI Commission F and ITU-R Study Group 5 (now Study Group 3) have made several effort in evaluating the climatic and regional effects on the radiometeorological parameters necessary for Earth-Satellite prediction models. Efforts of URSI include:

(i) URSI Commission F Special Open Symposium on "Regional Factors in Predicting Radiowave Attenuation due to Rain, held in Rio de Janeiro, Brazil, Dec. 1990.

(ii) Special Workshop during the Commission F Triennial Symposium at Ravenscar, U.K. on Climatic Classification of radiometeorological parameters for world-wide prediction models, June 1992.

(iii) CLIMPARA '94, Commission F Open Symposium on Climatic Parameters in Radiowave Propagation Prediction, Moscow, June 1994.

The ITU-R has created an ITU-R database for both radio and radiometeorological data.

1.1 Modelling and Climatic Parameters for precipitation (Ref. Hall et al, 1994).

(i) rain, clouds and snow.
(ii) rain cell and cloud structure, size and height
(iii) global and meso-scale modelling
(iv) attenuation (rainfall rate, rain/melt/ice, rain height)
(v) cross polarisation (rainfall rate, hydrometeor type, rain height).
(vi) interference from hydrometeor scatter (rainfall rate, cell size, rain height)
(vii) sky noise from clouds

1.2 Modelling and Climatic Parmeters for Clear-Air Conditions. (Ref: Hall et al, 1994).

(i) structure of the atmosphere (water vapour, temperature, pressure and gases and radio refractive index)
(ii) turbulence
(iii) global and meso-scale modelling
(iv) ducting (intensity, thickness, base height)
(v) layering (intensity thickness, height) for multipath (N_s, $dN/dh < -100N/km$ in the first 100m, ΔN).
(vi) scintillation
(vii) refraction.

Available data, measurements and instrumentation will have to be taken into consideration for both precipitation and clear-air conditions.

2. PHYSICAL OR EMPIRICAL OR PHYSICO-EMPIRICAL MODELLING

How many climatologically dependent variables are required?

Can such variables be determined by independent physical measurement or determined empirically?

For example:

(i) Directly measured meteorological parameter e.g. rainfall rate, R at a point, pressure P, temperature T, and humidity H.

(ii) Derived meteorological parameters: radio refractivity, n from P, T and H.
dN/dh in the first 100m or 1 km from radiosonde data.

(iii) Empirically derived

Effective rain height or effective rain distance from radio data and assumed model. Consider, N climatological dependent variables with loose physical significance, but may not be directly measurable. Each of the N variables is assumed to have an independent classification, with no physical meaning. This type of case results in extreme empirical approach.

In the case of physico-empirical approach, the model is based on relevant physical parameters, but made to fit propagation data, for areas where data are available, through the use of suitable coefficients. The choice of suitable coefficients and physical parameters lead to good predictions of a radio variable on a given path if the related radiometeorological data are available for the path. This technique is applicable to areas with good statistical data for both the radio variable and the radiometeorological parameters. Physical modelling will be able to account for several radiometeorological variables, that will influece the behaviour of the radio variable, thus leading to complexity in the modelling.

3. PRECIPITATION EFFECT AS CASE-STUDY

For estimation of attenuation due to rain or XPD, the rainfall rates, R exceeded for percentages of the year (especially $R_{0.01}$) are utilised. R is directly measurable, ITU-R climatic zones of rain intensity is based on R as parameter.

R has not taken into consideration the climatic factors such as seasonality (which influences the monthly distribution) and the occurrence of raintype which determines the horizontal and vertical structures of rain. The climatic effect is as shown below.

(a)

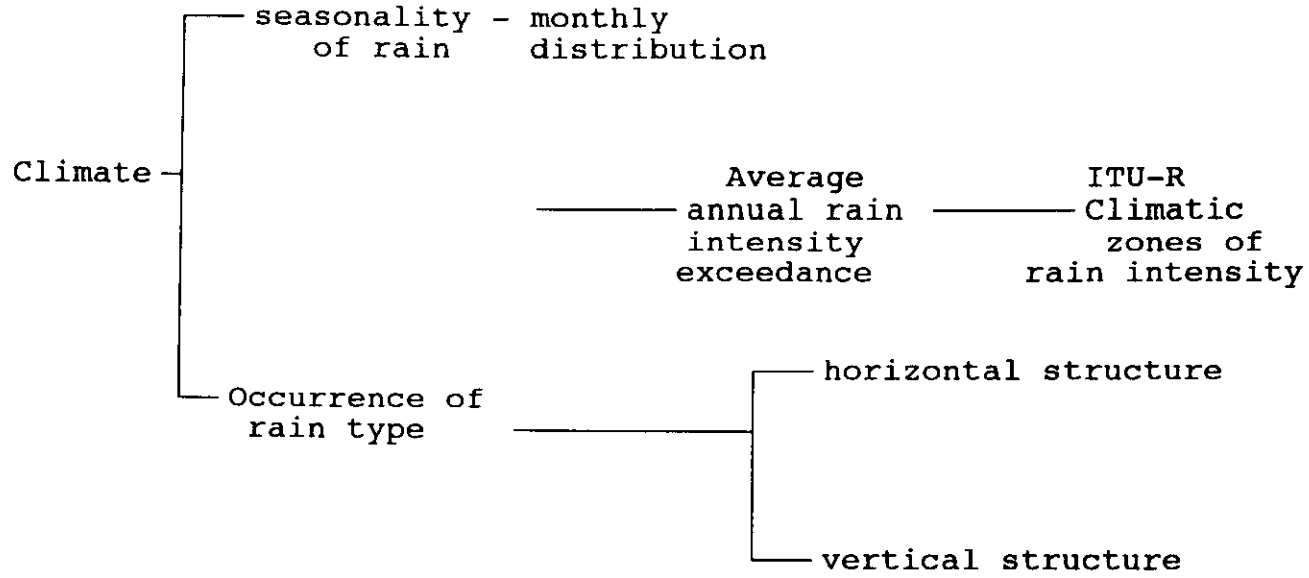

Rain type problem is hidden in R, which is important on Earth-space path since the structure of rainstorms is dependent on rainstorms, which has seasonal and climatic dependence.

Should rain type and seasonality be used for climatic classification?

Worst month factor allows for some seasonal adjustment, but it is not used currently for climatic classification.

Should worst month factor be used as part of input for climatic classification?

Recent low latitude slant path measurements indicate that the ITU-R slant path attenuation model is inadequate for low latitude stations.

Could this inadequacy be due to inadequate horizontal and vertical structures assumed? Is it necessary to provide parameters to account for seasonality and rain type factors?

In addition to taking care of the average year distribution, the seasonality and rain type will account for factors such as vertical and horizontal structures, dropsize distribution, rain cloud structure and occurrence of the melting zone.

Will physical modelling taking care of these parameters be the solution?

Rainstorms can be classified in many ways depending on application as shown below:

Classiciation of Rainstorms

Radio propagation
(Structure of rain)

- Stratiform
- Convective
- Drizzle
- Warm rain

Climatologists
(Process of generation)

- Orography
- Convective
- Frontal
- Cyclonic

For example, effective rain height has seasonal variation in some climates e.g. temperate regions, with strong influence on slant path attenuation. Pronounced diurnal variation of tropical rainfall has seasonal dependence.

Table 1 (Watson, 1994) shows comments on possible modelling parameters for attenuation prediction.

4. LAS AS CASE STUDY

The climatically-related parameters can be illustrated as follows:

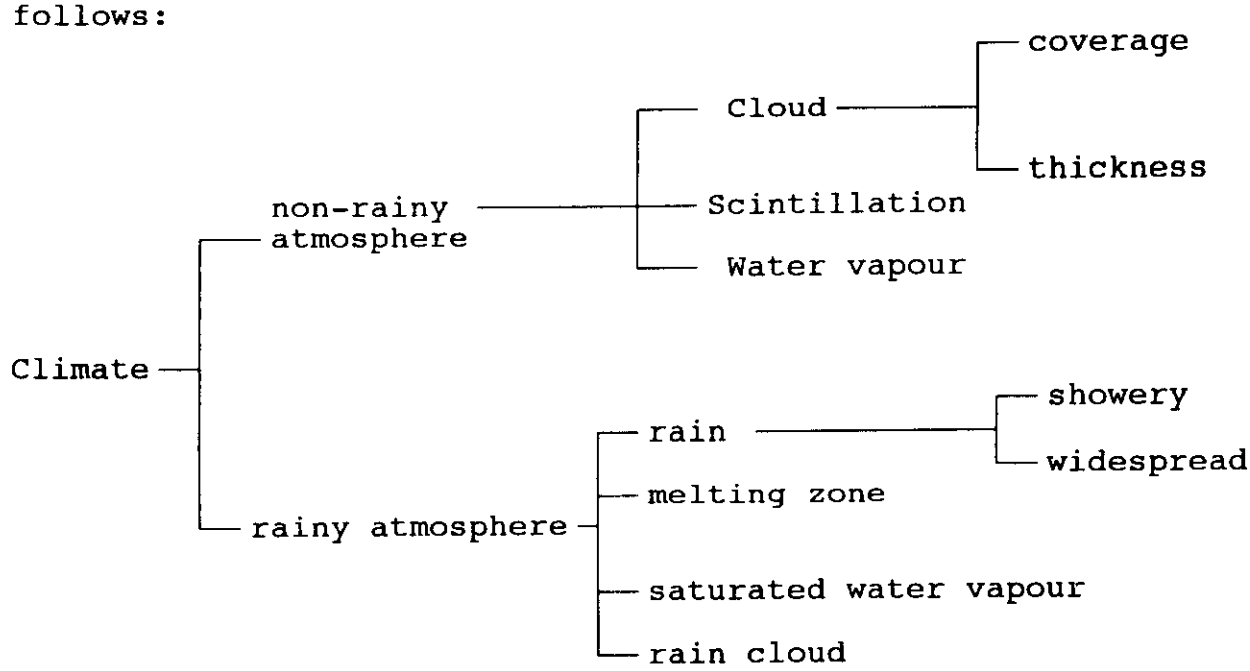

5. CLIMATIC CLASSIFICATION

What type of climatic classification should be used? The classification depends on application.

The main climatic classifications of Koeppen, 1936 is the mostly commonly used, which is based mostly on temperature and rainfall is shown in Table 2.

Is the Koeppen classification suitable for radiopropagation prediction?

Is it necessary to develop unique criteria of climatic classification suitable for radio-propagation prediction?

6. ACQUISITION AND PRESENTATION OF DATA FOR EARTH-SATELLITE PROPAGATION.

ITU-R Recommendation PN. 311 of ITU-R Study Group 3M (formerly of CCIR Study Group 5) deals with the acquisition, presentation and analyses of data in studies of tropospheric propagation. An ITU-R data bank now exists for use in tropospheric prediction models.

For reliable prediction methods of radio propagation effects, one of the essential requirements is the establishment of suitable computer data banks. Such data banks must:

(a) contain all data available that are of an adequate standard;

(b) be widely accepted as the source material on which to conduct testing;

(c) be readily available.

It is a principle of the data banks that they shall contain only such data as may be used for:

(a) testing prediction methods recommended by Study Group 5 (now SG 3) (and may of course be used to test other methods), and

(b) for the creation and updating of radiometeorological maps relevant to the prediction of radio propagation effects.

Appendix 1, which shows the description of the data banks of ITU-R Study Group 3M indicate that Parts II and VII deal with Earth-Space Path Data and Data for Mobile-Satellite Services respectively. Appendices 2 and 3 show respectivey the format for submission of data on Slant path annual rain attenuation and rain rate statistics as well as Slant Path Annual XPD statistics. Appendix 4 shows the results of the slant path attenuation measurements carried out at Ile-Ife submitted to ITU-R.

7. MAPPING OF RADIOCLIMATOLOGICAL PARAMETERS

This is based on the representation of radio-climatological parameters on a high resolution spherical grid with a quasi-constant density of points around the globe.

The relevant data will be made available on a digital computer in digital form. A contouring algorithm will be used to produce contour maps. It makes it possible to implement necessary transformation of coordinates.

The resolution of the digital "map" should be very high, around at least the Nyquist rate for mesoscale phenomena that are in the order of 30 to 50km. This requires a resolution of about 15 to 25 km. The number of points to represent a radioclimatological variable on the earth will be over a million points. Filtering of the original high resolution data should be possible.

The first attempt is the production of the digital form of the ITU-R Rain Climate Map into a "spherical" matrix with an average desntiy of points of at least 25km. The number of points on the sphere is equal to $(N + 1)^2$, where N is the seed for the computer algorithm utilised.

In order to obtain an average density of points equal to around 20km, N should be bigger than 1012 (i.e. total of 1,026,169 points). Figs.1,2,3 show examples for different projections of the Earth of the results obtained with N = 36 (i.e. total number of points on the Earth = 1,369). The digital map will be in terms of rain intensities corresponding to used yearly probability levels rather than in terms of climate letters.

The other radioclimatological parameters to be considered for mapping include Total Rainfall, parameters related to Refractivity, Integrated Liquid Water, Integrated Water Vapour Content, Height of the O C isotherm, Humidity and Surface Temperature.

8. REFERENCES

(1) Dutton, E.J., H.T. Dougherty and R.F. Martin: Prediction of European rainfall and link performance coefficiencts at 8 to 30GHz, Tech. Report ACC-ACO-16-74, Institute for Telecommunication Sciences, U.S.A., Aug. 1974.

(2) Hall, M.P.M., S.E. Benedict, J.V.P. Baptista: Climatic parameters in radiowave propagation prediction-Workshop Objectives, CLIMPARA '94 URSI Open Symposium on Climatic Parameters in Radiowave Propagation Prediction in Moscow, June 1994.

(3) Koeppen, W. : Das geographische system der klimate, Vol.1, Part C of Handbaook der Klimatologre, Gebruder

Borntraeger, Berlin, 1936.

(4) Rice, P.L. and N.R. Holmberg: Cumulative time statistics of surface point rainfall rates, IEEE Trans. Comms COM-21 (10) 1973, 1131-1136.

(5) Watson, P.A.: Climatically-related parameters for prediction of attenuation and cross-polarisation in rainfall, CLIMPARA '94, Moscow, June 1994, 2.1.1 - 2.1.6.

Parameter / Rain Type	1 minute ground rainfall intensity	Rain vertical structure	Rain height	Rain horizontal structure	Rain drop-size distribution
Convective/ Showery	Attenuation prediction possible both from directly measured data and (less accurately) from predicted 1 min intensities from long term data.	Fall velocity variations with barometric pressure in rain region (5 to 10% error over uniform case).	Considerable variability with continentality. Effects of clouds important above ~30 GHz.	Characterised by model cells (or cells plus debris) or point-to-path transformations.	Intensity-related on-average functions appear to be satisfactory (included in AR^B constants). Variability < 10%.
Stratiform/ Widespread	Attenuation less accurately predicted from gauges designed for intense short duration rains. Longer term data may be better	Smaller range of dsd and fall velocity variations, but coalescence towards ground may be significant especially in coastal tropical climates ("warm" rain).	Melting zone must be included (proportionally less significant as frequency increases). Effects of clouds important above ~40 GHz. Uncertainty in tropical climates over occurrence of "warm" rain below 0° isotherm.	Different point-to-path transformations required. Simple uniform models probably not adequate owing to small zones of embedded convection.	Intensity-related dsd becomes dubious for light rains, which for higher frequencies are of some significance.

TABLE 2 MAIN CLIMATIC TYPES OF THE KOEPPEN CLASSIFICATION

Af	Tropical rain forest. Hot; rainy in all seasons
Am	Tropical monsoon. Hot; seasonally excessive rainfall
Aw	Tropical savanna. Hot; seasonally dry (usually winter)
BSh	Tropical steppe. Semiarid; hot
BSk	Mid-latitude steppe. Semiarid; cool or cold
BWh	Tropical desert. Arid; hot
BWk	Mid-latitude desert. Arid; cool or cold
Cfa	Humid subtropical Mild winter; moist all seasons; long, hot summer
Cfb	Marine. Mild winter; moist all seasons; warm summer
Cfc	Marine. Mild winter; moist all seasons; short cool summer
Csa	Interior Mediterranean. Mild winter; dry summer; hot summer
Csb	Coastal Mediterranean. Mild winter; dry summer, short warm summer
Cwa	Subtropical monsoon. Mild winter; dry winter; hot summer
Cwb	Tropical upland. Mild winter; dry winter; short, warm summer
Dfa	Humid continental. Severe winter; moist all seasons; long, hot summer
Dfb	Humid continental. Severe winter; moist all seasons; short, warm summer
Dfc	Subarctic. Severe winter; moist all seasons; short cool summer
Dfd	Subarctic. Extremely cold winter; moist all seasons; short summer
Dwa	Humid continental. Severe winter; dry winter; long hot summer
Dwb	Humid continental. Severe winter; dry winter; warm summer
Dwc	Subarctic. Severe winter; dry winter; short, cool summer
Dwd	Subarctic. Extremely cold winter; dry winter; short, cool summer
ET	Tundra. Very short summer
EF	Perpetual ice and snow
H	Undifferentiated highland climates

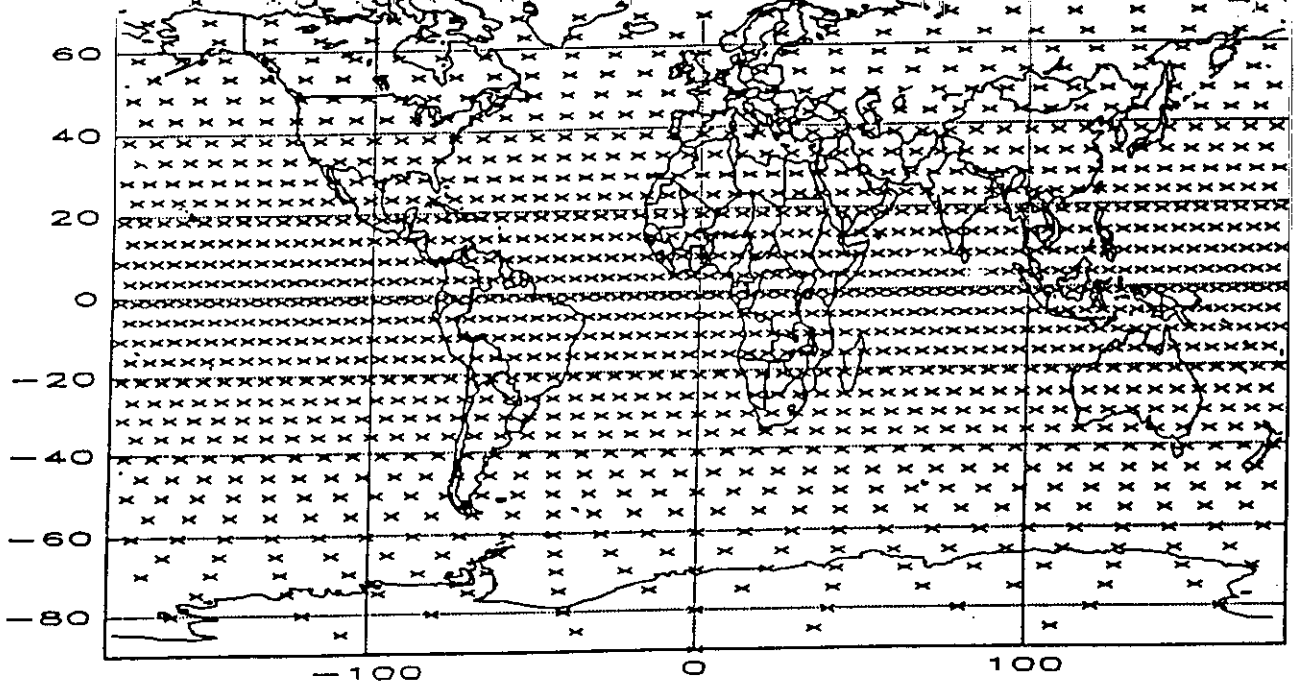

FIGURE 1

Cartesian projection of the map of the world with smapling points for N = 36

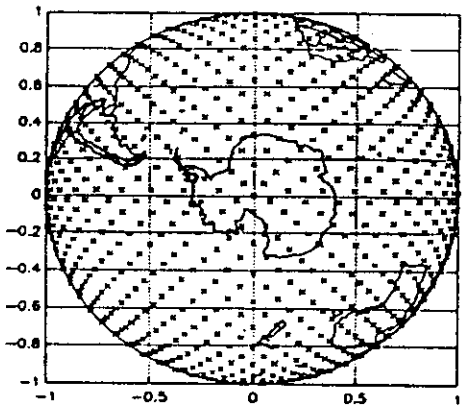

FIGURE 2

The Earth seen from above the Antarctic with N = 36

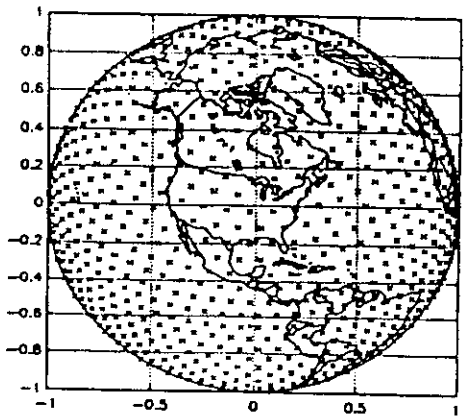

FIGURE 3

as Figure 2 but seen from 40 N, 90 W

10

Description of the data banks of Study Group 5

PART I - TERRESTRIAL LINE-OF-SIGHT PATH DATA

Table I-1: Line-of-sight rain attenuation statistics

Table I-2: Line-of-sight average worst-month multipath fading and enhancement in narrow bandwidths

Table I-3: Line-of-sight diversity data

Table I-4: Line-of-sight clear sky XPD and CPA statistics

Table I-5: Line-of-sight XPD and CPA statistics due to precipitation

Table I-6: Line-of-sight multipath channel characteristics and outage times

PART II - EARTH-SPACE PATH DATA

Table II-1: Slant path annual rain attenuation and rain rate

Table II-2: Slant path worst-month rain attenuation statistics

Table II-3: Slant path fade duration statistics

Table II-4: Slant path site diversity statistics

Table II-5a: Slant path annual XPD statistics

Table II-5b: Slant path annual XPD statistics conditioned to CPA

Table II-6: Slant path statistics of amplitude scintillations

Table II-7: Slant path standard deviations of scintillations

PART III - TERRESTRIAL TRANS-HORIZON PATH AND RAIN SCATTER DATA

Table III-1: Clear-air trans-horizon basic transmission loss statistics

Table III-1a: Clear-air spot measurement data[1]

Table III-2: Rain Scatter on terrestrial paths

PART IV - RADIOMETEOROLOGICAL DATA

Table IV-1: Statistics of rain intensity

Table IV-2: Rain integration time conversion factor

Table IV-3: Annual statistics of sky noise temperature

Table IV-4: Statistics of refractivity

PART V - TERRESTRIAL LAND MOBILE DATA

Table V-1: Terrestrial land mobile wideband statistics

Table V-2: Terrestrial land mobile narrowband statistics

PART VI - TERRESTRIAL BROADCASTING DATA

Table VI-1: Terrestrial broadcasting signal level variation with time

Table VI-2: Terrestrial broadcasting signal level variation with location

PART VII - DATA FOR MOBILE-SATELLITE SERVICES

Table VII-1: Wideband statistics for mobile-satellite services

Table VII-2: Narrowband statistics of maritime mobile satellite links

Table VII-3: Narrowband statistics of land mobile satellite links

Table VII-4: Narrowband statistics of aeronautical mobile satellite links

Part II: Earth-space path data

TABLE II-1 · Slant path annual rain attenuation and rain rate statistics

Station number
Receive station
RX site name
RX country (1)
RX latitude (-90..+90) (deg)
RX longitude (0..360) (deg) E
RX altitude amsl h_{gr} (m)
RX antenna height ag h_r (m)
RX 3 dB beamwidth Θ_r (deg)
RX rain zone (2)
RX antenna type
RX antenna diameter D (m)
RX antenna feed type
RX radome (Y/N)
RX figure of merit (dB/K)
RX clear-sky level XPD_0 (dB)
RX max. side-lobe angle < 4 (deg)
RX rel. level of maximum side lobe (dB)
RX dynamic range (dB)
RX integration time (s)

Measurement: Exp Nr
Satellite name
Satellite orbital position (deg) E
Type of experiment
Start date (yyyy.mm.dd)
End date (yyyy.mm.dd)
Duration (days)
Frequency (GHz)
Polarization (L/C)
Polarization tilt φ_p(deg)
Elevation angle (deg)
RG data concurrent (Y/N)
Medium temp. (if radiometer) T_{med} (K)
Data sampling interval (s)
Calibration interval (days)
Data resolution (dB)
Rain gauge type
RG resolution (mm/h)
RG integration time (s)
RG location relative to receiver
Attenuation presented as excess or total (E/T)

Table: (3)

Rain rate exceeded for percentage of the year, R (mm/h)

Attenuation exceeded for percentage of the year, A (dB)

Perc. of year (%)	0.001	0.002	0.003	0.005	0.01	0.02	0.03	0.05
R (mm/h)	.	.	.	.	.	.	.	.
A (dB)	.	.	.	.	.	.	.	.
Perc. of year (%)	0.1	0.2	0.3	0.5	1	2	3	5
R (mm/h)	.	.	.	.	.	.	.	.
A (dB)	.	.	.	.	.	.	.	.
Perc. of year (%)	10	20	30	50				
R (mm/h)	.	.	.	.				
A (dB)	.	.	.	.				

References:

Comments:

(1) See § 6.1 for list of country codes.

(2) See Recommendation ITU-R PN.837.

(3) It is preferred that cumulative distributions for individual years (= 12 consecutive months) be submitted rather than distributions averaged over several years. For beacon measurements an indication should be given, how the 0 dB reference level was established in the comments (i.e. by radiometer, by pre- and post event level linking, etc.).

APPENDIX 3

TABLE II-5a - Slant path annual XPD statistics

Station number
Receive station
RX name
RX country (1)
RX latitude (-90..+90) (deg)
RX longitude (0..360) (deg) E
RX altitude amsl h_{gr} (m)
RX antenna height ag h_r (m)
RX 3 dB beamwidth Θ_r (deg)
RX antenna type
RX antenna diameter D (m)
RX antenna feed type
RX radome (Y/N)
RX figure of merit (dB/K)
RX clear-sky level XPD_0 (dB)
RX maximum side-lobe angle < 4 (deg)
RX rel. level of maximum side lobe (dB)
RX dynamic range (dB)
RX integration time (s)

Measurement: Exp Nr
Satellite name
Satellite orbital position (deg) E
Start date (yyyy.mm.dd)
End date (yyyy.mm.dd)
Duration (days)
Frequency (GHz)
Polarization (L/C)
Polarization tilt φ_p (deg)
Elevation angle (deg)
Rain zone (2)
RG data concurrent (Y/N)
Data sampling interval (s)
Calibration interval (days)
Data resolution (dB)
Rain gauge type
RG resolution (mm/h)
RG integration time (s)
RG location relative to RX
Attenuation presented as excess or total (E/T)
Cancellation method (3)

Table:
XPD not exceeded for percentage of time (dB)
Attenuation exceeded for percentage of time (dB)
Rain rate exceeded for percentage of time (mm/h)

Percentage of year (%)	0.001 0.1 10	0.002 0.2 20	0.003 0.3 30	0.005 0.5 50	0.01 1	0.02 2	0.03 3	0.05 5
XPD not exceeded (dB)								
Attenuation exceeded (dB)								
Rain rate exceeded (mm/h)								

References:

Comments:

(1) See § 6.1 for list of country codes.
(2) See Recommendation ITU-R PN.837.
(3) For XPD cancellation, the following options apply: 1: none, 2: static, 3: software.

Subject: DATA BANKS

INTELSAT and NIGERIA

CONTRIBUTION(*) TO THE PROPAGATION DATA BANKS: SIMULTANEOUS RAINFALL RATE AND Ku-BAND EARTH-SPACE RADIOMETRIC MEASUREMENTS IN NIGERIA

Introduction

An experiment was conducted using an 11.6 GHz radiometer in Ile-Ife, Nigeria, from 1 July 1987 to 30 June 1989. Only the results of the second year of simultaneous measurement of skynoise and rainfall rate are reported here [1].

Experiment details and results

The characteristics of the Ile-Ife site are described in the information set out in the three tables, which conform to the format of Reference [2]. Two of the tables give the annual statistics of rain attenuation and sky-noise temperature, while the third gives the worst month rain attenuation information.

Table No.	Statistics Recorded	Reference 2 Table
Table 1	annual rain attenuation	Table II-1
Table 2	worst month	Table II-2
Table 3	sky noise temperature	Table IV-3

(*)This document contains the results of studies conducted within INTELSAT, with the close participation of the Signatory of Nigeria and COMSAT Laboratories, and which the Signatory of Nigeria and the Board of Governors/Technical have authorised to be submitted to WP 3J and WP 3M of ITU-R Study Group 3 to contribute to the ongoing discussions of the matters discussed therein.

References

[1] D.K. McCarthy, J.E. Allnutt, W.E. Salazar, E.C. Omeata, B.R. Owolabi, T. Oladiran, E.B. Ojeba, G.O. Ajayi, T.I. Raji, and C. Zaks, 'Results of an 11.6 GHz radiometric experiment in Nigeria: Second Year', *Electronics Letters*, 1994, **Vol. 30**, No. 17.

[2] 1992-CCIR Recommendations, RPN Series: Propagation in Non-Ionized Media, Rec. 311: 'Acquisition, Presentation and Analysis of Data in Studies of Tropospheric Propagation', p. 1, et seq.

Table II-1 Annual rain attenuation and rain rate

Experiment	**Joint African Radiometric Measurement Program**	**Data sample interval [s]**	**strip charts <15s; digital: 6s**
Experiment number X#	**Year 2**	**Calibration interval [days]**	**see ref.**
		Data resolution [K/LSB]	**0.4**
Receive station		**Rain gauge type**	**TB - Tipping Bucket**
CCIR zone	**N/P**	**RG resolution [mm/h]**	**1 mm/h**
RX site name	**Ile-Ife**	**RG integration time [s]**	**1 min approx.**
RX country	**Nigeria**	**RG location rel. to receiver**	**<10 m**
RX latitude [deg] N	**7.33° N**		
Rx longitude [deg] E	**4.34° E**	**Satellite name**	**n/a**
RX altitude amsl [m]	**274 m**	**Satellite orbital pos.[deg]**	**n/a**
RX antenna height ag [m]	**20 m**	**Type of experiment**	**R - skynoise radiometer**
RX 3dB beam-width [deg]	**1.0°**		
RX antenna type	**symmetrical paraboloid**	**Start date (yyyy.mm.dd)**	**1988.07.01**
RX ant. diameter D [m]	**1.8 m**	**End date (yyyy.mm.dd)**	**1989.06.30**
RX ant. feed type	**front-fed**	**Duration [days]**	**8769 h (RM); 8771 h (RG)**
RX radome (Y/N)	**no**	**Frequency [GHz]**	**11.6 GHz**
RX figure of merit [dB/K]	**n/a**	**Polarization (L/C)**	**linear**
RX clear sky level XPD [dB]	**n/a**	**Polarization tilt [deg]**	**0°**
RX max side lobe [dB] angle<4 [deg]	**n/a**	**Elevation angle**	**48.3°**
RX rel level of max side lobe [dB]	**n/a**	**Rg data concurrent (Y/N)**	**yes**
RX dynamic range [dB]	**n/a**	**Medium temp. (if Radiometer) [K]**	**285**
RX integration time [s]	**3 s**		

Attenuation presented as Excess or Total (E/T): Total

Table:
Rain rate exceeded for % of the year R [mm/h]
Attenuation exceeded for % of the year A [dB]

% of Year	0.001	0.002	0.003	0.005	0.01	0.02	0.03	0.05
Attenuation [dB]	-	-	-	-	-	14.3	12.0	10.2
Rainrate [mm/h]	143	122	112	99	82	67	60	50
% of Year	0.1	0.2	0.3	0.5	1	2	3	5
Attenuation [dB]	8.0	5.3	3.7	2.7	1.7	1.2	1.1	1.0
Rainrate [mm/h]	34	17	11	5	2	1	-	-
% of Year	10	20	30	50				
Attenuation [dB]	0.9	0.8	0.8	0.7				
Rainrate [mm/h]	-	-	-	-				

References: D.K. McCarthy, J.E. Allnutt, W.E. Salazar, E.C. Omeata, B.R. Owolabi, T. Oladiran, E.B. Ojeba, G.O. Ajayi, T.I. Raji, and C. Zaks, ' Results of an 11.6 GHz radiometric experiment in Nigeria', Electronics Letters, 1994, Vol. 30, No. 17.

Comments:

Note:

Table II-2 Worst month rain attenuation statistics

Experiment	Joint African Radiometric Measurement Program	Data sample interval [s]	strip charts <15s; digital: 6 s
Experiment number X#	Year 2	Calibration interval [days]	see ref.
		Data resolution [K/LSB]	0.4
Receive station		**Rain gauge type**	TB - Tipping Bucket
CCIR zone	N/P	RG resolution [mm/h]	1 mm/h
RX site name	Ile-Ife	RG integration time [s]	1 min approx.
RX country	Nigeria	RG location rel. to receiver	<10 m
RX latitude [deg] N	7.33° N		
Rx longitude [deg] E	4.34° E	Satellite name	n/a
RX altitude amsl [m]	274 m	Satellite orbital pos.[deg] E	n/a
RX antenna height ag [m]	20 m	Type of experiment	R - skynoise radiometer
RX 3dB beam-width θ_r [deg]	1.0°		
RX antenna type	symmetrical paraboloid	Start date (yyyy.mm.dd)	1988.07.01
RX ant. diameter D [m]	1.8 m	End date (yyyy.mm.dd)	1989.06.30
RX ant. feed type	front-fed	Duration [days]	8769 h (RM); 8771 h (RG)
RX radome (Y/N)	no	Frequency [GHz]	11.6 GHz
RX figure of merit [dB/K]	n/a	Polarization (L/C)	linear
RX clear sky level XPD [dB]	n/a	Polarization tilt [deg]	0°
RX max side lobe [dB] angle<4 [deg]	n/a	Elevation angle	48.3°
RX rel level of max side lobe [dB]	n/a	RG data concurrent (Y/N)	yes
RX dynamic range [dB]	n/a	Medium temp. (if Radiometer) [K]	285
RX integration time [s]	3 s		

Attenuation presented as Excess or Total (E/T): Total

Table:
Rain rate exceeded for % of the month R [mm/h]
Attenuation exceeded for % of the month A [dB]

% of Month	0.001	0.002	0.003	0.005	0.01	0.02	0.03	0.05
Attenuation [dB]	-	-	-	-	-	-	-	-
Rainrate [mm/h]	191	162	150	134	115	88	75	68
% of Month	0.1	0.2	0.3	0.5	1	2	3	5
Attenuation [dB]	12.4	9.5	7.9	5.8	3.3	2.4	1.6	1.1
Rainrate [mm/h]	57	42	29	18	7	3	2	1
% of Month	10	20	30	50				
Attenuation [dB]	1.0	0.9	0.8	0.8				
Rainrate [mm/h]	-	-	-	-				

References: D.K. McCarthy, J.E. Allnutt, W.E. Salazar, E.C. Omeata, B.R. Owolabi, T. Oladiran, E.B. Ojeba, G.O. Ajayi, T.I. Raji, and C. Zaks, 'Results of an 11.6 GHz radiometric experiment in Nigeria', Electronics Letters, 1994, Vol. 30, No. 17.

Comments:

Note: For the definition of the worst month refer to recommendation 581.

Table IV-3 - Annual statistics of sky noise temperature

Experiment Joint African Radiometric Measurement Program

Experiment number X#	Year 2
CCIR rain zone	N/P
Radiometer station	
Type of RM	Dicke-switched
RM site name	Ile-Ife
RM country	Nigeria
RM latitude [deg] N	7.33° N
RM longitude [deg] E	4.34° E
RM altitude amsl [m]	274 m
RM antenna height ag [m]	20 m
RM 3 dB beam-width θ_r [deg]	1.0°
RM antenna type	symmetrical paraboloid
RM ant. diameter D [m]	1.8 m
RM ant. feed type	front-fed
RM radome (Y/N)	no
RM max side lobe angle <4° [dB]	n/a
RM rel level of max side lobe [dB]	n/a
RM dynamic range [dB]	n/a
RM integration time [s]	3 s
RM bandwidth [MHz]	n/a
	5 - 300

Data sample interval [s]	strip charts <15s; digital: 6s
Calibration interval [days]	see ref.
Data resolution [K/LSB]	0.4
Rain gauge type	TB - Tipping Bucket
RG resolution [mm/h]	1 mm/h
RG integration [s]	1 min approx.
RG location rel. to receiver	<10 m
RG data concurrent (Y/N)	yes
RG accumulation per tip [mm/tip]	0.254
RG aperture [cm^2]	314
Start date (yyyy.mm.dd)	1988.07.01
End date (yyyy.mm.dd)	1989.06.30
Duration [days]	8769 h (RM), 8771 h (RG)
Frequency [GHz]	11.6 GHz
Polarization (L/C)	linear
Polarization tilt [deg]	0°
Elevation angle [deg]	48.3°
Radiosonde data collected (Y/N)	N
Temperature recorded (Y/N)	Y
Humidity measured (Y/N)	N
Pressure measured (Y/N)	N
Cloud cover recorded (Y/N)	N

Table:
Sky noise temperature exceeded for % of the year T_{SKY} [K]
Rain Rate exceeded for % of the year R [mm/h]

% of Year	0.001	0.002	0.003	0.005	0.01	0.02	0.03	0.05	0.1	0.2	0.3	0.5
	1	2	3	5	10	20	30	50				
T_{SKY}	294	292	290	288	285	275	268	258	240	199	163	126
[K]	86	60	51	46	43	41	39	35				
Rain Rate	143	122	112	99	82	67	60	50	34	17	11	5
[mm/h]	2	1	-	-	-	-	-	-				

References: D.K. McCarthy, J.E. Allnutt, W.E. Salazar, E.C. Omeata, B.R. Owolabi, T. Oladiran, E.B. Ojeba, G.O. Ajayi, T.I. Raji, and C. Zaks, 'Results of an 11.6 GHz radiometric experiment in Nigeria', Electronics Letters, 1994, Vol. 30, No. 17.

Comments: